DEPARTAMENTO DE FÍSICA TEÓRICA Y DEL COSMOS

Universidad de Granada

ANALYSIS OF THE BRIGHT GALAXY POPULATION IN THE CORE OF CLUSTERS OF GALAXIES AT MEDIUM REDSHIFT

Begoña Ascaso Anglés

Memoria de Tesis

presentada en la Universidad de Granada

para optar al grado de Doctor en Astrofísica.

Director de la Tesis

Prof. Mariano Moles Villamate

INSTITUTO DE ASTROFÍSICA DE ANDALUCÍA-CSIC

Junio-2008

Editor: Editorial de la Universidad de Granada
Autor: Begoña Ascaso Anglés
D.L.: GR.1611-2008
ISBN: 978-84-691-4848-8

A mis padres

Lo mejor para la tristeza -contestó Merlin, empezando a soplar y resoplar- es aprender algo. Es lo único que no falla nunca. Puedes envejecer y sentir toda tu anatomía temblorosa; puedes pemanecer durante horas por la noche escuchando el desorden de tus venas; puedes echar de menos a tu único amor, puedes ver al mundo a tu alrededor devastado por locos perversos; o saber que tu honor es pisoteado por las cloacas de inteligencias inferiores. Entonces sólo hay una cosa posible: aprender. Aprender por qué se mueve el mundo y lo que hace que se mueva. Es lo único que la inteligencia no puede agotar, ni alienar, que nunca la torturará, que nunca le inspirará miedo ni desconfianza y que nunca soñará con lamentar, de la que nunca se arrepentirá. Aprender es lo que te conviene. Mira la cantidad de cosas que puedes aprender: la ciencia pura, la única pureza que existe. Entonces puedes aprender astronomía en el espacio de una vida, historia natural en tres, literatura en seis. Y entonces después de haber agotado un millón de vidas en biología y medicina y teología y geografía e historia y economía, pues, entonces puedes empezar a hacer una rueda de carreta con la madera apropiada, o pasar cincuenta años aprendiendo a empezar a vencer a tu contrincante en esgrima. Y después de eso, puedes empezar de nuevo con las matemáticas hasta que sea tiempo de aprende a arar la tierra."

Terence White, 'The Once and Future King'

Acknowledgements

A lo largo de esto cuatro años de doctorado, además de realizar una tesis, he tenido la ocasión de conocer y trabajar con muchísimas personas. Muchas de ellas, son hoy las responsables de que esta tesis se haya llevado a cabo por una infinidad de motivos que voy a intentar resumir.

En primer lugar, quiero agradecer a las personas que han hecho posible que mi sueño de trabajar en Astrofísica haya sido posible. A Mariano Moles, mi jefe, y la persona que me brindó la oportunidad de hacer un doctorado en Astrofísica y a mis dos jefes 'adoptivos', Alfonso Aguerri, quien en mi etapa inicial del doctorado me brindó gran parte de su tiempo y sus conocimientos, enseñándome a ser rigurosa y metódica en la Ciencia y a Txitxo Benítez, quien en mi etapa final, me ofreció la oportunidad de trabajar con él y su equipo en Estados Unidos, me dió el privilegio de intercambiar todo tipo de ideas científicas y siempre fue raudo en prestarme su apoyo y sus consejos. Millones de gracias.

Seguidamente, debo mi agradecimiento a otras tres personas por su ayuda directa con el trabajo de esta tesis. Jesús Varela, quien con paciencia y amabilidad, siempre estuvo dispuesto a ayudarme a solventar cualquier pequeño detalle que pudiera surgir con el tratamiento de los datos y fue una fuente de inspiración para seguir muchos de sus pasos. Ruben Sánchez-Janssen, por sus pacientes lecciones de IDL y sus valiosos comentarios y Jairo Méndez-Abreu por el enorme trabajo de calidad realizado en en análisis de brillo superficial.

Aussi, je suis très reconnaissant à Chantal Balkowski, qui m'a fait sentir à la maison dans mon étape à Paris et má encouragé à interagir et de discuter de nombreux sujets astrophysiques. Thanks a lot to Holland Ford too, who let me collaborate with him and his group and gave me many good pieces of advice during my stage in Baltimore. Gracie mille to Daniella Bettoni and Giuseppe Galletta, for leading me in my first steps in Astrophysics, not only during my stage in Padova but with my first observations in La Palma. Asímismo, nunca dejaré de agradecer a una de las personas que me dió el lujo y la oportunidad de aprender a su lado, me introdujo en la Astrofísica y me dió la llave para continuar después, Guillermo González-Casado.

Por otra parte, quiero agradecer a esas personas que hemos coincido en Granada y que me han prestado su apoyo en cualquier momento difícil y su sonrisa en cualquier otro. En primer lugar, a Carlos Barceló, desde la primera semana uno de mis pilares granainos, un buen amigo y una de las personas más sabias del mundo. Gracias, mozo, por todos los consejos, el apoyo y las laaaargas conversaciones sobre la vida, la cosmología, la filosofía y cualquier cosa que se nos viniera a la cabeza.

A Silbieta López de la Calle, una de las personas más honesta que he conocido a lo largo de mi vida, y que me ha brindado la oportunidad de ser su amiga. Gracias por todo, día tras día, conversación tras conversación, risa tras risa, bajón tras bajón, paseo tras paseo. A Cristiñiña Rodriguez, que su ejemplo de esfuerzo continuo y su apuesta por un sueño, me ha dado fuerza en muchas ocasiones para seguir adelante. Además, un placer arreglar el mundo cuando este se nos venía encima, y volver a levantarlo, y volver a sonreír. Graciñas. A Emilio García, un cielazo siempre dispuesto a ayudarme en cualquier momento, ya sea empollándose los paquetes de Fortran para explicármelos luego, con una palabra de ánimo en el momento justo o con un muñequito de la suerte. Mil gracias también por hacer de los meses de escritura mucho más llevaderos.

A Geli Martínez y Omaira González, por todos los momentos que caben en estos cuatro años y la suerte de haber compartido piso, despacho(s), nombres falsos (Yenni, Monica y Sofía) y muchas cosas más con ellas. Gracias por todos los ánimos, cables, plastilina y muchos etcéteras prestados. A Susi Vidal, esa personita que aún tarde nos dimos cuenta que estábamos hechas de material muy parecido, y disfrutamos de todo ello. A David Orozco, una ayuda de IDL andante eternamente despistado. A Yoli Jimenez, que sus 'claridades' han hecho esfumar cualquier 'bulto' que se infiltrara por el camino y su admirable tenacidad, que me ha servido de ejemplo en numerosas ocasiones. Infinitas gracias, quilla. A Gabriella Gilli, por lo bien que me sientan esos paseos Albayzineros o en cualquier lugar del mundo, que hayan muchos más.

También quiero agradecer a Pepa Masegosa, Isabel Márquez y Choni del Olmo por ayudarme a entender que si no hubiera bajadas no habría subidas en el camino. Gracias guapas. A Jaime Perea por sus valiosas indicaciones sobre cualquier asunto informático. A Juande, por estar siempre dispuesto a echar un cable, de cualquier tipo, desinteresadamente, y en cualquier momento. A Antxon Alberdi, por esa honestidad combinada siempre con una palabra amable para Carmencita. A Lucas Lara, por haber sido un ejemplo de ilusión y entusiasmo en todos los aspectos. A Benja Montesinos, por esos ánimos y esa buena memoria. A Jose Luis Jaramillo, por todas las largas conversaciones sobre ciudades remotas o granadas. Y a todos y cada uno de los becarios, gracias por todos los buenos ratos que hemos pasado.

Cómo no, a Silvia y a Carmen, por enseñarme a vivir al 100% y a saber apreciar lo que es realmente importante de manera definitiva. Mi gratitud también a Simon Verley, quién desinteresadamente, me ofreció su apartamento en París, con vistas a la Torre Eiffel, y él, junto con su familia, me trataron como una más de su familia haciendo de París uno de los mejores períodos de mi vida. Y a Vic Serey y Nacha Echevarría, quienes me acogieron, me cuidaron y me trataron tan bien, en mi estancia en Baltimore. Gracias por el mapa tan genial con las zonas chungas de Baltimore y por las buenas conversaciones, la buena música, y los buenos momentos.

Por último, he de agradecer a todos mis amigos que aunque estén fuera de Granada, me siguen apoyando en cualquiera de mis empresas y que han permitido conservar nuestra amistad a pesar de la distancia.

A mis clavelinas oscenses: Aneta O., Cristifina, Blanquita, Mariajo, Jareta C, Marieta G, Maria S., Patri, Jareta S., Aneta B., Beita, Marcus, Vane, Eva.. por llenar mi vida de alegria continua, de amparo, de buenos consejos, de risas, juergas cubiteras, de San Lorenzos increibles, y también por hacerme participe de vuestras penas e ilusiones. En concreto a Patricia, por esas largísimas conversaciones que nunca acabamos, y que me tanto bien me hacen.

Al meus primitivos (i allegados) barcelonins: Gemma, Laia, Meritxell, Gemmita, Maria, Miquel, Tito, Pau, Rut, Ferran, Francesc, Aly, Marc, Marcel, Helena, Eva, Joan, Arruebo, Àngel, M. Carmen, Beto... merci per ser així. Ja sabeu la meva teoria sobre la formació definitiva de cadascú. Jo estic segura que tots estem de la mateixa pasta i m'encanta. Gràcies. A Gemmita, en particular, per obligar-me a ser feliç definitivament i donar-me el millor dels consells.

A Núria Font, per la seva força i el seu empeny de ser feliç. A Pere Pascual, por haberme animado a hacer el doctorado y haber sido mi 'padre adoptivo' durante los años de facultad, a la vez que un amigo. A Ade La Sierra, por todos las palabras de ánimo regaladas desde siempre. A los Agripinos oscenses, en especial a Elena Alayeto, por esos tropecientos años que llevamos arreglando el mundo y a Jorge Vidal, por el ímpetu que le pones a la vida. A Lloi Burdalo, por tener siempre la mesa del cafetín lista para un café. A Manu, por esos largos mails llenos de luz y fuerza, y por todos los lazos de lana rojos diseminados por el mundo. A Maca, por toda la fuerza, ánimos, ejemplo y alegría que me ha proporcionado desde que nos conocemos.

Finalmente, a mis padres, Leoné y Carmencita y mi a hermana y cuñao, Magda y Albert. Millones de gracias por respetar y apoyar cada una de mis decisiones, por estar siempre, inquebrantablemente allí y por haber sido el mejor de los ejemplos de esfuerzo, tenacidad, alegría y sabiduría. Os quiero.

Y, a todos aquellos que estos años han pasado a ser parte de mi vida, no los cito, porque afortunadamente, son muchos, pero no les olvido.

Contents

Acknowledgments **7**

I Introduction **17**

Resumen **19**

1 Introduction **23**

1.1 Clusters of Galaxies 24

1.2 Brightest Cluster Galaxies 26

1.3 Motivations and Aims of the thesis 26

1.4 Brief description of the thesis chapters 27

2 Clusters Sample **29**

2.1 Nordic Optical Telescope Cluster Sample 30

2.1.1 Comments on the sample 31

2.1.2 Data reduction 33

2.1.3 Calibration 33

2.1.4 Astrometrical Calibration. 34

2.1.5 Extraction of the sources 35

2.1.6 Photometric corrections 37

2.2 Advanced Camera for Surveys Clusters 40

2.2.1 Comments on the sample 41
2.2.2 Reduction and Calibration of the frames 43
2.2.3 Extraction of the sources 44
2.2.4 Photometric corrections 45

II Characterization of the bright central galaxy population in Clusters 47

3 Color-Magnitude Relation 49

3.1 Color-Magnitude Diagram 51
3.1.1 Completeness Limit 51
3.1.2 Interlopers 52
3.1.3 Color-Magnitude Fit 54
3.1.4 Color-Morphology 56
3.1.5 CMR slope-Redshift 57
3.2 The Butcher-Oemler Effect 62

4 Galaxy Morphology 69

4.1 Visual classification 70
4.2 The concentration parameter 75
4.3 Interaction systems 76

5 Galaxy Surface Brightness Analysis 79

5.1 Previous analysis 81
5.2 Two dimensional surface brightness fit 82
5.2.1 GASP-2D 82
5.2.2 Simulations 84
5.2.3 Galaxies with one photometrical component 85
5.2.4 Galaxies with two photometrical components 87

5.2.5 Number of components 90
5.3 Quantitative Morphology 93
5.3.1 Qualitative versus Quantitative Classification 94
5.4 Structural parameters 95
5.4.1 Sersic Parameters 95
5.4.2 Disc Parameters 103
5.4.3 Bulge and disc parameters 105

6 Spatial Distribution **109**
6.1 Galaxy Density 110
6.1.1 Density Estimation 110
6.1.2 Morphology-Density Relation 114
6.1.3 Luminosity-Density Relation 116
6.2 Radial Distribution 121
6.2.1 Center of the cluster 121
6.2.2 Radius-Density Relation 122
6.2.3 Radius-Morphology Relation 123

7 Luminosity Function **131**
7.1 Background Contamination Estimation 132
7.2 The Composite Luminosity Function 135
7.3 Fit of the Luminosity Function 137
7.3.1 Chi-Square fitting 138
7.3.2 Chi-Square integral fitting 147
7.3.3 Maximum Likelihood Method 149
7.4 Luminosity - Morphology relation 155
7.5 Luminosity - Color relation 160
7.6 Universality 167

III The Brightest Cluster Galaxies 169

8 The Brightest Cluster Galaxies: BCGs 171

8.1 BCGs population . . . 172

8.2 Extraction Algorithm . . . 173

8.3 Analysis . . . 178

8.3.1 Degree of Dominance . . . 178

8.3.2 Morphology . . . 183

8.3.3 Surface Brightness . . . 184

8.3.4 Hubble Diagram . . . 189

8.4 Are they Standard Candles? . . . 195

IV Results and Conclusions 197

9 Conclusions and Future Prospects 199

9.1 Conclusions . . . 200

9.1.1 Bright Galaxy Population . . . 200

9.1.2 Brightest Cluster Galaxies . . . 204

9.2 Future Prospects . . . 206

9.3 Conclusiones . . . 207

9.3.1 Población Galáctica Brillante . . . 207

9.3.2 Galaxia Más Brillante del Cúmulo . . . 211

Bibliography and references 215

V Appendix 231

A Catalogue of galaxies belonging to the NOT sample 233

B Surface Brightness Fit of the NOT clusters galaxies **243**

C NOT BCGs sustraction **283**

D ACS BCGs sustraction **287**

List of Figures

2.1 Magnitude difference for different frames for A1952 and A2111 . 39

3.1 Absolute magnitude histogram of the galaxies in the NOT clusters sample 51

3.2 Absolute magnitude histogram of the galaxies in the ACS clusters sample 52

3.3 CM Diagrams and B-r distance to the CMR histograms for the NOT sample 56

3.4 CM Diagrams and g-r distance to the CMR histograms for the ACS sample 57

3.5 CM Morphological Diagrams and B-r distance to the CMR histograms for the NOT sample 59

3.6 CM Morphological Diagrams and g-r distance to the CMR histograms for the ACS sample 61

3.7 Comparison of the slopes of the CMR for the sample of López-Cruz et al. (2004) and this thesis sample 62

3.8 Galaxy Blue fraction of NOT and ACS sample compared with Aguerri et al. (2007) sample within an aperture of 420 and 475 Kpc 65

3.9 Galaxy Blue fraction of NOT and ACS sample compared with Aguerri et al. (2007) sample within an aperture of 735 Kpc . . . 66

4.1 The visual classification differences between Fasano et al. (2000) and this work. 71

4.2 The visual classification differences between Duc et al. (2002) and this work for A1689. 72

4.3 The visual classification differences between Treu et al. (2003) and this work for CL0024. 72

4.4 The visual classification differences between Fabricant, Franx & van Dokkum (2000) and this work for MS1358. 73

4.5 Comparison of the concentration parameter from this work clusters sample, a low-redshift compilation (Butcher & Oemler (1978)) and a higher redshift sample (Dressler et al. (1997)) 76

4.6 Histogram of the f-parameter values for the galaxies belonging to NOT sample. 78

4.7 Histogram of the f-parameter values for the galaxies belonging to ACS sample. 78

5.1 Plots of the magnitudes versus parameters of the Sersic profile . 85

5.2 Cumulative distribution of the simulations versus area for a Sersic Profile 86

5.3 Absolute Gunn-r magnitude Versus Area for the galaxy population in NOT sample 87

5.4 Cumulative distribution of the simulations versus area for a Sersic +Disc Profile 88

5.5 Sersic+ Disc profile parameters versus its error 89

5.6 Plots of the Sersic+ Disc profile parameters versus its error for $m_r \leq 20$, $\mu_{0,B} \leq 25.3$ and $\mu_{O,D} \leq 25.3$. The green and red lines are the quartile and percentile of the error respectively in bins. (Landscape) 91

5.7 Plots of the Sersic+ Disc profile parameters versus its error for $m_r \leq 20$, $\mu_{0,B} \leq 25.3$ and $\mu_{O,D} \leq 25.3$ and B/T ≤ 0.7. The green and red lines are the quartile and percentile of the error respectively in bins. (Landscape) 92

5.8 Examples of profiles 1 to 5 following the notation of MGC. . . . 93

5.9 The visual classification differences between Sánchez et al. (2007) and this work for A2218. 95

5.10 Kormendy relation between effective ratius and mean surface brightness for all the sample of galaxies 97

5.11 Relation between effective ratius and shape parameter for one component galaxies 98

5.12 Absolute Gunn-r Magnitude versus μ_o, n and B/T 99

5.13 B-r color versus μ_o, n and B/T 100

5.14 Radius versus Bulge Scales for Coma and NOT sample 101

5.15 Radius versus shape parameters for Coma and NOT sample . . . 102

5.16 Absolute Gunn-r Magnitude versus disc scale. 103

5.17 Radius versus Bulge Scales for Coma and NOT sample 104

5.18 Cumulative function of disc scales for the NOT sample, Aguerri et al. (2004) Coma Cluster and Graham (2001) isolated sample . 105

5.19 Adimensional parameters. n versus r_e/h and B/T versus r_e/h . . 106

5.20 Relation between effective ratius and disc scales 107

6.1 Distribution of the local density for the whole NOT sample. . . . 111

6.2 Distribution of the local density for the whole ACS sample. . . . 112

6.3 Distribution of the local density for each cluster in NOT sample 112

6.4 Distribution of the local density for each cluster in ACS sample . 113

6.5 Distribution of the local density into three morphological types for the whole NOT sample. 115

6.6 Distribution of the local density into three morphological types for the whole ACS sample. 116

6.7 Distribution of the local density into three morphological types for individual clusters in NOT sample. 117

6.8 Distribution of the local density into three morphological types for individual clusters in ACS sample. 117

6.9 Absolute Gunn-r magnitude versus local density into 3 morphological types for the whole NOT sample. 118

6.10 Absolute Gunn-r magnitude versus local density into 3 morphological types for the whole ACS sample. 118

6.11 Absolute Gunn-r magnitude versus local density into 3 morphological types for the individual clusters in NOT sample. 119

6.12 Absolute Gunn-r magnitude versus local density into 3 morphological types for the individual clusters in ACS sample. 120

6.13 Radius-Density Relation for NOT sample 124

6.14 Radius-Density Relation for ACS sample 125

6.15 Radius-Morphology Relation by morphological types in NOT sample clusters 126

6.16 Radius-Morphology Relation by morphological types in ACS sample clusters 127

6.17 Cumulative functions of the different morphological types as a function of the projected radius to the center of the cluster for the NOT sample 128

6.18 Cumulative functions of the different morphological types as a function of the projected radius to the center of the cluster for the ACS sample 129

7.1 Background Contamination Subtraction for NOT sample 133

7.2 Background Contamination Subtraction for ACS sample 134

7.3 Composite Luminosity Function for NOT sample 136

7.4 Composite Luminosity Function for ACS sample 136

7.5 Best Schechter fit of the Composite LF for the NOT sample . . . 141

7.6 Best Schechter fit of the Composite LF for the ACS sample . . . 142

7.7 Best fit of the differential LF for the NOT sample 143

7.8 Best fit of the differential LF for the ACS sample 144

7.9 Best fit of the differential LF for the NOT sample with α=-1.15 . 145

7.10 Best fit of the differential LF for the ACS sample with α=-1.15 . 146

7.11 Best fit of the cumulative LF for the NOT sample 149

7.12 Best fit of the cumulative LF for the ACS sample 150

7.13 LF for Early Types galaxies in NOT sample clusters 156

7.14 LF for Late Type galaxies in NOT sample clusters 156

7.15 LF for Early Type galaxies in ACS sample clusters 157

7.16 LF for Late Type galaxies in ACS sample clusters 157

7.17 Composite LF for Early Type galaxies in NOT sample 158

7.18 Composite LF for Late Type galaxies in NOT sample 158

7.19 Composite LF for Early Type galaxies in ACS sample 159

7.20 Composite LF for Late Type galaxies in ACS sample 159

7.21 LF for Red galaxies in NOT sample clusters 161

7.22 LF for Blue galaxies in NOT sample clusters 162

7.23 LF for Red galaxies in ACS sample clusters 163

7.24 LF for Blue galaxies in ACS sample clusters 164

7.25 Composite LF for Red galaxies in NOT sample 164

7.26 Composite LF for Blue galaxies in NOT sample 165

7.27 Composite LF for Red galaxies in ACS sample 165

7.28 Composite LF for Blue galaxies in ACS sample 166

8.1 BCGs population in NOT sample 173

8.2 BCGs population in ACS sample 174

8.3 A1689 (ACS) and A1952 (NOT) smoothed images 176

8.4 A1689 BCGs inadequate subtractions 177

8.5 A1689 BCGs subtraction 179

8.6 Degree of Dominance versus BCG magnitude 180

8.7 Degree of Dominance versus Δm_2 182

8.8 Redshift versus Degree of Dominance 182

8.9 Cluster Richness Class versus Degree of Dominance 183

8.10 Deviation of the surface brightness profiles from the De Vaucouleurs profiles for the NOT BCGs 185

8.11 Deviation of the surface brightness profiles from the De Vaucouleurs profiles for the ACS BCGs 186

8.12 Four model fits to the surface brightness profiles for the NOT BCGs 191

8.13 Four model fits to the surface brightness profiles for the ACS BCGs193

8.14 Hubble Diagram for the BCGs in NOT and ACS sample 194

8.15 K-band Hubble Diagram for this work BCGs sample and Collins & Mann (1998) sample 195

B.1 One and Two dimensional Surface Brightness Profiles for the Galaxies in NOT sample 281

C.1 A1643 BCG subtraction 283

C.2 A1878 BCG subtraction 284

C.3 A1952 BCG subtraction 284

C.4 A2111 BCG subtraction 284

C.5 A2658 BCG subtraction 285

D.1 A1689 BCG subtraction 287

D.2 A1703 BCG subtraction 287

D.3 A2218 BCG subtraction 288

D.4 CL0024 BCG subtraction 288

D.5 MS1358 BCG subtraction 288

List of Tables

2.1 The global sample of NOT Clusters 30

2.2 NOT Clusters Observations 31

2.3 Calibration Coefficients in NOT Cluster Sample 34

2.4 Errors Measurements 38

2.5 The global sample of ACS Clusters 40

2.6 ACS WFC Clusters Observations 40

2.7 Errors Measurements for the ACS sample 45

3.1 Redshift Information for the ACS Clusters 53

3.2 Foreground Galaxies for the NOT Clusters 54

3.3 Foreground Galaxies for the ACS Clusters 54

3.4 CMR parameters in NOT sample 55

3.5 CMR parameters in ACS sample 55

3.6 Blue galaxy fraction of galaxies in NOT sample 64

3.7 Blue galaxy fraction of galaxies in ACS sample 64

4.1 Fraction of Morphological Types in NOT sample 73

4.2 Fraction of Morphological Types in ACS sample 74

4.3 Concentration Parameter in NOT Clusters 75

4.4 Median Perturbation f-Parameter for NOT Clusters Sample . . . 77

4.5 Median Perturbation f-Parameter for ACS Clusters Sample . . . 77

5.1 Visual Morphological Types versus Quantitative Morphological Types for the NOT sample 94

5.2 Bulge parameters for Coma and NOT sample 102

5.3 Disc parameters for Coma and NOT sample 104

6.1 Mean Densities for NOT Clusters 114

6.2 Median Densities for ACS Clusters 114

6.3 Centers Considered in NOT Clusters 122

6.4 Centers Considered in ACS Clusters 123

7.1 Best Schechter Parameters of the Luminosity Function with and without the BCG for the NOT sample 143

7.2 Best Schechter Parameters of the Luminosity Function with and without the BCG for the ACS sample 144

7.3 Best Schechter Parameters of the Luminosity Function with α=-1.15 for the NOT sample 146

7.4 Best Schechter Parameters of the Luminosity Function with α=-1.15 for the ACS sample 147

7.5 Best Schechter Parameters of the Cumulative Luminosity Function for the NOT sample 150

7.6 Best Schechter Parameters of the Cumulative Luminosity Function for the ACS sample 151

7.7 Best Schechter Parameters of the Luminosity Function using the Maximum Likelihood method with $\alpha = -1.15$ for the NOT sample 154

7.8 Best Schechter Parameters of the Luminosity Function using the Maximum Likelihood method with $\alpha = -1.15$ for the ACS sample 155

7.9 Best Schechter Parameters of the Cumulative Luminosity Function for Early and Late Types for the NOT sample 160

7.10 Best Schechter Parameters of the Cumulative Luminosity Function for Early and Late Types for the ACS sample 160

7.11 Best Schechter Parameters of the Cumulative Luminosity Function for Red and Blue Galaxies for the NOT sample 167

7.12 Best Schechter Parameters of the Cumulative Luminosity Function for Red and Blue Galaxies for the ACS sample 167

8.1 BCGs in NOT Clusters 174

8.2 BCGs in ACS Clusters 175

8.3 Degree of Dominance in NOT BCGs Sample 181

8.4 Degree of Dominance in ACS BCGs Sample 181

8.5 BCGs de Vaucouleurs fit 187

8.6 BCGs Sersic fit 187

8.7 BCGs Sersic plus Exponential fit 188

8.8 BCGs Sersic plus Sersic fit 189

Part I

Introduction

Resumen

Yo deshojé las constelaciones, hiriéndome,
afilando los dedos en el tacto de estrellas,
hilando hebra por hebra la contextura
helada de un castillo sin puertas,
oh estrellados amores cuyo
jazmín detiene su transparencia en vano.

Pablo Neruda, 'El hondero. Canto General. Yo Soy.'

El preguntarse sobre nuestros orígenes es una característica inherente de la Humanidad. Qué somos, qué estamos haciendo aquí, cómo es el mundo que nos rodea, cómo es el Universo en el que estamos inmersos, qué son toda la infinidad de puntos allá arriba .. A finales del siglo XX, el mundo pareció olvidarse de esto, los cielos dejaron de estar limpios y cada vez es más y más difícil encontrar lugares con cielo limpio.

Es, sin embargo, en este siglo, cuando se han realizado los mayores pasos para la comprensión de nuestro Universo, fuera de nuestro Sistema Solar local. Entre 1920 y 1924, Edwin Hubble demostró que la nebulosa de Andrómeda era, en realidad, una galaxia y que, muchas agrupaciones de puntos luminosos eran enormes universos estelares, situados mucho más allá de nuestra propia Galaxia, la Vía Láctea. Con el desarrollo de la fotografía y la construcción de telescopios cada vez más potentes, se observó que las galaxias se alejaban unas de otras con una velocidad proporcional a sus distancias, así como aumentaban, a su vez, el tamaño del Universo.

En la actualidad, la Astrofísica ha experimentado un avanze impresionante gracias al desarrollo en las últimas décadas de los recursos de observación (telescopios espaciales, como el Telescopio Espacial Hubble (HST), XMM-Newton, Chandra ...) y herramientas de cálculo (simulaciones, con ordenadores cada vez más potentes). Estamos viviendo una época de sorprendentes descubrimientos. La Humanidad es consciente de su pequeñez, día tras día.

Esta tesis recoge el trabajo realizado en una muestra de diez Cúmulos de Galaxias a *redshift* intermedio. Las principales motivaciones para el estudio de estos objetos son, por un lado, el hecho de que hay muy pocos grupos analizados en un rango intermedio de *redshift* hasta la fecha, (Fasano et al., 2000; Trujillo et al., 2001c; Fasano et al., 2002), debido a las dificultades en la profundidad y la calidad de las observaciones.

Con la llegada de telescopios espaciales, ha crecido el número de cúmulos observados a distancias cada vez más grandes, pero se ha seguido prestando poca atención a este rango de *redshift*. Sin embargo, se piensa que es especialmente interesante y sorprendente en lo que respecta al análisis de la velocidad de la evolución de las características de las galaxias. El estudio de la evolución cósmica o las propiedades de cúmulos de galaxias y su varianza con el *redshift* es un pilar básico para comprender el origen y formación de estos objetos, así como también, del Universo.

Por otro lado, el estudio de las Cúmulos de Galaxias no locales hace necesaria la aproximación práctica de considerar que todas las galaxias en el cúmulo estan al mismo *redshift* que el del propio cúmulo. Este hecho, convierte a estos objetos en excepcionales agrupaciones de galaxias para analizar sus propiedades y compararlas con otras poblaciones de galácticas.

En la presente tesis, se ha estructurado el contenido en cuatro partes. La primera parte está dedicada a la introducción de las materias generales en que se han trabajado, junto con una presentación de la muestra de los Cúmulos de Galaxias que se han analizado y una explicación detallada sobre la reducción y el proceso de calibración de la muestra investigada.

La segunda parte está dedicada al análisis de las principales características de la población de galaxias brillantes en la parte central de la muestra de cúmulos. En el Capítulo 3, hemos estudiado la relación Color-Magnitud y el Efecto Butcher-Oemler. En el Capítulo 4, se han asignado los diferentes tipos morfológicos visuales de la población de galaxias, y se ha profundizado en el estudio de la concentración de galaxias de los Cúmulos y la distribución de las fuerzas de marea.

El siguiente Capítulo, 5 se refiere al análisis del brillo superficial de la población galáctica del NOT, con su correspondiente análisis de los parametros estructurales derivados. Más adelante, encontramos el Capítulo 6, que describe la investigación realizada en la distribución espacial de la muestra. Finalmente, el último capítulo de esta parte, Capítulo 7 , examina el análisis de la Función de Luminosidad, proporcionando diferentes métodos para la realización del ajuste y estudio de sus parámetros deducidos.

La tercera parte de la tesis está completamente dedicada a la Galaxia más brillantes del Cúmulo o BCG, de sus siglas en inglés. Hemos detallado un algoritmo para la extracción de la BCG del potencial del cúmulo en la primera parte

y seguidamente, hemos analizado las principales características de la población de BCGs, en cuanto a su grado de dominancia, morfología o distribución de brillo superficial. La última parte ha sido dedicada al estudio de la identidad de estos objetos como 'Candelas Estándares'.

Por último, la parte final es una recopilación de los principales resultados y conclusiones del trabajo desarrollado en la tesis, con una observación final sobre las perspectivas futuras.

El Anexo contiene el catálogo de galaxias y el análisis de los perfiles de brillo superficial de la muestra NOT por una lado, y por otro, los resultados de la extracción de las BCG para ambas muestras.

Chapter 1

Introduction

Recordo una nit, a l'altra banda del Pirineu,
que sortí de la fosca una nena que cantava amb veu de fada.
Vaig demanar-li que em digués quelcom en la seva llengua pròpia
i ella, tota admirada, signà'l cel estrellat i féu només així:
'Lis esteles...'

Joan Maragall, 'Elogi de la Paraula Viva'

To wonder about our origins is an inherent characteristic of humanity. Who we are, what we are doing here, how the world around us is, how the Universe in which we are embedded is, what all the infinity of points up there are, etc... At the end of the XX century, people in the world seemed to forget about that, as the skies were not clear anymore and everytime is more and more difficult to find a piece of clean sky.

It is however, in this century, when the greatest steps for understanding our Universe, outside our local Solar System, have been performed. Between 1920 and 1924, Edwin Hubble proved that Andromeda nebula was a Galaxy and that, many point of lights were huge stellar universes, placed much farther than our own Galaxy, the Milky Way. With the development of the photography and the building of more powerful telescopes, the Galaxies were observed to move away from each other with a velocity that was proportional to their distances, as well as they increased, at the same time, the size of the Universe.

At present, the Astrophysics has experimented a stunning progress thanks to the development in the last decades of observational resources (spacial telescopes, like Hubble Space Telescope (HST), XMM-Newton, Chandra...) and calculus tools (simulations with more and more powerful computers). We are living an astonishing era of discoveries. The Humankind realizes about its smallness, day after day.

This thesis is based on one of the most exciting structures in the Universe: Clusters of Galaxies. It is entitled *Analysis of Bright Galaxy Population in the Core of Clusters of Galaxies at medium redshift.* Throughout this introduction, we have elaborated a historical and conceptual motivation of the objects we are going to study in this thesis.

1.1 Clusters of Galaxies

Cluster of galaxies are the largest structures, gravitationally bounded, in the Universe, with sizes of several Mpcs and masses from $10^{14} - 10^{16}$ $M_{\odot}$. They are composed by many to thousand of galaxies and millions of stars. Clusters are usually formed by a core, where the highest concentration of galaxies are found. Moreover, between the galaxies, a **plasma or gas** composed mainly by ionized hydrogen exits, which is detected due to its X-ray emission. In addition, studies of gas and galaxy dynamics in cluster show that the largest part of these systems distributes continously, througout the region occupied by gas and galaxies. That matter, known as **dark matter** does not emit any kind of electromagnetic radiation and it's only interacting gravitationally with gas and galaxies, forming the **halo**.

Prior to 1949, only a few dozen clusters were known. In the fifities and early sixties, the first catalogues of hundreds to thousands of clusters were published (Zwicky et al. (1952, 1953, 1956); Abell (1958)). In particular, two main catalogs of rich clusters of galaxies established the definitive criteria for the present definition of a cluster. The catalog of rich clusters by Abell (1958) and the Catalogue of Galaxies and Clusters of Galaxies by Zwicky et al. (1961). Both authors identified clusters on the Palomar Sky Survey plates.

Abell catalogue lists 2712 clusters in the redshift range $0.02 \leq z \leq 0.2$. He set some requirements for including the clusters in his catalogue regarding to their richness, compactness or galactic-latitude. On the other hand, Zwicky catalogue contained more clusters and also systems that are less rich than those of Abell, as he set less strict criteria concerning their properties.

Also, different classification schemes for clusters of galaxies were developed. The **Rood-Sastry (RS) classification** was given by Rood & Sastry (1971), who classified clusters according to the distribution of the ten brightest members. Their classification account of five different types, *cD-type (supergiant)* which refer to those clusters dominated by a cD galaxy, *B-type (binary)*, referring to clusters dominated by a bright binary system, *L-type (line)*, which are those clusters which three or more of the ten brightest members are arranged in a line. *C-type (core)* are clusters with at least four of the ten brightest members are located with comparable separations in the cluster core and *F-type (flat)* allude to clusters with several of the brightest ten galaxies are distributed in a flattened configuration and, finally, the *I-type (irregular)* are an irregular distribution of the galaxies with a no well-defined center.

Additionally, the **Bautz-Morgan (BM) classification** system was provided by Bautz & Morgan (1970) and their system was based on the relative contrast of the brightest galaxy to the other galaxies in each cluster. The following types were set, *Type I* refers to cluster dominated mainly by a single, centrally located, cD galaxy. *Type II* are for those cluster whose brightest members are intermediate in appearance between cD galaxias (with extended envelopes) and normal giant ellipticals. Finally, *Type III* contains all the clusters without a dominant galaxy. That classification also include intermediate types: *Type I-II* and *Type II-III*.

Furthermore, Morgan (1962); Oemler (1974) introduced the classification of clusters according to the morphological type of their bright members. They can be divided in the following groups: *spiral-rich clusters* which have a composition similar to that of the field, with a high proportion of spiral galaxies. They are also irregular in appearance, with low mean densities, no tendency to central concentration, flat central density gradient and no segregation by morphological type or evidence of relaxation by two-body encounters. *cD clusters* are dominated by central supergiant galaxies and have no spirals in their cores. They contain a much higher proportion of ellipticals in the central regions than other cluster types. They are dense, centrally concentrated, spherical in appearance, have steep central density gradients, and show evidence of two-body relaxation. Finally, *spiral-poor clusters* are referred to those clusters with a composition dominated by SO galaxies. They show segregation by mass and morphological type, they are not as regular, compact or centrally condensed as the cD clusters.

A number of fenomena is produced in clusters of galaxies. They are real laboratories to study processes such as **Gravitational Lensing**, (Tyson & Fischer, 1995; Kneib et al., 1996; Broadhurst et al., 2005a; Diego et al., 2005) or effects that only are noticeable on very large structures, **the Sunyaev-Zel'dovich effect** in X-ray clusters, (Sunyaev & Zel'dovich, 1970, 1972; Bonamente et al., 2006; Ascaso & Moles, 2007), etc. They allow also to model their dark matter density profiles, (Navarro, Frenk & White, 1995; Ascaso & González-Casado, 2003).

An additional advantage of studying clusters of galaxies is that we can consider that all the galaxy population remains at the same distance. Therefore, we can perform different comparison between the galaxies properties, (Fasano et al., 2000; Aguerri et al., 2004; Varela, 2004), study their evolution with redshift, (López-Cruz et al., 2004; Mei et al., 2006; Driver, 2006) or even the galaxy kinematics inside the clusters, (Navarro, Frenk & White, 1995; Łokas et al., 2006).

Numerous studies up to date have been devoted to the formation of clusters of galaxies. However, two main scenarios for its clarification still remain. On one hand, we have the monolithic scenario in which the clusters were formed first (Bower et al. (1998)) and on the other, we have the hierarchical scenario (Kauffmann, Guiderdoni & White (1994); De Lucia & Blaizot (2007)), in which the galaxies were formed at the outset.

The monolithic scenario implies that the galaxies are not suffering substantial transformations after the cluster collapse (Merritt, 1984) while the hierarchical scenario would imply that the environmental effects and interactions are transforming the galaxy population due to mechanisms that were operational until recent epochs, such as harassment (Moore et al. (1996)), gas-stripping (Gunn & Gott , 1972; Quilis et al., 2000), starvation (Bekki, Couch & Shioya (2002)), or merging (Gerhard & Fall, 1983; Aguerri, Balcells & Peletier, 2001; Eliche-Moral et al., 2006). Likewise, the evolution of the galaxy population in clusters of galaxies has been broadly studied in many works.

Few works have been dedicated to study the morphology of the galaxy population at z$\approx$ 0.2. The morphological studies have been generally confined to rather local samples, in part due to the need to establish a visual classification (Dressler (1980); Fasano et al. (2000)) and more generally, to the difficulties to get deep and high-resolution images for relatively large fields. Some of these studies have tried to establish an automatic morphological classifications by inspecting the galaxies surface brightness and their main structural parameters. Nevertheless, those samples have often been preselected to be only late type (De Jong (1996b); Graham & de Blok (2001)) or early type (Graham (2003)). As a consequence, the present number of clusters that have been studied in that redshift range is small (Fasano et al. (2000); Trujillo et al. (2001c); Fasano et al. (2002)).

1.2 Brightest Cluster Galaxies

The **Brightest Cluster Galaxies (BCGs)** are the most luminous and massive galaxies in the universe. They are usually placed close to the center of its host cluster and seem to be aligned with the cluster galaxy distribution. As a consequence, they have been suggested to lie at the bottom of the cluster's gravitational potential well. The origin of BCGs appears to be closely connected to the formation of the cluster.

The typical characteristics of the BCGs can be summarized as elliptical galaxies that are much brighter and much more massive than the average, with luminosities $\approx 10L_*(L_* = 1.0 \times 10^{10}h^2L_\odot)$, (Schombert, 1986; Dubinski, 1998; Seigar, Graham & Jerjen, 2007), with very little rotational support and central velocity dispersions around $\approx 300 - 400kms^{-1}$, (Fisher, Illingworth & Franx, 1995).

The term **cD galaxy** was introduced by Matthews, Morgan & Schmidt (1964) to describe a galaxy with the nucleus of a giant elliptical surrounded by an extended, slowly decreasing envelope. Not all the BCGs are cD galaxies. They are extremely large, with high luminosity, and frequently contain multiple nuclei. They are half of the way between usual galaxies and clusters as far as size and luminosity is concerned.

In addition, those objects has been set as candidates to 'standard candles' for the measurement of cosmological distances, (Sandage, 1972a,c; Gunn & Oke, 1975;

Hoessel & Schneider, 1985; Lauer & Postman, 1994; Postman & Lauer, 1995). In fact, one of the most studied subjects in the literature regarding to BCGs is the increase of the range of k-band Hubble Diagram, (Aragón-Salamanca, Baugh & Kauffmann, 1998; Collins & Mann, 1998; Burke, Collins & Mann, 2000; Brough et al., 2005), achieving a dispersion of 0.3. However, the matter still remains unsolved as a number of BCGs are needed still to set a conclusion. What it is true is that BCGs are remarkably homogeneous in luminosity, specially those selected within X-ray properties.

1.3 Motivations and Aims of the thesis

This thesis collects the work performed in a sample of ten clusters of galaxies at medium redshift. The main motivations for the study of these particular objects are, on one hand, the fact that there are very few analyzed clusters in a medium range of redshift up to date, (Fasano et al., 2000; Trujillo et al., 2001c; Fasano et al., 2002). This fact is due to difficulties in the depth and quality of the observations.

With the advent of spatial telescopes, the number of clusters imaged at larger and larger redshift has grown but these range of redshift continues being overlooked. However, we think that that range of redshift can be specially interesting and surprising as far as the examination of the speed of the evolution of the galaxies' features is concerned. The study of the cosmic evolution or the properties of clusters of galaxies and their variance with redshift is a basic point for understanding the origin and formation of these objects, and likewise, the Universe.

On the other hand, the study of non-local clusters of galaxies makes necessary the feasible approximation of considering that all the galaxies in the cluster are at the same redshift that the cluster itself. That fact makes that objects exceptional aggregations of galaxies to analyze its properties and compare them with other galactic populations.

Throughout this thesis, we have adopted the standard ΛCDM cosmology with H_0=71 km s^{-1} Mpc^{-1}, Ω_m=0.27 and Ω_Λ=0.73.

1.4 Brief description of the thesis chapters

In this report, we have structured the contents into four parts. The first part is devoted to the introduction of the general subjects we have worked, together with a presentation of the sample of clusters of galaxies we have analyzed and an explanation of the reduction and calibration process of this sample set.

The second part is dedicated to the analysis of the main characteristics of the bright galaxy population in the central part of the clusters samples. In Chapter 3, we have studied the Colour- Magnitude Relation and the Butcher-Oemler

Effect. The Chapter 4 is dedicated to the assignment of morphological visual types to the galaxy population, the study of the galaxy concentration of the clusters and the tidal forces distribution.

The subsequent Chapter, 5 refers to the analysis of the surface brightness of the NOT galaxy population, with the corresponding investigation into the derived structural parameters. Further on, we find Chapter 6, which describes the research performed in the spatial distribution of the sample. Finally, the last Chapter in this part, Chapter 7 examines the analysis of the Luminosity Function, providing different methods for performing the fits and studying their extracted parameters.

The third part of the thesis is completely dedicated to the Brightest Cluster Galaxies or BCGs. We have detailed an algorithm for the extraction of the BCG from the cluster potential in the first part and subsequently, we have analyzed the main characteristics of the BCG population, regarding to the degree of dominance, morphology or surface brightness. We have dedicated the last part to the study of the identity of these objects as Standard Candles.

Finally, the last part is a compilation of the main results and conclusion of the work developed in the report, with a final remark on the future prospects.

The Annex contains the catalogue of the galaxies in NOT sample and the analysis of surface brightness profiles for the NOT sample on one hand and on the other, the results of the extraction of the BCG for both samples.

Chapter 2

Clusters Sample

Mercurio de rampas y hélices,
grumos de luna entre tensores y placas de bronce;
pero el hombre ahí, el inversor, el que da vuelta a las suertes,
el volatinero de la realidad:
contra lo petrificado de una matemática ancestral,
contra los husos de la altura destilando sus hebras
para una inteligencia cómplice,
telaraña de telarañas,
un sultán herido de diferencia yergue su voluntad enamorada,
desafía un cielo que una vez más propone las cartas transmisibles.

Julio Cortazar, 'Prosa del Observatorio'

In this Chapter, we describe the observational cluster sample at medium redshift is described. The sample consist on ten clusters of galaxies within the medium redshift range $0.17 \leq z \leq 0.39$. On one hand, five of those clusters were imaged with Nordic Optical Telescope (NOT) from the Ground and, therefore, we will refer to them as **NOT sample**. On the other hand, the other half of the sample consist on five more clusters imaged with Advanced Camera of Surveys (ACS) in the Hubble Space Telescope (HST) and consequently, we will allude to them as **ACS sample**.

Both samples are centered in the very central part or the core, covering the ≈ 1 central Mpc^2, being somewhat smaller for the ACS sample. The NOT sample is complete up to $M_r^* + 1$ magnitude, while the ACS sample achieves the completeness at $\approx M_r^* + 3$. As a consequence, we will perform most of the work in the $M_r^* + 1$ magnitude range, except in some cases that we will take advantage of the good quality of the ACS data set.

That medium redshift galaxy cluster sample was conceived in order to continue and explore the establishment of the clusters properties in the immediately

following redshift range respect to local samples (such as Wide-Field Imaging Nearby Galaxy-Cluster Survey (WINGs); Fasano et al. (2006), Sloan Digital Sky Survey (SDSS), York et al. (2000)). That range of redshift ($0.15 \lesssim z \lesssim 0.4$) has been very little observed for a long time, due to its technical limitations. They need a very good quality of seeing to be observed from the Ground, to be able to resolve the galactic population inside the clusters, for example. In addition, the size of the CCD needs to be large enough to be able to sample a sustancial part of the cluster. With the advent of the Hubble Space Telescope (HST), those compromises were solved at the same time, as we will see in the ACS sample. However, the NOT sample is the first sample of clusters at medium redshift, observed from the Ground with very good conditions of seeing.

2.1 Nordic Optical Telescope Cluster Sample

The first half of the sample consist on five galaxy clusters imaged at the 2.5m Nordic Optical Telescope (NOT). That Telescope is located at the Roque de Los Muchachos Observatory (La Palma, Canary Islands). The observations were taken from May to June 1995 with the Stand Camera whose field of view is $3^{'} \times 3^{'}$. This CCD has a plate scale of $0.176^{''}$/pix, a gain of 1.69 e^{-}/ADU and a readout noise of 6.36 e^{-}.

In Table 2.1, the information about the observed galaxy clusters is collected. Columns 1, 2,3 and 4 show the cluster name, the center obtained by Nasa Extragalactic Data Base (NED)[1]. The redshift, Bautz-Morgan Type, Rood-Sastry type and Richness Class is listed in the four last columns, respectively.

Table 2.1: The global sample of NOT Clusters

Name	$\alpha(2000)$			$\delta(2000)$			z	$BMtype$	$RStype$	RC
A 1643	12	55	54	+44	04	46	0.1980	III	B	1
A 1878	14	12	49	+29	12	59	0.2540	II	C	1
A 1952	14	41	04	+28	38	12	0.2480	III	C	2
A 2111	15	39	38	+34	24	21	0.2290	II – III	C	3
A 2658	23	44	58	−12	18	20	0.1850	III	F	3

Those clusters were selected from the catalogue by Abell, Corwin & Olowin (1989) to accomplish the requirements of being massive, apparently relaxed systems, with an intermediate richness class and high galactic latitudes to avoid problems with extinction

[1]The NASA/IPAC Extragalactic Database (NED) is operated by the jet propulsion laboratory, California Institute of Technology, under contract with the national Aeronautics and Space Administration

The clusters were observed through two broad-band optical filters: Gunn-r (r) and Bessel B (B). In Table 2.2, the information about the observations is collected. The number of pointings observed for each cluster are indicated in column 1. These pointings cover different cluster areas which are showed in column 2. The third and fourth columns of the Table gives the exposition time in r and B filters respectively for the different cluster. The last column of the table shows the seeing of the images. The different areas covered were sampled as an effort to sample the whole cluster in a considerable part of the ≈ 1 Abell diameter. Due to the relative medium-redshift of those clusters, that aim was achieved. Note that all images were taken under photometric sky conditions and very good seeing (between 0.5 and $0.8''$).

Table 2.2: NOT Clusters Observations

Name	$\#Frames$	Area (Mpc) ^{2}	ExpTime(r) (s)	ExpTime(B) (s)	seeing ($''$)
A 1643	2	0.6810	600	900	0.55
A 1878	2	0.7894	600	600	0.7
A 1952	2	0.7989	900	900	$0.55 - 0.8$
A 2111	2	0.8030	600	900	0.7
A 2658	1	0.3055	600	1200	0.7

2.1.1 Comments on the sample

Given the scarce information existing on those clusters, we have gathered the few available literature, which refers, above all, to redshift data and the environmental situation of each of them.

A1643. The redshift of this cluster was given from the work by Humason, Mayall & Sandage (1956), who obtained a spectrum of the brightest galaxy in the area, finding z = 0.198. Our images were centered at that position, $\alpha(J2000)$=12h 55m 54.4s, $\delta(J2000)$= +44d 04m 46s. More recently, (Gal et al. (2003)) detected an overdense region centered at $\alpha(J2000)$=12h 55m 42.4s, $\delta(J2000)$= +44d 05m 22s, identified as a cluster designed by NSC J125542+440522. They have determined a photometric redshift of 0.2515. Both clusters do appear in our frames where we can identify A1643 as the one dominated by the galaxy observed by Humason, Mayall & Sandage (1956) and, therefore, at z = 0.198. This is the value we adopt in this work. We will exclude the frames that could be contaminated by the presence of NSC J125542+440522 in all the analysis regarding the galactic content of A1643. The area and number of frames values given in Table are already corrected.

A1878. This clusters appears with z = 0.254 in the NED. A closer inspection shows that there is another value given to a galaxy in the field, namely z =

0.222. Both redshift values come from Sandage, Kristian & Westphal (1976), who observed the brightest galaxy in the field, placed at $\alpha(J2000)$=14h 12m 52.13s, $\delta(J2000)$ = +29d 14m 29s, and another, fainter galaxy at $\alpha(J2000)$=14h 12m 49.13s, $\delta(J2000)$ = +29d 12m 59s. As quoted by the authors, the spectra were of low quality. The low z value corresponds to the brightest object that appears at the center of a strong concentration of galaxies that do correspond to the cluster catalogued as A1878. More recently, Gal et al. (2003), identified a cluster labeled as NSCJ141257+291256, with a photometric redshift z = 0.22. Its position and redshift value coincide with that of the bright galaxy observed by Sandage, Kristian & Westphal (1976) that is accepted here as the brightest galaxy of A1878.

A1952. The redshift attributed to this cluster, z = 0.248, also comes from the work by Sandage, Kristian & Westphal (1976) who observed the brightest cluster galaxy. The possible confusion regarding this cluster comes from the fact that the position given by Abell, Corwin & Olowin (1989), $\alpha(J2000)$=14h 41m 04.2s, $\delta(J2000)$= +28d 38m 12s, does not coincide with that of its Brightest Cluster Galaxy (BCG) as given by Sandage, Kristian & Westphal (1976), $\alpha(J2000)$= 14h 41m 03.6s, $\delta(J2000)$= +28d 36m 59.68s. To add to the confusion, Gal et al. (2003) detected a cluster designed by NSC J144103+283622, at almost exactly the position of A1952's BCG, but the redshift they have determined photometrically amounts to 0.2084. Taking all the information at hand, we consider that the cluster identified by Gal et al. (2003) is A1952, but the redshift we adopt here is that measured by Sandage, Kristian & Westphal (1976), z = 0.248. The analysis we present of the Color-Magnitude Relation in Chapter 3, support this conclusion.

A2111. That cluster has the largest amount of information available in the literature of all the clusters in that sample. The redshift was established from spectroscopic observations by Lavery & Henry (1986). The center given by NED comes from the ACO catalogue given by Abell, Corwin & Olowin (1989), namely, $\alpha(J2000)$=15h 39m 38.3s, $\delta(J2000)$ = +34d 24m 21s. However, the subsequent analysis of the X-ray data by Wang, Ulmer & Lavery (1997); Henriksen, Wang & Ulmer (1999); Miller et al. (2006), let them to conclude that the cluster center position is at $\alpha(J2000)$=15h 39m 40.9s , $\delta(J2000)$= +34d 25m 04s, only 7.65 kpc away from the Brightest Cluster Galaxy. Miller et al. (2006) also provides a large number of spectra.

Interestingly, that cluster is thought to be merger of two clusters due to the fact that the cluster contains a distinct comet-shaped X-ray subcomponent that appears hotter than the rest of the cluster Wang, Ulmer & Lavery (1997). Furthermore, the orientation between the two central major galaxies coincides with the elongation of both the galaxy and X-ray distributions. And also it has the distinction of being the richest cluster in the original Butcher & Oemler (1984) study. A2111 was also among the larger blue fraction clusters noted in Butcher & Oemler (1984), at f_b=0.16 $\pm$ 0.03.

A2658. That cluster is the only one from the sample that is observable from the South Hemisphere. The redshift of that cluster is set from Fetisova (1982). The center, as given by Abell, Corwin & Olowin (1989) is at $\alpha(J2000)$ =23h 44m 58.8s, $\delta(J2000)$= -12d 18m 20s. However, our BCG is located at $\alpha(J2000)$=23h 44m 49.83s, $\delta(J2000)$= -12d 17m 38.93. After a visual inspection of the cluster image in the Digital Sky Survey, we conclude that the center of the cluster is given by the BCG, where a high concentration of galaxies is visually detected.

In Chapter 6, we will discuss the determination of the center of the cluster, giving the final coordinates in Table 6.3.

In the following sections, we are going to summarize the procedure for the reduction, calibration, (already performed by Fasano et al. (2002)), astrometrization of the clusters, and extraction of the sources.

2.1.2 Data reduction

At least two exposures for each field in both filters (r) and (B) were usually taken, allowing to clean-up the combined images for cosmic-rays and spurious events. Here, we sum up the basic steps of the data reduction process, following the procedure explained in Fasano et al. (2002).

The bulk of the data reduction of the images was achieved using standard IRAF tasks. The electronic bias level was removed from the CCD by fitting a Chebyshev function to the overscan region and subtracting it from each column. By averaging ten bias frames, a master bias per night was created and subtracted from the images in order to remove any remaining bias structure.

Dark images were also observed in order to remove the dark signal from the CCD. This correction turned out to be negligible, and was not considered. Twilight flats were also observed at the beginning and at the end of every observing night. They were combined and used for removing the pixel-to-pixel structure of the images.

2.1.3 Calibration

The photometric calibration of the images was obtained by observing several standard stars from the Landolt (1992), Jørgensen (1994), and Montgomery (1993) catalogues. They were observed every night at different zenith distances in order to measure the atmospheric extinction. The calibration constant was taken from Fasano et al. (2002).

Table 2.3 shows the calibration coefficients with its error in the r band for each cluster. As different clusters were observed different nights, the information in the log of the observations has been compiled to know which night a particular galaxy cluster was observed. In the two first columns, the photometric zero points Z_c and the color coefficients C_c is set, the third column shows the extinction coefficients and the last column shows the calibration errors.

Table 2.3: Calibration Coefficients in NOT Cluster Sample

Name	Z_c	C_c	k_r	rms
A 1643	24.704 ± 0.004	0.085 ± 0.003	-0.128 ± 0.013	0.0222
A 1878	24.704 ± 0.004	0.085 ± 0.003	-0.128 ± 0.013	0.0222
A 1952	25.111 ± 0.005	0.117 ± 0.005	-0.088 ± 0.005	0.0232
A 2111	24.704 ± 0.004	0.085 ± 0.003	-0.128 ± 0.013	0.0222
A 2658	25.111 ± 0.005	0.117 ± 0.005	-0.088 ± 0.005	0.0232

2.1.4 Astrometrical Calibration.

Images need to be calibrated spatially. In other words, we need to obtain world (α,δ) coordinates from the CCD pixels (x, y) in order to locate an object exactly in the sky. This procedure is commonly known as **astrometrization**.

Usually, the field can be geometrically distorted by the optical layout of the camera. Such distortions can significantly affect the astrometric measurements as well as the photometry, due to the mis-shaped smearing of the light on the pixel array. In order to map and correct distortions in the images, it's quite useful to compare coordinates or a given sample of point-like sources (stars) in the field. Strong distortions require sizeable astrometric samples of stars uniformly spread throughout the field.

Hence, we have used an interactive software developed and maintained by the *Centre de Données astronomiques de Strasbourg*, called **Aladin Sky Atlas**, (Bonnarel et al. (2000)). *Aladin* visualizes digitized astronomical images and place entries from astronomical catalogues or databases over them. It also interactively access related data and information from the different databases and archives for all known sources in the field. The steps required for achieving the astrometrization of the NOT sample images are summarized here.

- Digitalizated Sky Survey (DSS) images of the different NOT clusters were downloaded, ensuring that their sizes were larger than our $3' \times 3'$ fields. A typical size of $14' \times 14'$ was selected. This images are previously astrometrizated.
- A NOT image, previously reduced, was opened with *Aladin*.
- We performed a visual comparison between both images to identify the same object, ideally stars, in both images. We obtain a list of (x, y) pixels in our observed frame and the corresponding (α,δ) coordinates for the DSS.
- In *Aladin*, we select the options: *Tools*, *Image astrometrical (re)calibration* and finally *By matching stars*. An iterative window will open and we can introduce the pixels and their relative world coordinates.

- An initial astrometrization of the image is shown. Then we superimpose a star catalogue in that frame to improve the initial astrometrical solution. In *Aladin*, we select: *Load*, *All VO* and *Catalogs* where we can choose a number of different catalogues. In that case, we selected NOMAD.

- If desired, we can manually re-astrometrizate the result by selecting the option *Modify*.

- Once we are satisfied, we can save the image by selection *Save* and *Export some planes* and we obtain the NOT original image with galactic astrometry.

2.1.5 Extraction of the sources

We have selected and extracted the sources of our images in order to study their individual characteristics. For that purpose, we used *SExtractor* (Source-Extractor), Bertin & Arnouts (1996), which is a well-known astronomical program that builds a catalogue of objects from an astronomical image and measures their photometry.

We have included here an explanation about the most essential parameters for the extraction of the objects in our images. SExtractor gets some image information from the FITS header of the image but it also needs some of the parameters to be specified in the configuration file.

- Extraction Parameters

  They are setting the constraints for the objects to be detected. The most relevant parameters relating to that are *DETECT_THRESH* and *DETECT_MINAREA* . The first one determines the level of brightness we want to detect, usually specifying a number of times over the σ of the image and the second one sets up the minimum number of pixels above a threshold that the object has to have to be selected.

  As far as the deblending is concerned, the most interesting and important parameters are *DEBLEND_NTHRESH*, which designates the number of intensity levels that each detection is going to be divided in to analyze the deblending and *DEBLEND_MINCONT*, which stipulates the minimum contrast to split one detections into one or more detections.

  We decided to fix the *DETECT_THRESH*=1.5σ in order to detect galaxies which arrived to Gunn-r isophote of 25.3 and *DETECT_MINAREA* =150 pixels, which corresponds to galaxies with radius at least of 7 pixels, which is twice the medium full-width at half maximum ($FWHM$) for our images. After performing different tests in our images and checking that the deblending was accurately performed, we resolved to set *DEBLEND_NTHRESH*= 32 and *DEBLEND_MINCONT*=0.0001.

- Photometry Parameters

  SExtractor allows us to choose between five different magnitudes for each detected galaxy on our images: isophotal, isophotal-corrected, automatic, best estimate and aperture. We have chosen two of them.

  The first one corresponds to a fixed-aperture *MAG_APER* of radius five kpc, useful to compare colors in the same physical region, (Bernardi et al., 2003; Varela, 2004). The other one is the magnitude called by SExtractor 'MAG_BEST' that is determined in an automatic aperture which depends on the neighbours around the galaxy. If those neighbours are bright enough to affect the magnitude corresponding to an aperture enclosing the whole object by more than 10%, then that magnitude is taken as the corrected isophotal magnitude, which corresponds to the isophotal magnitude together with a correction. This magnitude provides the best measures of the total light of the objects, (Nelson et al., 2002; Stott et al., 2008).

- Star/Galaxy Separation Parameters

  In a catalogue of objects, we expect to know the kind of object we're dealing with. SExtractor is able to work out the probability (*stellar index*), that an object is an star (a point-source) by using a neural network which was trained with more than 10^6 images of stars and galaxies simulated with different conditions of pixel-scale, seeing and detection limits. Therefore, if the *Stellar index* is close to 1, the object is predictable a star and if it is close to 0., it is likely to be a galaxy. The parameters demanding by SExtractor are the *SEEING_FWHM* which is the $FWHM$ of the image and can be measured directly from the image.

  For our sample, we have considered that an object was a galaxy when its stellar index was smaller then 0.2. In contrast, an object was considered as star if the stellar index was larger than 0.8. The rest of the objects were considered as doubt objects. Those values were selected as the best partition of the galaxy population. As the field of view of our frames is not large we have considered the FWHM being constant in the whole image.

- Background Parameters

  Estimating the local background is a crucial step in achieving good quality photometry. SExtractor estimates the background of the image as well as the RMS noise in that background. The most important values for a proper estimation of the background are *BACK_SIZE* and *BACK_FILTERSIZE*. The first parameter, *BACK_SIZE* is the size of the area where SExtractor works out the mean and the σ of the distribution of pixel values is computed. The process consist then on discarding the most deviant values and working out again the median and standard deviation σ until all the remaining pixel values are within mean $\pm$ 3 σ. Then, the value for the background in the area is the mean of those pixels.

The background map is an bi-cubic-spline interpolation over all the area's of size *BACK_SIZE*, after filtering.

The second parameter, *BACK_FILTERSIZE* is the median filter for the background map. That is, before the fit of the background values is done, the background image is smoothed over this number of meshes. In order to obtain a good value of these parameters, we have measured the largest objects in our images and we have set *BACK_SIZE* parameter larger than them, that is 128, and a *BACK_FILTERSIZE* of at least 3, in order to get rid of the possible deviations between different estimations in contrasting parts of the image. However, as the field of view is relatively small, the background maintains nearly constant, what implies a good quality subtraction.

SExtractor also allows one to perform on-line cross-identification of each detection with and ASCII list. This is the ASSOC mode and it's very useful for extracting the same objects in different filters, for example. In our case, the extraction of the galaxies was performed in the r images, as they are deeper than the B band images. The photometry of the galaxies in the B-band was obtained using the ASSOC mode of SExtractor.

2.1.6 Photometric corrections

Although SExtractor produces the photometry of the objects in the image, those magnitudes need to be corrected of at least two effects: the **k -correction effect** and the **galactic extinction**. The k-correction is defined as the corrective term that needs to be applied to the observed magnitude in a certain band due to the effect of redshift, (Oke & Sandage, 1968; Pence, 1976; Poggianti, 1997).

The k-correction effect was then applied to the SExtractor magnitudes of the galaxies in both filters. For the B-band filter we used the k-correction given by Pence (1976), being $k_B = 4.4225z + 0.0294$. The fit was taken from Varela (2004), and it is valid for data between redshift 0.08 and 0.24. The magnitudes of the $Gunn - r$ filter were corrected by using the approximations $k_r = 2.5\ log(1 + z)$ (Jørgensen, Franx & Kjaergaard (1992)) due to the flat spectral shape of elliptical in this wavelength range. The galactic extinctions in both filters were derived from Schlegel et al. (1998).

Hence, the corrections for the SExtractor magnitudes were transformed to reliable magnitudes, using the Bouger equations, in the following way:

$$\begin{cases} m_r = m_{SEx,r} + Z_{c,r} + k_{n,r}X_r + C_{c,r}(B-r) - A_r - k_r \\ \\ m_B = m_{SEx,B} + Z_{c,B} + k_{n,B}X_B + C_{c,B}(B-r) - A_B - k_B \end{cases} \tag{2.1}$$

The true color (B-r) can be easily evaluated solving Equation 2.1:

$$(B-r) = \frac{Z_{c,B} - Z_{c,r} + k_{n,B}X_B - k_{n,r}X_r + m_{SEx,B} - m_{SEx,r}}{1 - C_{c,B} + C_{c,r}}$$

Tab 2.4 shows the errors provided by SExtractor for the two different magnitudes measured in Gunn-r. The last column shows the errors in colour obtained as the quadratic sum of the errors of the fixed-aperture magnitude in the two filters B and r. As we see, the errors are in all cases not affecting the final results.

Table 2.4: Errors Measurements

Name	ErrAper	ErrBest	ErrCol
A 1643	0.005	0.006	0.033
A 1878	0.007	0.008	0.052
A 1952	0.006	0.007	0.040
A 2111	0.007	0.009	0.045
A 2658	0.007	0.008	0.028

After extracting all the objects, we checked if there were some part of the frames overlapped and consequently, some of the objects were measured twice. There were two cases: A2111 and A1952. As a way of control, we checked that their magnitudes were consistent between them. In Figures 2.1, we show their absolute magnitudes versus their magnitude differences. The solid line, shows the mean value of the difference (0.012 for A1952 and 0.026 for A2111), while the dotted lines show the standard deviation of the difference (0.052 for A1952 and 0.034 for A2111).

We see that the mean differences are less than 0.028 and the standard deviation for the galaxies brighter than $M_r \geq -19.5$ (corresponding to $m_r \leq 20.8$) are the same order of magnitude than the calibration errors. The larger differences of A1952 rather than A2111, can be explained as it is the only cluster with a relevant difference in seeing (from 0.5 to 0.8) between the different frames. However, that fact does not affect our results.

We finally obtained a first catalogue of 488 objects, including stars and galaxies. The final galaxy catalogue was formed by 456 galaxies. We also obtained 27 stars and 5 doubt objects.

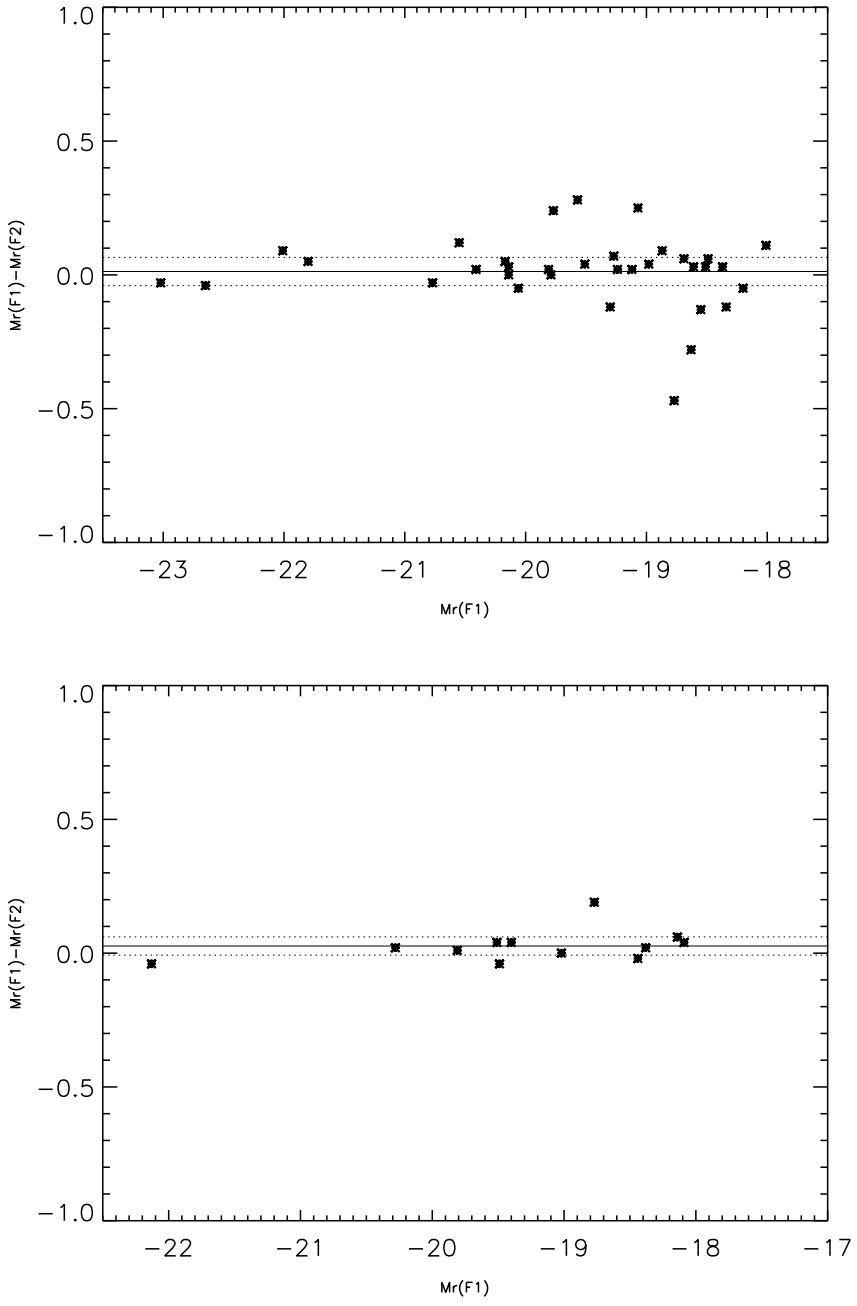

Figure 2.1: Absolute Gunn-r magnitude difference versus absolute Gunn-r magnitude for A1952 and A2111. The solid line indicates the mean value of the difference and the stripped lines refer to the standard deviation of the difference.

2.2 Advanced Camera for Surveys Clusters

The other half of the sample at medium redshift consist on five multi-band clusters imaged with the Wide Field Camera (WFC) of the Advanced Camera for Surveys (ACS) in the Hubble Space Telescope (HST) in the same range of redshift.

The CCD of ACS has a field of view of $202'' \times 202''$ and plate scale of $0.05''$/pix. The clusters have been imaged in the full spectral range of the Advanced Camera. In total, twenty orbits were imaged for A1689 in four filters, twenty for A1703, CL0024+1654 and MS1358.4+6245 in six filters and sixteen for A2218 in six filters. The quality of those images is unprecedented due to their depth, wavelength coverage and exceptional resolution from the space.

That main characteristics of the sample are collected in table 2.5: name of the cluster, the centers obtained by NED, the redshift, the Bautz-Morgan Type, and the richness class.

Table 2.5: The global sample of ACS Clusters

Name	α(2000)			δ(2000)			z	BMtype	RC
A 1689	13	11	29	−01	20	17	0.1832	II − III	4
A 1703	13	15	00	+51	49	10	0.2836	II	4
A 2218	16	35	54	+66	13	00	0.1756	II	4
CL0024 + 1654	00	26	36	+17	08	36	0.3900		
MS1358.4 + 6245	13	59	54	+62	30	36	0.3280	I	≥ 4

In Table 2.6, the main characteristics for the five clusters ACS observations are set in F475W band (SDSS-r) and F625W (SDSS-g). Those bands were selected from the whole multi-band set as being the more similar to the NOT bands. Although the SDSS-g has a wavelength centered in TAL and in TAL for the Bessel -B band, the difference in not too significative.

Table 2.6: ACS WFC Clusters Observations

Name	Area(Mpc) ^{2}	ExpTime(r) (s)	ExpTime(B) (s)	seeing ($''$)
A 1689	0.615	9500	9500	0.105
A 1703	0.801	5664	9834	0.105
A 2218	0.594	5640	8386	0.105
CL0024 + 1654	1.062	5072	8971	0.105
MS1358.4 + 6245	0.949	5470	9196	0.105

2.2.1 Comments on the sample

Contrary to the NOT sample, the clusters sample imaged with the ACS are clusters largely explored and they have a great amount of literature. In this section, we have summarized some of the main results regarding to those clusters.

A1689. This cluster is one of the best studied in the literature. It presents many gravitational arcs associated with 30 systems or sources with redshift in the range $1 < z < 6$, (Diego et al. (2005)). The Sunyaev-Zeldovich effect, (Sunyaev & Zel'dovich (1970, 1972)), has also been detected and computed in that cluster, (Bonamente et al. (2006)).

Several studies have analyzed its mass profiles by estimating its dark matter halo with different methods such as gravitational lenses, (Tyson & Fischer (1995); Taylor et al. (1998); Broadhurst et al. (2005b); Diego et al. (2005); Zekser et al. (2006); Halkola, Seitz & Pannella (2006, 2007)), galaxy kinematics, (Łokas et al. (2006)) or X-ray imaging, (Xue & Wu (2002); Demarco et al. (2003); Andersson & Madejski (2004); Bonamente et al. (2006)).

Although the lensing techniques tend to agree in the mass giving a mass around $(0.1 - 0.5)10^{15}h^{-1}M_{\odot}$ for the mass contained in a radius of 51 to 110 arcsecs, a systematic discrepancy of about 2 is found with the estimations provided by X-ray data.

The redshift of this cluster (z=0.1832) was given originally by the work by Teague, Carter & Gray (1990), who obtained sixty-six spectra of the field of each cluster providing a wide coverage of the bright galaxy population. Later on, Duc et al. (2002) gave positions and redshift for all cluster members with red magnitude R<18 and within $2^{''}$ of the brightest central galaxy. The X-ray center has been set as prescribed in Bonamente et al. (2006) using Chandra X-ray measurements at the position, $\alpha(J2000)$ =+13d 11m 29.5s, $\delta(J2000)$ = -01h 20m 28.2s. That center has been found to be in agreement with the peak of the mass distribution Diego et al. (2005), which falls very close to the central dominant galaxy.

Molinari, Buzzoni & Chincarini (1996) performed an study of the ground-based photometry of this cluster in Gunn g, r and i band, discussed its r versus g-r color diagram, concluding that a ridge line for the ellipticals clearly appeared for this compact cluster. Additionally, De Propris et al. (2003b), analyzed the Butcher-Oemler Effect in the K-band for this cluster, finding a blue-fraction of 0.046 ± 0.038 in the K-band and 0.029 ± 0.025 in the optical within a 0.5 Mpc aperture.

A1703. This cluster is a massive X-ray cluster that contains a large number of gravitational arcs, Limousin et al. (2008). In particular, this cluster exhibits an outstanding bright 'ring' formed by galaxies at z=0.888 located very close to the cD galaxy.

The redshift of A1703 (z=0.2836) is given by a work by Allen et al. (1992) who identified the redshift of the two brightest X-ray members of the cluster. The

coordinates provided by NED are for the center of the cluster are $\alpha(J2000)$ =+13h 15m 00.7s, $\delta(J2000)$= +51d 49m 10s, extracted from the Abell optical Catalogue, Abell, Corwin & Olowin (1989). Later works by Crawford et al. (1999); Limousin et al. (2008), based on the ROSAT Brightest Cluster Sample, set the center of the cluster as the coordinates provided by the dominant galaxy in X-ray, $\alpha(J2000)$=+13h 15m 05.27s, $\delta(J2000)$= +51d 49m 02.85s.

A2218. A2218 is one of the richest clusters of the Abell catalogue. That cluster is 'famous' due to its ring around its cD galaxy, (Kassiola & Kovner, 1993). Numerous gravitational lenses studies came after the discovery of that 'ring', (Kneib et al. (1996); Soucail, Kneib & Golse (2004); Kneib et al. (2004)), suggesting that the multiple lens system arises from a high-redshift (z>6) source.

Additionally, many attempts to determine the dynamical state of the cluster by studying its X-ray emission have been performed, (Neumann & Böhringer (1999); Cannon, Ponman & Hobbs (1999); Machacek et al. (2002); Pratt, Böhringer & Finoguenov (2005)), even with the analysis of the Sunyaev-Zeldovich effect, (Uyaniker et al. (1997); Tsuboi et al. (1998); Lieu, Mittaz & Zhang (2006); Morandi, Ettori & Moscardini (2007)). A discrepancy between mass estimates from X-ray and strong lensing analyses is evident, (Miralda-Escudé & Babul, 1995; Pratt, Böhringer & Finoguenov, 2005). More complete X-ray studies with ROSAT, (Markevitch, 1997; Neumann & Böhringer, 1999) or Chandra, (Machacek et al., 2002), revealed a complicated X-ray structure near the core, suggesting that the cluster is dynamically active. The most likely explanation is the merger status of A2218. The clumpy X-ray emission appears as a direct consequence of the ongoing merging of the two sub-units, (Kneib et al., 1995).

The redshift of this cluster (z = 0.17) is provided by Kristian, Sandage & Westphal (1978); Le Borgne, Pelló & Sanahuja (1992). The coordinates given by NED, $\alpha(J2000)$=+16h35m54.0s, $\delta(J2000)$= +66d13m00s, were extracted from the Abell catalogue, Abell, Corwin & Olowin (1989). However, the peak of the X-ray surface brightness distribution is coincident with the location of the cD galaxy, $\alpha(J2000)$=+16h35m48.9s, $\delta(J2000)$= +66d12m42s, (McHardy et al. (1990)). The photometric and spectroscopic study of the clusters center suggest that the cluster consist in fact of two galaxy concentration, of which one is centered about the cD galaxy.

Besides, a number of photometrical studies have been performed in that cluster. Butcher & Oemler (1984) gave a concentration parameter of C=0.59, one of the largest in their sample. Jørgensen et al. (1999), extracted the photometry for a magnitude-limited sample, deriving the corresponding Fundamental Plane, adding important knowledge about the properties of E and S0 galaxies. Also, Rakos, Dominis & Steindling (2001); Rakos & Schombert (2005), completed a four color intermediate-band photometry of the cluster population, finding an unusually low fraction of blue galaxies and a large fraction of E/S0 galaxies. They also analyzed the B-r color-magnitude relation finding a slope of 0.068 ± 0.032. Complementary, a morphological study in the core of that cluster has been recently performed by Sánchez et al. (2007).

Furthermore, the luminosity function has been studied in that cluster by Pracy et al. (2005). They find that the total projected luminosity distribution within 1 Mpc of the cluster centre can be well represented by a single Schechter function with moderately flat faint-end slopes: $\alpha = -1.14$, also finding that the brightest galaxies in that cluster exhibit a more compact spatial distribution.

CL0024+1654. That cluster, hereafter CL0024, is the more distant from all the clusters analyzed in this thesis with a redshift of z=0.39. It has a velocity dispersion of $\sigma_v = 1200 kms^{-1}$, (Dressler & Gunn (1992)), and an X-ray luminosity $L_x = 3.7 \times 10^{44} ergss^{-1}$, (Soucail et al., 2000). A single background galaxy, is multiply imaged, (Colley, Tyson & Turner (1996); Tyson, Kochanski & Dell'Antonio (1998); Böhringer et al. (2000b); Broadhurst et al. (2000); Rögnvaldsson et al. (2001); Kneib et al. (2003)). Several analysis with X-ray data have been performed, (Kodama et al. (2004); Zhang et al. (2005); Kotov & Vikhlinin (2005)), finding a complex structure in the core region. Evidence of the Sunyaev-Zel'dovich effect, (Zemcov et al. (2007)), has also been found.

The original redshift was obtained by Gunn & Oke (1975). The position listed in NED comes from the Catalogue by Zwicky et al. (1961) and is set at $\alpha(J2000)$= 00h 26m 36s, $\delta(J2000)$=17d 08m 36s. However, the X-ray center, (Soucail et al., 2000; Treu et al., 2003) is $\alpha(J2000)$=00h 26m 36.3s, $\delta(J2000)$=17d 09m 46s, which is very close to the position of the cD galaxy, $\alpha(J2000)$=00h 26m 35.7s, $\delta(J2000)$= 17d 09m 43s, (Treu et al. (2003)).

In addition, Czoske et al. (2001); Alexov & Silva (2003), provided this cluster with a wide-field spectroscopic survey of 618 spectra. The morphological distribution has been analyzed to 5 Mpc radius by Treu et al. (2003) up to I=22.5. Also, the original value of the blue fraction given by Butcher & Oemler (1984) is 0.16 ± 0.02 and later on, (De Propris et al., 2003) estimated this to be 0.153 ± 0.068 in the central 0.5 Mpc and 0.200 ± 0.068 in the central 0.7 Mpc.

Additional works have performed deep analysis of different properties such as the Fundamental Plane, (van Dokkum & Franx, 1996), the Tully-Fisher relation in that cluster, (Metevier et al., 2006) or the nature of strong emission-line galaxies in that cluster, (Koo et al., 1997). Also the concentration parameter has been estimated by Dressler et al. (1997) to be 0.53. QUE AREA?

MS1358.4+6245. That cluster , hereafter MS1358, is an X-ray, extremely rich cluster, with a compact, concentrated core of galaxies. The Sunyaev-Zeldovich effect has been widely explored on it, (LaRoque et al. (2006); Morandi, Ettori & Moscardini (2007); Hashimoto et al. (2007)). It also has weak gravitational lensing of faint distant background objects, (Hoekstra, Franx & Kuijken (1998)).

The redshift (z=0.328) and position of that cluster $\alpha(J2000)$= 13h 59m 54.3s, $\delta(J2000)$= 62d 30m 36s, is set from a work based on Einstein Observatory extended Medium-Sensitivity Survey by Stocke et al. (1991). However, most works have adopted the brightest cluster galaxy set as $\alpha(J2000)$=13h 59m 50.5s, $\delta(J2000)$= 62d 31m 05s, (Fisher et al., 1998; van Dokkum et al., 1998; Fabricant, Franx & van Dokkum, 2000)

Likewise, Yee et al. (1998) created a redshift catalogue of the galaxies in the field of this cluster in a wide are ranging in magnitude from $r = 20$ to $r = 22$ and Fisher et al. (1998) added more spectroscopic information in the central 3.5 Mpc. The morphological composition of a sample of galaxies in the central 53 arc minutes have been carried out by Fabricant, Franx & van Dokkum (2000).

In addition, Luppino et al. (1991) presented an analysis of four-color (BVRI) photometry. They included the cluster luminosity function and color-magnitude diagrams and also computed the blue galaxy fraction finding it be $0.10 < f_b < 0.18$ depending on the background galaxy correction.

Additionally, Fabricant, McClintock & Bautz (1991) obtained V,R and I photometry of the galaxy population in the cluster center complete to rest band $M_V = -19.5$ and spectra of 70 galaxies within 2 arc minutes. They also estimated the concentration value of being 0.49.

The color-magnitude relation was analyzed by van Dokkum et al. (1998) finding a slope of -0.012 $\pm$ 0.003. Also, Kelson et al. (2000) performed an study based on the surface photometry and structural parameters for 55 galaxies in that cluster.

In Chapter 6, we will set and discuss the determination of the center of the cluster. The final coordinates are provided in Table 6.4.

2.2.2 Reduction and Calibration of the frames

The ACS images were previously reduced using Apsis, the automatic image processing pipeline for the ACS GTO (ACS Guaranteed Time Observations), (Blakeslee et al., 2003). Apsis is able to rotate, align, cosmic-ray-reject, and drizzle the imaging observations together.

Likewise, the images were astrometrizated and calibrated taking advantage of the 2002 February 25 CALACS zero points Hack (1999), offset by small amounts necessary for the errors present in this calibration.

2.2.3 Extraction of the sources

The sources in that sample, were detected by using SExtractor. The procedure is the same already explained in the last section referring to NOT sample. In that subsection, we only remark the most relevant parameters, specifying its relation with the parameters set from the NOT sample.

- Extraction Parameters

  We have set the $DETECT\_THRESH$=1.5σ, detecting galaxies that arrived to r isophote of 27.8. Also, we have opted for a $DETECT\_MINAREA$ value of 150 pixels, corresponding to galaxies with radius at least of 7 pixels, which is $\approx$ three times the medium FWHM for our images.

Concerning the deblending parameters, we have set $DEBLEND\_NTHRESH = 32$ and $DEBLEND\_MINCONT$=0.005 as the result of different analysis to maintain the accuracy of the deblending image.

- Photometry Parameters

  As in the NOT sample, we have used the MAG_APER of radius five kpc, useful for the color determination and the MAG_BEST for the computation of the magnitudes.

- Star/Galaxy Separation Parameters

  The stellar index has been consider in the same way than the NOT sample. A value less or equal than 0.2 is chosen to consider an object a galaxy while a stellar index value larger than 0.8 is considered an star. The rest of the objects are considered doubt objects.

- Background Parameters

  We have taken the value sof $BACK\_SIZE$ and $BACK\_FILTERSIZE$ parameters to have enough statistics to have a good estimation of the background. We have then set $BACK\_SIZE = 128$ and $BACK\_FILTERSIZE$= 3.

The extraction of the galaxies was performed in the r images, to be comparable with the NOT sample. The photometry of the galaxies in the g-band was obtained using the ASSOC mode of SExtractor.

2.2.4 Photometric corrections

We have applied a k-correction effect to the SExtractor magnitudes of the galaxies in both filters. For the g-band filter we have used an interpolation of the k-correction given by Poggianti (1997) for the Gunn-g band in the range 0.16 to 0.4, being $k_g = 4.7026z + 0.351$. For the r-band filter, we used the same approximation as in the NOT sample, $k_r = 2.5\ log(1+z)$ (Jørgensen, Franx & Kjaergaard (1992)). Likewise, the galactic extinctions in both filters have been derived from Schlegel et al. (1998).

We have set in Table 2.7, the errors provided by SExtractor for the two different magnitudes measured in Gunn-r. Also, the last column shows the mean errors in colour obtained as the quadratic sum of the errors of the fixed-aperture magnitude in the two filters, g and r. As we see, the errors are in all cases not affecting the final results.

The catalogue of detections contains 2341 objects, consisting of 2239 galaxies, 91 stars and 11 doubt objects.

Table 2.7: Errors Measurements for the ACS sample

Name	ErrAper	ErrBest	ErrCol
A 1643	0.003	0.003	0.007
A 1878	0.002	0.002	0.007
A 1952	0.003	0.002	0.008
A 2111	0.002	0.006	0.009
A 2658	0.002	0.002	0.007

Part II

Characterization of the bright central galaxy population in Clusters

Chapter 3

Color-Magnitude Relation

Puedo escribir los versos más tristes esta noche.
Escribir, por ejemplo,: 'La noche está estrellada,
y tiritan, azules, los astros, a lo lejos.'

Pablo Neruda, 'Veinte poemas de amor y una canción desesperada.'

The existence of a **Color-Magnitude Relation (CMR)** for elliptical galaxies was first noted by Baum (1959). He noted that field elliptical colors become redder as the galaxies become brighter. Locally, the elliptical galaxies in individual clusters form a red sequence with a well-defined slope and small scatter (Bower, Lucey & Ellis, 1992a,b). A simple straight line fit can describe the CMR for elliptical galaxies in an interval of about eight magnitudes in local clusters such as Virgo (Sandage (1972b)) or Coma (Thompson & Gregory (1993); López-Cruz et al. (1997); Secker, Harris & Plummer (1997)). The large coverage in luminosity, suggests that within this range galaxies have shared a similar evolutionary process.

Later on, in the seventies and eighties, a number of works by Visvanathan & Sandage (1977); Visvanathan & Griersmith (1977); Sandage & Visvanathan (1978); Griersmith (1980); Visvanathan (1981),etc; concluded on the universality of the so called CMR for early type galaxies and even early spirals although it depends on the bands used, (Tully, Mould & Aaronson, 1982; Mobasher, Ellis & Sharples, 1986).

The physical origin of the CMR seems to be a consequence of the process of the formation process of the galaxies in clusters. The most massive galaxies are able to retain largest quantity of enriched gas of the supernova explosions in the maximum of the stellar formation activity, (Arimoto & Yoshii, 1987). Two main scenarios for the formation of clusters of galaxies still remain in the literature. On one hand, we have the monolithic scenario in which the clusters were formed first ((Bower et al., 1998)) and on the other, we have the hierarchical scenario,

(Kauffmann, Guiderdoni & White, 1994; De Lucia & Blaizot, 2007), in which the galaxies were formed at the outset.

The evolution of the slope of the color-magnitude with redshift in clusters of galaxies has been widely explored (van Dokkum & Franx (1996); Kelson et al. (1997); Ellis et al. (1997); Andreon, Davoust & Heim (1997); Bender et al. (1998); López-Cruz et al. (2004); Mei et al. (2006); Driver (2006); De Lucia et al. (2007a)) and it seems to be an agreement with the no variation of it up to redshift z $\sim$1. Recent results from the Hubble Space Telescope (HST) demonstrate the existence in clusters at redshift up to z $\sim$ 0.9 of a tight red sequence, comparable in scatter and slope to that observed in the red sequence of the Coma Cluster, Ellis et al. (1997); Stanford, Eisenhardt & Dickinson (1998); Mei et al. (2006). That result suggest that the majority of the stellar population in early-type galaxies in clusters have been formed in epoch before z=0.9 and have passively evolved since then.

Not only the CMR has been used to restrict the formation and evolution of the galaxy population but it also has been applied to many other practical issues such as the clean-up of background galaxies in clusters, (Fasano et al., 2002; Barkhouse, Yee & López-Cruz, 2007), the determination of distances between clusters, (Visvanathan & Griersmith, 1977; Bower, Lucey & Ellis, 1992a) or the detection of clusters of galaxies, (Yee, Gladders & López-Cruz, 1999; López-Cruz et al., 2004).

Another interesting feature related to the galaxy colors is the **Butcher-Oemler effect**, (Butcher & Oemler, 1984). In this pioneering work, they studied 33 clusters of galaxies up to redshift 0.54 and found an increasing fraction of blue galaxies at progressively higher redshift, in particular from z $\geq$ 0.1. Many works have tried to quantified and explained this blue galaxy fraction increment at low redshift, (Garilli et al., 1995, 1996; Margoniner & De Carvalho, 2000; Margoniner et al., 2001; Goto et al., 2003; De Propris et al., 2004; Aguerri et al., 2007) and high redshift (Rakos & Schombert, 1995; De Lucia et al., 2007a). For example, Rakos & Schombert (1995) concluded that the galaxy blue fraction increases and they quantified it from a 20 % at z =0.4 to 80% at z =0.9, suggesting that the evolution in clusters is even stronger than previously thought. Also, Margoniner & De Carvalho (2000) completed an study of 48 clusters in the low-medium redshift range 0.03 <z< 0.38 obtaining similar results. However, many examples such as Garilli et al. (1995, 1996) observed and studied a sample of clusters in the redshift range 0.05 $\leq$ z $\leq$ 0.25 finding no signs of evolution or Aguerri et al. (2007), who analyzed a large sample of SDSS clusters up to redshift z $\leq$ 0.1, arriving at the same conclusion. Actually, nearly all the works up to date have reported a wide range of blue fraction values at fixed redshift even with a trend with the redshift.

Additionally, the blue fraction galaxies have been found to depend on the cluster richness in the sense that richer clusters have smaller blue fractions, on the area surveyed, with the trend of larger radius have larger blue fractions, in agreement with the idea of Butcher & Oemler (1984) that the fraction of blue galaxies

increases in the outer parts of the cluster and on the interval of the luminosity function used to compute the blue fraction, obtaining larger blue fractions at fainter objects are included, (Margoniner & De Carvalho, 2000; Margoniner et al., 2001). They claimed that all this dependences causes a large scatter in the blue fraction - redshift diagram. Therefore, it is extremely interesting to explore an origin of the scatter in the blue fraction despite the redshift tendency.

In this Chapter, we present the study of the CMR and blue fraction for the galaxies found in our clusters samples. Throughout this Chapter, the BEST SExtractor magnitudes has been used and the color index B-r and g-r, respectively, has been determined by measuring a five kpc aperture as prescribed by Bernardi et al. (2003); Varela (2004), to be able to compare the same regions of the galaxy at different redshift.

3.1 Color-Magnitude Diagram

3.1.1 Completeness Limit

We have computed the magnitude up to which our samples are complete in order to be sure that our results are not biased and that we are studying a complete sample of galaxies for our clusters sample. To do that, we have plotted in Figure 3.1 and 3.2 the absolute magnitude distribution of the NOT ad ACS sample respectively. The completeness limit has been set as the maximum of histogram, due to the increase of the number of galaxies with fainter magnitudes. The completeness limit for each cluster and for the whole sample is overplotted in the figures with a dotted and dashed line respectively. The NOT sample appears to be complete up to $M_r \approx$ -19.5, while the ACS sample manifests to be complete up to $M_r \approx$ -17.6. In Figure 3.2, we have overplotted also with a dashed-dotted lined the completeness limit adopted for the NOT sample.

Therefore, to avoid problems with the magnitude limit, we have considered only galaxies brighter than M_r=-20 for the analysis of the CMR for the NOT sample and brighter than M_r=-17.8 for the analysis of the CMR for the ACS sample.

3.1.2 Interlopers

A previous remark that we must have into account for the characterization of the cluster population is the identification and exclusion of the possible interlopers that may be found projected in the same field of view. The definitive criterion to find the galaxies that actually belong to a given cluster is the redshift. Unfortunately, the redshift information is in general scant for clusters at redshift ~ 0.2 except for some particular cases. For the NOT sample, we only have found in the literature 22 galaxies in A2111 with redshift data provided by Miller et al. (2006), whereas for the other clusters there are just one or two redshift entries in the NED.

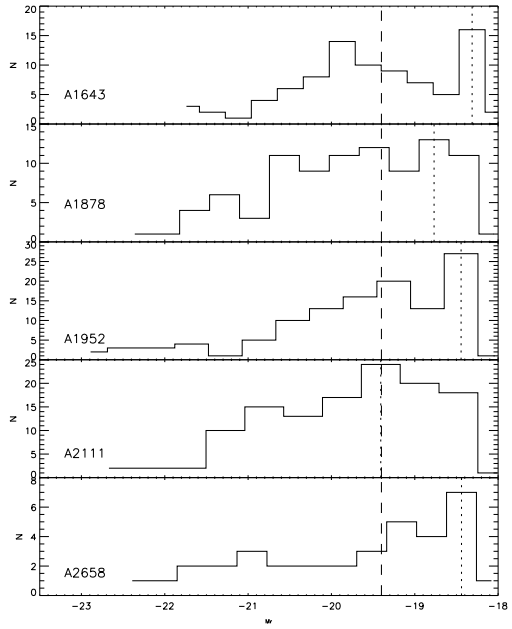

Figure 3.1: Absolute magnitude histogram of the galaxies in the five clusters. The dotted line shows the completeness magnitude limit for each cluster, whereas the dashed line shows the common magnitude limit we have adopted for the NOT clusters sample.

Opportunely, the panorama changes for the ACS sample, as we have already explained, four out of five clusters observed with the ACS have spectroscopy studies, (A1689, (Teague, Carter & Gray, 1990; Duc et al., 2002), with 91 galaxies in the central Mpc and foreground and background estimation up to R<17.5; A2218, Sánchez et al. (2007), who obtained 31 spectra in the central 200 kpc up to I< 22.5mag; CL0024, (Czoske et al., 2001), who presented 650 identified objects in the central four Mpc of the cluster, with a completeness of more than 80% up to V=22 in the central 3 arcmin and also identify an overdensity of galaxies a z $\sim$ 0.18 with no obvious centre. Finally, MS1358.4+245 has been performed two spectroscopic surveys: Fisher et al. (1998), in the central 3.5 Mpc, obtaining 232 cluster members and Yee et al. (1998), who obtained 361 galaxies in the range of Gunn-r from 20 to 22.

In Table 3.1, we have compiled the number of galaxies with redshift recovered from the literature. The first column shows the number of detected galaxies in the frames, the second column indicates the number of galaxies that belongs to the cluster, assuming a velocity range of 2400 kms^{-1}. However, we have detected an important number of galaxies with velocity differences of 4800 kms^{-1}. Those galaxies, even not considering for the analysis as they must not be close

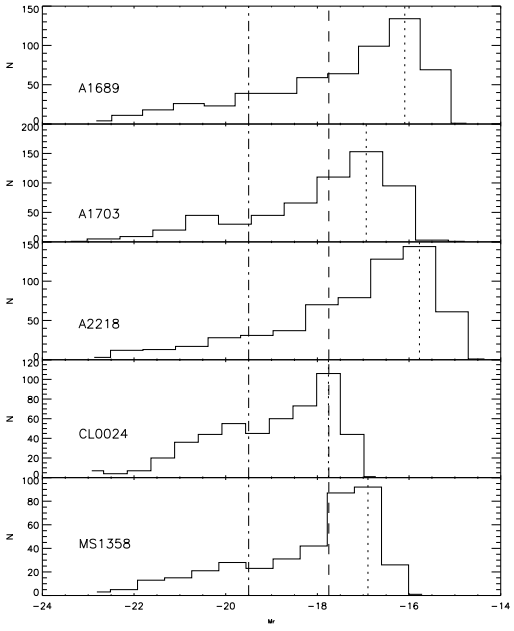

Figure 3.2: Absolute magnitude histogram of the galaxies in the five clusters. The dotted line shows the completeness magnitude limit for each cluster, the dashed line shows the common magnitude limit for the five ACS clusters and the dashed-dotted line shows the magnitude completeness adopted for the NOT sample.

to the core, they can be considering as cluster population, that is the third column. Finally, the number of foreground and background galaxies are set in the last two columns.

Of course, those numbers are not complete for our sample. However, through this work we are going to study the galactic population in both samples, up to the more restrictive completeness limit, (the NOT sample one), except for computing the luminosity function and colour-magnitude diagrams, where we will take benefit of the completeness limits in ACS sample.

As far as the foreground galaxies are concerned, we can work out the number of field galaxies that are expected in our field of view up to our completeness magnitude by integrating the luminosity function of field galaxies in the solid angle corresponding to each of our clusters. The number of foreground galaxies per frame up to magnitude -19.5 that we have obtained are collected in Tables 3.2 and 3.3. These estimation are in good agreement with previous findings by Fasano et al. (2000) for the NOT sample and also with the foreground galaxies obtained from the literature for the ACS cluster as up to magnitude -19.5. The only case for which the number of foreground galaxies is higher is for CL0024.

Table 3.1: Redshift Information for the ACS Clusters

Name	N_{gal}	$N_{z,cl}$	$N_{z,f,cl}$	$N_{z,f}$	$N_{z,b}$
A 1689	586	34	10	2	62
A 1703	583	2	0	1	1
A 2218	624	58	7	2	22
CL0024	502	83	1	12	21
MS1358	387	54	4	2	5

However, as Czoske et al. (2001) identified an overdensity of galaxies a z $\sim$ 0.18 with no obvious centre. Consequently, the foreground contamination for our medium-redshift clusters is therefore statistically negligible as they have been already corrected.

Table 3.2: Foreground Galaxies for the NOT Clusters

Name	$N_{gal,fg}/frame$	$N_{gal,fg}/coverage$
A 1643	0.52	1.04
A 1878	0.67	1.34
A 1952	0.88	1.45
A 2111	0.73	1.40
A 2658	0.44	0.44

Table 3.3: Foreground Galaxies for the ACS Clusters

Name	$N_{gal,fg}/frame$
A 1689	0.65
A 1703	1.76
A 2218	0.59
CL0024	3.35
MS1358	2.39

Regarding to the background objects, the CMR provides a robust method, (Secker, Harris & Plummer, 1997; Fasano et al., 2002; López-Cruz et al., 2004; Barkhouse, Yee & López-Cruz, 2007), for determining the red early-type background galaxies. We know that the cosmological k-effect (Oke & Sandage (1968); Pence (1976); Frei & Gunn (1994); Poggianti (1997)), makes early-type galaxies look redder as their redshift increases. Then, if we find redder galaxies than those defined to belong to the cluster by the CMR, their distances must be larger

than the cluster distance. We have identified background galaxies as those objects that are 0.2 magnitudes redder than the value from the fitted CMR. After applying this criterion the final number of galaxies retained as members of one of our sample. amounts to 408. They are collected in the Table presented in the Table A.1 in the Appendix. The first column of that table gives the name of the cluster. The second and third columns give the coordinates of the galaxy, whereas we give in the fourth column the z information when available. The fifth and sixth columns give the r and B absolute magnitudes of each galaxy, assuming that they are located at the cluster redshift.

Similarly, the same correction have been applied to the g-r diagrams for the ACS clusters. The final number of galaxies is 2239. We have not shown these data in this report due to its size. However, they will be soon available electronically, Ascaso et al. (2008c).

3.1.3 Color-Magnitude Fit

The fit of the red sequence of the CMR for each cluster has been determined by carrying out a least absolute deviation regression fit to the observed data (Armstrong & Kung, 1978). The fit of the CMR for each cluster was obtained using an iterative procedure. A first fit was obtained using all the galaxies brighter than $M_r = -19.5$ for a given cluster of the NOT sample and $M_r = -17.8$ for the ACS sample. Then, the distance of each galaxy in B-r and g-r respectively, to the fitted CMR was computed. Those galaxies with a distance larger than three times the *rms* of the fitted relation were rejected, and a new fit to the CMR was done with the remaining ones. This process was repeated until the fit to the CMR did not change anymore . The final fit has been estimated by using a nonparametric bootstrap method, Efron & Tibshirani (1986), with $n \log^2 n$ resamplings, being n the number of galaxies up to the completeness limit, as prescribed in Babu & Singh (1983). The slope and zero point are the median value of the resampling, while the standard errors have been estimated as the *rms* of the bootstrap samples.

In Figures 3.3 and 3.4, we show the colour-magnitude diagrams for all the galaxies in NOT and ACS clusters, together with the fit to the CMR, showing also the upper 0.2 magnitude limit for considering a galaxy a member cluster (dotted line). The corresponding apparent magnitude to the M_r=-19.5 and M_r=-17.8 limit respectively, is marked with a vertical line. We have also plotted in the right column of that figure the histogram of the color differences between the observed and the CMR-fitted values. We give in Tables 3.4 and 3.5 the zero point, a_0, the slope, a_1 and the *rms* of the fitted CMRs for each cluster in NOT and ACS sample.

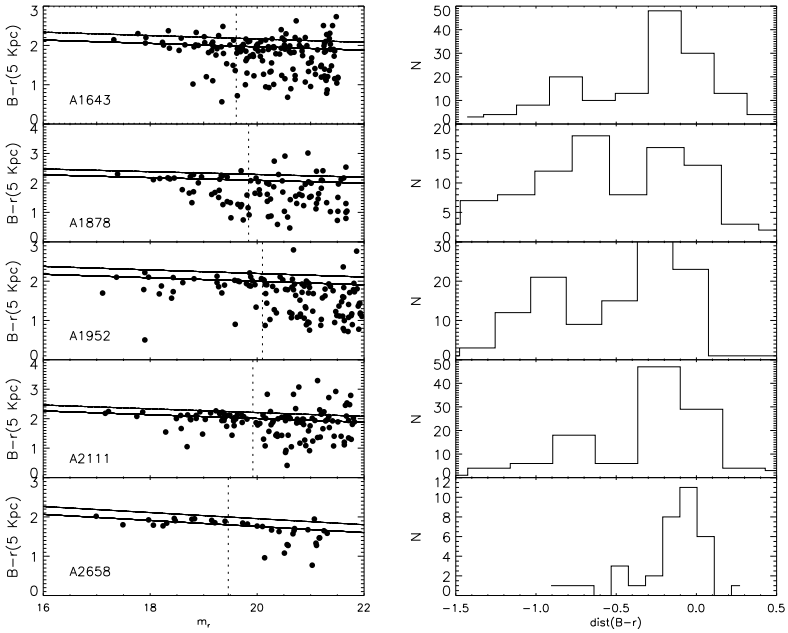

Figure 3.3: Left panels: The color-magnitude diagrams for the NOT clusters. The solid line is the fit to the red sequence and the dotted line is the upper 0.2 magnitude limit. The vertical line corresponds to the limit M_r = -20 at the cluster redshift. Right panels: The histograms of the B-r distance of the galaxies to the corresponding red sequence

3.1.4 Color-Morphology

In the left column of Figure 3.5 and 3.6, the colour-magnitude diagrams for the galaxy population to the sample has been plotted and the visual morphology (explained in Chapter 4) has been overplotted with different colours. Complementary, in the right hand, we have set the histogram of differences from the CMR for each morphological types. We can point out several features. A1643 has a wide population of late-type galaxies at a mean distance from the CMR of 0.3, although they populate the red sequence as well, they also have a peak of elliptical and lenticular galaxies which are defining the CMR, in particular, is quite noticeable that the brightest galaxy cluster is a lenticular galaxy, we will study that galaxy in Chapter 8. A different late-type galaxy dominated cluster is A1878. It has two main blue peaks, one placed very close the CMR relation and the other at a mean distance of 1 from the CMR. That last peak coincides with the irregular peak at approximately the same distance. In that case, the BCG is a elliptical galaxy, but the main fraction of galaxies belonging to the CMR are late type galaxies. We also note that A1689, A1703, A2218 and

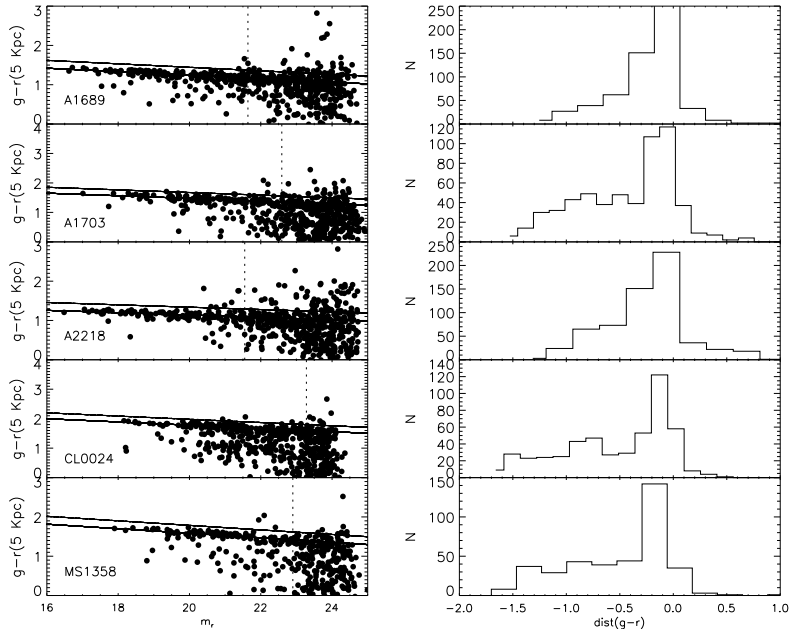

Figure 3.4: Left panels: The color-magnitude diagrams for the five clusters. The solid line is the fit to the red sequence and the dotted line is the upper 0.2 magnitude limit. The vertical line corresponds to the limit M_r = -17.8 at the cluster redshift. Right panels: The histograms of the B-r distance of the galaxies to the corresponding red sequence

MS1358 are mainly dominated by late-type galaxies, although, the red population dominates in the brightest part of the sequence.

The contrary happens to the rest of the clusters, we find that a strong peak of elliptical plus lenticular galaxies are dominating the core of the cluster and the CMR for A1952, A2111, A2658 and CL0024 and the four brightest galaxy clusters are elliptical galaxies. However, we find some differences. The lenticular population is completely dominant of the CMR for A2111 and CL0024 and it is skewed towards bluer colours for A1952 and towards redder colors for A2658. Also, for A2111, we find a large blue galaxy population already noticed by several works, (Butcher & Oemler, 1984; Miller et al., 2006)

3.1.5 CMR slope-Redshift

In order to compare the results of the fits to the colour-magnitude diagrams with a lower redshift sample, we have plotted in Figure 3.7, the slope values of the fitted CMRs in our clusters at medium redshift together with those obtained by López-Cruz et al. (2004) for clusters with $z < 0.15$. As the figure illustrates,

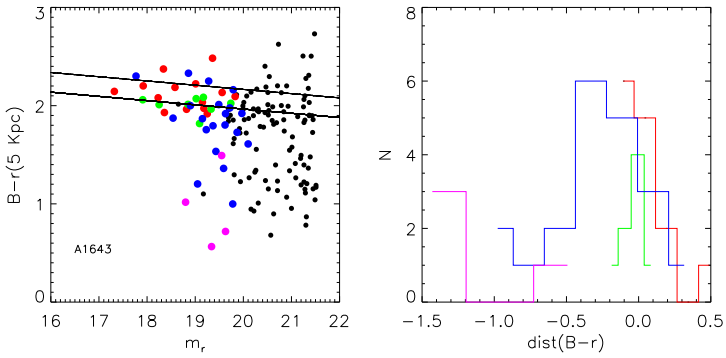
B−r(5 Kpc)
A1643
m_r
N
dist(B−r)

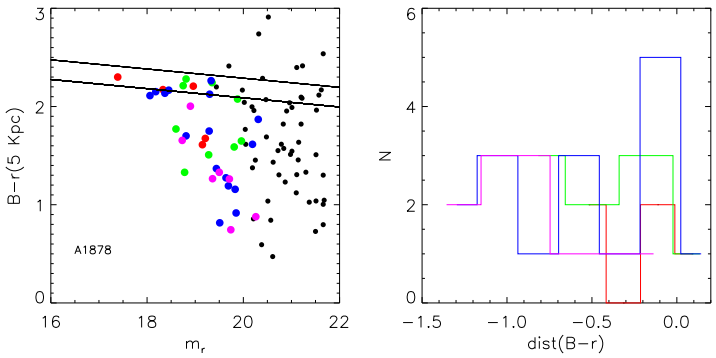
B−r(5 Kpc)
A1878
m_r
N
dist(B−r)

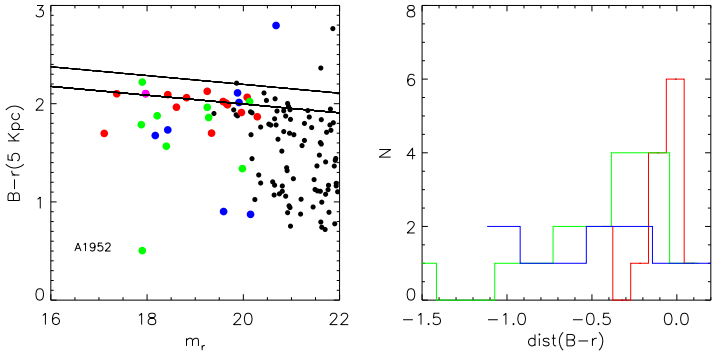
B−r(5 Kpc)
A1952
m_r
N
dist(B−r)

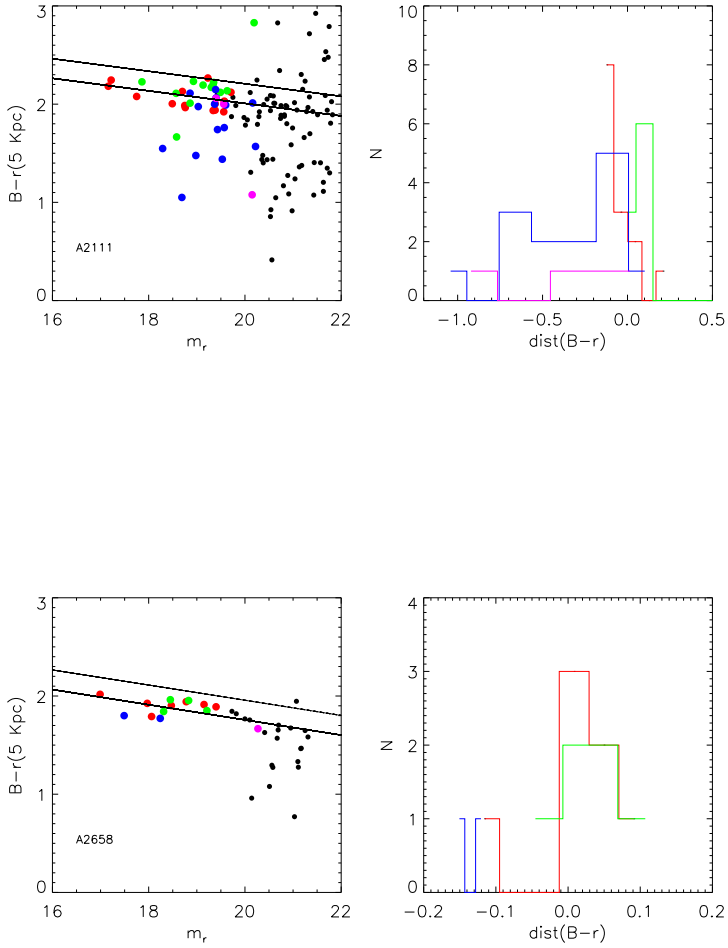

Figure 3.5: Left panels: The color-magnitude diagrams for the five clusters galaxy population. The solid line is the fit to the red sequence and the dotted line is the upper 0.2 magnitude limit. Right panels: The histograms of the B-r distance of the galaxies to the corresponding red sequence. Red, green, blue and purple colors refer to galaxies classified as Elliptical, Lenticular, Spiral and Irregular galaxies respectively.

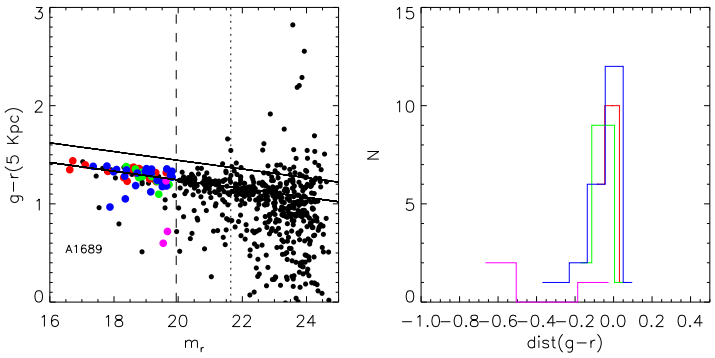
g−r(5 Kpc)
A1689
m_r
N
dist(g−r)

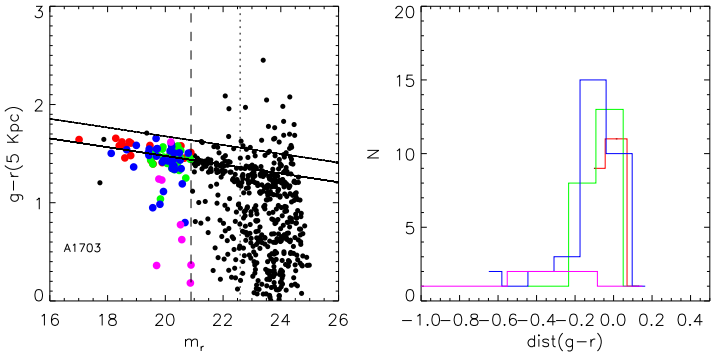
g−r(5 Kpc)
A1703
m_r
N
dist(g−r)

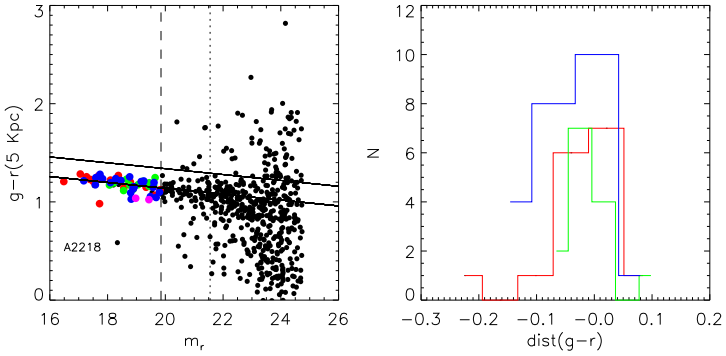
g−r(5 Kpc)
A2218
m_r
N
dist(g−r)

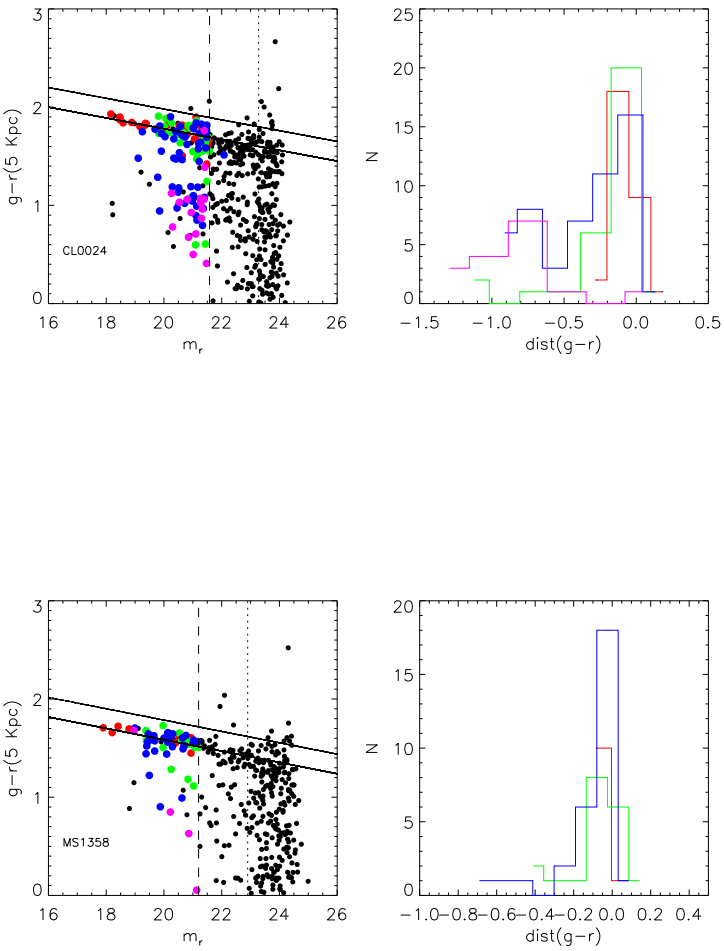

Figure 3.6: Left panels: The color-magnitude diagrams for the five clusters galaxy population. The solid line is the fit to the red sequence and the dotted line is the upper 0.2 magnitude limit. Right panels: The histograms of the g-r distance of the galaxies to the corresponding red sequence. Red, green, blue and purple colors refer to galaxies classified as Elliptical, Lenticular, Spiral and Irregular galaxies respectively.

Table 3.4: CMR parameters in NOT sample

Name	$a0$	$a1$	rms
A 1643	2.825 ± 0.224	-0.043 ± 0.011	0.035
A 1878	3.022 ± 0.390	-0.046 ± 0.021	0.060
A 1952	2.893 ± 0.257	-0.044 ± 0.013	0.009
A 2111	3.285 ± 0.079	-0.063 ± 0.004	0.053
A 2658	3.301 ± 0.257	-0.077 ± 0.013	0.037

Table 3.5: CMR parameters in ACS sample

Name	$a0$	$a1$	rms
A 1689	2.131 ± 0.017	-0.044 ± 0.0008	0.003
A 1703	2.367 ± 0.021	-0.044 ± 0.0010	0.006
A 2218	1.736 ± 0.008	-0.029 ± 0.0004	0.004
CL0024	2.878 ± 0.017	-0.054 ± 0.0008	0.006
MS1358	2.740 ± 0.035	-0.057 ± 0.0016	0.004

there is no clear tendency of the slope of the CMR with redshift. The mean value of the slope of the CMR for our sample together with López-Cruz et al. (2004) is -0.050 ± 0.008. Only for the NOT sample, we obtain -0.055 ± 0.014 and for the ACS sample, -0.046 ± 0.010. The mean value for both samples together is -0.050 ± 0.013, which is the same that the whole mean. In addition, those values are very similar to the slope value found by Mei et al. (2006) for two clusters at z$\sim$1.26.

In other words, the slope values we find for our clusters at z $\sim$ 0.3 are completely consistent with the values found for lower and much higher redshift values. Moreover, the range of values found at any redshift are also similar. Thus, we find no indication of change of the CMR slope up to z $\sim$ 0.3 and even up to z$\sim$1.26. This result would indicate that the stellar population of the bright, early type galaxies defining the cluster red sequence was settled afterwards the galaxy formation.

3.2 The Butcher-Oemler Effect

As we have previously seen, Butcher & Oemler (1984) found a possible evolutionary aspect of the cluster population: an increasing trend of the galaxy blue fraction in clusters with redshift, usually called the Butcher-Oemler Effect. Subsequent works, (Rakos & Schombert, 1995; Margoniner & De Carvalho, 2000;

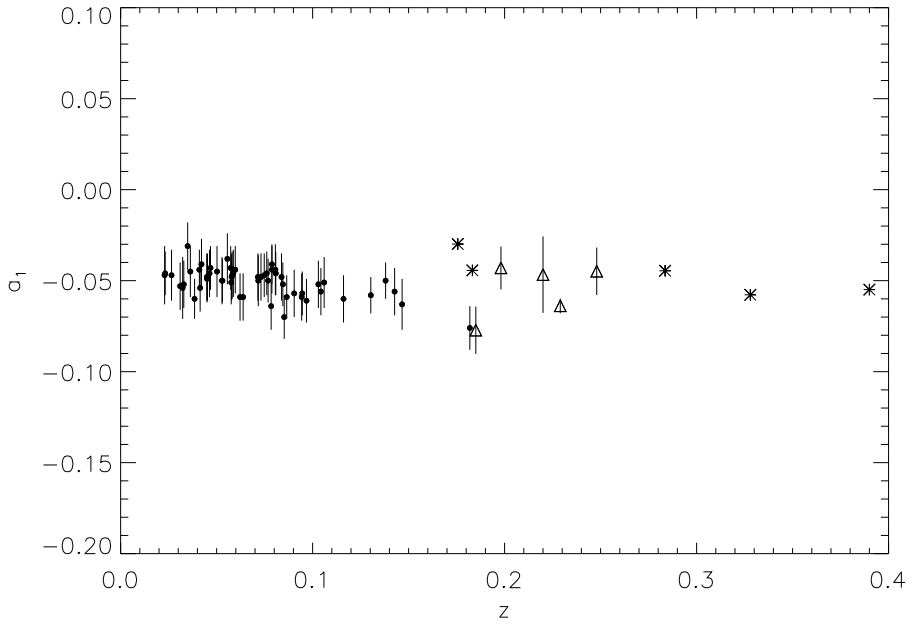

Figure 3.7: Slopes of the CMR for the sample of López-Cruz et al. (2004) (black circles), NOT sample (empty triangles) and ACS sample (asteriks).

Margoniner et al., 2001), confirmed that tendency, quantifying also its large dispersion and its dependence with other clusters characteristics. The original analysis of this effect by Butcher & Oemler (1984), defined blue galaxies as those within a radius containing 30 % of the cluster population, which are brighter than M_v=-20 and bluer by 0.2 mag in B-V than the colour-magnitude relation defined by the cluster early-type galaxies.

In this section, we have studied the fraction of blue galaxies, f_b of the bright population, $M_r \leq -20$, for the clusters sample presented in this work. We have considered blue galaxies those with B-r color at least 0.26 magnitudes bluer than the red sequence for the NOT sample. This color index corresponds to the original Butcher-Oemler definition and the transformations has been performed following the prescriptions by Quintana et al. (2000); Goto et al. (2003); De Propris et al. (2004). For the ACS we have adopted a g-r index of 0.2 as prescribed by Goto et al. (2003). Given the photometric errors and the statistical nature of the k-correction we have just adopted that common value of the color index for all the clusters in spite of their differences in redshift. The results are not affected if individual color values were adopted.

Several authors have noticed that the fraction of blue galaxies strongly depend on the magnitude limit ant the cluster-centric distance used, (Margoniner & De Carvalho, 2000; Ellingson et al., 2001; Goto et al., 2003; De Propris et al., 2004;

Andreon et al., 2006). They observed that f_b grows when the magnitude limit is fainter and the aperture is larger, which reflects the existence of al large fraction of faint blue galaxies in the outer regions of the clusters.

The fraction of blue galaxies has been computed for each cluster using all the surveyed area. In order to be able to compare our results for the different clusters and with other studies, we have considered that our results are representative of the area corresponding to a circular aperture that, centered at the center of the cluster, includes all the area that we have actually covered. For comparison purposes, we have adopted two apertures for the NOT sample, of radius 420 and 735 Kpc respectively. For the cluster A2658, only the smaller aperture could be used. For the ACS sample, an aperture of 475 Kpc has been selected. In the original definition given by Butcher & Oemler (1984), the fraction was calculated for an aperture containing 30% of the cluster population (R_{30}). Since only the central parts of our clusters were sampled we could not determine the value of R_{30} for them. The fixed apertures we have used are a substitute of the canonical value. We notice that they are in the range of the expected R_{30} values as given by Butcher & Oemler (1984).

The errors attributed to the measured fractions were computed assuming Poissonian statistics following the prescriptions set in De Propris et al. (2004). In other words, if the blue fraction is defined as the ratio of m blue galaxies observed out of n total galaxies and assuming that m and n obey Poissonian statistic, the blue fraction is

$$f_b = \frac{m}{n}$$

and its likelihood probability function has the following form with n fixed in advance.

$$L \sim f_b^m (1 - f_b)^{n-m}$$

whose maximum is m/n. Let's note that the form of that function is the same for a Poisson or binomial statistics. The variance of the blue fraction can be computed as

$$\sigma^2(f_b) = \begin{cases} \left(\frac{d^2 \ln L}{df_b^2} \right)^{-2} = \frac{m(n-m)}{n^3} & \text{if } n \neq 0 \\ 1/2n & \text{if } n = 0 \end{cases}$$

The value for $m = 0$ is set as $1/2n$ as a reasonable error bar to adopt for the $m = 0$ case, (De Propris et al., 2004).

In Figure 3.8, we show the blue fraction of galaxies in the NOT and ACS clusters as a function of redshift within a radius of 420 and 475 Kpc, respectively. Also, in Figure and 3.9, the blue fraction for the NOT sample within a radius of 735 Kpc is given. We have also plotted for comparison the blue fraction of galaxies obtained from a sample of nearby galaxy clusters by Aguerri et al. (2007). The different error bars for the two samples simply reflects the different sizes of the

samples used to compute the blue fraction. We notice here that our errors bars are very similar to those given by De Propris et al. (2004). In all cases, we have more than 10 galaxies per cluster to compute the blue fraction. The comparison with the data by Aguerri et al. (2007), or with the results shown in Figure 2 of De Propris et al. (2004), clearly indicate that there is no relation between the value of the blue galaxy fraction and the cluster redshift. The blue fraction values are listed in Tables 3.6 and 3.7 for both samples.

Table 3.6: Blue galaxy fraction of galaxies in NOT sample

Name	$f_b(420Kpc)$	$f_b(735Kpc)$
A 1643	0.090 ± 0.086	0.090 ± 0.086
A 1878	0.363 ± 0.102	0.517 ± 0.092
A 1952	0.250 ± 0.088	0.285 ± 0.085
A 2111	0.031 ± 0.030	0.125 ± 0.052
A 2658	0.083 ± 0.079	

Table 3.7: Blue galaxy fraction of galaxies in ACS sample

Name	$f_b(475Kpc)$
A 1689	0.048 ± 0.034
A 1703	0.111 ± 0.049
A 2218	0.024 ± 0.024
CL0024	0.315 ± 0.054
MS1358	0.111 ± 0.052

The range of values found is similar to that found by De Propris et al. (2004); Aguerri et al. (2007) for lower redshift clusters. In particular, the very high blue fraction we obtain for A1878 is procured for some lower z clusters in the quoted references. The central median values we find for our sample are 0.090 ± 0.138 for the 420 Kpc and 0.285 ± 0.194 for the 735 Kpc aperture in NOT sample and 0.111 ± 0.114 for the 475 Kpc aperture in ACS sample, in agreement with the median f_b value, 0.090 ± 0.063 of Aguerri et al. (2007).

We find a nominal difference in the blue fraction as a function of the aperture, in the sense of an increase with the aperture. This is in agreement with the findings by Margoniner & De Carvalho (2000); Goto et al. (2003); De Propris et al. (2004). Unfortunately the statistic errors are too large for the difference to be significant. The apertures used by Aguerri et al. (2007) refer to r_{200}, with a mean value of 1.295 Mpc for the clusters in their sample, somewhat larger than our 735 Kpc aperture. Following Margoniner & De Carvalho (2000), our values should be slightly increased to be directly comparable with those by Aguerri

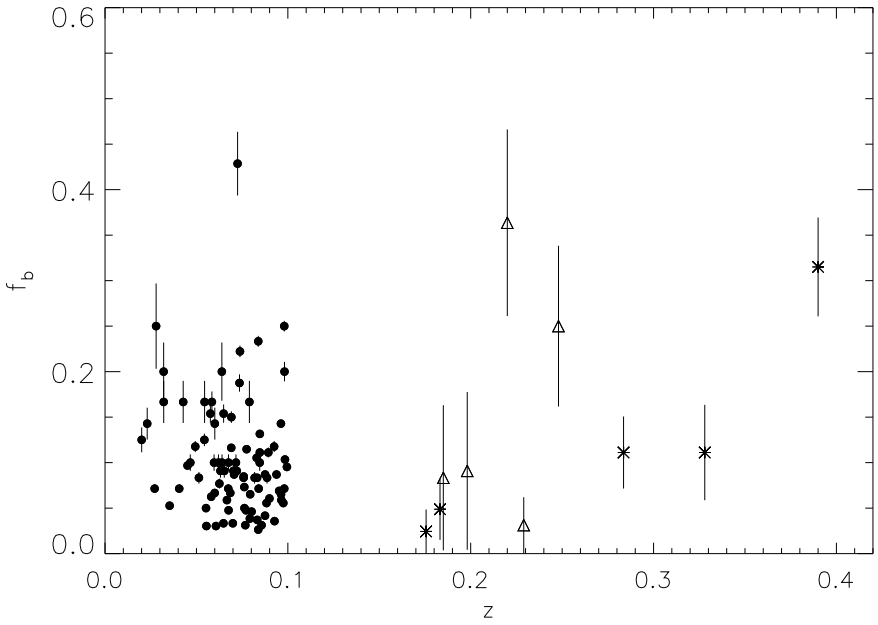

Figure 3.8: Blue fraction of galaxies in NOT (empty triangles) and ACS (asteriks) sample of clusters compared with those obtained by Aguerri et al. (2007) (black circles) computed within a radius of 420 Kpc (NOT sample) and 475 Kpc (ACS sample)

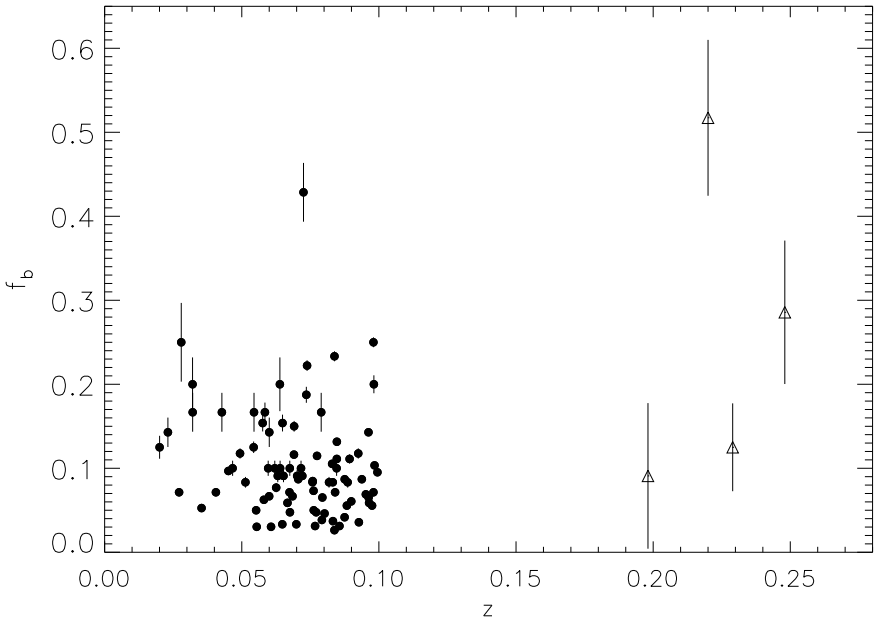

Figure 3.9: Blue fraction of galaxies in NOT sample of clusters (empty triangles) compared with those obtained by Aguerri et al. (2007) (black circles) computed within a radius of 735 Kpc.

et al. (2007). Nevertheless, as the differences between both apertures in our sample are not significant, we considered that the comparison is sound.

Regarding the cluster A2111, Butcher & Oemler (1984) obtained a blue fraction of 0.16 ± 0.03 within a r_{30} that, for this cluster, corresponds to 892 kpc. Miller et al. (2006) obtained, for the same aperture, the values of 0.15 ± 0.03 and 0.23 ± 0.03 using photometric data or only galaxies with spectroscopic data, respectively. We have obtained 0.031 ± 0.030 and 0.125 ± 0.052 for our 420 kpc and 735 Kpc aperture, a smaller value even if not significantly different when the errors are taken into account.

Chapter 4

Galaxy Morphology

Centellas y meteoros se cruzan con mis gritos
te amo mientras mis pulmones crean la Vía Láctea de nuevo
y el sol vuelve a nacer redondo y amarillo de mi boca
la luna se me suelta de los dedos
Marte, Plutón, Neptuno, Venus, Saturno y sus anillos
las novas, súper novas, los agujeros negros
anillos concéntricos de galaxias innombrables.

Gioconda Belli, 'Nueva teoría sobre el Big Bang'

Since the discovery of the nature of the first galaxies, by Edwin Hubble Hubble (1926), a number of attempts to set a morphological classification for the galaxies has been tried. The most popular classification, given by the same Hubble, was initially developed to classify nearby galaxies in the optical and slightly modified later on by de Vaucouleurs (1959, 1963); van den Bergh (1997). Sandage (1961) illustrated the final Hubble revision. Additional classification systems are for example, Yerkes system (Morgan, 1958, 1962) or the luminosity system for spiral galaxies by van den Bergh (1960).

Hubble's classification separated galaxies into two big groups. On one hand, the early type galaxies (elliptical and lenticular) and on the other hand, late-types (spiral and irregular). Those types were initially thought to form an evolutive sequence. In particular, the sequence was best defined for spirals since three classification criteria were available: the relative strength of the bulge, the degree of the resolution of the arms and the openness of the arms.

At present, that system continues being still used as some physical trends, even with a large dispersion, seems to be associated to each morphological type such as the mean luminosity or the mean colors. For example, early type galaxies possess an older red stellar population, have very few hydrogen and are usually

very bright. On the contrary, late type galaxies have a blue young stellar population, are rich in gas and have generally lower surface brightness than early types. Intermediate types have transitional properties between these extremes.

Furthermore, a number of works have found different correlations between galaxy parameters for a fixed Hubble morphological type. For example, elliptical galaxies present a tight sequence between color index and magnitude, called the Color-Magnitude Relation, (Visvanathan & Griersmith (1977)), relationship between luminosity and central velocity dispersion (Faber & Gallagher (1976)), metallicity (Terlevich et al., 1981) or between surface brightness, radius and velocity dispersion, more commonly known as the Fundamental Plane (Dressler et al., 1987; Djorgovski & Davis, 1987; Jørgensen, Franx & Kjaergaard, 1992). Likewise, spiral galaxies show correlations between luminosity and rotation velocity (Tully & Fisher, 1977), among others.

However, with the new advances of the technology and the advent of huge telescopes and spatial telescopes, we are able to observe more and more distant galaxies. It has been noticed that the morphologies observed for the nearby galaxies as well as the interaction rate of galaxies are changing as the redshift grows, Patton et al. (2000); Consolice, Gallagher & Wyse (2001); De Propris et al. (2007) and the number of galaxies to process grows exponentially as we arrive deeper in the Universe.

In addition, the projected size of the galaxy diminishes as they are further and their morphological details are much more difficult to distinguish with our perception. Therefore, the need of establishing a quantitative morphological classification, without relying on the subjective human eye is more and more compelling. Nevertheless, that aim has not been still solved successfully.

We must not forget that we are dealing with two-dimensional images or in the best of the cases, we have also spectra. Consequently, we suffer a lack of information at analyzing these data that translates into uncertainty. For example, the high inclination of a galaxy can lead us to completely misinterpret its morphology. Nevertheless, we can not recover that information by quantitative morphologies neither for a particular galaxy and we have to appeal to statistical methods.

In that Chapter, we have classified visually our sample of bright galaxies with the Hubble system into Elliptical, Lenticular, Spiral and Irregular galaxies. That procedure has been possible as the range of redshift is within the limit to allow the human eye to distinguish the morphological procedures of the bright ones. We have explored the differences with other classifications and stablished the common undertermination in the visual classification.

4.1 Visual classification

All the galaxies brighter than $M_r = -19.5$ in both samples, were classified visually into four different Hubble types: Ellipticals (E), Lenticulars (S0), Spirals

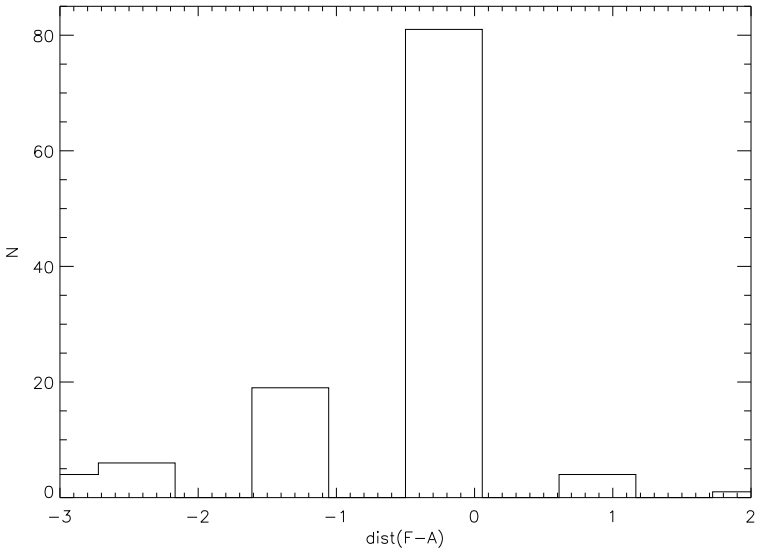

Figure 4.1: The visual classification differences between Fasano et al. (2000) and this work.

(Sp) and Irregulars (I). For NOT sample, we have compared our classification with that reported by Fasano et al. (2000) for the galaxies in common. The morphological classification for that bright subsample is given in the last column of the table A.1 in the Appendix.

In Figure 4.1, we show the result of that comparison. Notice that 70% of the galaxies were classified with the same type, whereas 20% more differ by only one type. Additionally, the difference distribution seems to be skewed to negative values. In other words, the classification given by Fasano et al. (2000) tends to classify more early types than our work. That deviation may exist due to the difficulty of distinguishing between lenticular and early spiral galaxies or even between Elliptical and Lenticular Galaxies.

Concerning the ACS, sample, we have also compared our visual classification with the classification obtained by different authors in the literature. For A1689, we have compared our visual classification with the one obtained by Teague, Carter & Gray (1990) and Duc et al. (2002), the results of that comparison are set in Figure 4.2. We have obtained that 75% of the objects have the same type in both classifications.

The more complete classification in the literature for the sample is given for CL0024 by Treu et al. (2003). We have obtained 86 galaxies in common, with a 76.74 % of them classified with the same morphological type, shown in Figure 4.3.

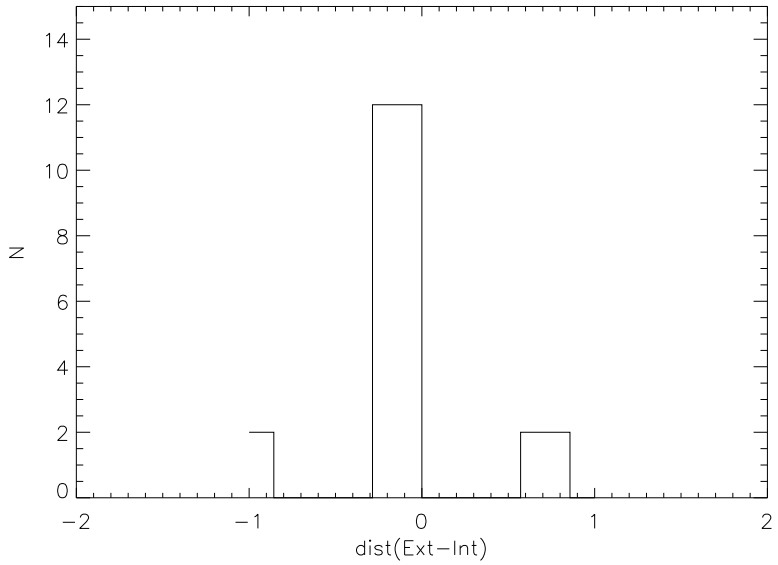

Figure 4.2: The visual classification differences between Duc et al. (2002) and this work for A1689.

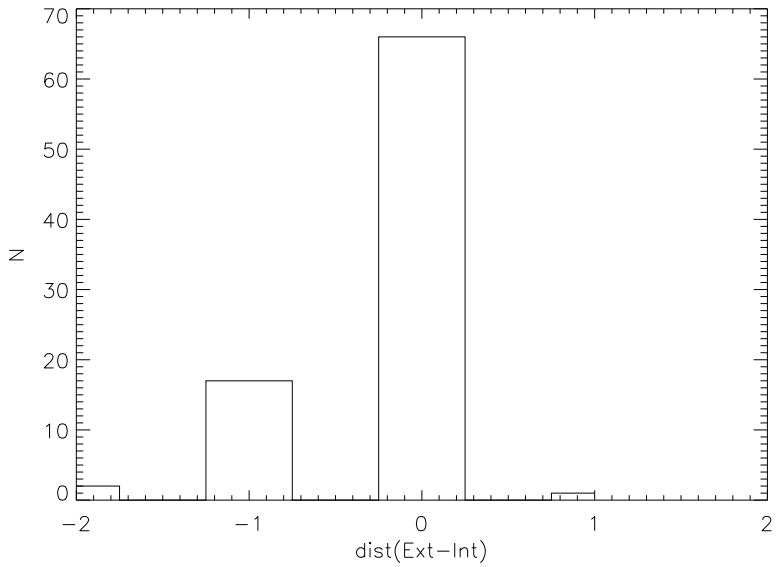

Figure 4.3: The visual classification differences between Treu et al. (2003) and this work for CL0024.

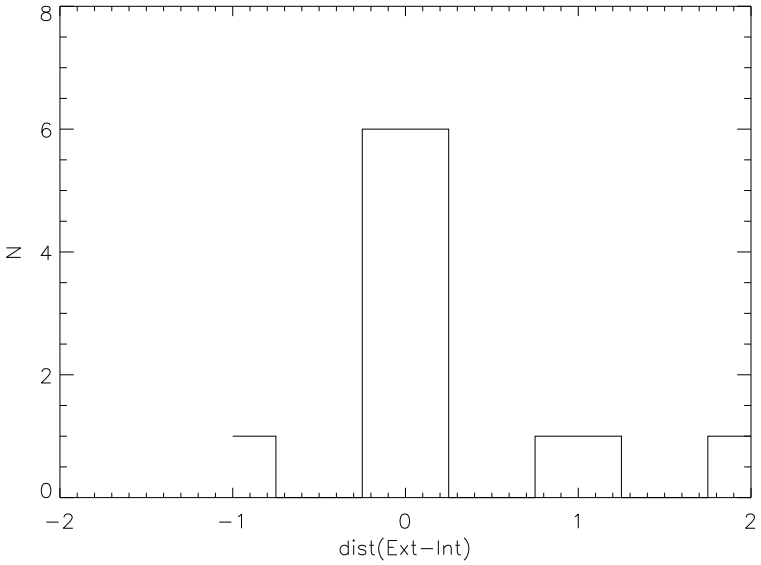

Figure 4.4: The visual classification differences between Fabricant, Franx & van Dokkum (2000) and this work for MS1358.

Finally, Fabricant, Franx & van Dokkum (2000) performed a classification of MS1358, but we have only found nine galaxies in common, of which, six are of the same type, achieving a 66.6%. The results have been plotted in Figure 4.4

In Table 4.1 we show the percentages of the different galaxy types in the central part of each cluster of the NOT sample. Similarly, in Table 4.2, the percentages of the different galaxy types in the central part of each cluster of the ACS are collected. Notice that A1643 has a large number of spiral galaxies (around 57%). On the other hand, A1878 contains also a great proportion of late-type galaxies (around 60%), including a large fraction of irregular galaxies (19%). Also MS1358, has a 49% of late-type galaxies and CL0024 a 51 %, including a 12% of irregular galaxies.

We do not have any cluster with a elliptical fraction larger than 31 % in the ACS sample. On the contrary, we obtain two elliptical-rich clusters in the NOT sample, A1952 and A2111. A diversity is clear as far as morphological populations is concerned.

Table 4.1: Fraction of Morphological Types in NOT sample

Name	420Kpc				735Kpc			
	E	S0	S	I	E	S0	S	I
A 1643	0.22	0.22	0.56	0.00	0.24	0.19	0.57	0.00
A 1878	0.11	0.22	0.41	0.26	0.14	0.24	0.43	0.19
A 1952	0.52	0.28	0.20	0.00	0.45	0.31	0.24	0.00
A 2111	0.38	0.28	0.28	0.00	0.35	0.28	0.30	0.08
A 2658	0.54	0.31	0.15	0.00				

Table 4.2: Fraction of Morphological Types in ACS sample

Name	475Kpc			
	E	S0	S	I
A 1689	0.31	0.22	0.42	0.05
A 1703	0.24	0.28	0.38	0.09
A 2218	0.29	0.25	0.42	0.04
CL0024	0.24	0.25	0.39	0.12
MS1358	0.20	0.31	0.44	0.05

4.2 The concentration parameter

The Concentration Parameter was introduced by Butcher & Oemler (1978) as a measurement of the degree of regularity of the morphological content in each cluster. It was defined as:

$$C = \log(R_{60}/R_{20})$$

where R_{60} and R_{20} are the radii containing 60% and 20% of the cluster populations. Ideally, we would measure the galaxy density in all the cluster area to determine the radius. However, it is very difficult to obtain the whole cluster coverage. However, we have estimated that the calculus for the concentration parameters is well in the range given by Butcher & Oemler (1978).

We have calculated the concentration parameter of our clusters in the central 735 Kpc. Only the four clusters from the NOT sample were analyzed as the rest of the cluster were not covering enough area to compute that quantity. The concentration values we have found are collected in Table 4.3.

Table 4.3: Concentration Parameter in NOT Clusters

Name	C
A 1643	0.311
A 1878	0.389
A 1952	0.696
A 2111	0.329
A 2658	

We have plotted these values in Figure 4.5, together with the values for lower redshift clusters, as given by Butcher & Oemler (1978) and for a higher redshift sample presented in Dressler et al. (1997). As can be seen in the Figure, our concentration values span the full range of the values measured for lower redshfit clusters. Moreover, this range encompasses also that of the higher redshift clusters concentration values. It does not seem therefore, that there is any clear tendency of the concentration parameter with redshift or morphological types. At most, it could be argued that clusters tend to progressively populate the lower half of the plane when the redshift increases, but larger samples should be analyzed before extracting some conclusions.

Likewise, Butcher & Oemler (1978); Dressler et al. (1997) suggested that the more irregular, less concentrated clusters would be preferentially populated by late type galaxies. In that sense, we notice that A1643, the cluster with the largest global fraction of late-type galaxies, presents the lowest value of the concentration parameter. Moreover, A1878, another cluster with a low concentration index presents also a rather high fraction of late type and irregular

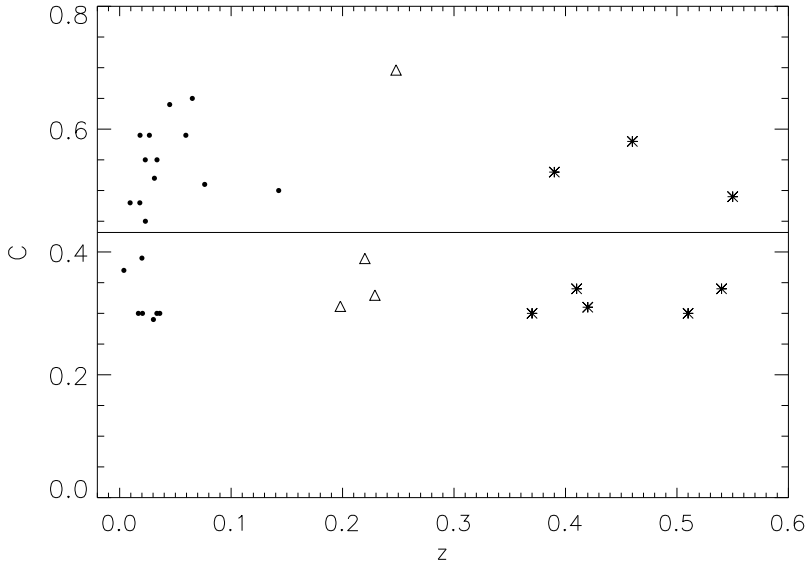

Figure 4.5: Concentration parameter versus redshift for our clusters (triangles), a low-redshift compilation (Butcher & Oemler (1978): triangles) and a higher redshift sample (Dressler et al. (1997): black points). The horizontal line is the mean concentration value of our the clusters with enough area coverage

galaxies and, in fact, is dominated by this population. However, A2111, our third cluster with a low concentration, is dominated by an early-type population. All in all, although there is an indication for the higher fraction of irregular clusters with increasing redshift, the small statistics prevent us to extract a firm conclusion.

4.3 Interaction systems

Other interesting feature that could deserve consideration in clusters at that range of redshift is the proportion of interacting systems compared to lower redshift clusters. To do that, we have calculated the distribution of the **perturbation, f-parameter** defined by Varela et al. (2004) for the galaxies in the final catalogue of cluster galaxies as

$$f = \log(\frac{F_{ext}}{F_{int}}) = 3\log(\frac{R}{D_p}) + 0.4 \times (m_G - m_p) \tag{4.1}$$

where m_G and m_P are the apparent magnitudes of the primary and perturber galaxies respectively. D_p is the projected distance between the galaxy and the perturber, and R is the size of the galaxy. Also, the second term of the equality

Table 4.4: Median Perturbation f-Parameter for NOT Clusters Sample

Name	C
A 1643	−1.92
A 1878	−1.60
A 1952	−1.29
A 2111	−1.67
A 2658	−1.39

Table 4.5: Median Perturbation f-Parameter for ACS Clusters Sample

Name	C
A 1689	−1.68
A 1703	−1.67
A 2218	−1.56
CL0024	−1.94
MS1358	−2.08

is the logarithm of the ratio between the tidal force exerted by the perturber, P, on the primary galaxy, G, and the internal force per unit mass in the outer parts of the primary.

That parameter gives an account of the relative importance of the tidal forces for every galaxy. The results are plotted in Figure 4.6 and 4.7 for the NOT and ACS sample, respectively. The median value of the distribution is -1.85 for the NOT sample and -1.76 for the ACS sample, whereas the median value found for the Coma Cluster amounts to -2.7 (Varela et al. (2004)). Moreover, we find that 63.97% of the galaxies have a perturbation parameter higher than -2 for the NOT sample and 60.05% of the galaxies for the ACS sample. This is the value chosen by Varela et al. (2004) to select truly interacting systems. These results are suggestive of the presence of a higher population of interacting systems in our sample, compared to Coma.

A particular view at the situation in each cluster is collected in Tables 4.4 and 4.5 for both samples. Those tables show the median f-values. We note that A1643 from the NOT sample and CL0024 and MS1358 from the ACS sample, have perturbation parameters which are very close to -2, while they descend to smaller values for A1878, A1952, A2111 and A2658 (NOT sample) and A1689, A1703 and A2218 (from ACS sample) pointing to a more disturbed population.

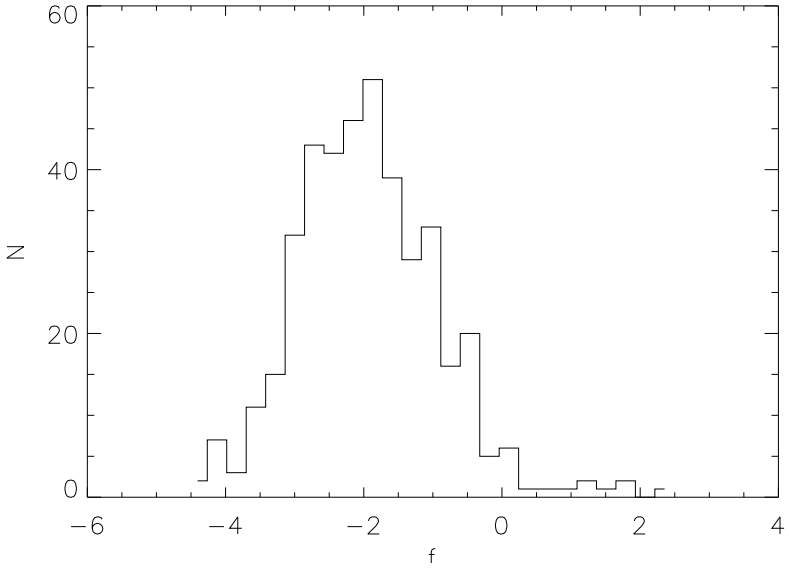

Figure 4.6: Histogram of the f-parameter values for the galaxies belonging to NOT sample.

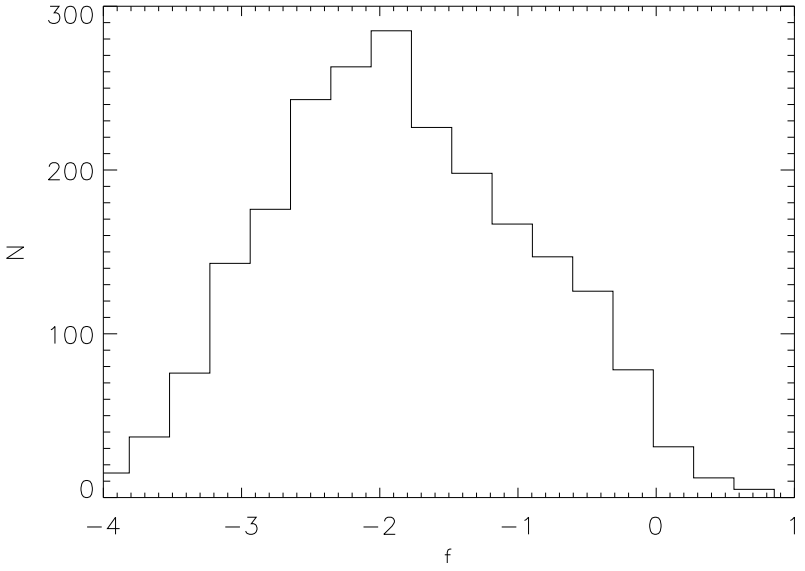

Figure 4.7: Histogram of the f-parameter values for the galaxies belonging to ACS sample.

Chapter 5

Galaxy Surface Brightness Analysis

L'ordinador simula el naixement dels estels
L'ordre matemàtic simula el món real,
crea un altre món -de càlcul, i mental-
regit per lleis exactes, hipòtesis, models:
en un ordinador reneixen els estels
com fa tants anys nasqueren, en brous primordials.
I som com creadors!: veiem a la pantalla
Un món tot just nascut. Una galàxia qualla.
Es formen els estels -i tot sota control!
I regulem el temps i dominem el Sol,
i musiquem i tot la còsmica rondalla!
-fins que el flux elèctric, de cop i volta, es talla.

David Jou, 'El color de la ciència'

The first observations of galaxies provided evidence about the radial symmetry of the galaxies and consequently, a number of pioneering works attempted to describe the light distribution in galaxies taking advantage of that fact. For example, in 1913, Reynolds, (Reynolds, 1913), proposed a variation of luminosity in the central region of M31 (without the spiral arms) with the following form:

$$SB = \frac{constant}{(x+1)^2}$$

where x is the projected distance to the centre.

Some years later, in 1930, Hubble introduced an analytical mathematical ex-

pression to fit the light distribution of the galaxies:

$$\log I = \log I_0 - 2\log\left(\frac{r}{a} + 1\right)$$

where I is the **surface brightness**, (that is, the energy flux per surface unit) at a distance r from the center of the galaxy, I_0 is the central surface brightness and a is a parameter depending on each galaxy.

It was, however, in 1948, when de Vaucouleurs, (de Vaucouleurs, 1948), introduced one of the most popular, obtained empirically, model for describing the light distribution in elliptical galaxies. It is the **de Vaucouleurs Law**, also called the $r^{1/4}$ **law** due to its mathematical form:

$$\log I = \log I_e - 3.33[(r/r_e)^{1/4} - 1] \tag{5.1}$$

where, again I is the surface brightness at a distance r from the center of the galaxy, r_e is the **effective radius** or the radius enclosing half of the total luminosity of the galaxy and I_e is the surface brightness at a distance r_e from the center of the galaxy.

Regarding to more complex morphological profiles, e.g. lenticular or spiral galaxies, two main components have to be differenced: the bulb and the disc. Bulbs usually are quite accurately described by a $r^{1/4}$ profile. On the contrary, discs are better approximated by a **exponential law**, which was introduced by Freeman (1970)

$$I(r) = I_0 e^{-r_d/h} \tag{5.2}$$

where I_0 and h are the central intensity and disc scale length, respectively. The exponential law has been habitually used in the literature to model the surface brightness profile of the discs showed by spiral galaxies (e.g. Trujillo et al. (2001c); Aguerri et al. (2005); Allen et al. (2006)).

Equations 5.1 and 5.2 are particular cases of a more general form of representing the galaxy surface brightness, introduced by Sersic (1968), the **Sersic law**. The radial variation of the intensity of this law is given by:

$$I(r) = I_e 10^{-b_n[(r/r_e)^{1/n}-1]} \tag{5.3}$$

where r_e is the effective radius, I_e is the intensity at r_e and n is the **shape parameter**, which regulates the steepness of the light profile in the model. Finally, b_n is coupled to n and it is obtained from solving the equation

$$\Gamma(2n) = 2\gamma(2n, b_n)$$

in which Γ and γ represent the mathematical function gamma and incomplete gamma, respectively. That equation can be approximated by $b_n = 0.868n - 0.142$ so that half of the total luminosity is within r_e (see Caon et al. (1993); Trujillo et

al. (2001c)). The Sersic law has been extensively used in the literature to model the surface brightness of elliptical galaxies (Graham & Guzman (2003)), bulges of early and late-type galaxies, (Andredakis et al., 1995; Prieto et al., 2001; Aguerri et al., 2004; Möllenhoff, 2004), the low surface brightness host of blue compact galaxies (Caon et al., 2005; Amorin et al., 2007) or dwarf elliptical galaxies, (Binggeli & Jerjen, 1998; Graham & Guzman, 2003; Aguerri et al., 2005) among others.

The Sersic model was initially conceived to be able to fit any morphological type with the flexible shape parameter n. For $n = 0.5$ a Sersic model becomes a gaussian profile, for $n = 1$, it turns into a pure exponential, while for $n = 4$, it reduces to a classical de Vaucouleurs profile.

All of those profiles are uni-dimensional. In other words, the fit is doing throughout an axis that crosses the galaxy or with an azimuthal average of the bi-dimensional surface brightness distribution. Therefore, they do not take into account some two dimensional features such as for example, the position angle of the bulge and disk component(Trujillo et al. (2001c)) or the intrinsic shapes (Prieto et al. (2001)), leading frequently to systematic errors in the results of the fit, (Byun & Freeman (1995)).

Many tools in literature have been developed in the last years in order to provide two-dimensional parametric bulge-disk decomposition of the galaxies surface brightness profiles as for example, GIM2D (Galaxy IMage 2D, Simard (1998)), GALFIT (Peng (2002)), BUDDA (Bulge/Disk Decomposition Analysis, de Souza, Gadotti & dos Anjos (2004)), GASPHOT (Galaxy Automatic Surface PHOTometry, Pignatelli, Fasano & Cassata (2006)) or GASP-2D (GALaxy Surface Photometry 2 Dimensional Decomposition, Méndez-Abreu et al. (2008)).

Those methods were developed to solve different problems of galaxy decompositions when fiting the two-dimensional galaxy surface-brightness distribution. They use different minimizations routines to perform the fit and different functions to parametrize the galaxy component.

In that work, the fits have been carried out using the automatic fitting routine (GASP-2D) developed and successfully validated by Méndez-Abreu et al. (2008). A number of reasons can be given for the selection of this routine. The algorithm is quasi-authomatical, what is very useful at dealing with a large number of galaxies. It is also very feasible and minimizes the interaction with the user. In addition, the computational time is not very high as it uses the Levenberg-Marquardt algorithm to fit the two-dimensional surface-brightness distribution of the galaxy (Press et al. (1992)).

5.1 Previous analysis

Preceding to the fit of the images, we have revised visually different photometrical features in order to obtain more information about the surface brightness fit.

First of all, for each galaxy, we created the **smoothed images** with the IRAF task *boxcar*. That task convolves the original image with a flat-topped rectangular kernel of a given dimension. The result images allows to stands out the possible small galaxies or globular clusters that can be found in the halo of the large galaxies, irregularities, arms, disc or even dust.

Secondly, we have also created a different but functional image: the **color images**, which contains the difference in color B-r for each pixel of the image. Those images are specially useful to be able to distinguish dust regions inside the galaxies. As the dust emits at larger wavelengths, the redder regions will indicate different dust features as: wisps, patches or dust disks (Ferrarese et al. (2006)).

5.2 Two dimensional surface brightness fit

5.2.1 GASP-2D

The GASP-2D routine (Méndez-Abreu et al. (2008)) is a routine that performs a fully two-dimensional fit to the surface brightness of a galaxy. The photometrical galaxy components were characterized by elliptical and concentric isophotes with constant (but possibly different) ellipticity and position angle. We have assumed a cartesian coordinates system (x, y, z) with origin in the galaxy center, the x-axis parallel to the direction of the right ascension and pointing westward, the y-axis parallel to the direction of declination and pointing northward, and the z-axis along the line-of-sight and pointing toward the observer. The plane of the sky is confined to the (x, y) plane, and the galaxy center is located at the position $(x_o,\ y_o)$.

The isophotes of the Sersic models are concentred ellipses centred at (x_o, y_o) with constant position angle PA_b and constant ellipticity $\epsilon_b = 1 - q_b$. Thus, the radius r_b is given by:

$$\begin{aligned} r_b &= [(-(x-x_o)sinPA_b + (y-y_o)cosPA_b)^2 \\ &\quad -((x-x_o)cosPA_b + (y-y_o)sinPA_b)^2/q_b^2]^{1/2} \end{aligned}$$

We have called *bulge* the photometric galaxy component fitted by a Sersic law in those galaxies fitted with two components. Similar to the photometrical component modelled by a Sersic law, we have considered that the disc isophotes are ellipses centered on the galaxy center (x_o, y_o) with constant position angle PA_d and constant ellipticity $\epsilon_d = 1 - q_d$, given by the galaxy inclination $i = arcos(q_d)$. Thus, the radius r_d is given by:

$$\begin{aligned} r_d &= [(-(x-x_o)sinPA_d + (y-y_o)cosPA_d)^2 \\ &\quad -((x-x_o)cosPA_d + (y-y_o)sinPA_d)^2/q_d^2]^{1/2} \end{aligned}$$

During each iteration of the fitted algorithm, the seeing effect has been taken into account by convolving the model image with a circular point spread function (PSF) extracted from the images using the fast Fourier transform (FFT) algorithm (Press et al. (1992)) in the Fourier domain. Many works have widely discussed the seeing effect on the scale parameters of Sersic surface brightness profile, (e.g. Trujillo et al. (2001a,b)).

The routine fits all free parameters iteratively using a non-linear least-squares minimization method. It was based on the robust Levenberg-Marquardt method (Press et al. (1992), a wide explanation can be found in Chapter 7). Also, Poissonian and constant weights can be chosen to performed the calculation of the χ^2 and the options of setting boundary constraints or fixing parameters are available.

One of the most important characteristics of that procedure consist on the adoption of accurate initial trials for the parameters to fit as it ensures the good convergence of the χ^2 distribution.

At first, the photometric package SExtractor (Bertin & Arnouts, 1996), measures positions, magnitudes and ellipticities of the sources in the image and afterwards, the elliptically averaged radial profiles of the surface brightness, ellipticity and position angle of the galaxy is derived with the *IRAF* task *ELLIPSE*. The spurious sources are masked automatically with SExtractor and the surface brightness is fitted with ellipses centered on the position of the galaxy center given by (x_0, y_0) in the two-dimensional fit. Also, the program has option which allows to rotate the image to create the masks. That option is useful for the deblending of galaxies in interaction or very close.

Finally, the trial values are obtained by performing a one dimensional decomposition technique as in Kormendy (1977); Prieto et al. (2001), for example. An exponential law is fitted to the radial surface-brightness profile at large radii, where the light distribution of the galaxy is assumed to be dominated by the disk contribution. Then, the central surface brightness and scale length of the exponential are adopted as initial trials for I_0 and h, respectively. The first estimation of the light distribution of the bulge is given by the residual radial surface-brightness profile, fitted with a Sersic law. Conclusively, the bulge effective radius, effective surface brightness and shape parameter and the disk parameters that provided the best fit are adopted as initial trials for r_e, I_e and n, respectively.

The initial trials for ellipticity and position angles of the disk are found by averaging the values in the outermost portion of the radial profiles of ellipticity and position angle. As for the bulge is concerned, they are estimated by interpolation at r_e the radial profiles of the ellipticity and position angle, respectively.

Once, the trials are obtained, the nonlinear least-squares are initialized with those values, allowing them to vary. A model is considered to be convergent when the χ^2 achieves a minimum and the relative change of the χ^2 between the iterations is less than 10^{-7}. The output of the procedure consist on a model built with the fitted parameters convolved with the adopted circular two

dimensional Gaussian PSF and subtracted from the observed image to obtain a residual image.

Two more iterations are performed to ensure the convergence of the algorithm and the no variation of the parameters with all the pixels and regions of the residual image with values greater or less than a fixed threshold, controlled by the user are rejected and initial trials the values obtained in the previous iteration.

Other packages, such as GALFIT, (Peng, 2002), were used to extract structural components from galaxy images. As GASP-2D, it uses a Levenberg-Marquardt downhill-gradient method to derive the best fit. However, GALFIT did not search for initial trials, so it often converges on fit solutions, that represent a local minimum instead of giving the global minimum.

The surface brightness of the galaxies in our medium redshift NOT clusters were modelled using one or two photometrical components, depending on the morphological type of the galaxy. The surface brightness of those galaxies modelled with only one component was described by a Sersic law (Sersic (1968)) while the surface brightness of those galaxies fitted with two photometrical components were described by a Sersic law plus an exponential one (Freeman (1970)).

5.2.2 Simulations

One of the advantages of the quantitative morphology is that the accuracy of the obtained results can be tested by simulating artificial galaxies similar to the real ones. We have created a large number of artificial galaxies with one and two galactic components described by the mentioned previous equation. These modeled galaxies are similar to the galaxies observed in our medium redshift galaxy clusters.

We generated 5000 images of galaxies with a Sersic component. The total magnitud, effective radius, shape Sersic parameter, and ellipticity of the simulated galaxies were similar to the observed in the real ones. They were asigned randomly to the models, and their values were in the ranges:

$$18 \leq m_r \leq 21;\ 0.5\,kpc \leq r_e \leq 4\,kpc;\ 0.5 \leq n \leq 6;\ 0.7 \leq \epsilon_b \leq 1 \tag{5.4}$$

We have also generated 5000 galaxies with two photometric components: Sersic and exponential. These artificial galaxies have a central photometric *bulge* component, modeled by a Sersic law, and an external *disc* component, modeled by an exponential law. The total magnitud of these galaxies span a range of $18 \leq m_r \leq 21$. The contribution to the total light of the galaxies by the bulge and disc components is given by the bulge-to-total light ratio. This parameter spreads over the range $0 \leq B/T \leq 1$. The bulge parameters of the simulated galaxies were:

$$0.5\,kpc \leq r_e \leq 4\,kpc;\ 0.5 \leq n \leq 6;\ 0.2 \leq \epsilon_b \leq 1 \tag{5.5}$$

And the disc free parameters of the galaxies were distributed in the ranges:

$$1.75\,kpc \leq h \leq 4.7\,kpc;\ 0.2 \leq \epsilon_b \leq 1 \tag{5.6}$$

In order to mimic the same instrumental setup, we added a background level and photon noise to these artificial images similar to the observed images. They were also convolved simulating the seeing that we have in our observations. Finally, these simulated galaxies were fitted in identical conditions as the real ones.

5.2.3 Galaxies with one photometrical component

In the present subsection, the results of the simulations for one Sersic component are examined. In Figure 5.1, we show the relative errors of the free parameters of those simulated galaxies with only one component as a function of their magnitudes. A galaxy is considered to be properly fitted when all free parameters are recovered with relative errors less than 20%.

We have previously explored the minimum conditions for the fits to extract reliable results, without depending on the image condition. The conclusion is that the goodness of the fits depends on the number of pixels (area) used by the fitting routine as the recovered fitted parameters have very large errors for areas below a minimum one. This area depends on the number of free parameters used in the fits, the seeing of the images and the S/N of the fitted galaxies.

In Figure 5.2, the fraction of simulated galaxies with one Sersic component for which their parameters were recovered with relative errors smaller than 20% is shown. We have defined the minimum area of the galaxies for which the image conditions were not affecting the goodness of the fit as the value where all the fits which the recovery of all the parameters are below 20% of error, achieves the 50 % of the cumulative distribution. Below this limit, more than 50% of the Sersic profile galaxies is retrieved with an error of more than 20 %. This correspond to 550 pixels for the galaxies modeled with only one Sersic component.

The Area of a galaxy is also broadly correlated with its total magnitude which means that imposing a minimum area in our fits is similar to imposing a limiting magnitude. In Figure 5.3, we have plotted the correlation between absolute magnitude and area of the galaxies. We obtain that the mean value of 550 pixels, correspond to $M_r \approx -19.5$.

5.2.4 Galaxies with two photometrical components

That subsection is devoted to the analysis of the results of the simulations for two photometrical components. Regarding to the minimum area for the fit to be reliable in two components, we have adopted the same procedure that for one photometrical component with the difference that in this case, the area at

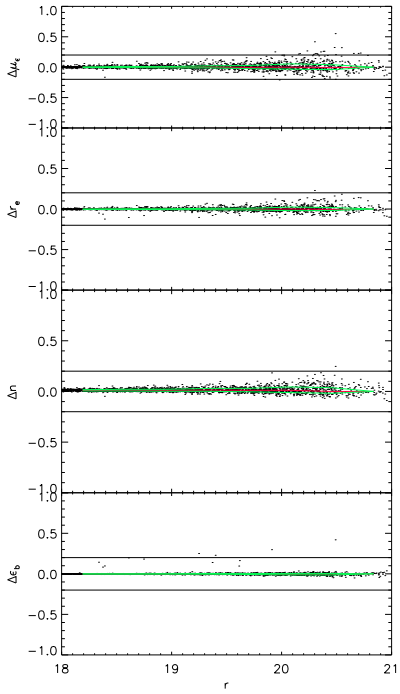

Figure 5.1: Plots of the magnitudes versus parameters of the Sersic profile. The horizontal lines are the 20% of the error. The green and red lines are the quartile and percentile of the error respectively in bins

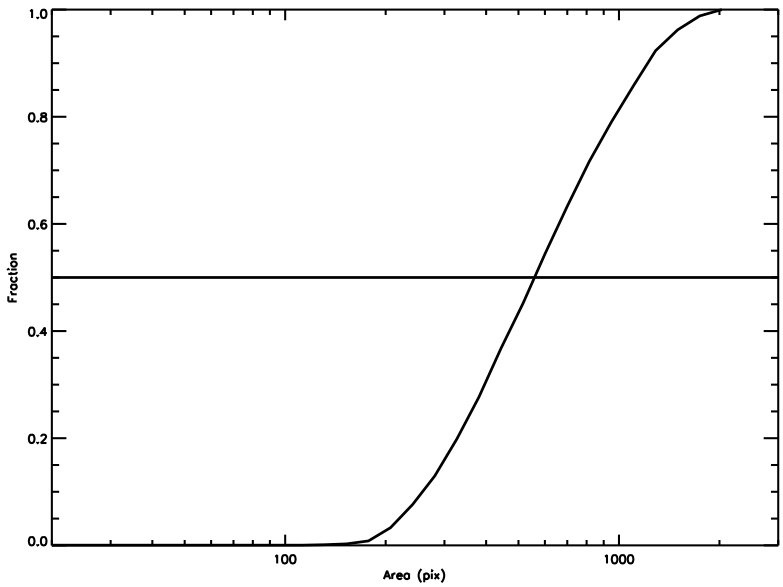

Figure 5.2: Cumulative distribution of the simulations with error within 20 % error versus area for the Sersic Profile. The horizontal line shows the 50 % of the distribution.

which 50% of the population is well fitted depends on their B/T values. Figure 5.4 shows the fraction of simulated galaxies which their free parameters are recovered within relative errors of 20% separated in three ranges of B/T 's. To be rigorous, we have adopted as the minimum area needed for a two-component fit, the maximum of the minimum areas for each B/T range. In our case, the minimum area adopted is then 800 pixels.

For all the artificial galaxies with larger areas than 800 pixels, we have plotted in Figure 5.5, the relative errors of the fitted free parameters of the simulated galaxies with bulge and disc components.

Notice that in general the disc parameters are better fitted than the bulge ones. It is also clear that those galaxies with large B/T show larger errors in the disc parameters than in the bulge ones. In contrast, galaxies with smaller B/T show larger errors in the bulge than in the disc. Let's note that the bulge and disc surface brightness are not well fitted for galaxies fainter than magnitude $m_r >$ 20 and with bulge surface brightness $\mu_{0,B} > 25.3$ and disc surface brightness $\mu_{O,D} > 25.3$.

We have set those restrictions in our parameters space, as it is shown in Figure 5.6. We do note that bulge parameters are the ones with the largest error. Consequently, we have selected those simulations with B/T ≤ 0.7 from the previous restricted sample as in Figure 5.7. We can conclude that the errors are

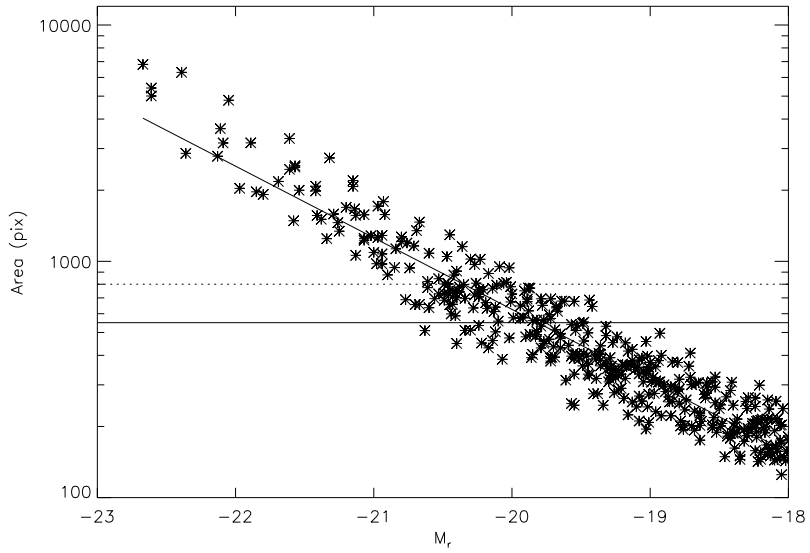

Figure 5.3: Absolute Gunn-r magnitude Versus Area for the galaxy population in NOT sample. The solid and dotted horizontal line show the limit of 550 and 800 pixels, respectively. A fit to the correlation is overplotted.

now within 20%.

5.2.5 Number of components

All the galaxies down to $M_r = -19.5$, corresponding to the 550 pixels limit, were fitted with one and two components. In order to decide the best fitted photometrical model, we have adopted a similar approach as in Allen et al. (2006) for the Millenium Galaxy Catalogue (MGC). This strategy is based on the radial analysis of the surface brightness profiles of the fitted models. Our aim is that those galaxies finally fitted with two components should be *classical* bulge and disc system, in other words, their central regions should be dominated by the bulge components, while the disc dominates at large radial distances from the galaxy center. Galaxies with different light distribution were fitted with only one component.

We have implemented a decision tree algorithm in order to obtain the number of fitted galactic components. The algorithm starts by comparing the magnitude of the galaxy obtained from the two component fit and the magnitude measure directly in the image using SExtractor. If this difference is larger than 0.5 mag then the galaxy is fitted with only one component as it will not be a good fit. In the second step of the algorithm , we have analyzed the bulge-to-total (B/T)

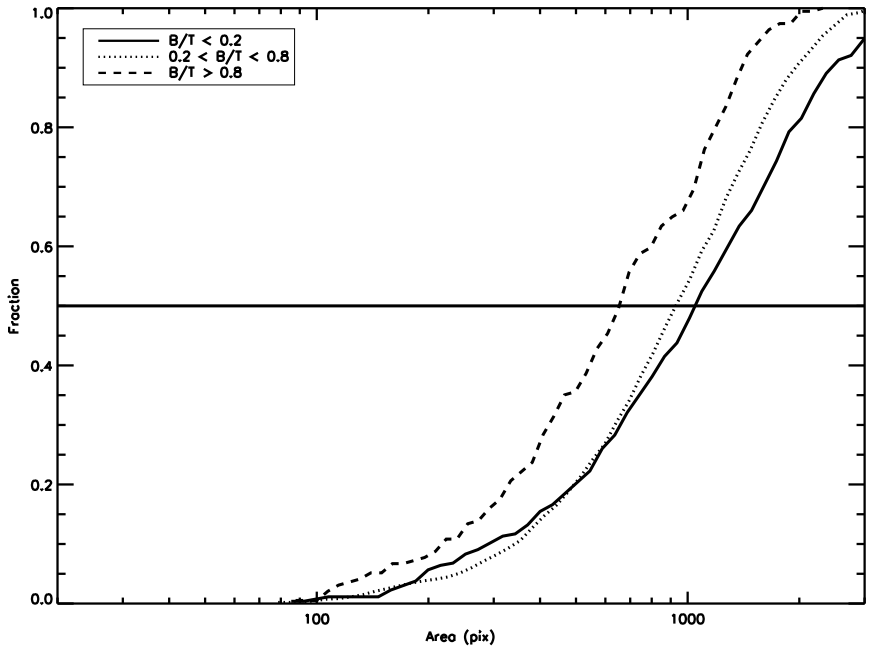

Figure 5.4: Cumulative distribution of the simulations with error within 20 % error versus area for the Sersic + Disc Profile. The horizontal line shows the 50 % of the distribution.

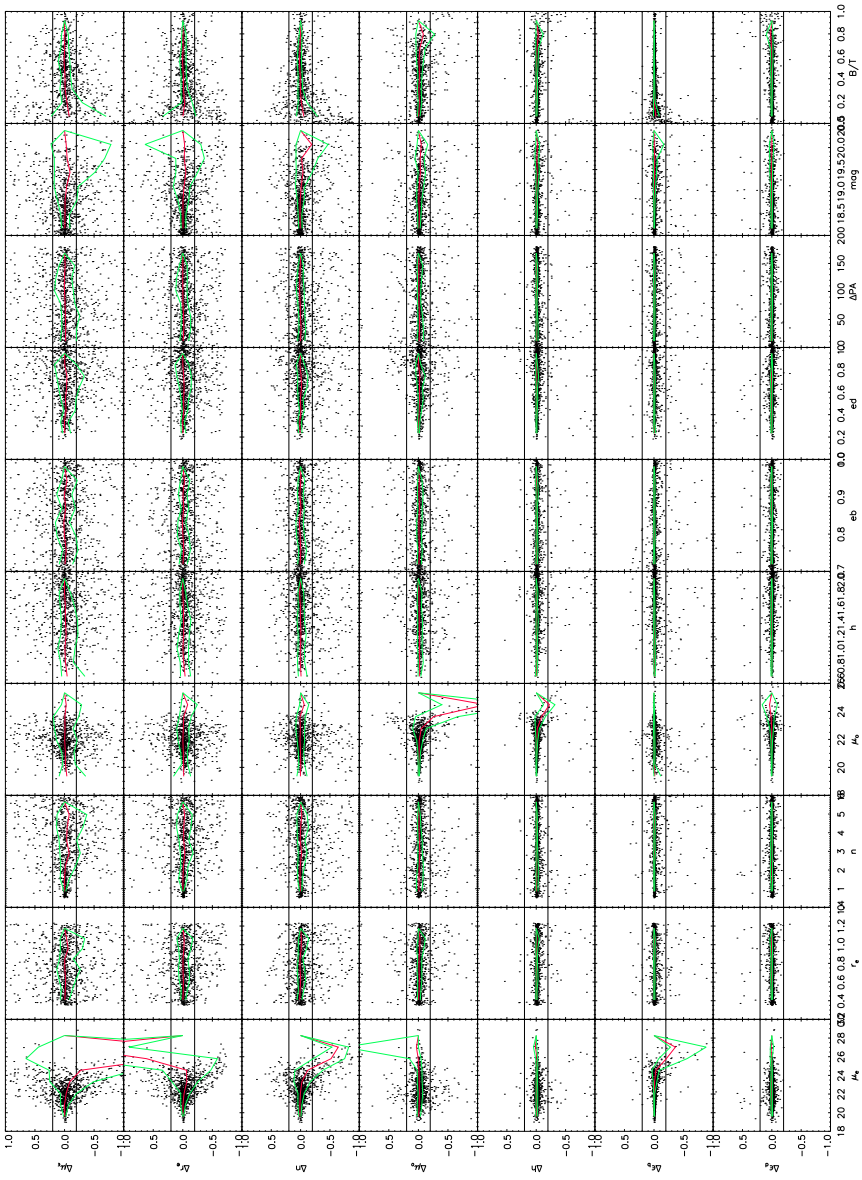

Figure 5.5: Plots of the Sersic+ Disc profile parameters versus its error for those galaxies with Areas larger than 800 pixels. The horizontal lines are the 20% of the error. The green and red lines are the quartile and percentile of the error respectively in bins. (Landscape)

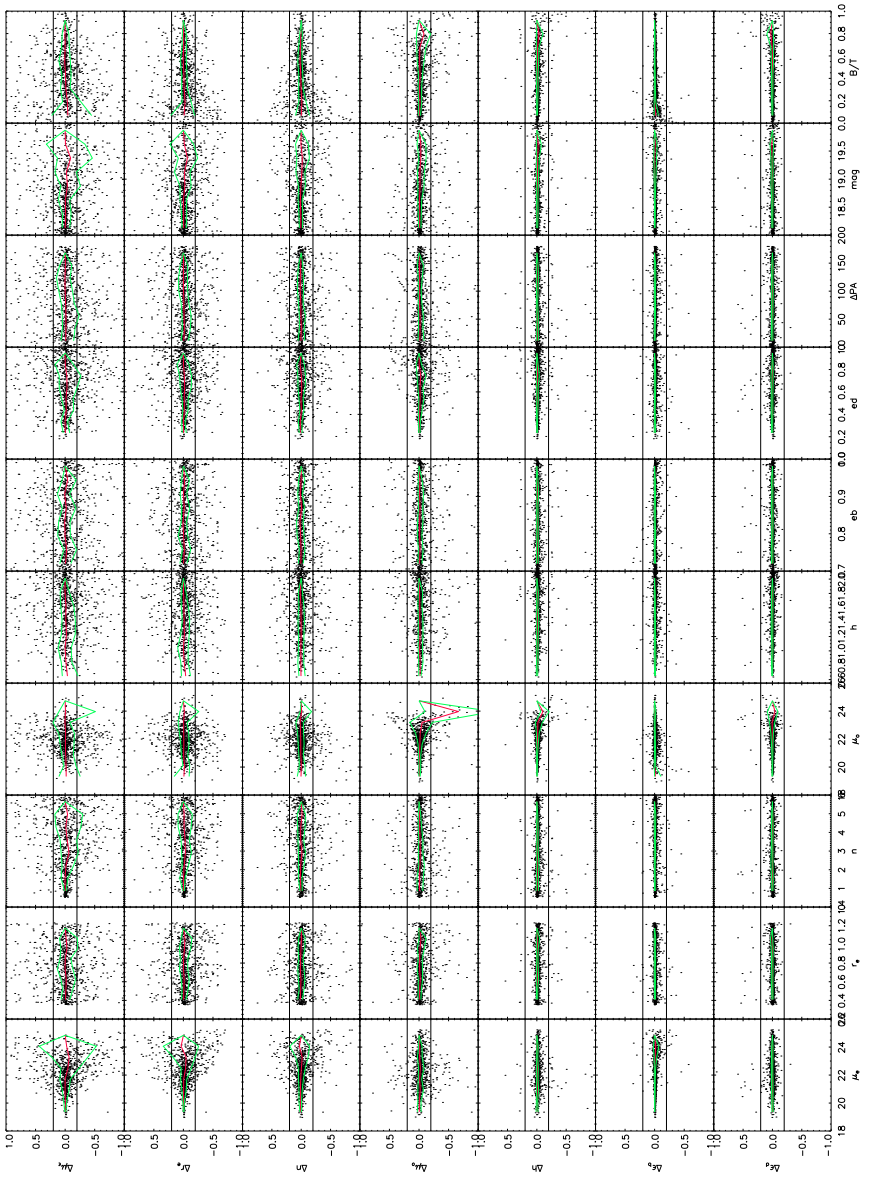

Figure 5.6: Plots of the Sersic+ Disc profile parameters versus its error for $m_r \leq 20$, $\mu_{0,B} \leq 25.3$ and $\mu_{O,D} \leq 25.3$. The green and red lines are the quartile and percentile of the error respectively in bins. (Landscape)

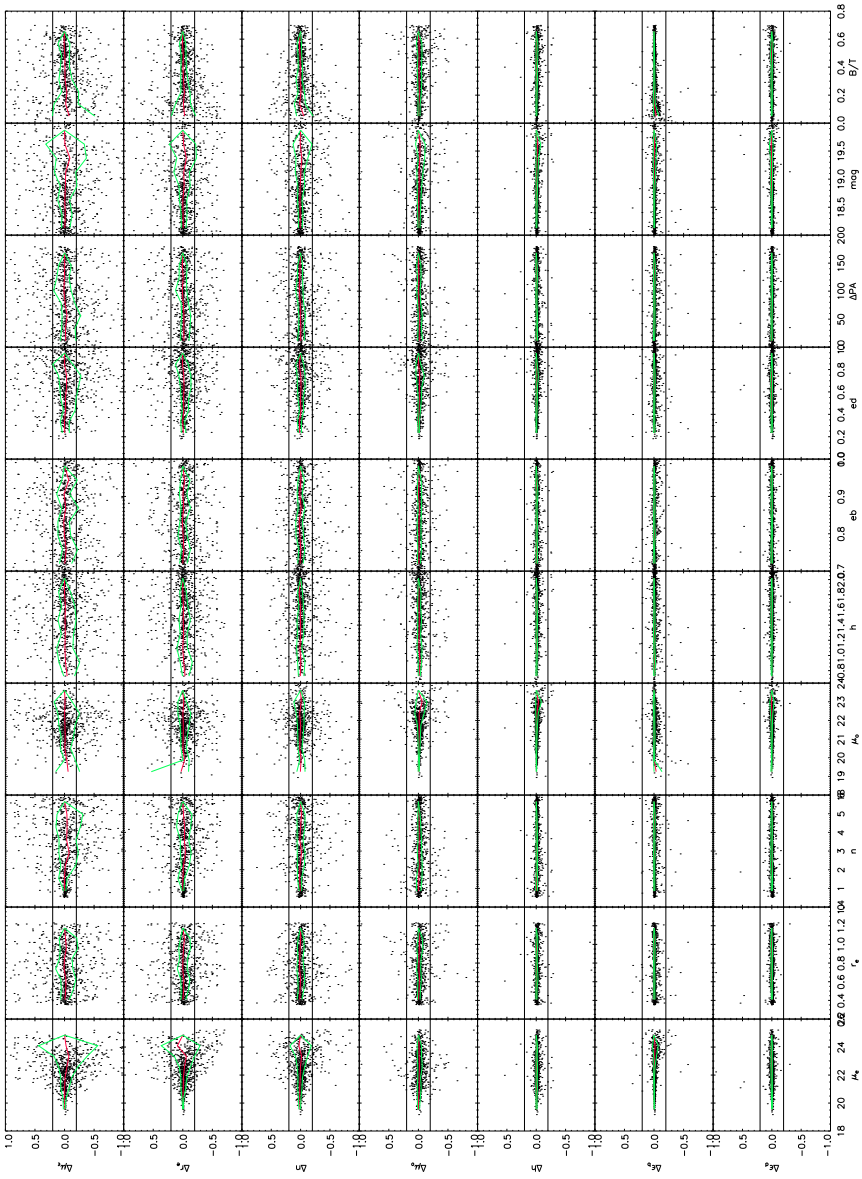

Figure 5.7: Plots of the Sersic+ Disc profile parameters versus its error for $m_r \leq 20$, $\mu_{0,B} \leq 25.3$ and $\mu_{O,D} \leq 25.3$ and B/T ≤ 0.7. The green and red lines are the quartile and percentile of the error respectively in bins. (Landscape)

ratio given by the two component fit. Those galaxies, clearly dominated by the Sersic components (B/T >0.7), were fitted with only one component.

The remaining galaxies were analyzed following a similar procedure as in Allen et al. (2006). We have identify five different types of fitted surface brightness profiles according with the number of intersection between the Sersic and the exponential fitted radial profiles. In Fig 5.8, we have plotted an example of each of those five types. We can identify those with one (Type 1, Type 2 and Type 4), two (Type 3) and zero (Type 5) intersections. Type 1 profiles were considered as *classical* bulge and disc galaxies. The remaining have bulges dominating in the whole galaxy (Type 5), or the disc dominates in the inner regions of the profile (Type 4), or the effective radius of the bulge is larger than the effective radius of the disc (Type 3), or the n Sersic parameter of the bulge have reached the maximum value allowed in the fit (Type 2). Finally, only the Type 1 profiles were considered two component fits. The remaining were fitted with only one component.

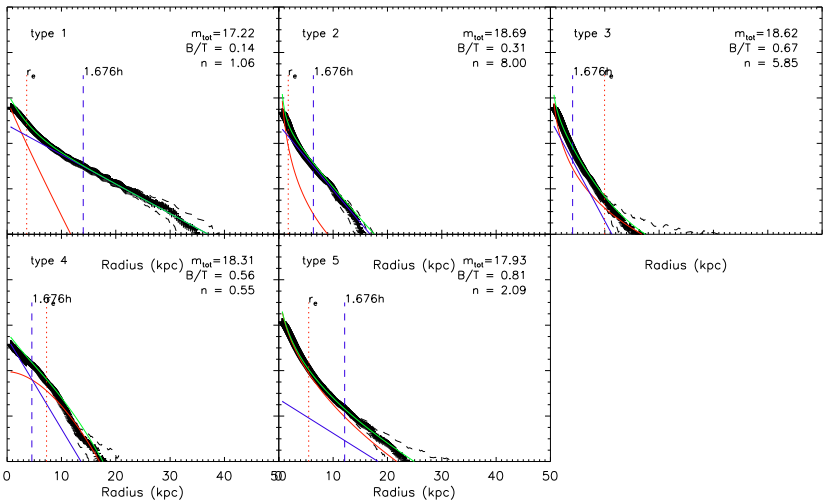

Figure 5.8: Examples of profiles 1 to 5 following the notation of Allen et al. (2006) for the MGC. The black line represents the profile of the galaxy, the red line corresponds to the Sersic profile, the blue line shows the disc profile and the green line designates the sum of both components profile.

By using this algorithm, we can ensure that galaxies which have been made a two component decomposition are real bulge plus disc galaxies, that is spirals or lenticular galaxies. For the rest, we can not confirm which type the one component galaxies are. In the next section, we will discuss the color information as a complement for determining the morphology quantitatively. The final results is that 47 % of the galaxies with larger areas than 800 pixels are better fitted by a Sersic-one component profile, while for the other 52 %, two components are

preferable.

In the Figures B.1 in the Annex, we have plotted the two dimensional images of the galaxies with $M_r \leq -19.5$ including the original galaxy, the model into one and two components and its corresponding residual image. The last column shows also the surface brightness profiles with the one and two component fit decomposition profiles and its parameters.

5.3 Quantitative Morphology

We have classified the galaxies in NOT sample, taking into account the number of fitted photometrical components and their B-r colors. Three diferent galaxy types has been considered as we are interested in study their structural components: Early-types (E/S0), Early-spirals (Spe) and Late-spirals (Spl).

The early-type galaxies were those fitted with one Sersic component and located in the red secuence of the color-magnitud diagrams (CMD) of the clusters. Early-type spirals were those fitted with two structural components and also located in the red secuence of the CMD. Finally, late-type spirals were those objects fitted with two components and have at least 0.2 bluer B-R color than the red secuence of the cluster.

For the NOT sample, this classification results that 36.20%, 29.31%, and 15.51% of the galaxies were early-type, early-spirals and late-spirals, respectively. The remaining 18.96% of the objects correspond to blue galaxies fitted with only one component. These objects could be a mix of different kind of objects (galaxies with more than two galactic components, blue spirals not well fitted with two components, irregular galaxies,...).

5.3.1 Qualitative versus Quantitative Classification

We have performed a comparison with the visual morphology. However, our visual classification is based on the visual characteristic shapes that the eye can distinguish. On the contrary, the quantitative classification tries to derive the morphological types from its color and structural components and this classification is not univocal.

We have checked the percentages of the morphological types that correspond with that quantitative classification. The results are collected in Table 5.1. We see that galaxies in one component are clearly identified. We find a 85.7 % of the galaxies classified as early-type are red and have one component. Also, we find that nearly 90% of the galaxies in one component are classified as Late Type galaxies.

The distinction for the galaxies classified in two components is somewhat more confusing. We obtain that a 41.16% of the galaxies classified as early spirals are lenticular or spiral, while a 22 % of the galaxies with blue colors and two

Table 5.1: Visual Morphological Types versus Quantitative Morphological Types for the NOT sample

	E	S0	S	I
E/S0	57.14	28.57	14.28	0.00
EarlySp	52.94	17.64	23.52	0.05
LateSp	0.11	0.66	0.22	0.00
Irr	0.10	0.00	0.70	0.20

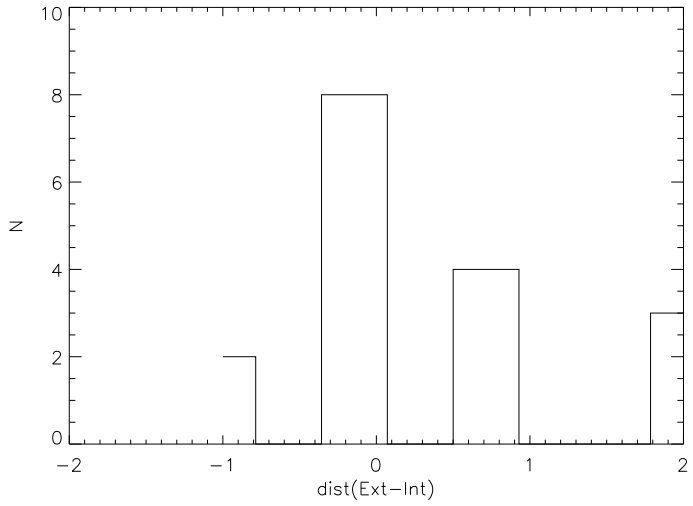

Figure 5.9: The visual classification differences between Sánchez et al. (2007) and this work for A2218.

components are classified as spirals. That differences come due to the difficulty of classifying visually.

In fact, A2218 has been also morphologically classified by Sánchez et al. (2007) in a small area of 200 kpc. They use a quantitatively classification method based on the values of the Sersic parameter. By comparing this classification, we find that a 47.05% of the galaxies have the same morphological type. The results are shown in Figure 5.9. Those results indicate that despite the numerous efforts that have been performed to achieve a quantitative description of galaxies, they have not succeed in assign the right morphologies.

5.4 Structural parameters

Numerous studies talk about the evidence of larger discs in field or isolated galaxies than in clusters (De Jong, 1996b; Graham, 2001; Graham , 2003). Also, the data at high redshift from HST seems to indicate that early-type galaxies have little evolved while late-type ones seem to change quickly. We want to quantify that evidences in our clusters.

5.4.1 Sersic Parameters

One of the most interesting relations for elliptical galaxies was introduced by Djorgovski & Davis (1987); Dressler et al. (1987). They established that the effective radius, the central velocity dispersion and the mean surface brightness are related for early type galaxies in the logarithmic space with a very low scatter. This relation is commonly known as the **Fundamental Plane (FP)**:

$$\log r_e = \alpha \log \sigma + \beta \log < I >_e + \gamma$$

The implications of the existence of the FP are directly related to the formation and evolution process of the galaxies. By assuming a constant M/L ratio and that galaxies are in virial equilibrium. The relation introduced by Dressler et al. (1987) is directly related to the FP, the $D_n - \sigma$ relation.

Those relations provide information on the properties of the galaxies as a class, and the relations may be used for distance determination, assuming that the relation is universally valid. That matter is still on debate, in relation with the uncertainty derived from the mislead of classify morphologically galaxies and also with the assumption that the E and S0 galaxies are derived from the same probability function, Jørgensen, Franx & Kjaergaard (1996). Several cosmological tests, as the Tolman test has been performed by using the FP, (Moles et al., 1998).

One of the projections of the Fundamental Plane, (σ=constant), is the so called **Kormendy Relation**, Kormendy (1977). He discovered a correlation between the size and the surface brightness of elliptical galaxies. Later on, Binggeli, Sandage & Tarenghi (1984) found that this relationship was only given in elliptical galaxies brighter than $M_B \geq -20$. For fainter galaxies, the tendency reverses.

In Figure 5.10, we have plotted the **Kormendy relation** $< \mu_e > -r_e$ for red E/S0 (red points), Early Spirals (green triangles) and Late -Spirals (Blue triangles). For the red-galaxies, the fit is the following

$$< \mu_e >= 20.32 \pm 0.15 + (2.18 \pm 0.23) \log(r_e) \tag{5.7}$$

while the fit for the whole set of galaxies is

$$< \mu_e >= 20.07 \pm 0.14 + (3.22 \pm 0.21) \log(r_e) \tag{5.8}$$

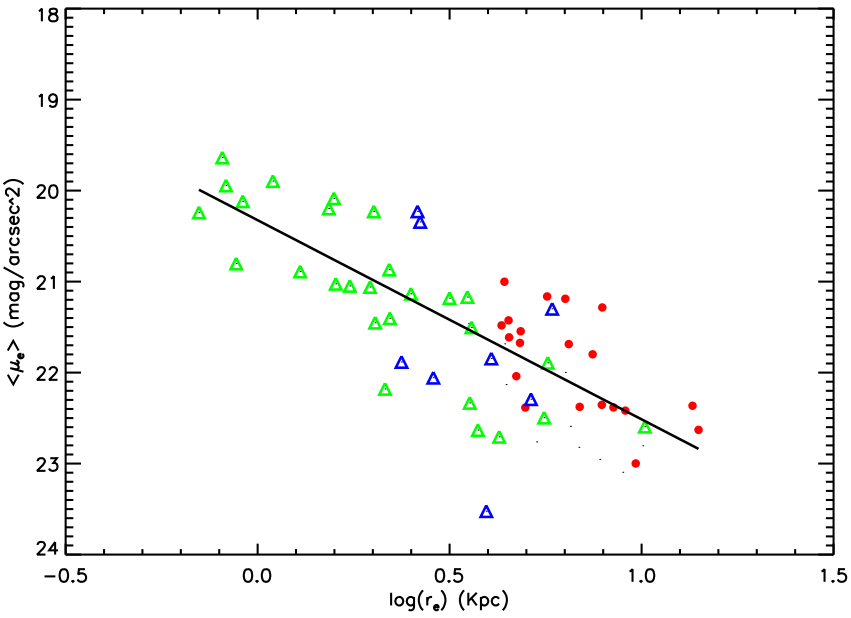

Figure 5.10: Kormendy relation between effective radius and mean surface brightness for all the sample of galaxies. Red points are the E/S0 galaxies, green triangles refer to early-Spirals and Blue triangles account for late-spiral galaxies. The solid line is the fit for the red galaxies.

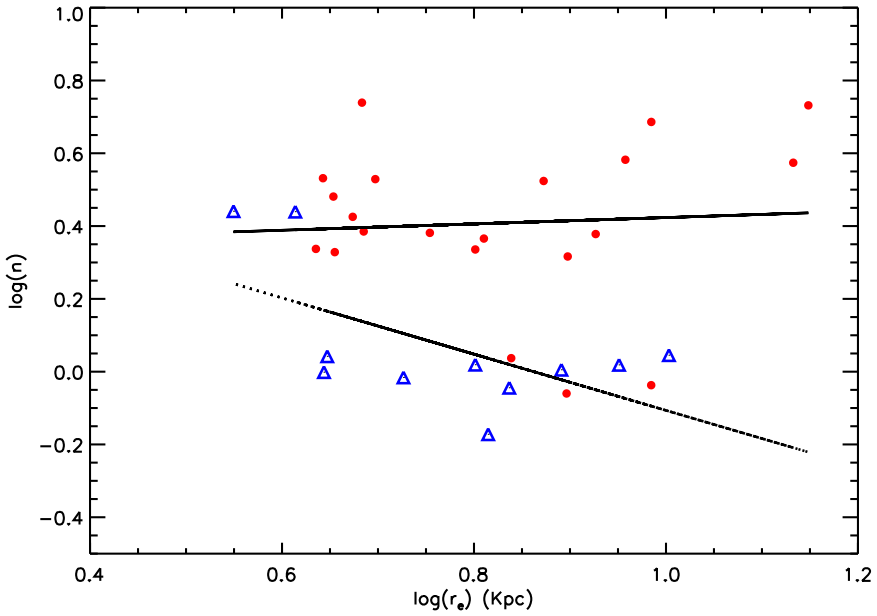

Figure 5.11: Relation between effective ratius and shape parameter for one component galaxies. Red points refer to red-one-component galaxies and blue triangles represent blue-one-component galaxies. Solid and dotted lines are the respective fits

We have also plotted in Figure 5.11 the relation between effective-radius and shape parameters for red galaxies fitted in one component (red points) and blue galaxies fitted in one component (blue triangles). Clearly, a dichotomy exists. We have fitted the tendency an we have found an opposite growing tendency between both types as we show in the following equations. That fact gives us information about which galaxies fitted by a one component model are a late-type galaxy.

$$\log n = 0.33 \pm 0.26 + (0.087 \pm 0.31) \log(r_e)$$

and for the blue ones

$$\log n = 0.66 \pm 0.27 - 0.77 \pm 0.35 \log(r_e)$$

Furthermore, in the Figure 5.12, it is shown the central surface brightness, the shape parameter and effective radius versus the absolute magnitude for the E/S0 (red points), Early Spirals (green triangles) and Late Spirals (blue Triangles). We see that at fainter magnitudes we determine fainter surface brightness. We can distinguish also as the early type galaxies have larger effective radius, while

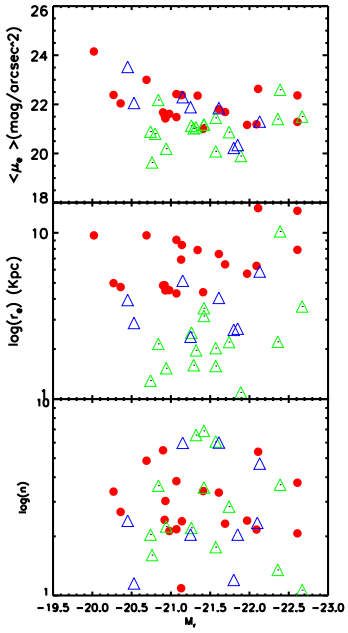

Figure 5.12: Absolute Gunn-r Magnitude versus μ_o, n and B/T for E/S0 (Red points), Early Spirals Bulges (Green Triangles) and Late Spirals Bulges (Blue Triangles).

the early and late type galaxies have smaller radius. We are not able to distinguish any trends of magnitude with shape parameters, as has been found in some works.

We have also plotted In Figure 5.13, the mean surface brightness, the effective radius and the shape parameter versus color. The symbols are the same as in the previous plot. By definition, we can distinguish a clear dichotomy between early and late galaxies. However, the effective radius also allow us to distinguish the two populations quite clearly.

Finally, we have compared our bulge scales with the bulge scales of the early type galaxies in the sample of Aguerri et al. (2004). Those galaxies have been selected in the same way as us. The results are plotted in Figures 5.14 and 5.15, the red points indicate the E/S0 galaxies while the blue triangles are the blue galaxies in one component . We see that our sizes are very similar to Coma. We do not find any galaxies in our sample below $\approx$ 2.2 kpc, as that is our seeing limitation to our sample at this distance. It's noticeable that our r_e values are in the same range as those in Coma, as it is shown in Table 5.2. The values for Coma have been computed for those galaxies in the central 735 kpc and effective radius larger than 2.2 kpc.

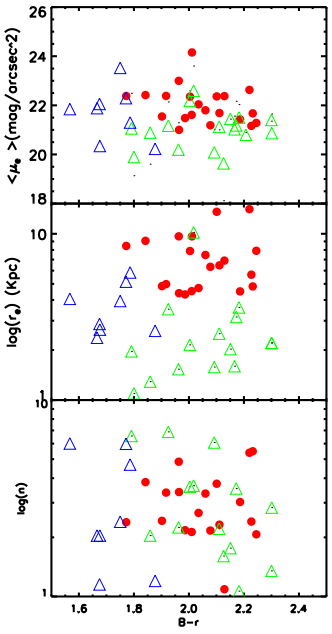

Figure 5.13: B-r color versus μ_o, n and B/T. for E/S0 (Red points), Early Spirals Bulges (Green Triangles) and Late Spirals Bulges (Blue Triangles).

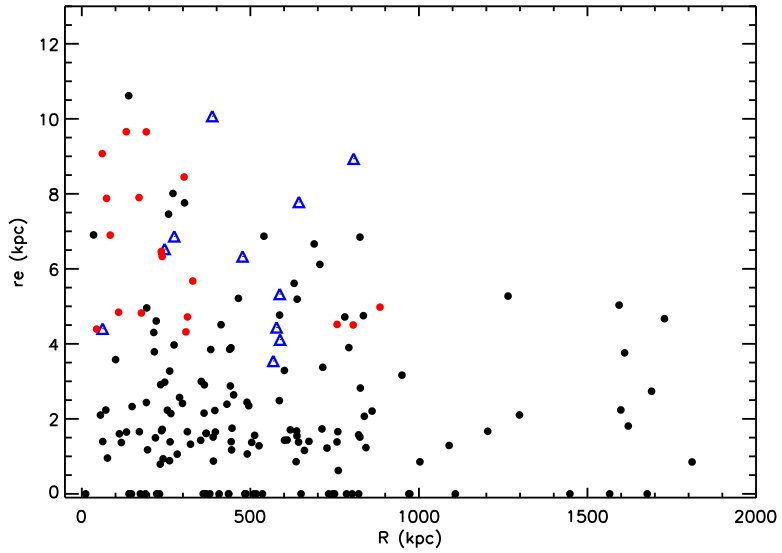

Figure 5.14: Radius versus Bulge Scales for Coma Sample, (Aguerri et al. (2004), black points) and NOT sample. The red points refers to red galaxies in one component while blue triangles represent blue galaxies in one component.

Table 5.2: Bulge parameters for Coma and NOT sample

Name	$< r_e >$	$\sigma(r_e)$	$< n >$	$\sigma(n)$	$<$ Dist(Kpc) $>$	σ(Dist(Kpc))
NOT	6.58	2.38	2.24	1.35	349.72	257.053
Coma	8.73	17.58	3.58	1.54	339.376	180.90

As far as the shape parameter is concerned, we also see as the range of values expand the range of values of Coma. However, we find a mean value somewhat smaller for NOT sample than for Coma but the values agree within the errors. Therefore, it seems that the bulge sizes are in the same range of magnitude as in Coma Cluster.

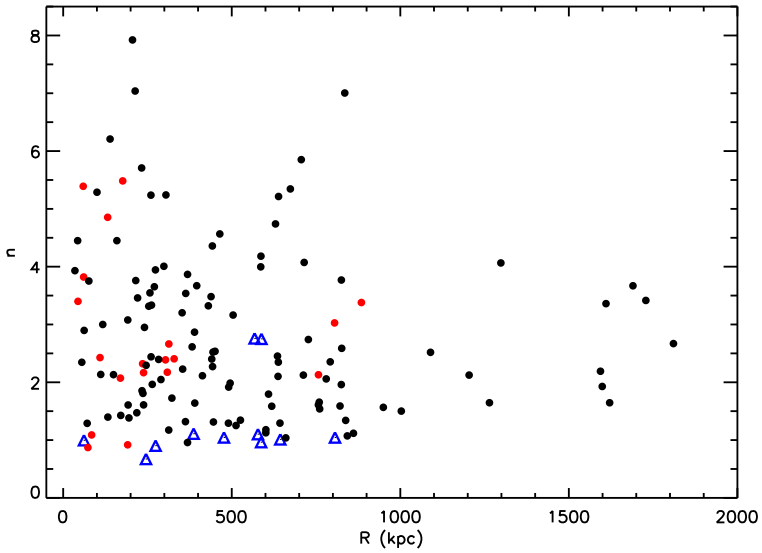

Figure 5.15: Radius versus Shape parameters for Coma Sample, (Aguerri et al. (2004), black points) and NOT sample. The red points refers to red galaxies in one component while blue triangles represent blue galaxies in one component.

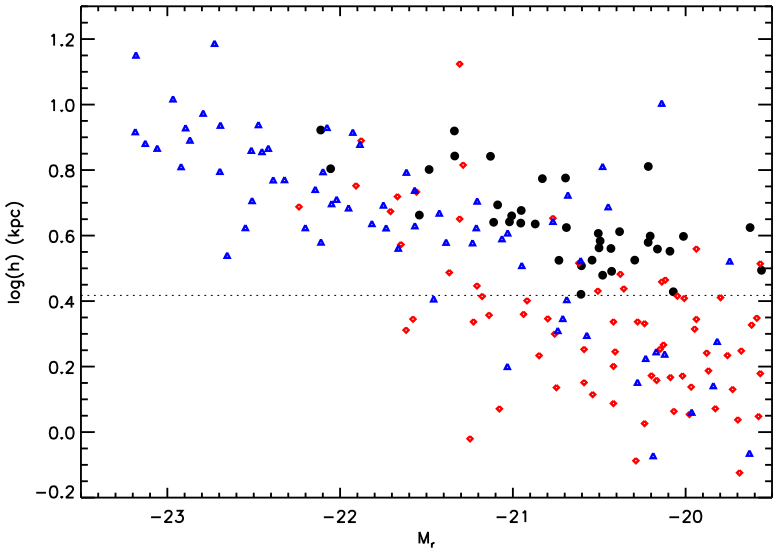

Figure 5.16: Absolute Gunn-r Magnitude versus disc scale. The blue triangles refer to the field galaxies by Graham (2001), red diamonds are the disks scales for the Coma sample by Aguerri et al. (2004) and black points represent the disc scales in NOT sample. The horizontal line shows the minimum disc scale we can resolve the disc due to the distance of the clusters

5.4.2 Disc Parameters

There are many works that have found that early-type galaxies in clusters remain invariant from redshift at least 1, as a result of the formation of the cluster (Simard et al., 1999; Trujillo & Aguerri, 2004). Thus, any variance in that range in redshift must be in the disk galaxy parameters.

In Figure 5.16, we have plotted the absolute magnitudes of the disks versus their scale parameters. The black points concerns to our NOT galaxy sample. The blue triangles refer to the field galaxies by Graham (2001) and the red diamonds are the disks in the Coma sample by Aguerri et al. (2004). The horizontal line shows the minimum disc scale we can resolve the disc due to the distance of the clusters.

It is quite interesting that our disc scales are as large as those of field galaxies, while those discs in Coma represent a minimum percentage. The fit for the Freeman law (Freeman (1970)), for our sample is

$$\log h = -2.52 \pm 0.57 - 0.152 \pm 0.027 M_r$$

Regarding to a quantitative description of the scales of the discs we have plotted in Figure 5.17, the discs scales in function to the distance to the center of

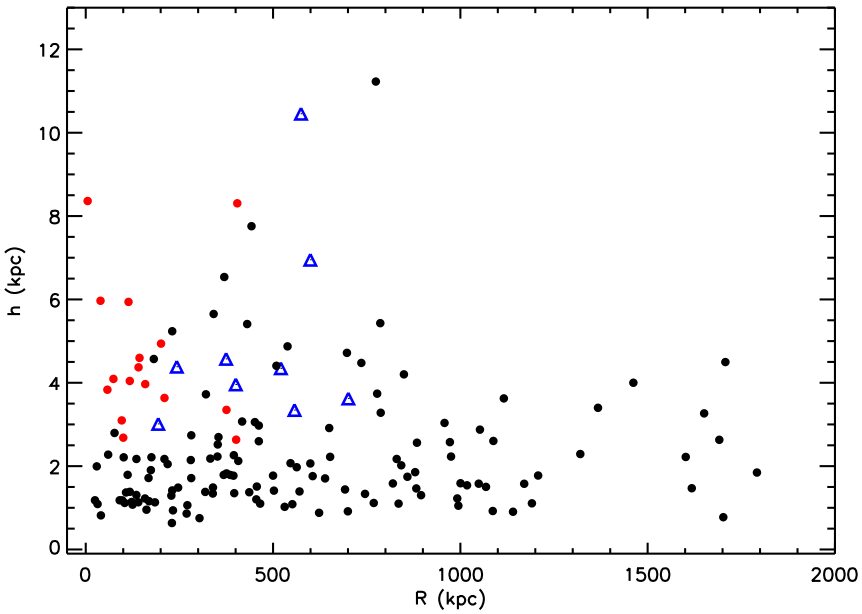

Figure 5.17: Radius versus Disc Scales for Coma Sample, (Aguerri et al. (2004), black points) and NOT sample. The red points are red galaxies in two components and the blue triangles are blue galaxies in two components

the cluster for NOT sample and Coma sample by Aguerri et al. (2004). The red points are early spiral galaxies while the blue triangles refer to late spiral galaxies. We find larger discs (a factor of two) in our sample than in Coma as collected in Table 5.3. Those results agree with a evolution hypothesis from lower redshift clusters to this redshift in the disc scales of the late type galaxy population in clusters.

We have then computed the probability that the distribution function of the discs scales of all clusters and different samples are significantly differents. With that purpose, we have applied again a Kolmogorov-Smirnov test between the cumulative function of the discs of all the clusters of our sample, and Coma

Table 5.3: Disc parameters for Coma and NOT sample

Name	$< h >$	σ(h)	$<$ Dist(Kpc) $>$	σ(Dist(Kpc))
NOT	4.738	1.941	272.16	202.10
Coma	2.47	21.48	524.383	359.080

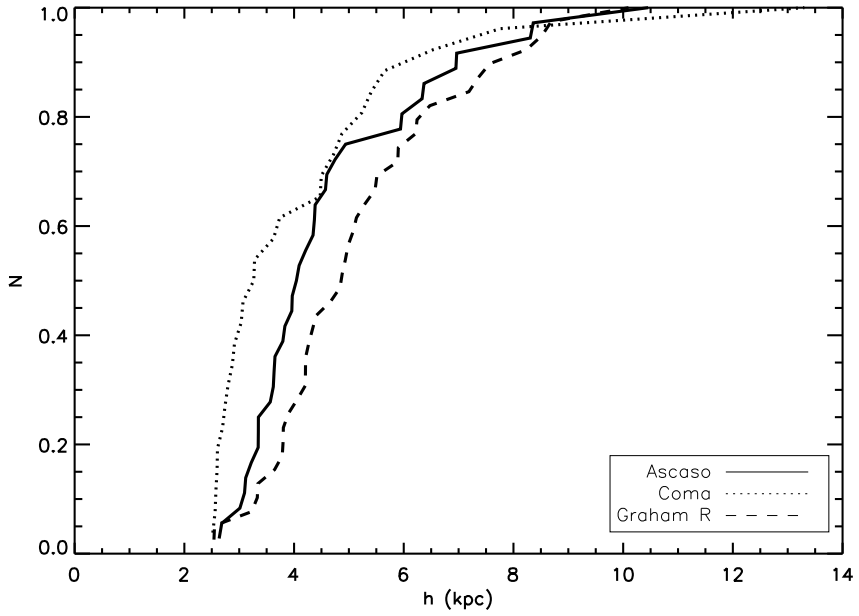

Figure 5.18: Cumulative function of disc scales for the NOT sample (solid line), Aguerri et al. (2004) Coma Cluster (dotted line) and Graham (2001) isolated sample (dashed line)

sample and also between a sample of isolated galaxies from Graham (2001) as it is set in Figure 5.18.

The results of the test give that for both tests the significance is that Coma is significantly different from our sample and the Graham (2001), as their probability is less than 0.05. However, the isolated sample from Graham (2001) and our sample has a probability superior than 0.05.

We can conclude that the accumulated function of our disc scales in our clusters are similar to the local field galaxies and different from Coma. Therefore, we have discs as large as those from field galaxies, which is quantitatively different from Coma.

5.4.3 Bulge and disc parameters

In Figure 5.19, we have plotted the ratio r_e/h versus shape parameter and bulge-to-total ratio for the two-component galaxies. We find a clear correlation between B/T and r_e/h for the early-spiral galaxies, as exists for local field galaxies (Andredakis et al., 1995; Graham & de Blok, 2001) and a much wider dispersion fror the late-spiral galaxies. We also find a relationship between n

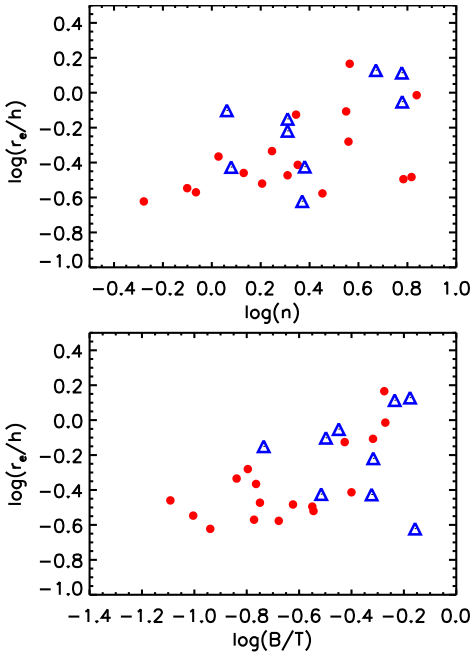

Figure 5.19: Adimensional parameters. n versus r_e/h and B/T versus r_e/h. Red points refer to the red two-component galaxies and blue triangles to the blue two-component galaxies

and r_e/h for the early spiral and again the late spiral shows a larger dispersion.

We show in Figure 5.20 the scale of discs versus the effective radius for the two component galaxies obtaining a growing tendency for the red population as it is shown in the following fit

$$\log r_e = -0.39 + 1.02 \log(h)$$

However, the the blue galaxies have larger effective radius than the red ones and the tendency is much flatter than the red population.

$$\log r_e = 0.06 + 0.61 \log(h)$$

Therefore, we obtain that larger discs are found in galaxies with larger bulge effective radius. Thus, more massive galaxies. That tendency was also noticed by MacArthur, Courteau & Holtzmann (2003). For the blue galaxies, the tendency grows slower.

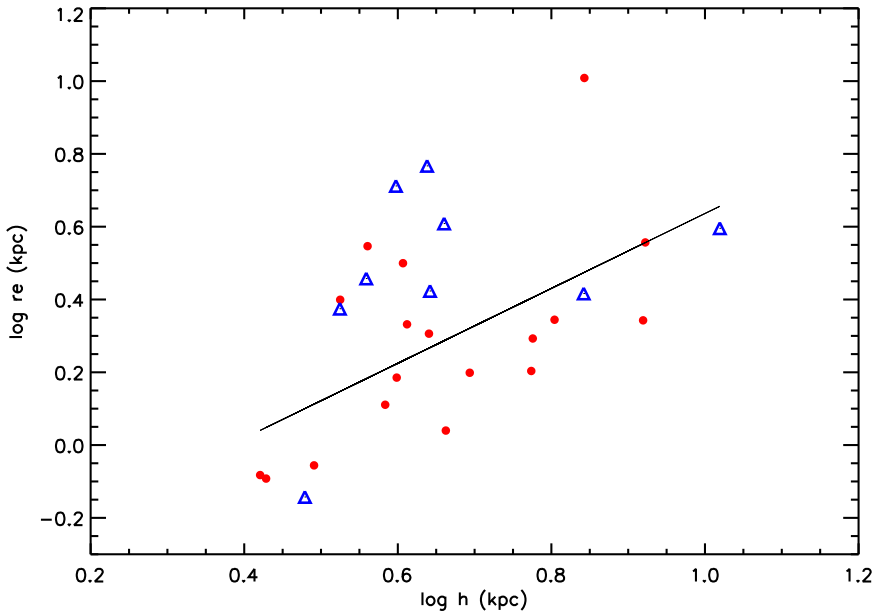

Figure 5.20: Relation between effective ratius and disc scales. Red points refer to the red two-component galaxies and blue triangles to the blue two-component galaxies. The solid line represents the red component fit.

Chapter 6

Spatial Distribution

Les gens ont des étoiles qui ne sont pas les mêmes.
Pour les uns, qui voyagent, les étoiles sont des guides.
Pour d'autres elles ne sont rien que de petites lumières.
Pour d'autres, qui sont savants, elles sont des problèmes.

Antoine de Saint-Exupéry. "Le petit prince"

The spatial distribution in clusters of galaxies is a favorable piece of the puzzle. By studying the location of the galaxies in the cluster, we are able to know important properties such as the presence of substructures, their dynamical state, etc.

Furthermore, if we have redshift information for a given cluster, we can determine the galaxy population composition by assuming that their redshift difference. However, that situation is not very frequent. Taken out some very well-known studied clusters such as Coma (Struble & Rood, 1991; Jørgensen, Franx & Kjaergaard, 1992; Wegner et al., 1999; Smith et al., 1999; Aguerri et al., 2004), Virgo, (Binggeli, Tammann & Sandage, 1987; Ferrarese et al., 2006)), Hercules (Struble & Rood, 1991; Jarrett et al., 1998; Wegner et al., 1999; Sánchez-Janssen et al., 2004; Smith et al., 1999; Crawford, 2005; Estrada et al., 2007), at low redshift and some more at medium redshift, some in our ACS sample, like A1689 (Teague, Carter & Gray, 1990; Duc et al., 2002; Łokas et al., 2006), A2218, (Kristian, Sandage & Westphal, 1978; Le Borgne, Pelló & Sanahuja, 1992; Sánchez et al., 2007), CL0024, (Czoske et al., 2001; Alexov & Silva, 2003), MS1358, (Fisher et al., 1998; van Dokkum et al., 1998; Yee et al., 1998; Fabricant, Franx & van Dokkum, 2000), we usually know a few redshift in the cluster. Therefore, we have to estimate the rest of the redshift of the galaxy population by different techniques such as the CMR (studied in the Chapter 3, (Yee, Gladders & López-Cruz, 1999; López-Cruz et al., 2004)) or, photometrical redshift (Koo (1985); Lanzetta, Yahil & Fernández-Soto (1996); Wang, Bahcall & Turner (1998); Benítez (2000)), if we have several filters.

The cluster's shape and spatial distribution is considered to be the consequence of the initial conditions of formation and evolution for the galaxies in the clusters, as well as the interaction with the environmental effects. Many numerical simulations based on semi-analytical methods have been performed in order to study the formation of clusters, based on the study of the gas dissipative process or the no-colissioness dark matter process, (White & Frenk, 1991; Lacey & Silk, 1991; Ascasibar et al., 2006).

A cluster is said to contain substructures when its surface density is characterized by multiple, statistically, significant peaks on scales larger than the typical galaxy size, Buote (2002); Ramella et al. (2007). Numerous works have been devoted also to the study of the statistical determination of substructures in clusters of galaxies, providing different tests, Fitchett (1988); Pinkney et al. (1996).

Additionally, a relation based on the spatial distribution of the cluster has been widely explored: **the Morphology-Density relation**. Observational evidence about the presence of more early-type galaxies in denser environments than late-types were originally notice by Curtis (1918); Hubble & Humason (1931); Oemler (1974). Later on, Melnick & Sargent (1977) showed that the fraction of lenticular and spiral galaxies depend on the distance from the cluster centre and Dressler (1980) concluded with the morphology -local density relation. Several authors, (Sanromà & Salvador-Solé, 1990; Whitmore & Gilmore, 1991; Whitmore, Gilmore & Jones, 1993) argued a correlation between morphology and global cluster properties, as for example, the clustercentric distance, instead.

The study of the spatial distribution can also provide us with useful information in two dimensions (studying relation of the different properties to density) and in a radial dimension (studying the relation between ratius and a particular scheme).

6.1 Galaxy Density

Obtaining density maps is a useful tool for studying its dependence with different parameters. However, the galaxies have a discrete nature and limitations in area or depth make difficult the process of determining the density. In our case, as we are studying the central bright galaxy population of the cluster, we have limitations in the field size as well as in the observational depth.

6.1.1 Density Estimation

The estimation of the density can be done by two different methods. The most common is considering different fixed apertures, *ap*, in the cluster and computing the number of galaxies, n_{gal}, that we have on it. We will obtain their **local density** with the following equation

$$\rho_{local}(ap) = \frac{n_{gal}(ap)}{\pi(ap)^2}$$

However, that method has the inconvenient that the density is a discrete variable, as it depends on the aperture we have used. Thus, we have used a different method, which consist on considering a fixed number of galaxies, n_{gal} and computing then the minimum area that contains that number, obtaining the density with the following equation

$$\rho_{local}(n_{gal}) = \frac{n_{gal}}{\pi r(n_{gal})^2}$$

where $r(n_{gal})$ is the minimum radius that contain n_{gal} neighbors. That method has been applied in different works (Dressler, 1980; Trevese et al., 1992; Dressler et al., 1997; Fasano et al., 2000; Varela, 2004). The main advantage of that method is that the radius is a continuous variable, so it allows to obtain continuous values of the density function.

We need to fix then the number of galaxies n_{gal} as a compromise between the possibility of detecting peaks corresponding to substructures in the density diagrams and the limited area of the images. We have decided to take n_{gal}=10, as it is able to provide substructures larger than these number, and therefore, dynamically important and it small enough for the area of the cluster to be contained in the image.

In Figure 6.1 and 6.2, we have plotted the logarithm densities distribution for the NOT and ACS sample, respectively. For the ACS sample, we have previously selected the galaxies brighter than $M_r \leq -19.5$. The corresponding mean values are collected in Tables 6.1 and 6.2. It is noticeable that four clusters in the ACS sample are much more dense that the clusters in NOT sample. That result can be explained in relation with the richness of the cluster. The richness class in NOT sample is ≤ 3, while the richness class for the ACS sample is above 4. Also, all the clusters in NOT sample emit in X-ray, while only one cluster in the NOT sample has X-ray data.

Also, in Figure 6.3 and 6.4, the logarithm densities distribution for each cluster in the NOT and ACS sample are presented respectively and the values are collected in Tables 6.1 and 6.2. The vertical lines show the mean value of the density in each cluster.

Let's note that two out of five clusters in NOT sample, A1878 and A2111 are denser statistically than the whole sample. It's interesting also that A1643, A1952 and A2111 present a second peak of lower density which might be related with the presence of subestructure. As far as the ACS sample is concerned, we see that nearly all the clusters are quite dense but MS1358, which seems to be as dense as the NOT sample. We find some peaks in less dense regions of the clusters in A1703 or A2218. That facts can be due to selection effects of the clusters due to its richness.

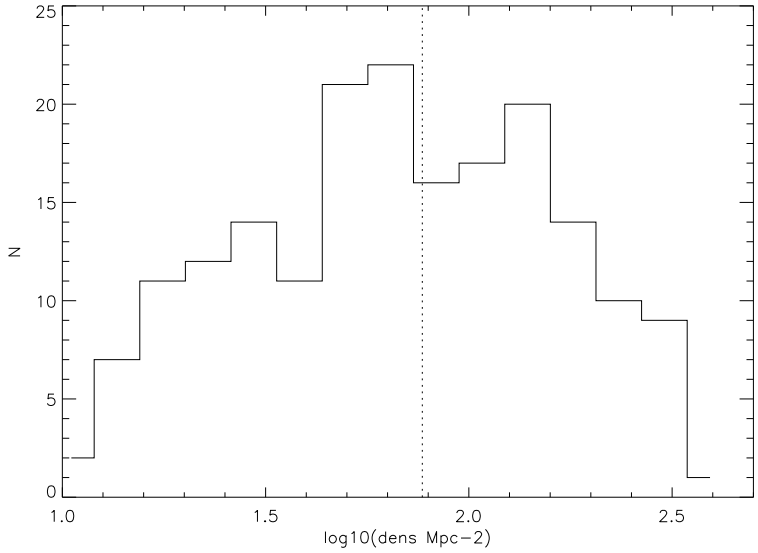

Figure 6.1: Distribution of the local density for the whole NOT sample. The vertical line shows the mean value of the density.

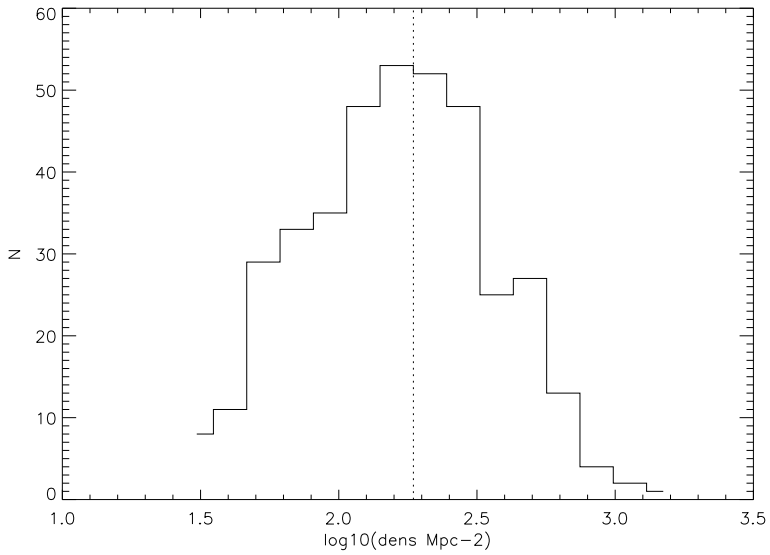

Figure 6.2: Distribution of the local density for the whole ACS sample. The vertical line shows the mean value of the density.

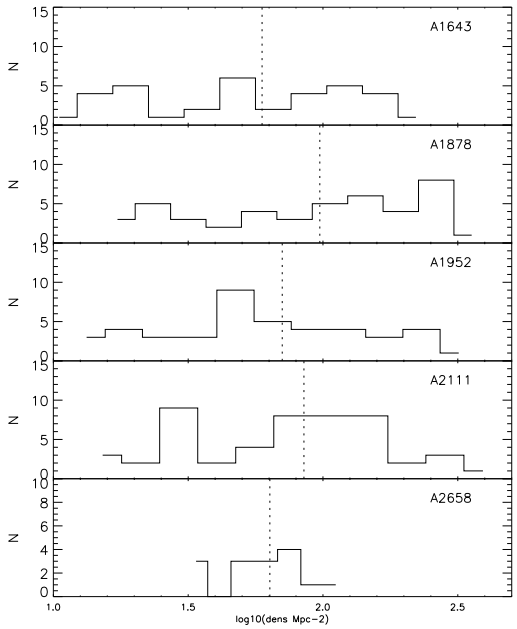

Figure 6.3: Distribution of the local density for each cluster in NOT sample. Vertical lines shows the mean value of the density of each cluster.

Table 6.1: Mean Densities for NOT Clusters

Name	$<\rho>$	$\sigma<\rho>$
A 1643	83.16	62.25
A 1878	140.15	106.30
A 1952	100.29	84.58
A 2111	116.83	94.29
A 2658	67.42	23.13
Sample	108.25	88.58

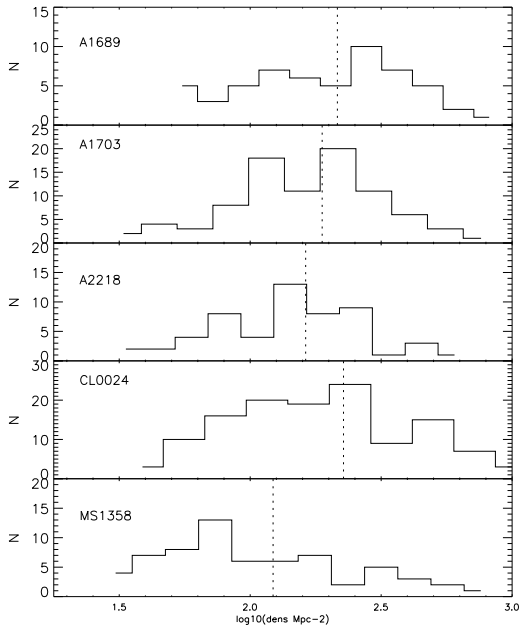

Figure 6.4: Distribution of the local density for each cluster in ACS sample. Vertical lines shows the mean value of the density of each cluster.

Table 6.2: Median Densities for ACS Clusters

Name	$<\rho>$	$\sigma<\rho>$
A 1689	271.37	182.13
A 1703	232.19	155.47
A 2218	200.81	132.11
CL0024	313.32	274.65
MS1358	175.65	168.71
Sample	250.58	210.50

6.1.2 Morphology-Density Relation

The study of the Morphology-Density Relation has been widely explored in numerous studies (Dressler, 1980; Dressler et al., 1997) at low-medium redshift and at higher redshift (z ∼1) with the Advanced Camera for Surveys (ACS), (Postman et al. (2005)). This relation is one of the fundamental in the study of clusters of galaxies. It gives us information about how dense are the different morphological types distributed in the cluster.

In Figures 6.5 and 6.6, we have plotted the logarithm densities distribution for the whole sample splitting them up into three morphological types. The vertical lines shows the mean value for each sample. Interestingly, we see that for the whole sample, the mean value for the ellipticals (E) is higher than the mean value for the lenticulars (S0) and late-type galaxies (S and I), which is very similar in the case of NOT sample. However, we see that the elliptical galaxies are somewhat skewed to higher densities and on the contrary, the late-type galaxies and lenticular are skewed to lower densities. That fact goes in the sense of the work by Dressler (1980), who found an increase of early types in the denser areas of the cluster and a decrease of late type as we approach to denser areas.

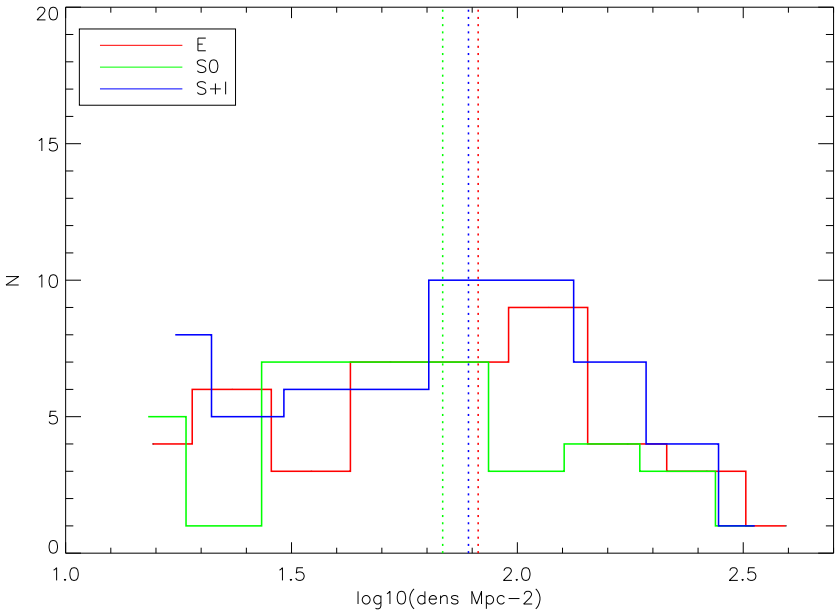

Figure 6.5: Distribution of the local density into three morphological types for the whole NOT sample. Vertical lines shows the mean value of the density of each cluster.

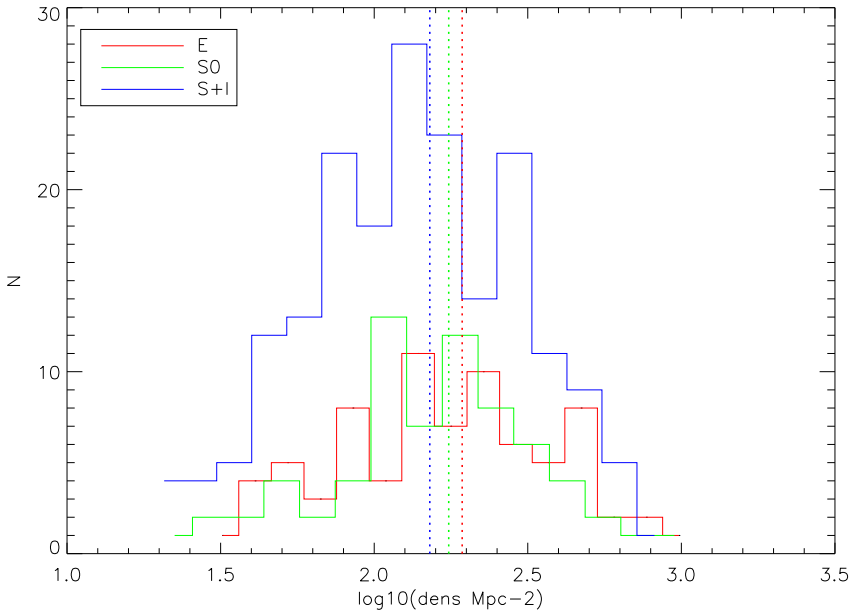

Figure 6.6: Distribution of the local density into three morphological types for the whole ACS sample. Vertical lines shows the mean value of the density of each cluster.

Looking at each cluster individually, we have plotted in Figure 6.7 and 6.8 the density function for each cluster separated into three morphological types. Although we have few galaxies for us to have a good resolution the results are significant. For instance, we see that A1643 is dominated by elliptical galaxies in the densest areas but the late-type galaxy population is completely dominating the rest of the the core of this cluster. We also see that A1878 has a strong gradient of late-type-galaxies which increases to less dense areas. On the other hand, A1952, A2111 and A2658 have a dense elliptical -dominated core.

As far as the ACS sample is concerned, in all cases the late-type galaxies dominate the clusters, except for the case of CL0024 and MS1358, were the denser areas have a slightly dominant early type population. This fact can be due to the presence of substructure of different bright galaxies, completely visually at simple sight.

6.1.3 Luminosity-Density Relation

We have also studied the relation between density and luminosity. With that purpose, we have plotted in Figures 6.9 and 6.10, the absolute r magnitude

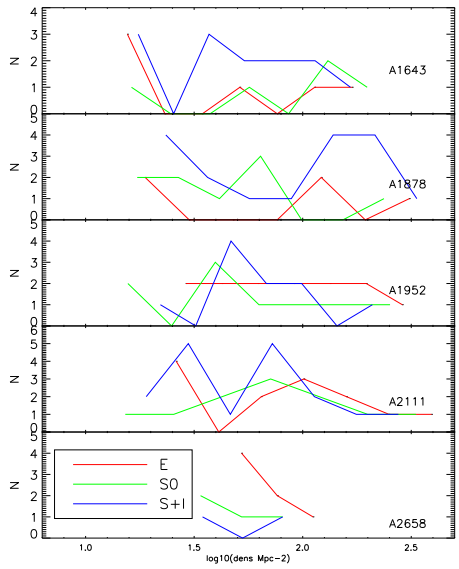

Figure 6.7: Distribution of the local density into three morphological types for individual clusters in NOT sample.

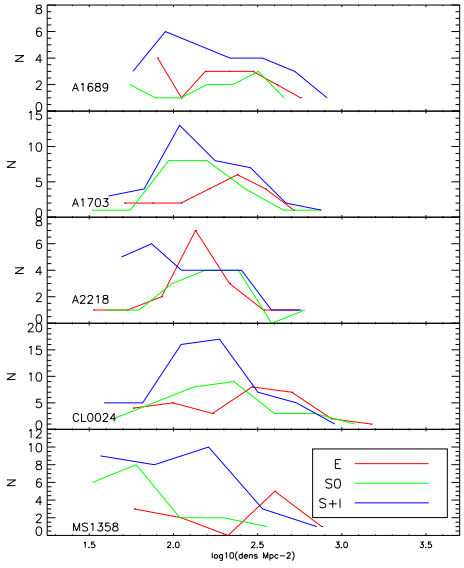

Figure 6.8: Distribution of the local density into three morphological types for individual clusters in ACS sample.

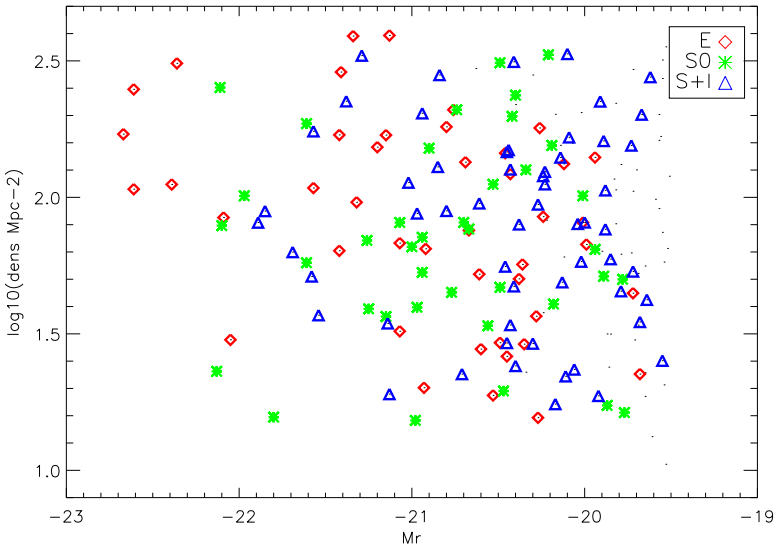

Figure 6.9: Absolute Gunn-r magnitude versus local density into three morphological types for the whole NOT sample. Red diamonds, green asterisks and blue triangles are the Elliptical, lenticular and Spiral galaxies, respectively.

for the whole NOT and ACS sample versus the local density for each galaxy separated into morphological types.

Apparently, we see a mixture of the morphological types in that spaces. However, we see as the brightest galaxies are elliptical and are placed in the denser regions. On the opposite, lenticular and spiral galaxies are fainter and spread in all range of densities.

The empty area at the left bottom hand of the panels refer to very bright galaxies with a low density. As numerous studies have confirmed, (Sandage, 1972a; Gunn & Oke, 1975; Jones & Forman, 1984; Hoessel & Schneider, 1985; Postman & Lauer, 1995; Smith et al., 2005), in clusters of galaxies, we do not find bright galaxies in low density environments, on the contrary, the brightest cluster galaxies are always placed at the center and denser areas of the cluster as they are also the more massive.

Regarding to the luminosity-density relation for the individual clusters in NOT and ACS sample respectively, we show them in Figures 6.11 and 6.12. It's quite remarkable the fact that A1878 has a blue bright highly concentrated population. On the contrary, as it was shown in the Chapter 3, A1643, presents also a high fraction of blue- fainter galaxies, being its brightest cluster a galaxy a lenticular galaxy. In addition, all the clusters present its brightest galaxy in the densest environments. Finally, in A1952, we detect a group of very bright

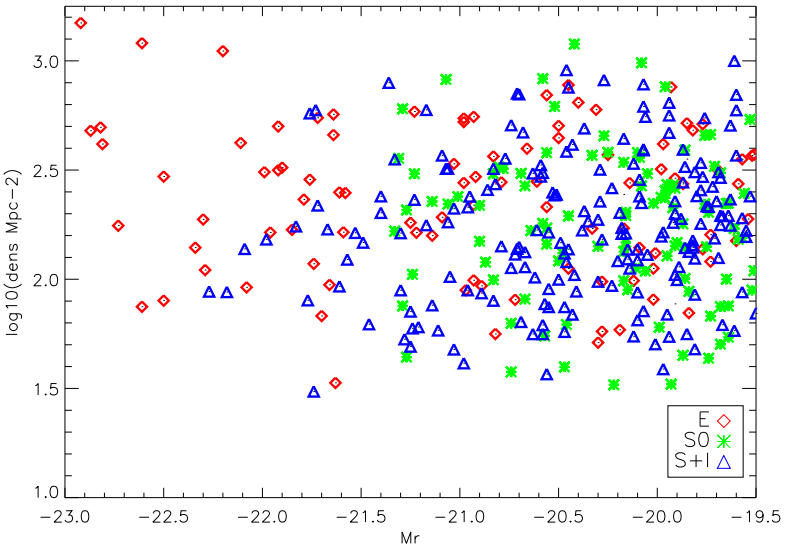

Figure 6.10: Absolute Gunn-r magnitude versus local density into three morphological types for the whole ACS sample. Red diamonds, green asterisks and blue triangles are the Elliptical, lenticular and Spiral galaxies, respectively.

lenticulars in dense environments, which can be a related strubestructure as explained in the First Chapter.

For the ACS sample, we see as that the elliptical galaxy population, on one hand, and lenticular and spiral galaxy population on the other, spread in a quite different range of luminosity. However, the mean density seems to remain constant. In all clusters the brightest galaxies are elliptical galaxies with the exception of a bright spiral galaxy in A1703, which might be a merger galaxy or foreground galaxy.

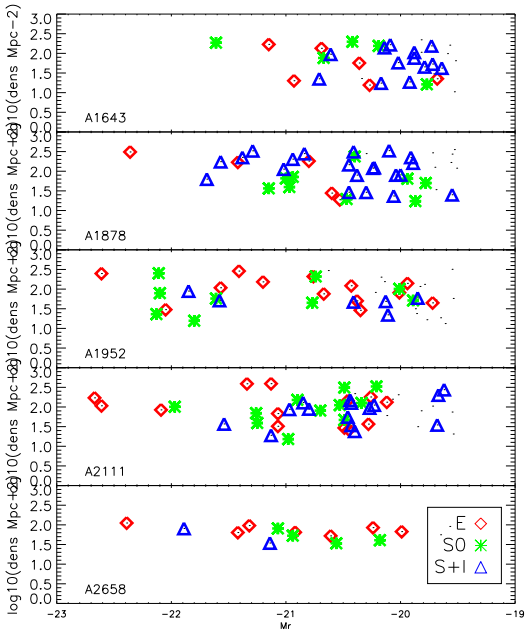

Figure 6.11: Absolute Gunn-r magnitude versus local density into three morphological types for the individual clusters in NOT sample. Red diamonds, green asteriks and blue triangles are the Eliptical, lenticular and Spiral galaxies, respectively.

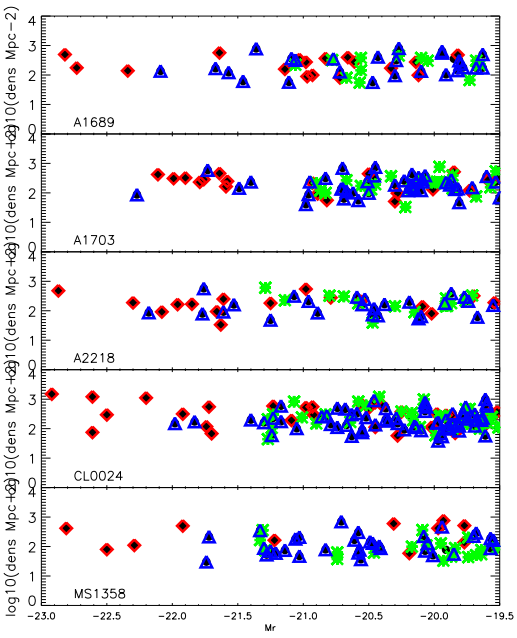

Figure 6.12: Absolute Gunn-r magnitude versus local density into three morphological types for the individual clusters in ACS sample. Red diamonds, green asteriks and blue triangles are the Eliptical, lenticular and Spiral galaxies, respectively.

6.2 Radial Distribution

6.2.1 Center of the cluster

The center of the cluster is defined to be the point placed at the minimum of the cluster gravitational potential, (Sandage, 1972a; Gunn & Oke, 1975; Postman & Lauer, 1995). In the practice, there are several methods to determine the center of the cluster.

- **X-ray distribution**

  Clusters of galaxies have a great proportion of hot gas or plasma at about 10^7 K. The intensity of the X-ray emission is directly related to the depth of the cluster gravitational potential well. In addition, as the X-ray are proportional to the square of the gas density, it is little affected by projection effects in comparison to those arising in optical cluster selection, (Romer et al., 1994; van Haarlem, Frenk & White, 1997). Unfortunately, only the more massive clusters emit in X-rays.

- **Brightest Cluster Galaxy (BCG)**

  The Brightest Cluster Galaxy are the galaxies which represent the brightest end of the luminosity function. Not only that, but they have particular properties, different from the rest of the whole sample. That subject will be treated in detail in Chapter 8. Numerous works have determined that they are positioned at the centre of the cluster gravitational potential as they lie close to the peaks of the X-ray emission in concentrated X-ray bright clusters (Jones & Forman, 1984; Rhee & Latour, 1991; Brough et al., 2002).

  According to theoretical hierarchical scenario (Aragón-Salamanca, Baugh & Kauffmann, 1998; Dubinski, 1998; De Lucia & Blaizot, 2007), that galaxies could have been originated by the cooling of the gas from the surrounding hot halo medium, together with the accretion of small galaxies falling to the cluster centre as result of dynamical friction and then merge. Other theories, (Merritt, 1985; Bird, 1994), suggest that BCGs were formed during or before the cluster collapse and they fell to the center of the cluster faster than less massive galaxies by dynamical friction.

- **Luminosity Barycenter**

  A different approach for locating the center of the cluster is assuming that the luminous mass distribution is tracing the non-luminous mass distribution. Then center of the luminosity distribution will be given then by the barycenter coordinates:

$$(X, Y) = \left(\frac{\sum_i I_i x_i}{\sum_i I_i}, \frac{\sum_i I_i y_i}{\sum_i I_i}\right)$$

Table 6.3: Centers Considered in NOT Clusters

Name	α(2000)			δ(2000)		
A 1643	12	55	54.00	+44	05	12.40
A 1878	14	12	52.18	+29	14	28.40
A 1952	14	41	03.57	+28	37	00.30
A 2111	15	39	40.60	+34	25	27.00
A 2658	23	44	49.80	−12	17	39.50

where I_i is the luminosity intensity for each galaxy and (x_i, y_i) are the spatial coordinates of the galaxy.

That determination can be dangerous due to the limit spatial coverage and their possible biases. Also, the interlopers contamination can also mislead the results. In addition, the dark matter distribution may behave in a different way from the luminous matter.

- **Dark Matter Center**

  Lensing techniques, (Tyson & Fischer, 1995; Kneib et al., 1996; Taylor et al., 1998; Kneib et al., 2004; Broadhurst et al., 2005b; Diego et al., 2005; Zekser et al., 2006), are used for determining the mass of the cluster by estimating from its dark matter halo profile and consequently, the mass centroid.

- **Density Maximum**

  Assuming the same hypothesis as the luminosity barycenter that the luminous mass distribution governs the non-luminous mass distribution, we can determine also the center of the cluster finding the peak of the maximum density. That supposition assumes that the center of the cluster must be the place where the largest fraction of luminous matter is concentrated. Again, that approach is valid if the dark matter distribution follows the luminous matter distribution.

Taking into account all the redshift and X-ray data available in the literature for those clusters, we have set the center of the cluster at the X-ray distribution center. For the rest, we have established the BCGs coordinates as the center, (see for example, Liu & Mohr (2004)). The coordinate of the center are collected In Tables 6.3 and 6.4. The BCG in A2111 is only 5.04 kpc from the X-ray center, while in the ACS sample, we find small distances from A1689 (23.02 kpc), A1703 (7.98 kpc), A2218 (6.15 kpc), and weighty differences from CL0024 (99.28 kpc) and MS1358 (195.301 kpc). That fact should be kept in mind in the analysis of the population, as the misalignment of the BCG with the X-ray center can be due to a non-relaxing state of the cluster.

Table 6.4: Centers Considered in ACS Clusters

Name	α(2000)			δ(2000)		
A 1689	13	11	29.5	−01	20	28.2
A 1703	13	15	05.2	+51	49	02.8
A 2218	16	35	48.9	+66	12	42.0
CL0024	00	26	36.3	+17	09	46.0
MS1358	13	59	54.3	+62	30	36.0

6.2.2 Radius-Density Relation

We have studied the density of the galaxies in function to the distance to the center for each cluster, as it is shown in Figures 6.13 and 6.14. The dotted line is a second degree interpolation of the relation.

All the clusters shows a smooth profile with the exception of A1643, for which the peak found is due to a discontinuity in the area surveyed, A2658 which we only cover the inner 420 kpc and therefore, we do not have enough area to note any significant tendency, and MS1358, where we do not find the decreasing tendency. This fact may be due to the slightly larger difference in the distance of the X-ray center from the BCG than the rest of the clusters.

6.2.3 Radius-Morphology Relation

It is well known from the pioneering work by Dressler (1980), that early-type galaxies in clusters at low redshift are located in denser regions and closer to the center of the cluster rather than than late-type galaxies. We want now to investigate the way that those clusters at medium redshift are populated. With that purpose, we have plotted in Figures 6.15 and 6.16 the radius-morphology relation for each cluster in NOT and ACS sample separated into early and late morphological types. We have used a linear interpolation in bins to obtain the curves in the Figure.

It's quite evident that for A1952, A2111 and A2658 we obtain that the main population in the central part of the cluster consist on early type galaxies and that fraction is decreasing as the distance to the center increases. We find a peak in A2111 of late-type galaxies which may be provided from a possible population of late-type galaxies of the merger cluster. On the other hand, we find that A1643 and A1878 have a large fraction of late-type galaxies in the central part of the cluster which decreases at larger radios, while the early-type population remains quite constant, for A1878 and shows a decreasing trend for A1643.

Looking at the ACS sample, we note a decreasing tendency of the early type population in nearly all clusters, with the exception of the inner 100 kpc, where the

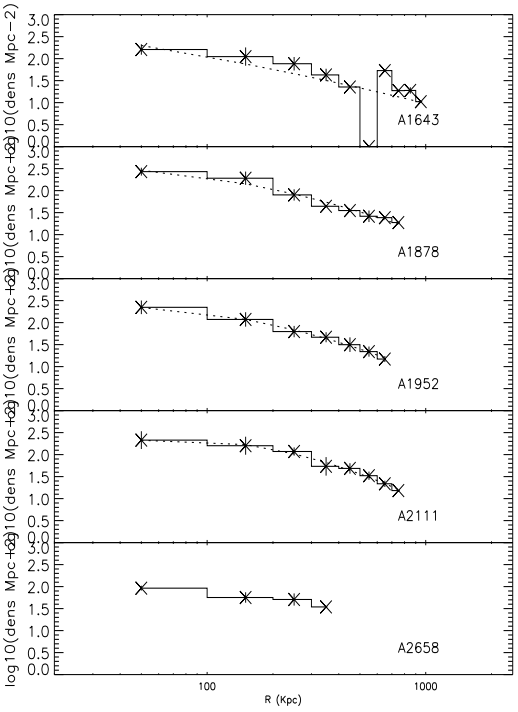

Figure 6.13: Radius-Density Relation for NOT sample

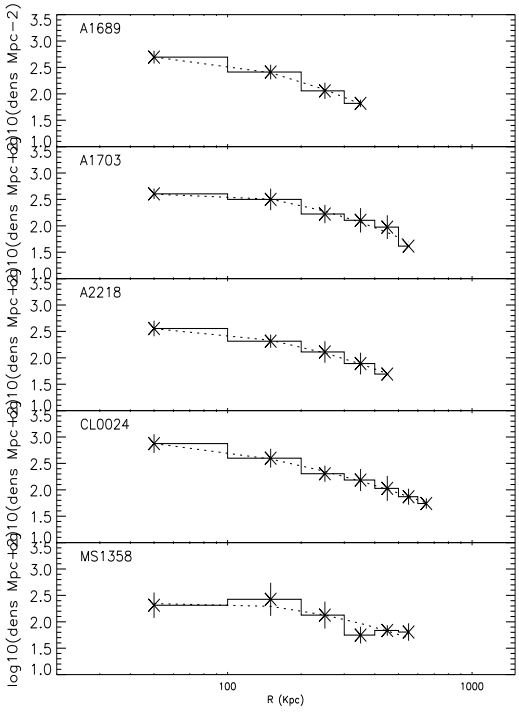

Figure 6.14: Radius-Density Relation for ACS sample

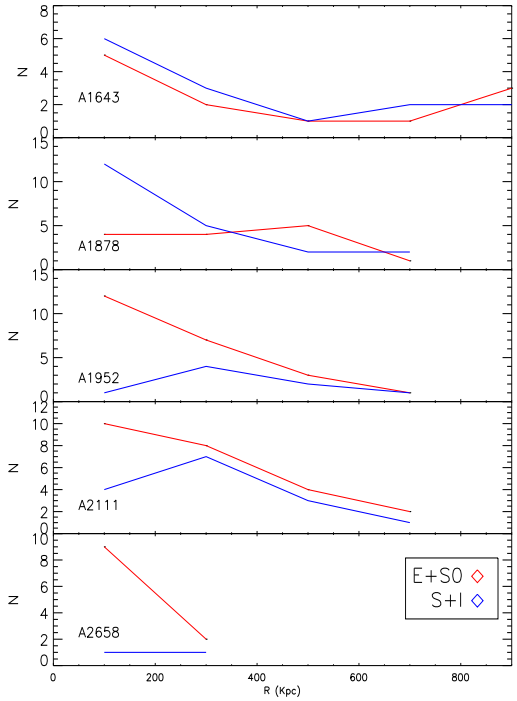

Figure 6.15: Radius-Morphology Relation by morphological types in NOT sample clusters.

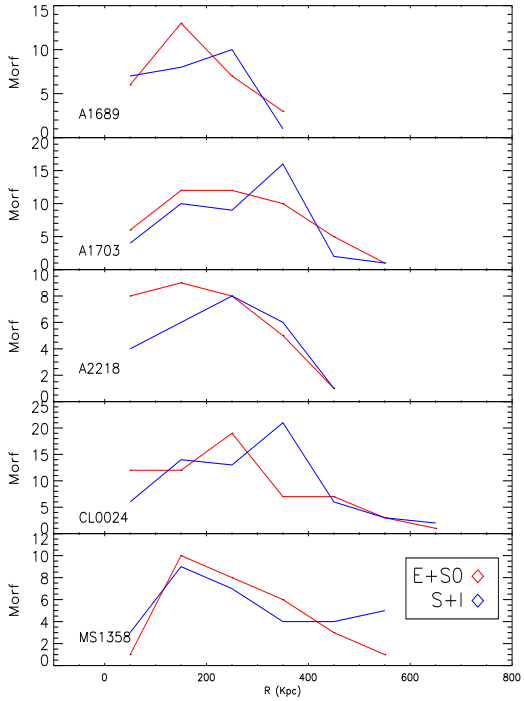

Figure 6.16: Radius-Morphology Relation by morphological types in ACS sample clusters.

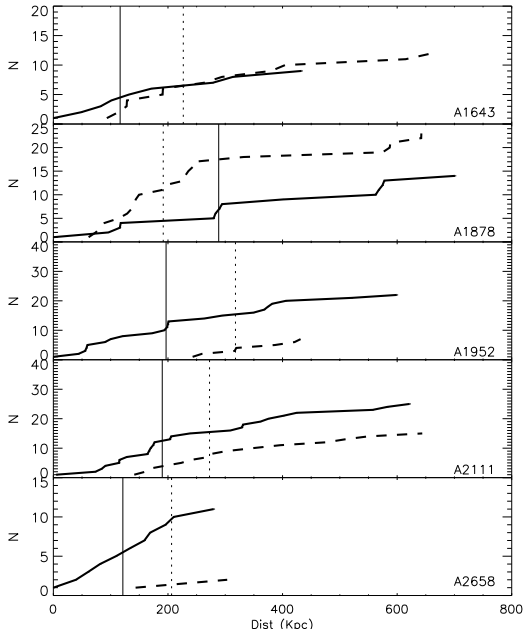

Figure 6.17: Cumulative functions of the different morphological types as a function of the projected radius to the center of the cluster for the NOT sample. Early types: solid lines; late types: dotted lines. The vertical lines indicate the radius where the distributions reach the 50% level.

tendency is decreasing. The late-type population shows a variety of behaviours. For A1689, A2218 and MS1358, we find a very similar shape in comparison with the early-type population, that is a decreasing fraction of late-type galaxies at larger radios. However, we find the contrary tendency again in the inner parts, which arrive to larger radius for this population, especially for A1689 and A2218. On the other hand, we have two clusters, A1703 and CL0024, with two late-type population peaks at radius $\approx$ 400 kpc. That peak contrasts with the smooth profile of A1703, while in the case of CL0024, a different peak provide by the early-type population can be found.

In Figure 6.17 and 6.18, we have plotted the cumulative functions of the different types of galaxies versus projected distance of each galaxy to the center of the cluster for both samples. The solid lines represent the accumulated distribution of early-type, elliptical and lenticular, galaxies, whereas the dotted lines correspond to the accumulated distribution of late-type galaxies, spiral and irregular. The vertical lines indicate the radius where the accumulated distributions reach the 50% of the distributions.

Regarding to the NOT sample, we see that all the clusters are dominated in their central regions by early type galaxies except A1878, that has a sizable

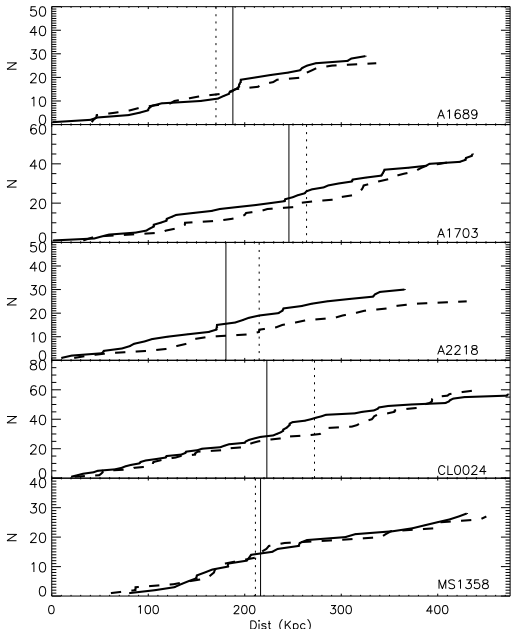

Figure 6.18: Cumulative functions of the different morphological types as a function of the projected radius to the center of the cluster for the ACS sample. Early types: solid lines; late types: dotted lines. The vertical lines indicate the radius where the distributions reach the 50% level.

fraction of late-type, including irregular galaxies. A fact that could explain its high (central) fraction of blue galaxies. This is however, not unique since similar cases can also be found at lower redshift (see for example Varela (2004)). A1643 has also a large global fraction of late-type, spiral galaxies, but they do not dominate the core of the cluster. The rest of the clusters are also centrally dominated by a population of elliptical galaxies, with an overall population with a smaller fraction of late-type galaxies.

As far as the ACS sample is concerned, we find one cluster, MS1358 that has a very similar morphological distribution, That is, the two morphological population are not quantitatively different. Also, we find three clusters dominated by an early type population, A1703, A2218 and CL0024 and finally, A1689, which presents a late-type galaxy population dominating in its core. As a result of this analysis, a diversity seems to be the dominant aspect in our ten clusters.

To test whether the distribution of early and late type galaxies are similar, we have performed a Kolmogorov-Smirnov test. Excluding A2658, for which there are not enough points to extract significant results, we find that the two populations are significantly different in all clusters except in A1878 and A1952, while for the whole ACS sample, A2111 and A1643, the test does not verify the hipothesis.

In conclusion, we find seven clusters out of ten dominated by an early-type population, two more clusters with the late-type population dominating in their core and one cluster with a very similar population. We also find two clusters out of ten (one with an early and late type population dominating respectively) which contain a significantly different population.

Chapter 7

Luminosity Function

Eres, serás, fuiste el Universo encarnado...
Para tí se encenderán las galaxias y se incendiará el sol...
Para que tú ames y vivas y seas...
Para que tú encuentres el secreto y mueras sin poder participarlo,
porque sólo lo poseerás cuando tus ojos se cierren para siempre...

Carlos Fuentes, 'La muerte de Artemio Cruz.'

The optical general **Luminosity Function** (LF) is the number of galaxies per unit volume in a magnitude interval M to M+dM. It can be considered a probability distribution $\phi(M)$ over absolute magnitude for an individual sample of galaxies. $\phi(M)$ is usually called the **Differential luminosity function**, in order to distinguish from $\Phi(M)$, the **Integrated Luminosity Function**, defined as:

$$\Phi(M) = \int_{-\infty}^{M} \phi(M^{'})dM^{'}$$

The LF has been used to study the way that the galaxies form and evolve, Dressler (1984). If we assume that galaxy mass-to-light ratios are nearly constant, $M/L \approx const$ for the different types of galaxies, the LF can set constraints in the initial mass function and the distribution of density perturbations that are expected to originate the galaxies, Press & Schechter (1974). Likewise, it can be used as a diagnostic for the changes in the galaxy population due to, for example, the influence of the cluster environment.

Numerous studies to date have noted the difference between the luminosity function for field galaxies and for cluster galaxies, (Hubble & Humason, 1931; Abell, 1965; Oemler, 1974; Binggeli, Sandage & Tammann, 1988). Currently, clusters and field LF of large samples of galaxies in the nearby universe have been computed.

7.1 Background Contamination Estimation

In Chapter 3, we fitted the Color-Magnitude Relation and dropped out from the cluster all the galaxies whose color was 0.2 magnitude redder than the fit, due to the reddeness provoked by the cosmological k- effect (Oke & Sandage, 1968; Pence, 1976; Poggianti, 1997). We also ensured that the foreground contamination was practically inexistent by integrating the field luminosity function for field galaxies.

There are two ways more at least for determining the contamination. The most common way of estimating the background contamination is studying the luminosity distribution in the close regions of the cluster (Oemler (1974)). The distance to the field must be enough to be placed outside the cluster and not too large in order to avoid the background variations. Then, the galaxy counts in the reference field direction are modeled (see Andreon (2004); Andreon, Punzi & Grado (2005)). After that, the difference in the number of counts in each magnitude interval is said to be due to the galaxies from the cluster. Unfortunately, the observation time is limited so that fields are often unavailable.

However, different measurements provided by a number of authors exist in the literature. We should control that the difference in the instrumentation, methodology and observation conditions are similar to our observations. For our r-band, we have several works which gives us the number of galaxies per relative magnitude bin (McLeod et al., 1995; Metcalfe et al., 2001; Yasuda et al., 2001). We have selected the Table 3 from McLeod et al. (1995) as their apparent magnitude range include ours. Metcalfe et al. (2001) give an approximation for galaxies with HST with $m_r > 21$ and Yasuda et al. (2001) arrive to magnitudes $m_r < 21.5$. Several authors, Liske et al. (2003); Berta et al. (2006), provide also reliable galaxy number counts, however they are in different filters than us.

In Figures 7.1 and 7.2, we have plotted the points corresponding to the number of galaxies per 0.5 magnitude bin square degree versus magnitude. The dotted line is a linear interpolation of the background contamination given by McLeod et al. (1995) and the red line is the linear interpolation of the magnitude distribution for all the galaxies detected without performing the subtraction in the Chapter 3. The blue line is the counts differences from these distributions and finally, the green lines are the galaxy distribution excluding the galaxies by the CMR procedures explained in Chapter 3. The vertical line represents the completeness limit for the sample.

Referring to the NOT sample, we see that only for A1643 and A1878 we have a slightly difference for magnitudes brighter than 19.5. For the rest, the difference of the distributions begins to be noticeable for fainter magnitudes than 20, which is very close to the completeness magnitude for the NOT sample, as was set in Figure 3.1. It's quite noticeable that the A2111, which is the cluster for which we had some redshift information has a very well background contamination estimated. As we have already seen, the population in A1643 is quite faint, in comparison with the rest of the clusters in the samples. This fact will be

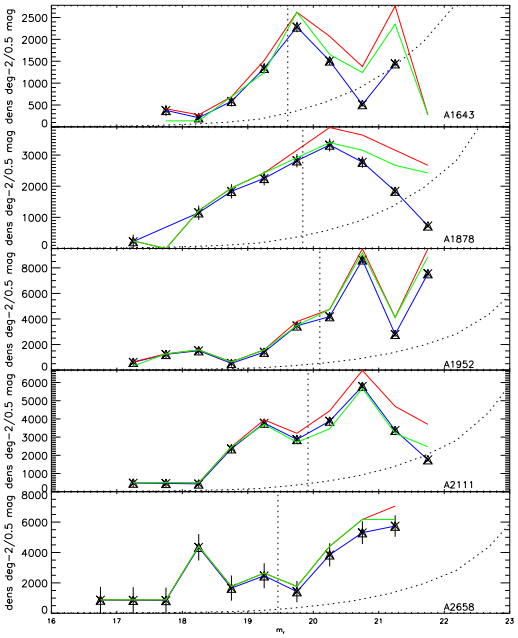

Figure 7.1: Number of galaxies per square degree and 0.5 magnitude versus apparent magnitude for all the galaxies detected in NOT sample (red line), without background contamination from McLeod et al. (1995) (blue line) and without background contamination from CMR (gree line). The dotted line represents the background contamination given by McLeod et al. (1995). The vertical line shows the completeness limit for each cluster of the sample.

translated into a bad fit of the LF.

For the ACS sample, we see that A1703, for which we did not have redshift information in literature and MS1358, for which we have very few redshift are the clusters that have a largest difference with the subtraction provided by McLeod et al. (1995). On the contrary, A1689, A2218 or CL0024 provide an excellent agreement for both distributions up to magnitude $m_r = 22$ at least. Therefore, we will consider the subtraction given by McLeod et al. (1995) as the real galaxy population for computing the luminosity function.

7.2 The Composite Luminosity Function

Since we do not have too many galaxies per magnitude bin in the individual LF, especially, in the NOT sample. We are going to consider the **Composite Luminosity Function** defined by Colless (1989). A number of works in the

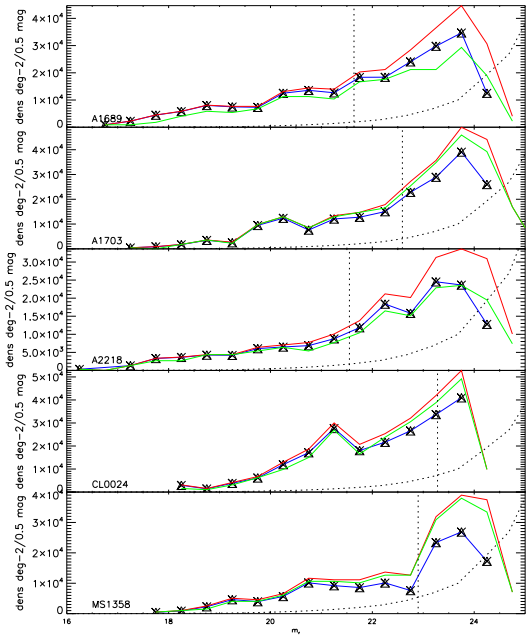

Figure 7.2: Number of galaxies per square degree and 0.5 magnitude versus apparent magnitude for all the galaxies detected in ACS sample(red line), without background contamination from McLeod et al. (1995) (blue line) and without background contamination from CMR (gree line). The dotted line represents the background contamination given by McLeod et al. (1995). The vertical line shows the completeness limit for each cluster of the sample

literature have used it, providing many reliable results (Lumsden et al., 1997; De Propris et al., 2003; Barkhouse, Yee & López-Cruz, 2007). It has been built by summing galaxies in absolute magnitude bins and scaling by the richness of their parent cluster. Specifically, the following summation was carried out

$$N_{c,j} = \frac{R_c}{n_{clus,j}} \sum_i \frac{N_{i,j}}{R_i}$$

where $N_{c,j}$ is the number of galaxies in the jth absolute magnitude bin of the composite LF, $N_{i,j}$ is the number in the jth bin of the ith cluster LF, $n_{clus,j}$ is the number of clusters contributing to the jth bin, R_i is the normalization used for the it cluster LF and R_c is the sum of all the normalizations:

$$R_c = \sum_i R_i$$

The formal errors in $N_{c,j}$ are computed according to

$$\delta N_{c,j} = \frac{R_c}{n_{clus,j}} \left[\sum_i \left(\frac{\delta N_{i,j}}{R_i} \right)^2 \right]^{1/2}$$

where $\delta N_{c,j}$ and $\delta N_{i,j}$ are the formal errors in the jth LF bin for the composite and ith cluster respectively.

Following Lumsden et al. (1997), we have used a different definition of R_i from the one given in Colless (1989). He used the total number of galaxies brighter than $M = -19$ and we have use the background -corrected number of cluster galaxies brighter than $M = -19.5$, as M_r=-19 is beyond our chosen completeness limit for the NOT sample. However, for typical values for the LF, the relationship between our definition of richness and that of Colless is $R_i(Colless) \sim 1.34\ R_i(thesis)$. In Figure 7.3 and 7.4, we have plotted the resulted composite Function for our cluster sample.

7.3 Fit of the Luminosity Function

After the first discoveries of galaxies, the first attempts to study and fit the Luminosity Function were done by Hubble & Humason (1931). Their results could be fitted by a gaussian function. Some decades later, the first clusters compilations were performed by Abell (1958) and Zwicky et al. (1961), who realized that the number of faint galaxies had been underestimated. The former (Abell, 1964, 1972), described then two asymptotic behaviors of $\phi(M)$ at the bright and faint end, separated by a 'break point', M* as follows

$$\begin{cases} \log N(\leq m) = K_1 + s_1 m & \text{if } m < m^* \\ \log N(\leq m) = K_2 + s_2 m & \text{if } m \geq m^* \end{cases}$$

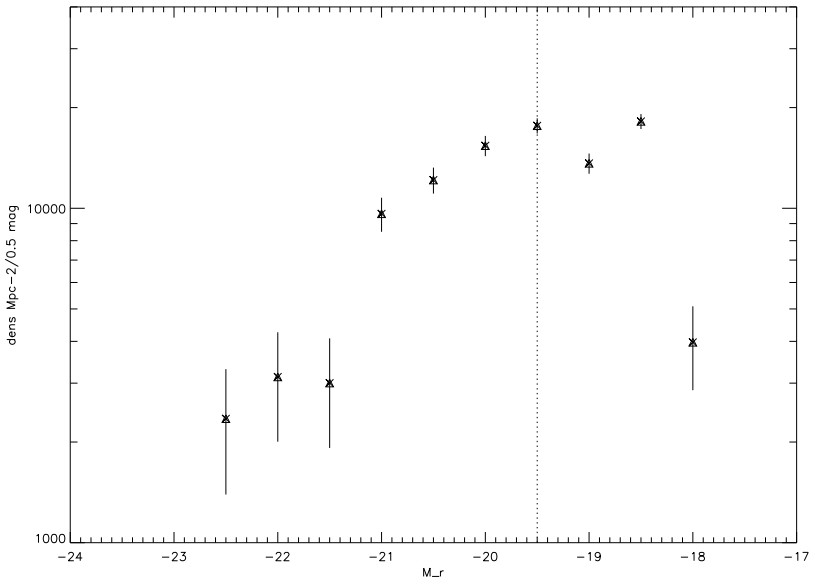

Figure 7.3: Composite Luminosity Function for NOT sample

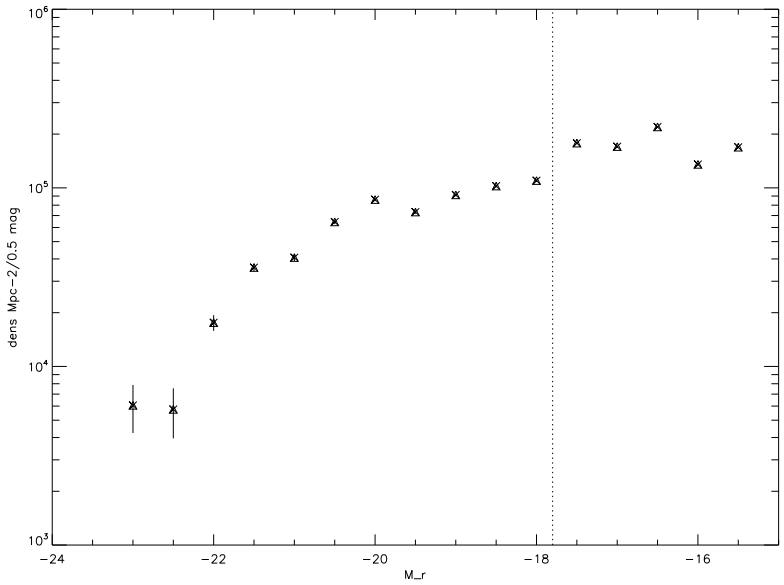

Figure 7.4: Composite Luminosity Function for ACS sample

where $N(m)$ is the number of galaxies per square degree brighter than m. Zwicky, (Zwicky et al., 1961), proposed the following analytical function

$$< n_{cl} > (\Delta m) = k(10^{\Delta m/5} - 1)$$

where $< n_{cl} >$ is the mean number of galaxies in the magnitude range Δm between the magnitude of the brightest galaxy and m.

However, although these estimations were very accurate for the data available, Schechter (1976) proposed an analytical distribution of the galaxies luminosity in the following way:

$$\phi_c(L)dL = n^*(L/L^*)^\alpha e^{-L/L^*} d(L/L^*)$$

where ϕ_c is the number of galaxies contained in a volume and in the luminosity range L to $L + dL$ and L^* is the characteristic luminosity corresponding to the 'break point' or *knee* where the slope changes, α is the slope of luminosity function at low magnitudes and n^* is the constant, which normalizes to the density of galaxies. The whole luminosity of the cluster can be found by integrating the last expression:

$$L_{cluster} = \int_0^\infty L n_c(L) dL = n^* \Gamma(\alpha + 2) L^*$$

where here, Γ represents the mathematical function *Gamma*,

$$\Gamma(a) = \int_0^\infty e^{-t} t^{a-1} dt$$

The analogous Schechter function can be expressed in absolute magnitudes by making the variable change $L/L^* = 10^{(M^*-M)/2.5}$, obtaining the following expression:

$$\phi_c(M)dM = 0.4 \ln(10) \phi^* 10^{0.4(M^*-M)(1+\alpha)} e^{-10^{0.4(M^*-M)}} dM$$

where $\phi_c(M)$ is the number of galaxies per volume unit and magnitude unit, $M^* = 10^{-0.4M^*}$ is the characteristic magnitude where the slope of the LF changes and ϕ^* represent the normalization constant to the galaxy density.

Some authors (Driver et al., 1994; Hilker, Mieske & Infante, 2003; González et al., 2006; Popesso et al., 2006; Barkhouse, Yee & López-Cruz, 2007), have argued that the sum of two Schechter functions provides a more adequate fit to the cluster LF than a single Schechter function. That fact is due to the emergence of had a rising faint end (M_r >-19), even though the bright end of the LF appeared to be well fitted by a Schechter function. Alternative LF fitting functions include a Gaussian and a single Schechter function for the bright and faint end respectively, (Thompson & Gregory, 1993; Biviano et al.,

1995; Parolin, Molinari & Chincarini, 2003), a single power-law fit to the faint end, (Trentham, Tully & Verheijen, 2001; Boué et al., 2008) or an Erlang plus a Schechter function, (Biviano et al., 1995).

In our case, we are going to fit the LF by a single Schechter function, as we are working in its bright end. We have discussed the influence of including the Brightest Cluster Galaxy in the fit as, in general, the presence of these galaxies is easily noticed by their effect on the brightest magnitude bin, whose value is usually offset from the best-fit Schechter function. Schechter (1976); Sandage (1976); Dressler (1978); Loh & Strauss (2006), remarked that BCGs do not seem to be a natural extension of the cluster LF.

We have explored in the following subsections, different ways of fitting the Luminosity Function, discussing the best accurate results for our samples.

7.3.1 Chi-Square fitting

On account of the differential character of the luminosity function, our abscissas in the fit must be, magnitudes bins, as their corresponding function values are the number of galaxies in a volume within a magnitude bin. As we do not have too many galaxies, we have obtained few bins, with a moderate number of galaxies.

In order to fit the luminosity function to the Schechter Function, we have minimized the chi-square residuals by using the Levenberg-Marquardt method (LM).

Levenberg-Marquardt Method

Let's call $y = y(x; \overrightarrow{a})$, the function we want to fit, in our case the Schechter function, where $\overrightarrow{a}$ is the set of n-parameters we want to determine. Then, the χ^2 function is defined as

$$\chi^2(\overrightarrow{a}) = \sum_{i=1}^{N} [\frac{y_i - y(x_i, \overrightarrow{a})}{\sigma_i}]^2 \tag{7.1}$$

where x_i and y_i are the set of points that we want to fit and σ_i is standard deviation in each point and N is the number of points where we have a value for the function.

When the solution is close enough to the minimum, the χ^2 can be approximated by a quadratic form:

$$\chi^2(\overrightarrow{a}) \approx \gamma - d.\overrightarrow{a} + \frac{1}{2}\overrightarrow{a}\mathbf{D}\overrightarrow{a} \tag{7.2}$$

where $\overrightarrow{d}$ is a vector with the same number of components as $\overrightarrow{a}$, n and $\mathbf{D}$ is the $n \times n$ Hessian matrix.

If the approximation is good enough, we will jump from the present solution $\vec{a}_0$ to the following that minimizes the χ^2 function $\vec{a}_{min}$ as follows:

$$\vec{a}_{min} = \vec{a}_{act} + \mathbf{D}^{-1}[-\nabla\chi^2(\vec{a}_{act})] \tag{7.3}$$

In case it is a bad approximation, we will go back with the gradient like that:

$$\vec{a}_{sig} = \vec{a}_{act} - constant[\nabla\chi^2(\vec{a}_{act})] \tag{7.4}$$

where the constant must be small enough not to leave the present descends direction.

To be able to use equation 7.3 and 7.4, we need to compute the gradient of the χ^2 for any set or parameters $\vec{a}$, as well as the Hessian matrix of χ^2.

The χ^2 gradient respect the M parameters that form $\vec{a}$ has the following form:

$$\frac{\partial\chi^2}{\partial a_k} = -2\sum_{i=1}^{N}[\frac{y_i - y(x_i,\vec{a})}{\sigma_i^2}]\frac{\partial y(x_i,\vec{a})}{\partial a_k} \qquad k = 1, 2, \ldots, M \tag{7.5}$$

and deriving again:

$$\frac{\partial^2\chi^2}{\partial a_k \partial a_l} = 2\sum_{i=1}^{N}\frac{1}{\sigma_i^2}[\frac{\partial y(x_i,\vec{a})}{\partial a_k}\frac{\partial y(x_i,\vec{a})}{\partial a_l}] - [y_i - y(x_i,\vec{a})]\frac{(\partial y(x_i,\vec{a}))^2}{\partial a_k \partial a_l} \tag{7.6}$$

Let's note that in that equation, we can ignore the second derivative term as it is negligible when comparing with the first derivative term. In addition, the factor which is multiplying is the error in each point, and therefore, it tends to cancel out when we sum over all i. So equations 7.5 and 7.6 have the following form:

$$\beta_k = \frac{-1}{2}\frac{\partial\chi^2}{\partial a_k} \tag{7.7}$$

and

$$\alpha_{kl} = \frac{1}{2}\mathbf{D} = \sum_{i=1}^{N}\frac{1}{\sigma_i^2}[\frac{\partial y(x_i,\vec{a})}{\partial a_k}\frac{\partial y(x_i,\vec{a})}{\partial a_l}] \tag{7.8}$$

and, therefore, equation 7.3 can be rewritten as

$$\sum_{l=1}^{M}\alpha_{kl}\delta a_l = \beta_k \tag{7.9}$$

and equation 7.4 as

$$\delta a_l = constant \times \beta_l \tag{7.10}$$

where δa_l denotes the increments that added to the present approximation are the following($\delta a_l = \vec{a}_{min} - \vec{a}_{act}$) for equation 7.3 or ($\delta a_l = \vec{a}_{sig} - \vec{a}_{act}$) for equation 7.4.

Therefore, the condition of χ^2 being a minimum, is that $\beta_k = 0$ for any k (i.e: the gradient is null) and it is independent of the way α is defined.

LM method realized that Hessian Matrix could give us information about the order of magnitude of the constant. If we compare the units in equation 7.10, we have that the constant must have dimensions of $1/\alpha_{kk}$. They divided the constant by an ad-dimensional factor λ so that the constant is not too large. We have the possibility of setting $\lambda \gg 1$ for stopping the process. That is, they replace equation 7.10 by

$$\delta a_l = \frac{1}{\lambda \alpha_{ll}} \beta_l \quad \text{o bien} \quad \lambda \alpha_{ll} \delta a_l = \beta_l \tag{7.11}$$

where α_{ll} is positive by definition in equation 7.8.

Then, LM method introduces a new matrix α' defined as

$$\alpha'_{jk} \equiv \begin{cases} (1+\lambda)\alpha_{jk} & \text{if } j = k \\ \alpha_{jk} & \text{if } j \neq k \end{cases}$$

and, finally, we can replace equations 7.9 and 7.11 by

$$\sum_{l=1}^{M} \alpha'_{kl} \delta a_l = \beta_k \tag{7.12}$$

Notice that when λ is too large, α' sets into a dominant diagonal matrix, so equation 7.12 tends to be identical to equation 7.11, and if λ tends to zero, the equation 7.12 approximates to equation 7.9.

The LM method can very sensible to the initial conditions. For example, it can find a local minimum (if we are not close enough) or a 'valley' (depending on the problem geometry). To avoid that problem, we have created a grid with initial conditions for the method and selects the one which returns the smallest χ^2 value. The values for the grid have been set to vary in the following ranges

$$-2.5 \leq \alpha \leq -0.5 \quad \text{and} -19.5 \leq \mathrm{M}^* \leq -22.5$$

with a step of 0.1. Surprisingly, we have obtained the same optimal parameters if we set our parameters at random or with the grid. This is an indication that the minimum is isolated inside that range.

In Figures 7.5 and 7.6, we have plotted the Schechter fit to the Composite Luminosity Function for the NOT and ACS sample. The black lines show the fit without including the BCGs and the dotted lined refers to the fit considering the brightest cluster galaxy. The results of the fit are α=-1.15 and M^*=-21.38 and

α=-0.95 and M_r^*=-20.93 with and without the inclusion of the BCG, respectively for the NOT sample and α=-1.11 and M^*=-21.64 and α=-1.11 and M_r^*=-21.65 for the ACS sample. We have considered in each case, the range of completeness for the fit.

Although the difference between including or not the BCG in the fit for the ACS luminosity composite function does not affect the fit, we have noted a different LF for the NOT sample. By excluding the BCG, we see as the fit is weighted by the fainter points, while if we consider the whole range of magnitude, the brighter points make the faint end appear steeper.

It is worth to see that at the faint end of the LF for the ACS sample, the tendency seems to be ascending, as not fittable by a single Schechter as several authors have already noted, (Biviano et al., 1995; Parolin, Molinari & Chincarini, 2003; Boué et al., 2008).

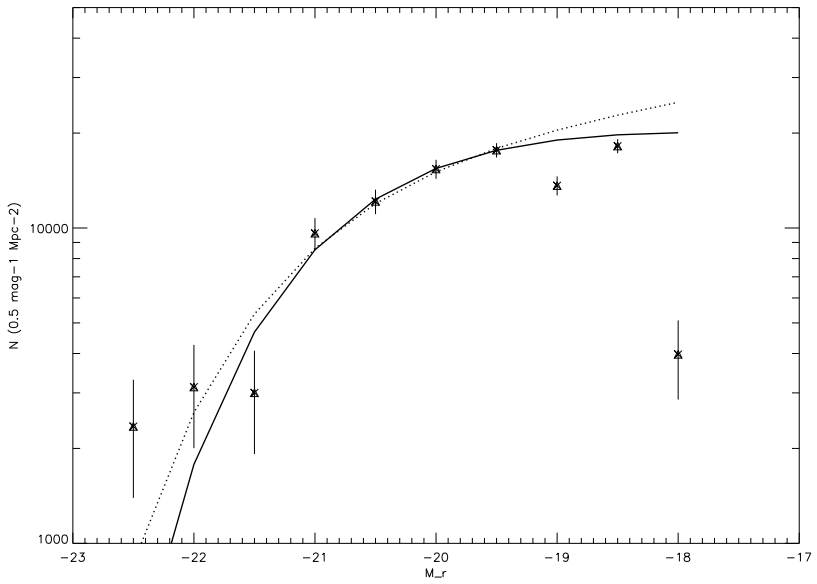

Figure 7.5: Best Schechter fit of the Composite LF for the NOT sample. The solid line refers to the fit excluding the BCGs and the dotted line is referring to the fit including the BCG

In Figure 7.7, we have plotted the Schechter function with the best parameters given by the Levenberg-Marquardt method for each individual cluster from NOT sample, up to the complete range ($M_r = -19.5$). The results of the fit are also collected in Table 7.1. The fits give a median value for the slope of -0.93 and -0.86, considering or not the BCG.

For the ACS sample, the panorama is completely different. In Figure 7.8, we have plotted the Schechter function with the best parameters given by the

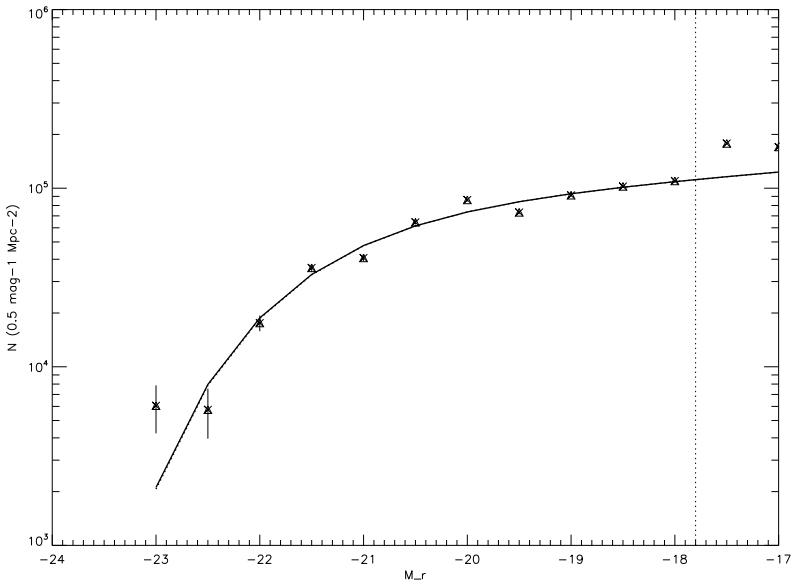

Figure 7.6: Best Schechter fit of the Composite LF for the ACS sample. The solid line refers to the fit excluding the BCGs and the dotted line is referring to the fit including the BCG

Levenberg-Marquardt method, up to the completeness limit $M_r = -17.8$). The parameters obtained in the fit are also collected in Table 7.2.

The fit for the ACS sample is considerably different from the NOT sample, as the extent in magnitude is much larger. Although we do not cover a large area, the results are much more reliable than NOT sample. We find a median value for the slope of -1.17 and -1.14, considering or not the BCG, which are considerably higher than the values of NOT sample. Remarkably for this sample, the differences between including or not the BCG are not relevant., while they are for two clusters in NOT sample, however, the errors are much larger than in ACS sample.

As noted by Barkhouse, Yee & López-Cruz (2007), etc... The results of that fit for two free parameters are not too reliable as there are few bins. Due to that, we have refitted again the FL but this time fixing the slope at the faint end $\alpha = -1.15$, as being the result of the Composite Luminosity Function and is in the range of values extracted from the individual clusters from the ACS sample.

So, in Figure 7.9 and 7.10, we show the results for the Schechter function with the slope at the faint end $\alpha = -1.15$ fixed as it is the result of the Composite Luminosity Function. The results of M^* are shown in Tables 7.3 and 7.4.

As we expected, the fits for the ACS sample continue being very good although we find two clusters of this sample with have a bright value of M*. That result is

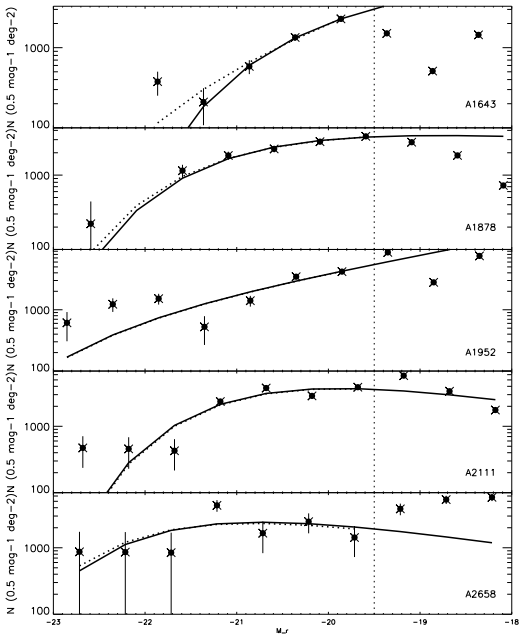

Figure 7.7: Best fit of the differential LF for the NOT sample. The vertical line shows the limit where the sample is complete. The solid line refers to the fit excluding the BCGs and the dotted line is referring to the fit including the BCG

Table 7.1: Best Schechter Parameters of the Luminosity Function with and without the BCG for the NOT sample

	WithBCG			WithoutBCG		
Name	α	M*	χ^2	α	M*	χ^2
A 1643	−2.00	−21.53	1.18	−1.26	−20.21	0.02
A 1878	−0.93	−21.08	0.72	−0.86	−20.94	0.84
A 1952	−1.70	−22.50	4.47	−1.70	−22.50	4.64
A 2111	−0.50	−20.63	4.79	−0.50	−20.64	4.60
A 2658	−0.50	−21.58	1.26	−0.50	−21.49	1.45

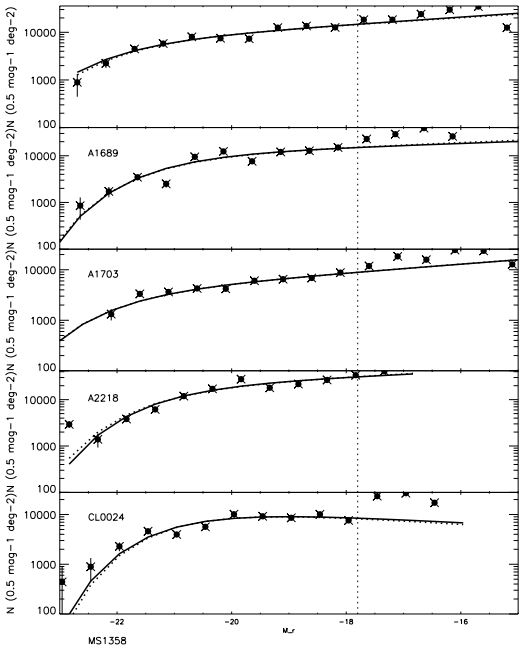

Figure 7.8: Best fit of the differential LF for the ACS sample. The vertical line shows the limit where the sample is complete. The solid line refers to the fit excluding the BCGs and the dotted line is referring to the fit including the BCG

Table 7.2: Best Schechter Parameters of the Luminosity Function with and without the BCG for the ACS sample

	WithBCG			WithoutBCG		
Name	α	M*	χ^2	α	M*	χ^2
A 1689	-1.19	-22.18	6.93	-1.20	-22.30	7.35
A 1703	-1.12	-21.51	17.78	-1.10	-21.46	18.41
A 2218	-1.22	-22.23	2.58	-1.22	-22.21	2.81
CL0024	-1.17	-21.53	53.79	-1.14	-21.41	54.95
MS1358	-0.82	-20.98	6.91	-0.85	-21.06	6.97

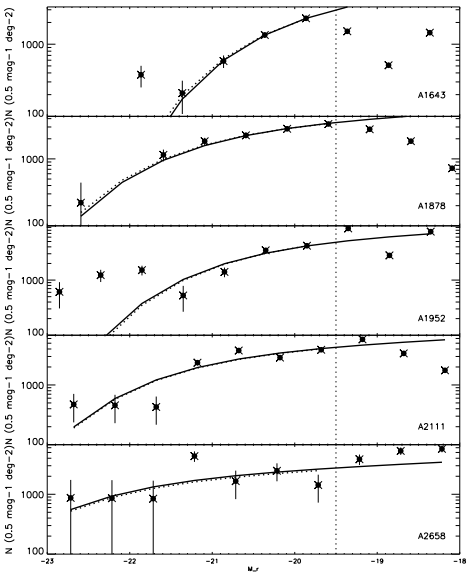

Figure 7.9: Best fit of the differential LF with α=-1.15, for the NOT sample. The vertical line shows the limit where the sample is complete. The solid line refers to the fit excluding the BCGs and the dotted line is referring to the fit including the BCG

in contrast with the values found for the ACS sample with two free parameters, which seems to indicate that the whole luminosity function can not be properly fit by a single Schechter Function. It is very clear now that the faint end of the Luminosity Function ($M_r \geq -18$) have a rising trend.

The LF in the NOT sample are better than a single luminosity function, but in some cases (A1643 or A2658) the LF seems to be disturbed and the fit is quite bad. It is remarkable the case of A1952, where the first three brightest bins are above the fit.

As many authors have already noted (see Sandage, Tammann & Yahil (1979); Popesso et al. (2004); Andreon (2004); Andreon, Punzi & Grado (2005), the fit of the Luminosity Function by binning the data, allows a quick analysis of the data and it's very 'visual' to see how data is distributed. However, continuity is lost in binning and therefore, information. In our case, it's very clear that the results of the fit for the NOT sample are too poor for giving reliable information. In the next sections, we are going to investigate additional methods.

Table 7.3: Best Schechter Parameters of the Luminosity Function with α=-1.15 for the NOT sample

	WithBCG		WithoutBCG	
Name	M*	χ^2	M*	χ^2
A 1643	−20.17	1.57	−20.11	0.02
A 1878	−21.46	0.87	−21.41	1.13
A 1952	−20.80	5.96	−20.85	6.23
A 2111	−21.56	6.49	−21.57	7.02
A 2658	−22.50	1.83	−22.50	2.08

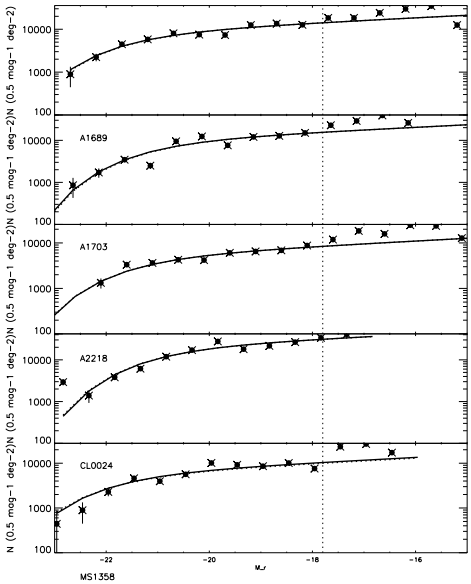

Figure 7.10: Best fit of the differential LF with α=-1.15, for the ACS sample .The vertical line shows the limit where the sample is complete. The solid line refers to the fit excluding the BCGs and the dotted line is referring to the fit including the BCG

Table 7.4: Best Schechter Parameters of the Luminosity Function with α=-1.15 for the ACS sample

	WithBCG		WithoutBCG	
Name	M*	χ^2	M*	χ^2
A 1689	−22.00	7.08	−22.02	7.60
A 1703	−21.62	17.83	−21.64	18.59
A 2218	−21.91	2.91	−21.91	3.13
CL0024	−21.47	53.87	−21.45	54.98
MS1358	−22.31	14.17	−22.25	12.89

7.3.2 Chi-Square integral fitting

One way of avoiding to deal with the binning, is fitting the integral of the luminosity function. We have used the a χ^2 Levenberg-Marquard minimization method explained in the last section. We are going to derive the partial derivatives of the integral function.

Let's work now with the LF expressed in function of the Luminosity instead of absolute magnitude, (see equation 7.3), for the simplicity of the calculus. If we set, $S = L/L^*$ and, therefore, $S_{max} = L_{max}/L^*$, we must calculate the following equation:

$$L(\geq L_i, \leq L_{max}) = \int_{S_i}^{S_{max}} n^* S^\alpha e^{-S} dS = n^*[\gamma(\alpha+1, S_i) - \gamma(\alpha+1, S_{max})]$$

where in this case, γ represents the incomplete mathematical function *gamma*,

$$\gamma(a, x) = \int_x^\infty e^{-t} t^{a-1} dt$$

We need to set the analytical derivates in order to use the Levenberg-Marquardt method.

$$\frac{\partial L}{\partial n^*} = \gamma(\alpha+1, S_i) - \gamma(\alpha+1, S_{max}) = \gamma(\alpha+1, L_i/L^*) - \gamma(\alpha+1, L_{max}/L^*)$$

$$\begin{aligned} \frac{\partial L}{\partial L^*} &= \frac{\partial L}{\partial S}\frac{\partial S}{\partial L^*} = -n^* S^{\alpha+1} e^{-S}/L^*|_{S_i}^{S_{max}} + \frac{\partial S_{max}}{\partial L^*} F(S_{max}) - \frac{\partial S_i}{\partial L^*} F(S_i) \\ &= 2\frac{n^*}{L^*}\left[(L_i/L^*)^{\alpha+1} e^{-L_i/L^*} - (L_{max}/L^*)^{\alpha+1} e^{-L_{max}/L^*}\right] \end{aligned}$$

where F is the intengrand, $F(S) = n^* S^\alpha e^{-S}$. We have used the Chain Rule, the Fundamental Calculus Theorem in the second and third step and the in the last equality, we have undone the variable change.

$$\frac{\partial L}{\partial \alpha} = \int_{S_i}^{S_{max}} n^* S^{\alpha} e^{-S} \ln(S) dS$$

In this equation, we have used that the Leibniz's rule considering that the integrand, F and $\partial F/\partial \alpha$ are continuous in the integration range. We obtain that integral now, which can not be solved analytically. We can express it by changing variables

$$\begin{cases} u = ln(S) & du = 1/SdS \\ dv = S^{\alpha} e^{-S} dS & v = \gamma(\alpha+1, S_i) - \gamma(\alpha+1, S_{max}) \end{cases}$$

in the following form

$$\begin{aligned} \frac{\partial L}{\partial \alpha} &= \gamma(\alpha+1, S_i) - \gamma(\alpha+1, S_{max}) \Big[\ln(S) \Big] |_{S_i}^{S_{max}} - \\ & \int_{S_i}^{S_{max}} \Big[\gamma(\alpha+1, S_i) - \gamma(\alpha+1, S_{max}) \Big] / SdS = \\ & \gamma(\alpha+1, S_i) \Big[\ln(S) \Big] |_{S_i}^{S_{max}} - \int_{S_i}^{S_{max}} \gamma(\alpha+1, S_i)/SdS \end{aligned}$$

In order to solve the integral term of the last equation, we're going to use that the integrand is continuous in the measurable integration range, as the integration limits are always positive.

$$\begin{aligned} \int_{S_i}^{S_{max}} \gamma(\alpha+1, S_i)/SdS &= \int_{S_i}^{S_{max}} 1/S^{'} dS^{'} \int_{S_i}^{\infty} S^{\alpha} e^{-S} dS = \\ \int_{S_i}^{S_{max}} \int_{S_i}^{\infty} S^{\alpha-1} e^{-S} dSdS &= \int_{S_i}^{S_{max}} \gamma(\alpha, S_i) dS = (S_{max} - S_i)\gamma(\alpha, S_i) \end{aligned}$$

Finally the α-derivative has the following form

$$\begin{aligned} \frac{\partial L}{\partial \alpha} &= \gamma(\alpha+1, S_i)(\ln(S_{max}) - \ln(S_i)) - (S_{max} - S_i)\gamma(\alpha, S_i) = \\ & \gamma(\alpha+1, \frac{L_i}{L^*})(\ln(\frac{L_{max}}{L^*}) - \ln(\frac{L_i}{L^*}) - (\frac{L_{max} - L_i}{L^*})\gamma(\alpha, \frac{L_i}{L^*}) \end{aligned}$$

In Figures 7.11 and 7.12, the results of the cumulative Schechter Function are plotted for the NOT and ACS samples, respectively. The fit parameters are set in Tables 7.5 and 7.6. We have applied the decontamination of the background counts by interpolating the counts given by McLeod et al. (1995). Then, we have integrated that interpolation and we have subtracted to our accumulated counts.

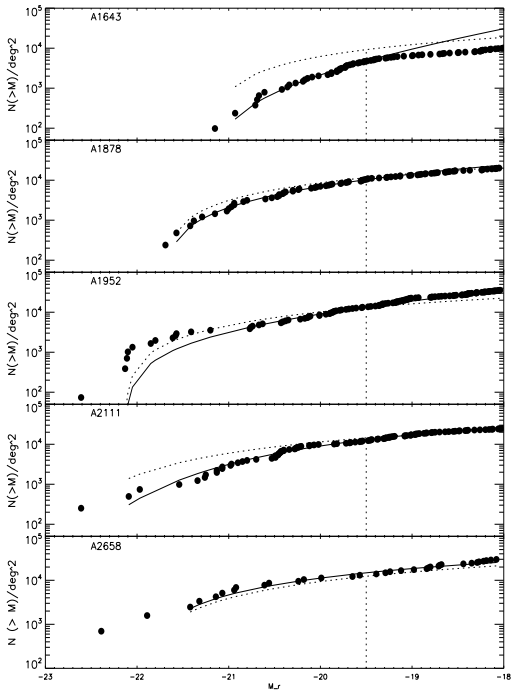

Figure 7.11: Best fit of the cumulative LF for the NOT sample. The vertical line shows the limit where the sample is complete.

Let's note that although the fits are good, the function 'has lost information' as any changes in the slope of the differential LF will be reflected in a much weaker variation in the slope of the cumulative LF. Mathematically, the integral of a continuous function is continuous but not inversely. That's the reason why nearly all the fits have an α parameter of -1 and the value of M* tends to achieve the extremes of the boundary extremes. We will have to take that results with caution.

7.3.3 Maximum Likelihood Method

The **Maximum Likelihood Method (MLM)**, (Sandage, Tammann & Yahil, 1979; Sarazin, 1980; Efstathiou, Ellis & Peterson, 1988), has a great advantage: it eliminates the bin dependence and in addition, the density parameter ϕ^* drops out as we're going to see in that section.

Consider a galaxy i observed at a redshift z_i, in a flux-limited survey. Let $m_{min,i}$ and $m_{max,i}$ denote the apparent magnitude limits of the field in which galaxy i is located. The probability that galaxy i has absolute magnitude M_i is given by

Table 7.5: Best Schechter Parameters of the Cumulative Luminosity Function for the NOT sample

	WithBCG			WithoutBCG		
Name	α	M*	χ^2	α	M*	χ^2
A 1643	-1.98	-20.61	1.25	-1.99	-20.95	1.54
A 1878	-1.01	-20.97	1.12	-1.27	-22.08	1.07
A 1952	-1.56	-22.50	3.80	-1.49	-22.50	6.39
A 2111	-1.01	-21.20	7.57	-1.01	-21.20	7.68
A 2658	-1.00	-22.50	0.51	-1.00	-22.50	1.35

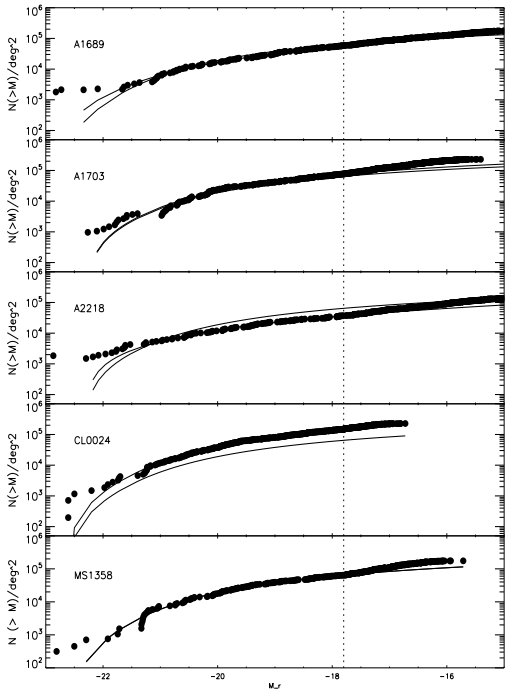

Figure 7.12: Best fit of the cumulative LF for the ACS sample. The vertical line shows the limit where the sample is complete.

Table 7.6: Best Schechter Parameters of the Cumulative Luminosity Function for the ACS sample

	WithBCG			WithoutBCG		
Name	α	M*	χ^2	α	M*	χ^2
A 1689	−1.25	−21.76	3.88	−1.25	−21.77	3.84
A 1703	−1.03	−20.98	21.01	−1.04	−21.04	20.80
A 2218	−1.14	−21.91	4.89	−1.16	−22.22	5.49
CL0024	−1.09	−21.07	5.40	−1.10	−21.08	12.83
MS1358	−1.00	−21.03	5.40	−1.00	−21.04	5.39

$$p_i = p(M_i|z_i) = \phi(M_i) / \int_{M_{min}(z_i)}^{M_{max}(z_i)} \phi(M) dM$$

In cluster of galaxies, the z_i is considered to be the same of the cluster and $M_{min}(z_i)$ and $M_{max}(z_i)$ fixed.

The likelihood function L of a set of N galaxies, with respective absolute magnitudes M_i are the product of the probabilities p_i

$$L = p(M_1, ..., M_N|z_1, ..., z_N) = \prod_{i=1}^{N} p_i$$

If we apply logarithms, we can express it in the following form:

$$\ln L = \sum_{i=1}^{N} \left[\ln \phi(M_i) - \ln \int_{M_{min}(z_i)}^{M_{max}(z_i)} \phi(M) dM \right]$$

Let's note that for clusters of galaxies, the redshift can be considered as constant, so the likelihood can be expressed as

$$\ln L = \sum_{i=1}^{N} \left[\ln \phi(M_i) \right] - (N-1) \ln \int_{M_{min}}^{M_{max}} \phi(M) dM$$

The method consist on assuming a parametric model for $\phi(M)$ and obtaining the parameters of $\phi(M)$ by maximizing the likelihood L (or $\ln L$) with respect to those parameters. Sandage, Tammann & Yahil (1979) described the so called **STY method** by fitting the Schechter function (equation 7.3) with the Likelihood method. Let's note that this method does not need to bin the data. On the contrary it takes information of each galaxy magnitude. Another convenience of this method is that the normalization ϕ^* drops out in equation 7.3.3

reducing the parameter space to two. It can be determined by

$$\phi^* = \frac{\bar{\rho}}{\int_{M_{min}}^{M_{max}} \phi'(M) dM}$$

where $\phi^{'}$ is the Schechter function with ϕ^* set to 1 and $\bar{\rho}$ is the mean galaxy density.

Also, error ellipses in the $M^* - \alpha$ plane may be drawn by finding the contour corresponding to

$$\ln L = \ln L_{max} - 1/2\Delta\chi^2$$

where $\Delta\chi^2$ is the change in χ^2 appropriate for the desired confidence level and a χ^2 distribution with 2 degrees of freedom.

As many authors have already noted (Press et al., 1992; Andreon, 2004; Popesso et al., 2004; Andreon, Punzi & Grado, 2005), it is necessary to use a robust minimizator as the desired global maximum may be often found hidden among many, poorer, local maxima in high dimensional spaces or in flat 'valleys'.

We have tried different methods for maximizing (or minimizing) the likelihood function: the *Downhill Simplex Minimization Method*, Nelder & Mead (1965); the *Powell Minimization Method*, Acton (1970); the *Davidson-Fletcher-Powell* and the *Truncated Newton Method* (see Press et al. (1992)). We're going to describe the strategy of each methods, underlying the main advantages for our minimization method.

Downhill Simplex Minimization Method

The method must be started with a non-degenerate *simplex*, that is a geometrical figure consisting in N dimensions, of $N + 1$ vertices which encloses a finite inner $N-$dimensional volume. Then, the method takes a series of steps or 'reflections', moving the point of the simplex where the function is the largest (highest point) through the opposite face of the simplex to a lower point. Thus, the simplex is expanded in one or another direction to take larger steps. When it reaches a 'valley floor', the simplex contracts itself in the transverse direction and tries to ooze down the valley. The algorithm finish when the vector distance moved in that step is fractionally smaller in magnitude than some tolerance. That method requires only function evaluations, not derivatives. However, it is not very efficient in terms of the number of function evaluations that it requires.

Powell Minimization Method

This method is a variation of a direction set method: Given as input the vector P (a set of directions, for example, the unit vectors) and n, the set of variables of the function f, we will find an scalar λ that minimizes $f(P + \lambda n)$. By replacing P by $P + \lambda n$ and n by λn, we will obtain a first direction to its minimum, then from there along the second direction to its minimum, and so on, cycling through

the whole set of directions as many times as necessary, until the function stops decreasing.

Powell was the first who discovered a direction set method that does produce N mutually conjugate directions (or 'non interfering' directions). Powell's quadratically convergent algorithm has an inconvenient: the procedure sets of directions may become linearly dependent. If this happens, then the procedure finds the minimum of the function f only over a subspace of the full N-dimensional case. Therefore, the algorithm we have used, Press et al. (1992), tried to find a few good directions along narrow valleys instead of N necessarily conjugate directions. For a valley whose long direction is twisting slowly, this direction is likely to give us a good run along the new long direction. The change is to discard the old direction along which the function f made its largest decrease.

Davidson-Fletcher-Powell Method

That algorithm belong to the so called, *variable metric* or *quasi-Newton* methods. The variable metric methods differ from the conjugate gradient ones in the way that it stores and updates the information that is accumulated. The former requires a matrix of size $N \times N$ while the later only need intermediate storage on the order of N.

Given an arbitrary function $f(x)$, it can be locally approximated by the quadratic form of equation.

$$f(x) \approx c - bx + \frac{1}{2}xAx$$

The variable metric methods build up, iteratively a good approximation to the inverse Hessian matrix A^{-1}, that is, to construct a sequence of matrices H_i with the property,

$$\lim_{i \to \infty} H_i = A^{-1}$$

Those methods are sometimes called *quasi-Newton* methods. Let's consider finding a minimum to search for a zero of the gradient of the function by using Newton's method . Near the current point x_i, we have the second order

$$f(x) = f(x_i) + (x - x_i)\nabla f(x_i) + \frac{1}{2}(x - x_i)A(x - x_i)$$

which can be expressed as

$$\nabla f(x) = \nabla f(x_i) + A(x - x_i)$$

In Newton's method, we set $\nabla f(x) = 0$ to determine the next iteration point:

Table 7.7: Best Schechter Parameters of the Luminosity Function using the Maximum Likelihood method with $\alpha = -1.15$ for the NOT sample

Name	M*	χ^2
A 1643	-19.64	47.42
A 1878	-21.12	47.19
A 1952	-21.75	42.32
A 2111	-21.25	49.63
A 2658	-21.86	17.11

$$x - x_i = -A^{-1}\nabla f(x_i)$$

And we have that the left-hand term is the finite step needed for getting to the exact minimum and the right-hand term is known once we have computed an accurate $H \approx A^{-1}$. The word 'quasi' is referred to the fact that we do not use the actual Hessian matrix of f, but instead we use an approximation, which allows the matrix to be a positive definite, symmetric hessian matrix.

From those methods, we have obtained the best results from the third method, which also is implemented in a CERN routine called MINUIT 94.1 (James & Roos (1975)). MINUIT allows the user to set the initial value, the resolution, and the upper and lower limits of any parameter in the function to be minimized. Values of one or more parameters can be kept fixed during a run. MINUIT can use several strategies to perform the minimization. Our choice is MIGRAD, Fletchter (1970), a stable variation of the *Davidon-Fletcher-Powell* variable metric algorithm for the convergence at the minimum, and the MINOS routine to estimate the error parameters in case of non-linearities. We also have placed constraints on the values of M^* and α that the fitting routine can accept, to avoid being trapped in a false minimum (M^* in the range between -18 and -22 mag and α between 0 and -2.5, (Lumsden et al., 1997; Popesso et al., 2004)).

The problem with that method is the Gamma Function, $\Gamma(\alpha)$ is undefined for constant values of α. Therefore, the fit tends to converge to those false minima. Therefore, we have decided to perform the fit of Luminosity Function using the Maximum Likelihood with a fixed $\alpha = -1.15$ for both samples. In Table 7.7 and 7.8, we have set the results of the fit.

As we see, the slope at the faint end, fixing $\alpha = -1.15$, M^* varies between $-21.$ to -21.75, with the exception of A1643, that we have previously seen that its shape does not correspond with the usual LF of a typical cluster. We see also some differences of that fit, with the LM fit with α fixed, the values obtained for M^* here are fainter than those obtained by LM, in particular for three clusters, A2658, A1689 and MS1358. Moreover, the dispersion in the M^* is much smaller than the obtained with that method.

Table 7.8: Best Schechter Parameters of the Luminosity Function using the Maximum Likelihood method with $\alpha = -1.15$ for the ACS sample

Name	M*	χ^2
A 1689	−21.26	55.39
A 1703	−21.25	86.96
A 2218	−21.99	52.13
CL0024	−21.09	125.85
MS1358	−21.21	62.97

After considering the advantages and drawbacks for each method, we conclude that the best fits for the whole ten clusters are provided by the Composite Luminosity Function. However, the fits provided by the ACS sample are good enough to be considered alone with the χ^2 method. Then, we will refer to this fits.

7.4 Luminosity - Morphology relation

We have studied the Luminosity function by separating them into different morphological types. In Figures 7.13 and 7.14, the luminosity distribution for early and late type galaxy population are shown for NOT sample, while in Figures 7.15 and 7.16 the corresponding distributions for the ACS sample are displayed.

Even if we have few galaxies to find a reliable fit for the luminosity function, we are able to distinguish some trends. For example, we note a nearly constant trend of the early type galaxy population for nearly all clusters, with the exception of A2111 and A1689, where we find a larger number of faint early type galaxies than bright. As far as the late type population is concerned, note an ascending tendency in a great proportion of clusters, finding a larger number of galaxies at fainter magnitudes. However, that tendency seems to be the opposite in A1878, A2111 and MS1358.

However, as we saw in the last section that the whole population in clusters with few area coverage and restrictions in magnitude is much better described by the Composite Luminosity Function. We have computed the Composite Luminosity Function for early types (Figures 7.17, and 7.19) and for late types (7.18 and 7.20) for the NOT and ACS sample respectively. The values given by the Schechter fit are collected in Tables 7.9 and 7.10.

As we see, the fits are not good for the NOT sample. That fact can be due to a large errors in the binning points or for the incapacity of fitting the morphological population with a Schechter function. In the ACS sample, however, we obtain a reliable better fit for both populations. The slope values we find are

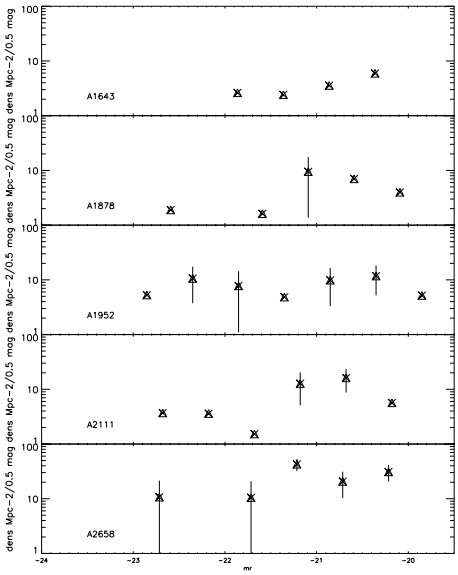

Figure 7.13: LF for Early Type galaxies NOT sample clusters

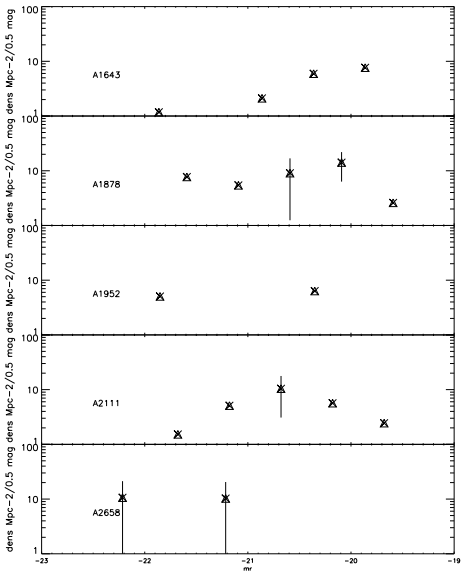

Figure 7.14: LF for Late Type galaxies NOT sample clusters

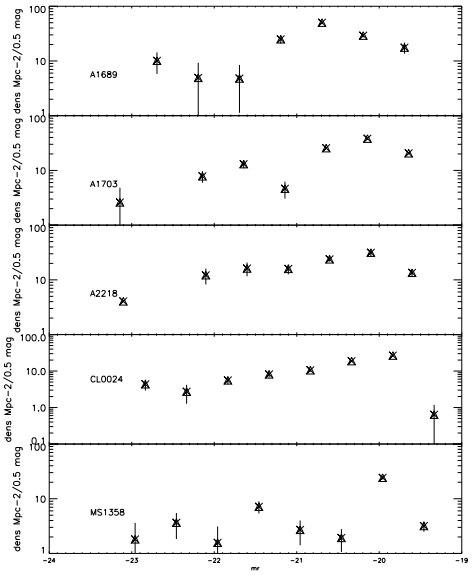

Figure 7.15: LF for Early Type galaxies in ACS sample clusters.

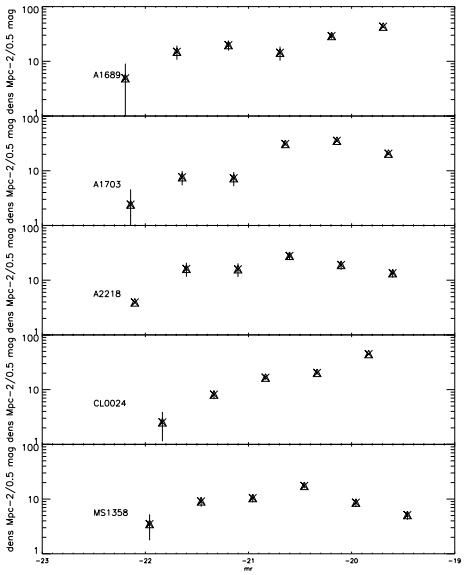

Figure 7.16: LF for Late Type galaxies in ACS sample clusters.

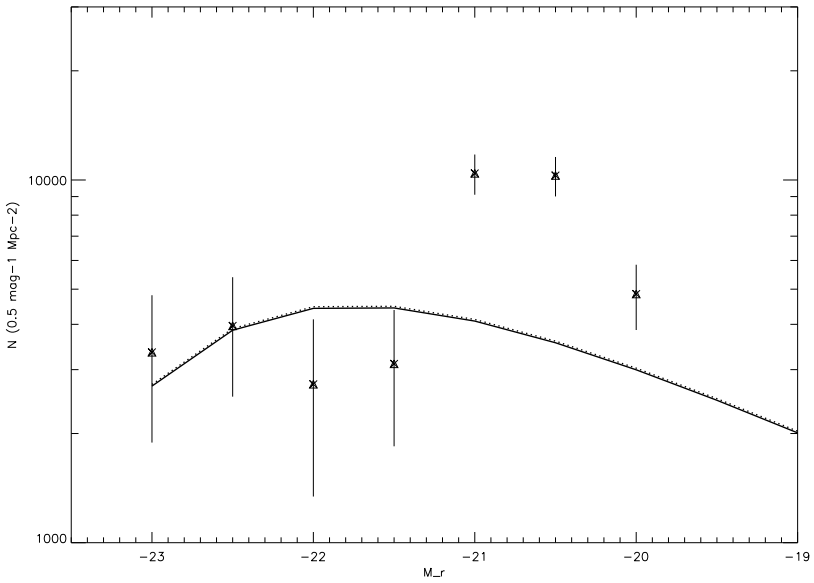

Figure 7.17: Composite LF for Early Type galaxies in NOT sample.

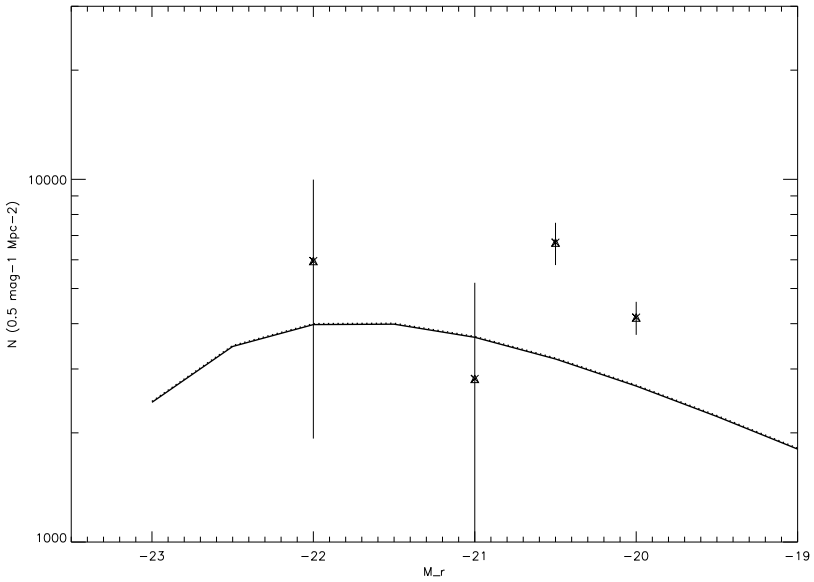

Figure 7.18: Composite LF for Late Type galaxies in NOT sample.

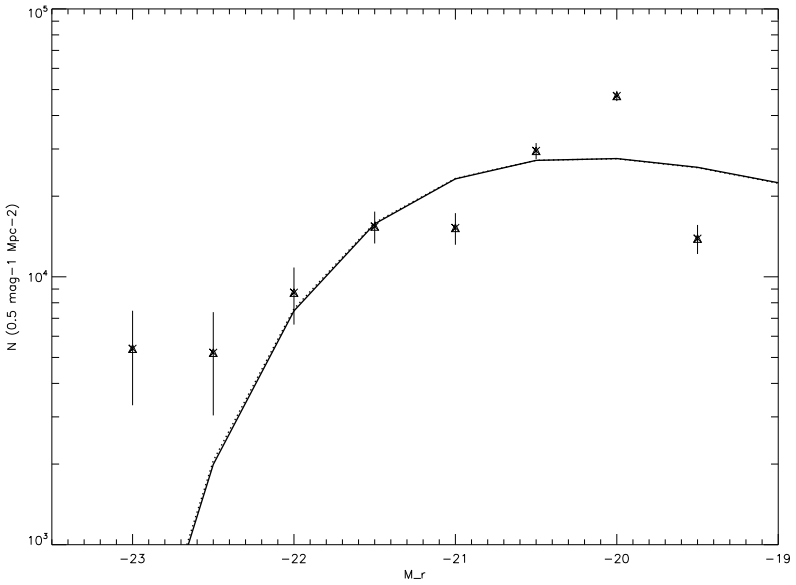

Figure 7.19: Composite LF for Early Type galaxies in ACS sample.

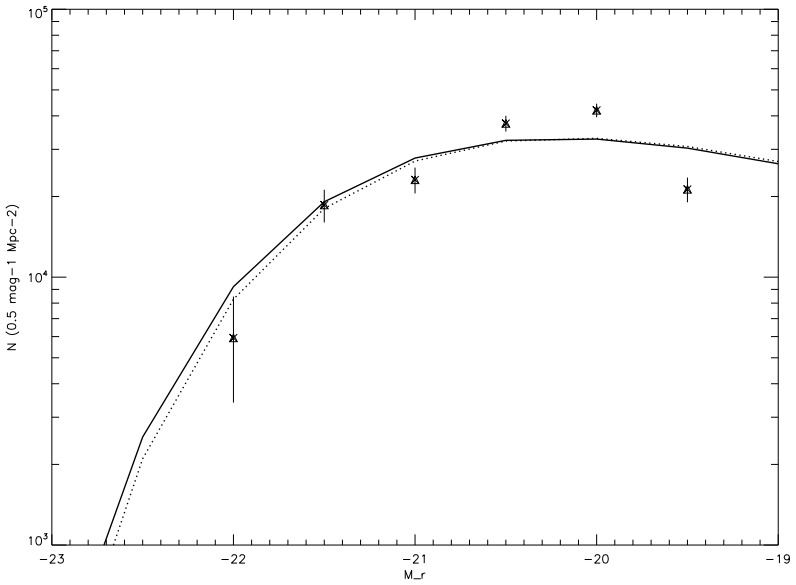

Figure 7.20: Composite LF for Late Type galaxies in ACS sample.

Table 7.9: Best Schechter Parameters of the Cumulative Luminosity Function for Early and Late Types for the NOT sample

	WithBCG			WithoutBCG		
Name	α	M*	χ^2	α	M*	χ^2
Early	-0.50	-22.50	13.89	-0.50	-22.50	12.18
Late				-0.50	-22.50	14.36

Table 7.10: Best Schechter Parameters of the Cumulative Luminosity Function for Early and Late Types for the ACS sample

	WithBCG			WithoutBCG		
Name	α	M*	χ^2	α	M*	χ^2
Early	-0.50	-20.95	20.27	-0.50	-20.94	22.28
Late				-0.50	-20.96	7.54

$\alpha = -0.5$ in all cases, while the mean value of M^* is -20.95 for the ACS sample. At the view of that results, we can conclude that the bright ($M_r \leq -20$) luminosity function depending on the morphological types is not well defined by a Schechter Function.

7.5 Luminosity - Color relation

The Luminosity Function for different colors galaxy population are shown in Figures 7.21, 7.22 for the red and blue galaxy population in NOT sample clusters and in Figures 7.23 and 7.24 for the ACS sample clusters.

As in the previous section, we have computed the Composite Luminosity Function for red and blue galaxy population (Figures 7.25 and 7.26) for the NOT sample, while the results for the red and blue galaxy population for the ACS sample is set in Figures 7.27 and 7.28. The results of the fit are collected in Tables 7.11 and 7.12 respectively.

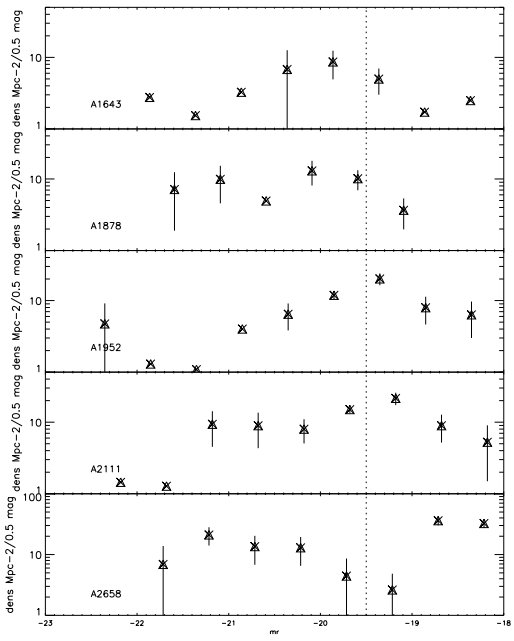

Figure 7.21: LF for Red galaxies NOT sample clusters

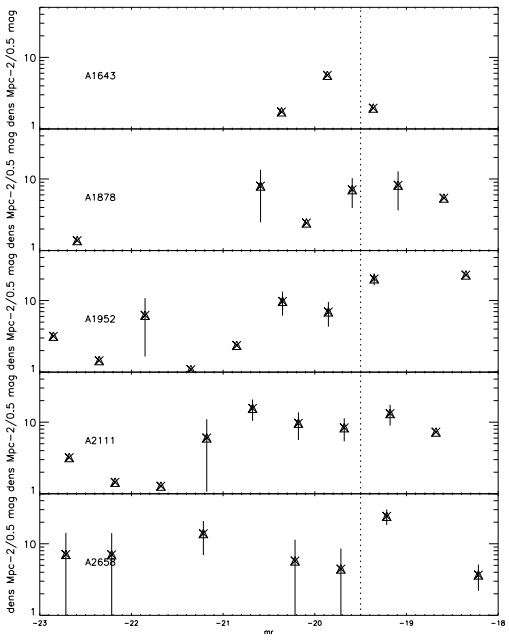

Figure 7.22: LF for Blue galaxies NOT sample clusters

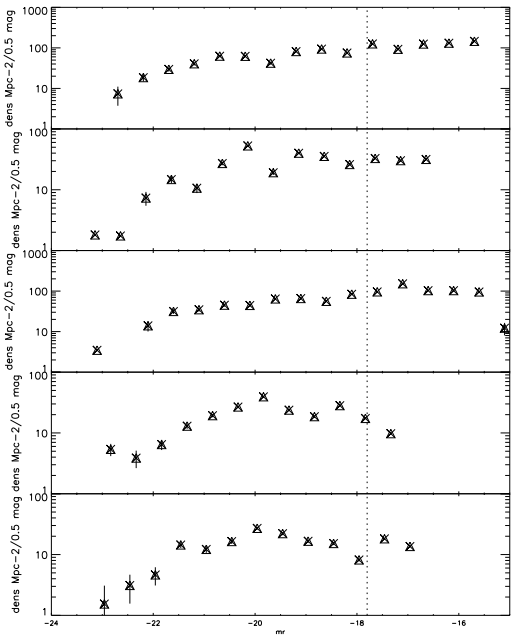

Figure 7.23: LF for Red galaxies ACS sample clusters

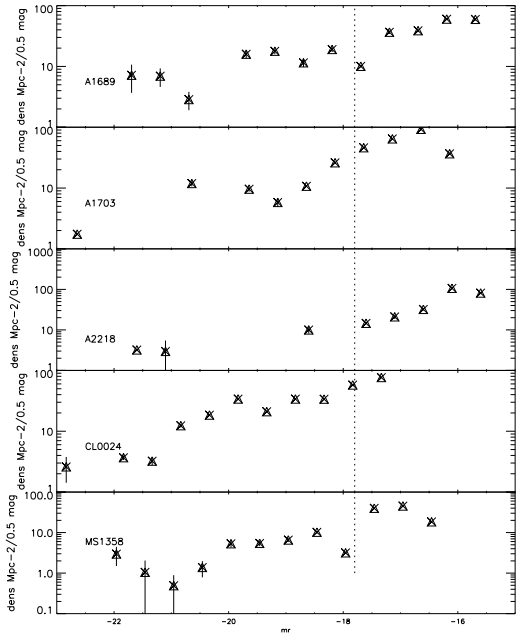

Figure 7.24: LF for Blue galaxies ACS sample clusters

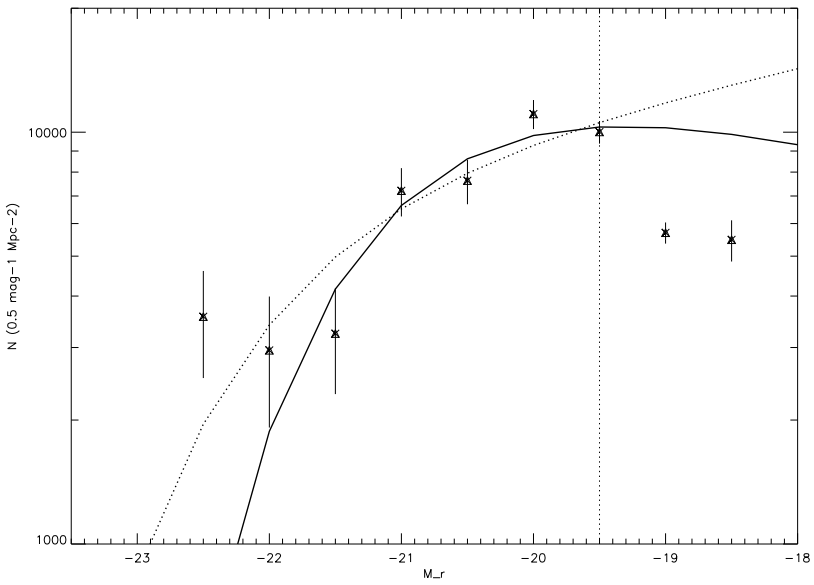

Figure 7.25: Composite LF for Red galaxies in NOT sample.

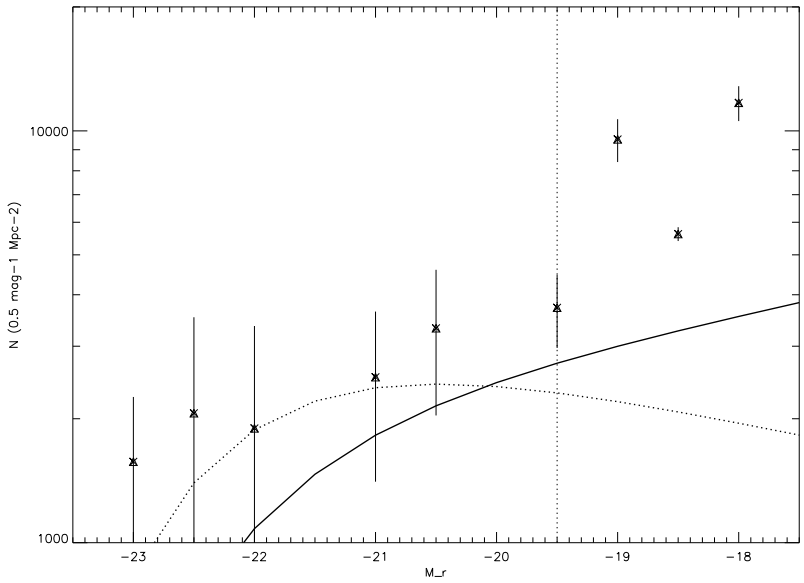

Figure 7.26: Composite LF for Blue galaxies in NOT sample.

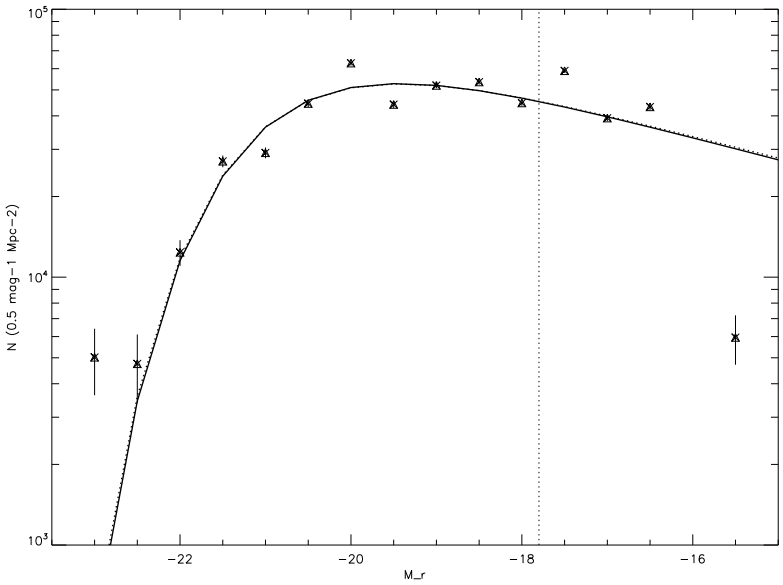

Figure 7.27: Composite LF for Red galaxies in ACS sample.

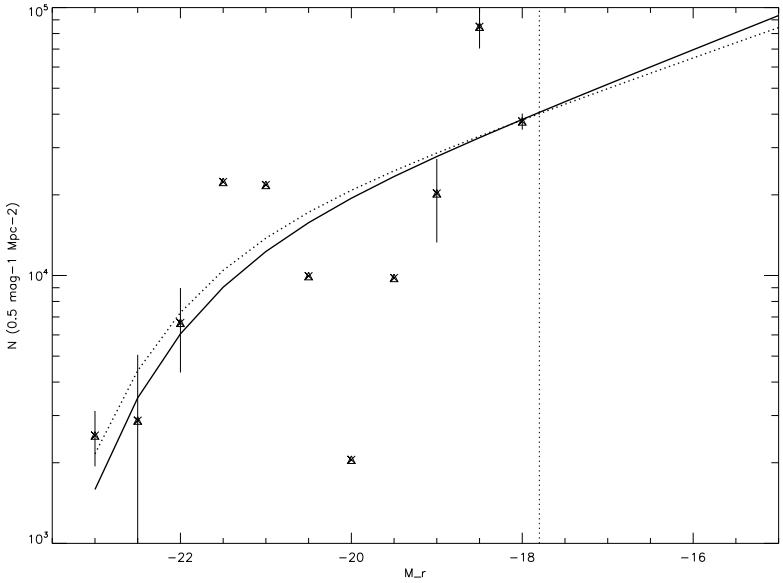

Figure 7.28: Composite LF for Blue galaxies in ACS sample.

Table 7.11: Best Schechter Parameters of the Cumulative Luminosity Function for Red and Blue Galaxies for the NOT sample

	WithBCG			WithoutBCG		
Name	α	M*	χ^2	α	M*	χ^2
Red	-1.17	-22.23	1.62	-0.80	-21.05	0.94
Blue	-1.16	-22.50	2.27	-0.84	-22.50	2.24

Table 7.12: Best Schechter Parameters of the Cumulative Luminosity Function for Red and Blue Galaxies for the ACS sample

	WithBCG			WithoutBCG		
Name	α	M*	χ^2	α	M*	χ^2
Red	-0.79	-21.13	17.64	-0.79	-21.15	16.99
Blue	-1.32	-22.40	1.53	-1.28	-22.50	1.47

As we see the values given for the red population in both samples have a much flatter slope than the blue galaxy population, for which, we obtain a much steeper luminosity function and a much fainter value of M^* for the blue galaxy population. Those results are in agreement with the results found in Barkhouse, Yee & López-Cruz (2007), where they find, by fixing $\alpha = -1$, a value of $M^* = -22.28$.

7.6 Universality

A central subject in the early studies (Hubble, 1936; Abell, 1962; Oemler, 1974), of the galaxy cluster LF has been to determine whether the LF is universal in shape. Schechter (1976) suggested that the cluster LF is universal in shape and can be characterized with a turnover of $M_B^* = -20.6 + 5\log h_{50}$ and a faint-end slope of $\alpha = -1.25$.

Further support for a universal LF has been provided by several studies such as (Lugger, 1986; Colless, 1989; Gaidos, 1997; Yagi et al., 2002; De Propris et al., 2003). For example, Dressler (1978); Lugger (1986); Colless (1989) studied samples of several clusters concluding that, with the good agreement of the parameters.

In contrast, a number of studies have also discussed that the shape of the cluster LF is not universal (see (Godwin & Peach, 1977; Dressler, 1978; Binggeli, Sandage & Tammann, 1988; Piranomonte, 2001; Hansen et al., 2005; Popesso et al., 2006; Barkhouse, Yee & López-Cruz, 2007)). Some of them have argued

that the results found by Dressler (1978) did not consider a consistent cluster radius or limiting absolute magnitude in comparing different clusters.

However, as many authors have showed (Binggeli, Sandage & Tammann (1988); Varela (2004); Barkhouse, Yee & López-Cruz (2007)), the luminosity function is different for different morphological types, so it seems evident that it can not be Universal. However, many authors claim about the universality of the luminosity function for different morphological types.

Part III

The Brightest Cluster Galaxies

Chapter 8

The Brightest Cluster Galaxies: BCGs

Avanza envuelta en belleza,
como la noche de regiones sin nubes y cielos estrellados;
y todo lo mejor de lo oscuro y lo brillante,
se une en su rostro y en sus ojos...

Ray Bradbury, 'Crónicas Marcianas.'

The **Brightest Cluster Galaxies (BCG)** are giant elliptical galaxies near the spatial and gravitational centre of a galaxy cluster. They are the brightest and most massive stellar systems in the Universe. BCGs are found very close to the centre of the clusters of galaxies determined from X-ray observations or gravitational lensing observations (Jones & Forman, 1984; Smith et al., 2005).

Those objects possess a number of singular properties. Their luminosities are remarkably homogenous, as noticed first by Humason, Mayall & Sandage (1956). A number of works (Sandage, 1972a; Gunn & Oke, 1975; Hoessel & Schneider, 1985; Postman & Lauer, 1995), verified their high luminosities and small scatter in absolute magnitude and consequently, were devoted to the establishment of those objects as 'standard candles' with which to measure cosmological distances. In fact, they were originally used to increase the range of Hubble's redshift - distance law ((Sandage, 1972a,c)).

Furthermore, there are numerous pieces of evidence, (see for example, Tremaine & Richstone (1997)), that show that BCGs are not extracted from the same luminosity distribution as the Schechter luminosity function of normal galaxies (Schechter (1976)) and that they are not statistical fluctuations in the luminosity function.

Diverse theories have been promoted to explain the formation and singular features: the accumulation of tidal stripped debris from cluster galaxies (Ostriker

& Tremaine, 1975; McGlynn & Ostriker, 1980; Malamuth & Richstone, 1984; Merritt, 1985), rapid merging in the collapse of the cluster core, galactic 'cannibalism' of giant galaxies spiraling into the center of the cluster under the influence of dynamical friction, or the creation by the X-ray emission-driven cooling flows of gas, Fabian, Nulsen & Canizares (1982).

However, there is considerable observational evidence that suggest giant ellipticals were formed at high redshift, and have been passively evolving to the present day (Bower, Lucey & Ellis, 1992a; Aragón-Salamanca et al., 1993; Stanford, Eisenhardt & Dickinson, 1998; van Dokkum et al., 1998). Passive evolution describes a situation where the stellar population in a galaxy formed in a single burst at a redshift z_f. This population then matures, without further star formation.

The latest hierarchical simulations of BCG formation De Lucia & Blaizot (2007), predict that the stellar components of BCGs are formed very early (50% at $z \sim 5$ and 80 % at $z \sim 3$). This star formation occurs in separate subcomponents which then accrete to form the BCG through 'dry' mergers. It is important to note that in these simulations local BCGs are not directly descended form high-z ($z>0.7$) BCGs. However, De Lucia & Blaizot (2007) find little physical difference between the progenitors of local BCGs and high-z BCGs or between the local BCGs and the descendants of the high-z BCGs. This means that observed evolution presented here can still be compared to simulation.

Also, in the halo of cD galaxies, we can find large numbers of Globular Clusters, that can provide diagnostics of the cD formation process, assuming that the total luminosities and masses of the cannibalized galaxies should be printed in their metallicities, (Brodie & Huchra, 1991; Jordán et a., 2004).

Some BCGs show an excess of light or usually called envelopes, over the de Vaucouleur ($r^{1/4}$) profile at large radii (Matthews, Morgan & Schmidt, 1964; Oemler, 1973, 1976; Schombert, 1986, 1987, 1988; Graham et al., 1996). Therefore, a large fraction of these BCGs are termed as cD galaxies (Jordán et a. (2004); Patel et al. (2006)). Although the origin of such extended envelopes is still not completely clear, Patel et al. (2006), the extended stellar haloes of BCGs to surface brightness are likely from BCGs themselves: the intra-cluster light has much lower surface brightenss and only dominates at large radius, (Zibetti et al., 2005; Bernardi et al., 2007; Lauer et al., 2007)

The study of the Brightest Galaxy Clusters (BCGs) for the NOT and ACS samples have been faced. Those BCGs were extracted from the cluster potential by developing an algorithm capable to extract the halo by means of an iterative process and a refinement of the masks located in the galaxy halo, Ascaso et al. (2008c). We have studied the nature of cD galaxy of these BCGs and also try to confirm the studies which consider the BCGs as standard candles for performing cosmological studies of the evolution in the Universe.

Table 8.1: BCGs in NOT Clusters

Name	$\alpha(2000)$			$\delta(2000)$			z	m_r	M_r	$B-r$	T
A 1643	12	55	54	+44	05	12		17.91	−21.61	2.06	$S0$
A 1878	14	12	52	+29	14	28	0.222	17.39	−22.36	2.30	E
A 1952	14	41	03	+28	37	00		17.37	−22.61	2.10	E
A 2111	15	39	40	+34	25	27	0.2282	17.16	−22.67	2.18	E
A 2658	23	44	49	−12	17	39		16.99	−22.39	2.01	E

Table 8.2: BCGs in ACS Clusters

Name	$\alpha(2000)$			$\delta(2000)$			z	m_r	M_r	$g-r$	T
A 1689	13	11	29	−01	20	27	0.1828	16.87	−22.75	1.348	E
A 1703	13	15	05	+51	49	03	0.2836	17.34	−23.09	1.643	E
A 2218	16	35	49	+66	12	44	0.1800	16.72	−22.79	1.207	E
CL0024	00	26	35	+17	09	43	0.3871	18.87	−22.57	1.931	E
MS1358	13	59	50	+62	31	05	0.3270	18.29	−22.13	1.707	E

8.1 BCGs population

The BCGs in NOT and ACS sample are shown in Figures 8.1 and 8.2. At examining the frames we can see that all the BCGs sample have an extended halo, surrounded by small galaxies. In Tables 8.1 and 8.2, their main characteristics are collected. The first four columns give the name of the cluster, the coordenates of the BCG and the redshift, if available. The fifth and sixth column also shows the apparent and absolute r magnitude. The next column refers to the inner color (B-r for the NOT sample and g-r for the ACS sample) and finally, the morphological type is listed in the last column.

We can observe an homogeneous range of properties in the BCGs sample. All the galaxies are very bright elliptical red galaxies, with the exception A1643, where it is a lenticular galaxy. Some of them have also a visible halo, and they look like cD galaxies (A1952 or A2658 in NOT sample and all the BCGs in ACS sample).

In some of them, especially in the ACS sample, with better resolution, we can distinguish small globular clusters in the halo. And, in any case, they are surrounded by a number of small gravitational attracted number of galaxies.

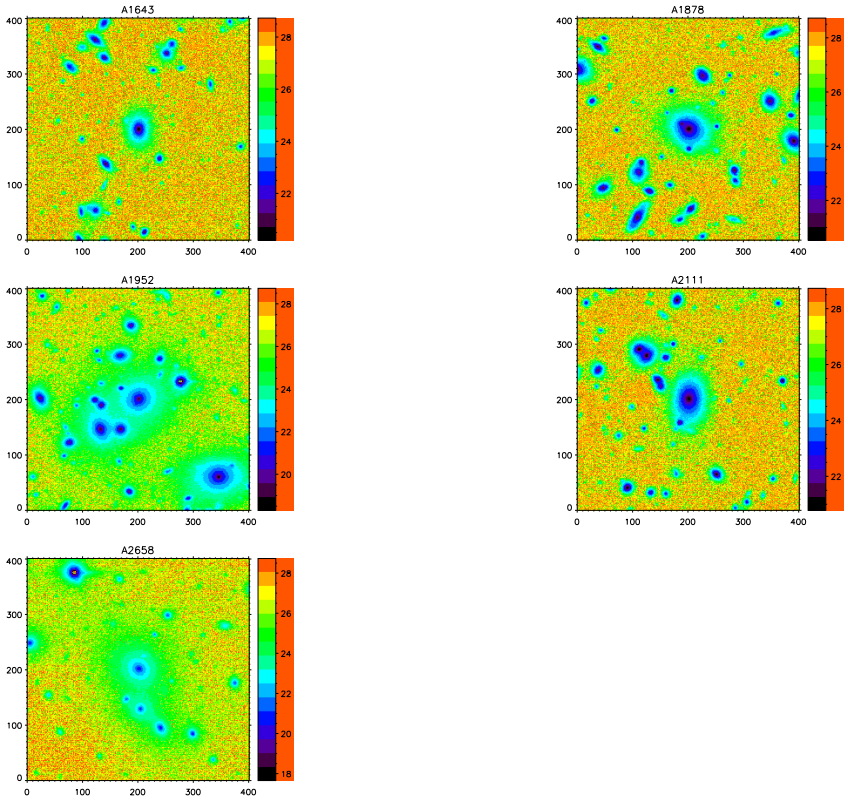

Figure 8.1: BCGs population in NOT sample

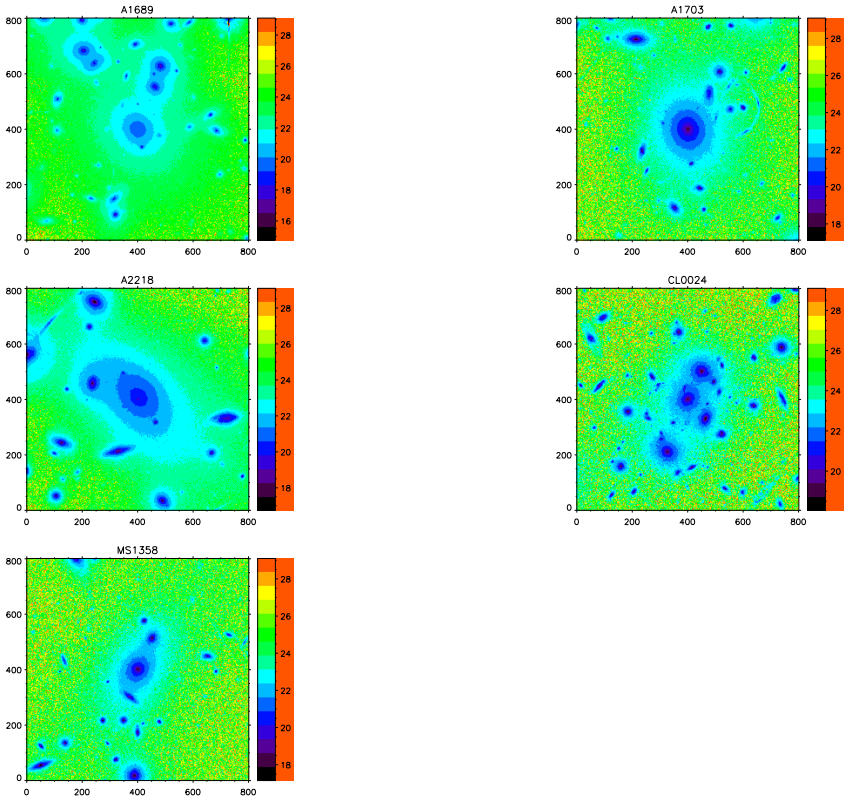

Figure 8.2: BCGs population in ACS sample

8.2 Extraction Algorithm

Background Subtraction Method

One of the most difficult subjects in studying the BCGs is to extract the cD galaxy from the galaxy cluster, as their halos extends much further than the elliptical galaxies. In many clusters, the halo of the cD extends nearly to the Abell Radius. As an illustration, we have shown in Figure 8.3, two frames from our sample (A1952 from the NOT sample and A1689 from the ACS sample), with a previous smooth of the light to make clear the extend of the light.

Therefore, we have investigated in the following questions: How to subtract it without changing the cluster properties? And without changing the light profiles of the rest of the galaxies? That matter is still not solved although many attempts have been carried out, (Patel et al., 2006; Seigar, Graham & Jerjen, 2007). We have built a procedure which achieves good results, (Ascaso et al., 2008c).

The initial idea consisted on masking all the galaxies in the frame except the BCG with SExtractor in order to avoid adding light from the sources to the BCG. Then, we fit a model to the cD galaxy with the IRAF tasks ELLIPSE and BMODEL. We subtract then the model to the BCG and estimate the background in that image with SExtractor, subtracting it from the original image. That last step was thought in order to subtract part of the light of the halo at subtracting the background. We then iterate that procedure and finally we obtained the model of the BCG and the rest of the galaxies without the BCG. In order to illustrate the difficulty of that process, we have set in Figure 8.4, two inadequate subtractions of one of our clusters, A1689. The upper panel shows an underestimation of the light of the halo, while the bottom panel is an overestimation fo the cD halo light.

After examining that results, we realized that spurious 'arcs' or 'black areas' were due to an inexact masking of the objects in the halo of the cD for the case of the underestimation, so we used an IRAF routine[1], which allows to mask any objects in the image by specifying the exact shape of the mask, (e.g. a circle, ellipse, rectangle, etc).

Regarding to the second case, the overestimation of the light, we performed different tests and the results were that the SExtractor parameter BACK_SIZE was crucial for the estimation of the background and the subtraction of the right level of light, as it has been already noticed by some authors, (e.g., Patel et al. (2006)). We chose then the value of BACK_SIZE as the area corresponding to the measure of the largest galaxy with enough ($\geq 50\,\%$) surrounding background to be estimated taking apart the BCG.

After applying such correction, we achieved good results as it is illustrated in Figure D.1 for the last example, A1689. In that plot, we have shown the original

[1]This referred IRAF routine was kindly provided by Jesús Varela

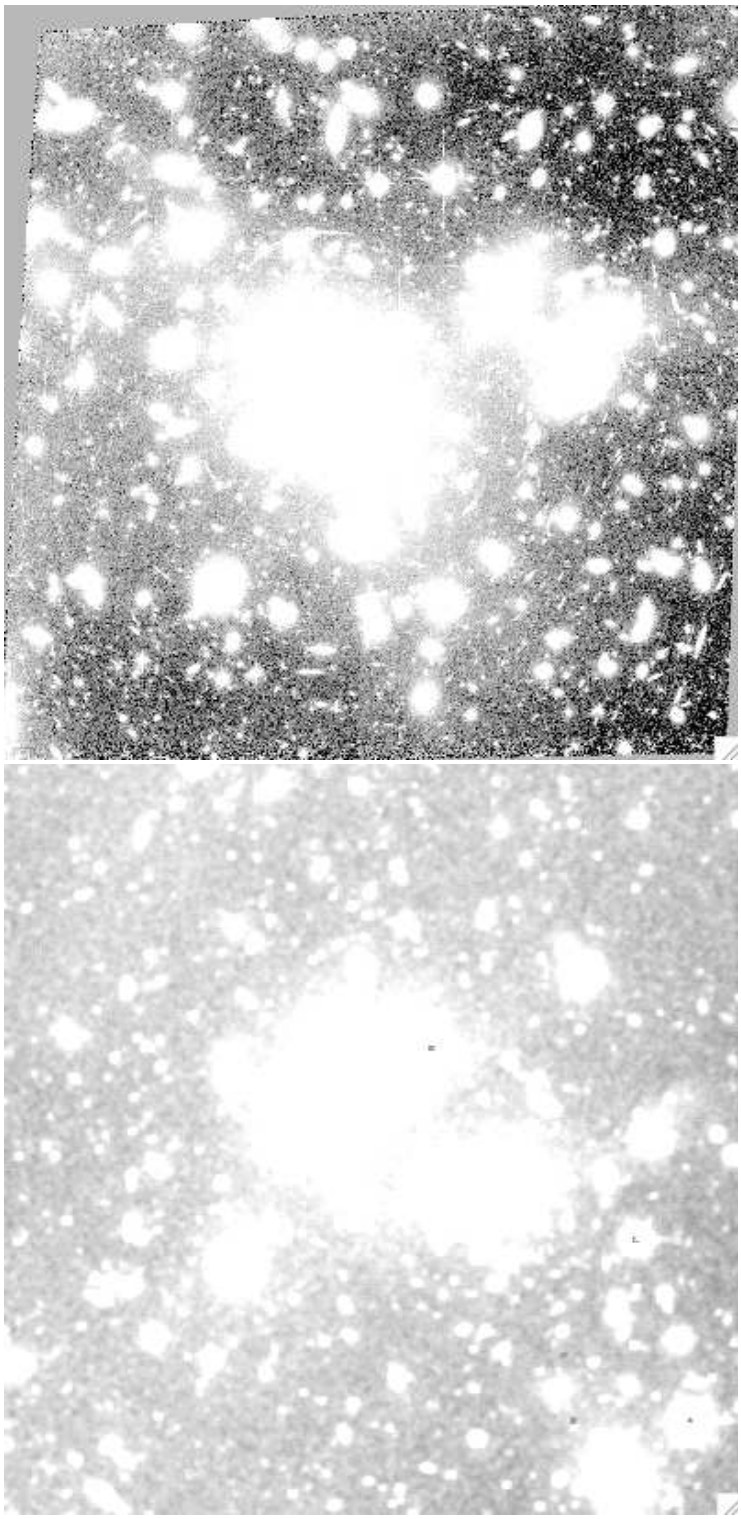

Figure 8.3: A1689 (ACS) and A1952 (NOT) smoothed images

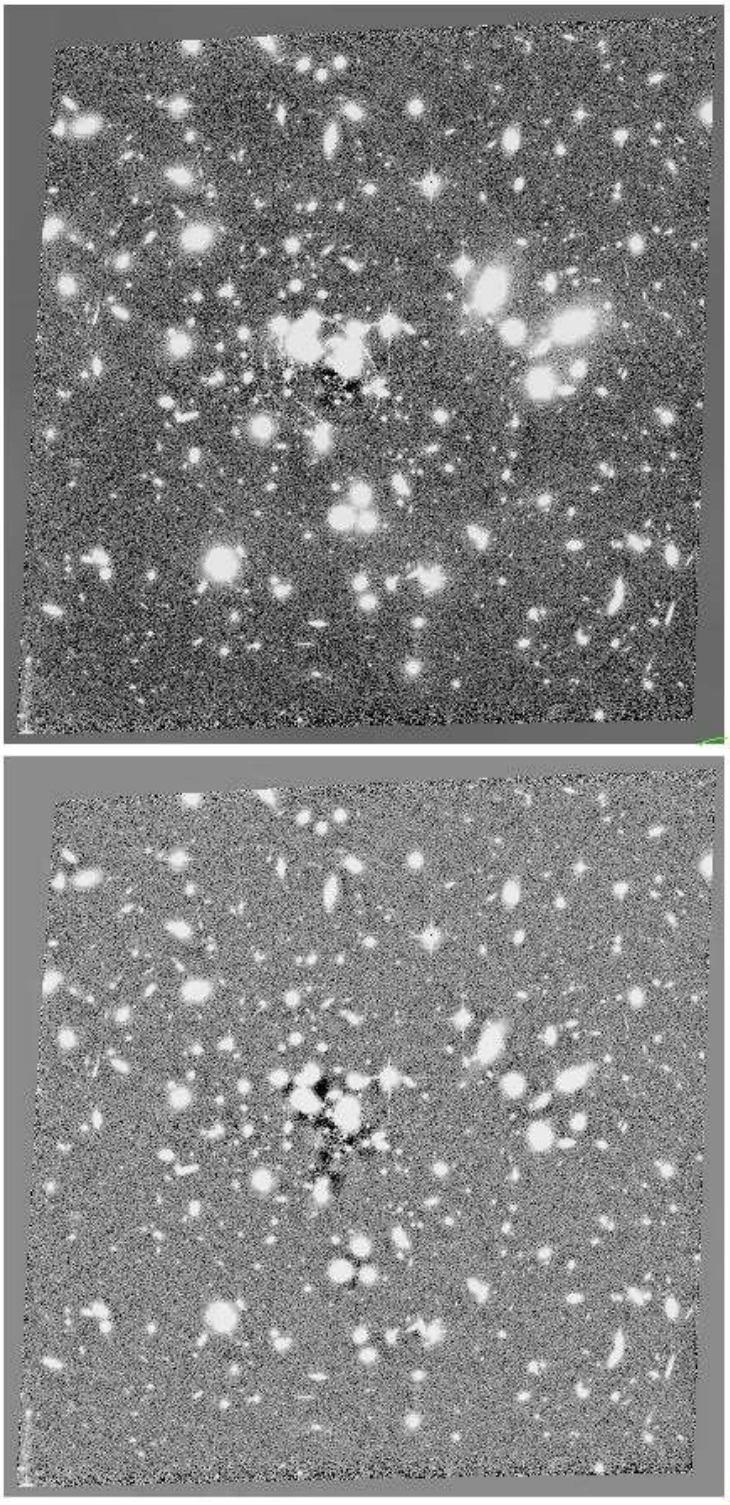

Figure 8.4: A1689 BCGs inadequate subtractions. More details in the text.

cluster in the upper panel, together with the 'right' subtraction of the BCG after the refinements. As we can see, the results are now excellent.

The rest of BCGs in the clusters belonging to both samples has been extracted also with excellent results. The resultant images are collected in the Appendix sections C and D.

8.3 Analysis

8.3.1 Degree of Dominance

The **Degree of Dominance,** Δm is the quantification of the bright dominance of the cD galaxy respect the rest of the galaxies in the cluster. The definition is given by Kim et al. (2002), as the magnitude difference between the BCG magnitude (m_1) and the average magnitude of the second (m_2) and third (m_3) brightest member. That is:

$$\Delta m = (m_2 + m_3)/2 - m_1$$

The second and third brightest galaxies are selected as the next two brightest galaxies on the cluster red sequence within a radius of 500 kpc of the BCG. Taking the average of the second and third ranked galaxies is slightly more robust to contamination than just using the second. It also removes the weighting from cases where there are two BCG candidates that are far more luminous than the rest of the cluster, as for example in the case of A2218, that has two main bright galaxies.

Some studies in the literature (Kim et al., 2002; Jordán et a., 2004; Stott et al., 2008) have used it to study the degree of alignment of the more dominant BCGs with the host cluster and extract therefore conclusions about the BCG and cluster formation. In this work, we only mapped the central region of the clusters, so in this work we have not been able to correlate it with extended properties of the cluster.

In Tables 8.3 and 8.4, we have set the values for the Degree of Dominance in each cluster for the NOT and ACS sample respectively. In the third column, we have also set the difference between the first and second member, (that we have called Δm_2). We have set a mark in the cluster A2658 as its maximum aperture is 420 kpc. Therefore, that aperture is very close to 500 kpc, so we will set this value in the analysis although we will take that fact on mind.

In Figure 8.6, we have compared the Degree of Dominance obtained for our sample with the absolute magnitude of the BCG of the given cluster. It does not seem like there are any tendency of the degree of dominance for the whole sample.

However, we know that X-ray cluster properties are directly related to the cluster mass properties and the depth of the cluster gravitational potential well. As

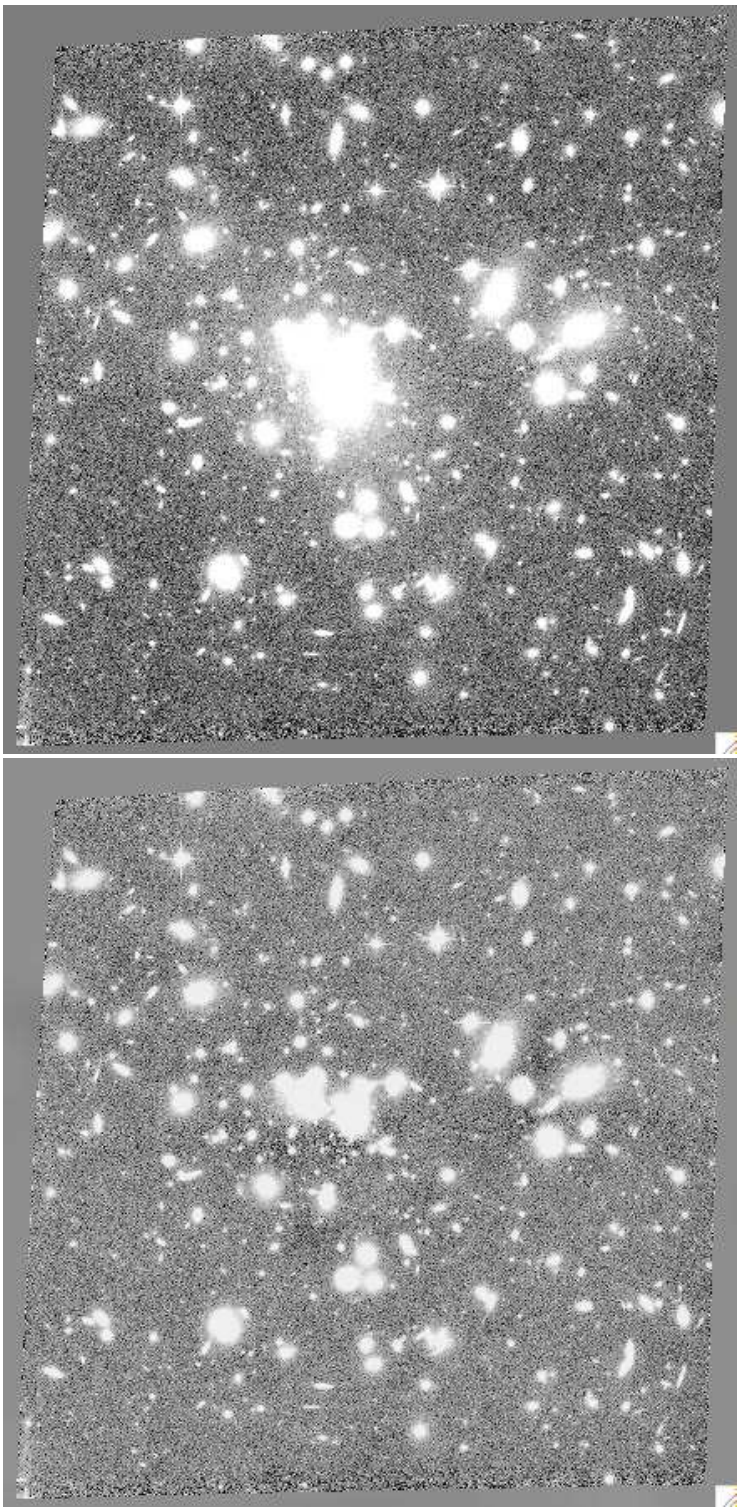

Figure 8.5: A1689 BCGs subtraction. More details in the text.

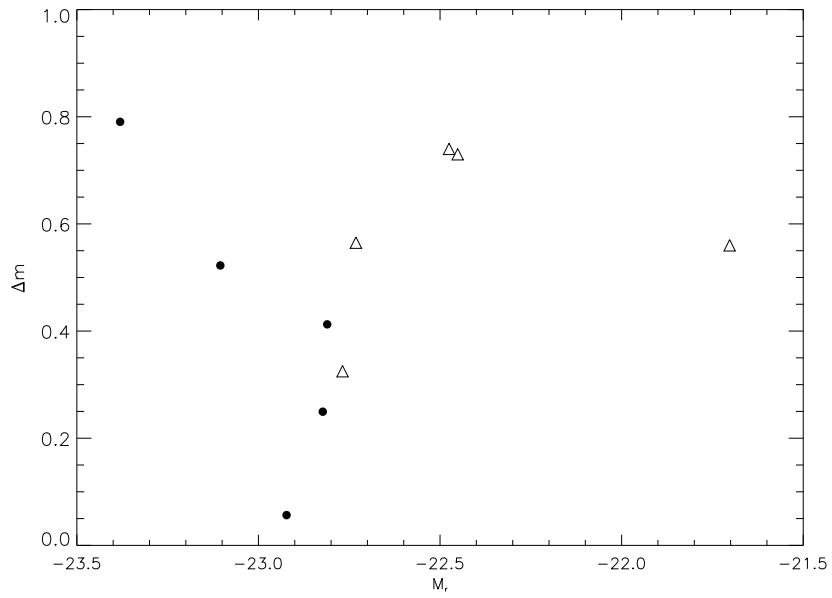

Figure 8.6: Degree of Dominance versus BCG magnitude. Triangles refer to NOT sample while black points refer to ACS sample.

a consequence, those cluster give us information about the evolution and environmental influence, Edge (1991). So, if we take only the X-ray clusters from the sample, (that is, the ACS sample and A2111 from the NOT sample), we observe a decreasing degree of dominance with brightness, indicating that the BCG becomes brighter as its predominance in the clusters is higher. That trend goes in the sense of the formation of the cluster through hierarchical models, De Lucia & Blaizot (2007). For the less massive clusters in NOT sample, however, we do not find any noticeable tendency.

We find that three BCGs, (A2111, A2218 and A1689), are affected by more than a factor of two between Δm and Δm_2, as it is clearly shown in Figure 8.7. As many it has been reported in literature, (Wang, Ulmer & Lavery, 1997; Henriksen, Wang & Ulmer, 1999; Miller et al., 2006; Kneib et al., 1995; Markevitch, 1997; Neumann & Böhringer, 1999; Machacek et al., 2002), A2111 and A2218 are thought to be two cluster mergers what will explain that there would be two large dominant galaxies. For the case of A1689, there are no evidences reported about the possible merging of that cluster but a factor of two of discrepancy between the masses estimated by X-ray and lensing techniques have been reported, (Andersson & Madejski, 2004; Diego et al., 2005). Furthermore, A2111 and A1689 have the smallest Δm value after CL0024, which would indicate a dominant very bright population in the cluster.

Table 8.3: Degree of Dominance in NOT BCGs Sample

Name	Δm	Δm_2
A 1643	0.560	0.450
A 1878	0.730	0.670
A 1952	0.565	0.529
A 2111	0.325	0.059
A 2658*	0.740	0.500

* Aperture of 420 kpc

Table 8.4: Degree of Dominance in ACS BCGs Sample

Name	Δm	Δm_2
A 1689	0.249	0.093
A 1703	0.790	0.723
A 2218**	0.522	0.237
CL0024	0.056	0.046
MS1358	0.412	0.309

** Aperture of 475 kpc

On the other hand, we find that the values for the Δm and Δm_2 for three BCGs, A1878, A1952 and A1703, remain nearly constant, what would indicate an outstanding BCG comparing to the rest of the galaxy population in the cluster. In addition, two clusters out of these three, A1878 and A1703, (and also A2658) have a Degree of Dominance higher than 0.65, the value selected by Kim et al. (2002) to call a dominant BCG. That fact is noticed also in the low number of iterations at extracting the cD galaxy in the last section.

In Figure 8.8, we have plotted the relation of the Degree of Dominance with redshift for both samples. We see as our cluster at highest redshift, CL0024, is the cluster with the smallest degree of dominance, or the similar range of luminosity in its bright population. However, if we take out that cluster, we do not see any tendency. We only note that at redshift ≈ 0.2 it seems to be a larger dispersion than a a redshift ≈ 0.25. We would need larger sample of clusters to account for this fact.

We have also looked for correlations with clusters richness class. The results are shown in Figure 8.9. Unfortunately, we have not been able to find in the literature the corresponding RC for our farthest cluster. We see a trend with Richness Class, indicating that very rich clusters have a wide range of values of the Degree of Dominance, while, on the contrary, poorer clusters, seem to have

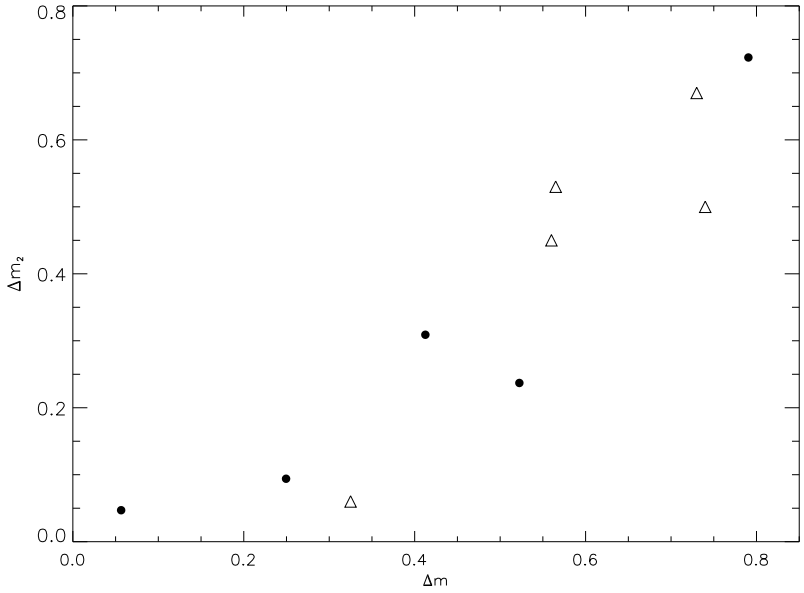

Figure 8.7: Degree of Dominance versus Δm_2. Triangles refer to NOT sample while black points refer to ACS sample.

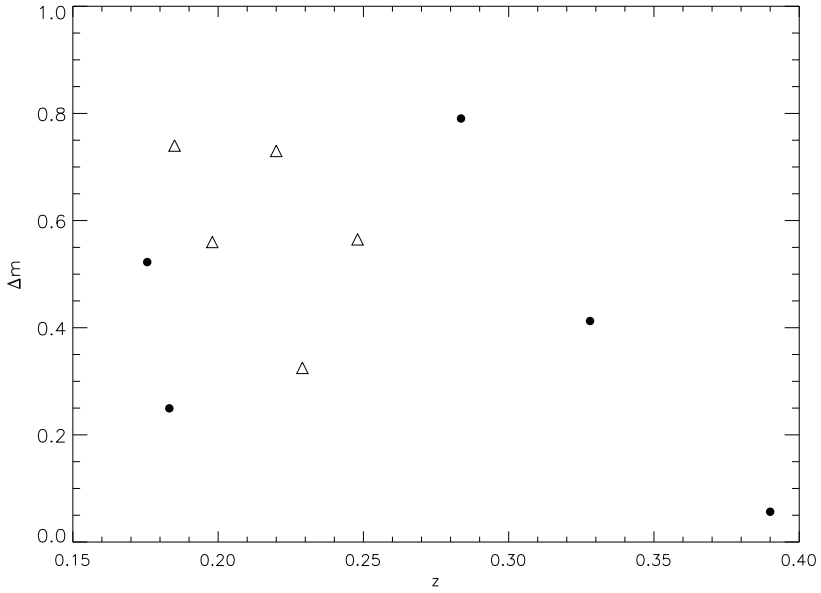

Figure 8.8: Redshift versus Degree of Dominance. Triangles refer to NOT sample while black points refer to ACS sample.

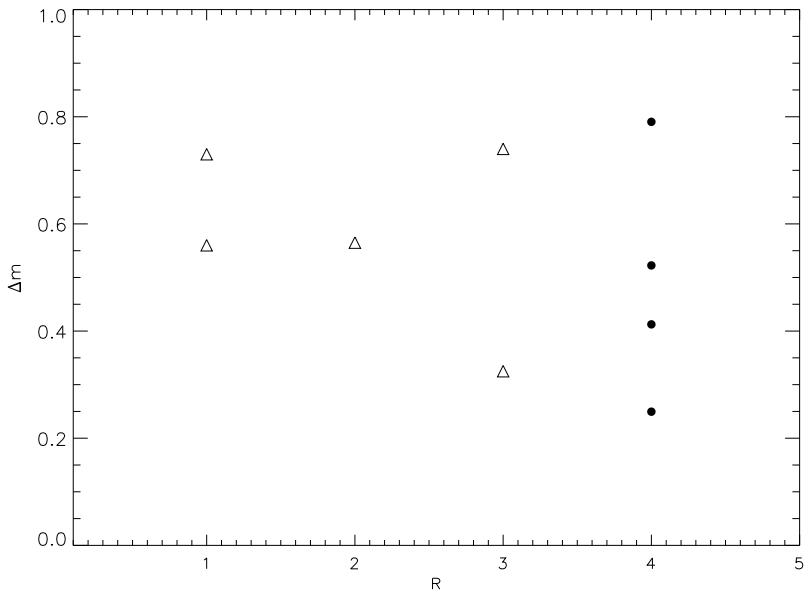

Figure 8.9: Cluster Richness Class versus Degree of Dominance. Triangles refer to NOT sample while black points refer to ACS sample.

large degree of dominance values, indicating to a more homogeneous luminosity between its members. Again, we can not conclude as we our sample may be biased to richer clusters.

8.3.2 Morphology

As we have already mentioned, Schombert (1986) conducted an extensive survey of BCG brightness profiles finding that not all BCGs galaxies were cD galaxies. A **cD galaxy** is considered a giant elliptical that has a separate extended low surface brightness envelope, which is evident as an inflection in the brightness profile typically at $\mu_V \sim 24$ or greater, ((Oemler, 1976; Schombert, 1986; Tonry, 1987; Kormendy & Djorgovski, 1989)). That is, cD's are elliptical galaxies with shallow surface brightness profiles

$$d \log \mu_V / d \log r \approx 2$$

at $\mu_V \sim 24$ mag arcsec^{-2}. Those galaxies exhibit a characteristic 'break' over an $r^{1/4}$ law, and are much brighter than typical elliptical galaxies, with luminosities $\sim 10 L_*$, Sandage & Hardy (1973); Schombert (1986). The cD classification itself was introduced by Matthews, Morgan & Schmidt (1964) to denote the very large D galaxies that they found in some clusters and the 'c' prefix was taken from the

notation for supergiants stars in stellar spectroscopy. Type cD galaxies behave in similar ways as BCGs galaxies. They are always found in dense regions, and in virtually all cases they are located near the spatial and kinematical center of their host cluster, or subcluster. A number of theories have been suggested to justify the formation of cD galaxies related to the cluster environment and their close link to their dynamical history.

Many authors have claimed that the envelopes themselves might be distinct entities from the galaxies themselves for a number of reasons. In first instance, cD envelope luminosity is weakly correlated with some properties of the host cluster, most notably with cluster richness and X-ray luminosity, Schombert (1988). Secondly, both the position angle and ellipticity of cD galaxy isophotes commonly show discontinuities at r_b, where the envelope begins to dominate the surface brightness profile, (Schombert, 1988; Porter, Schneider & Hoessel, 1991). Finally, the envelopes have surface brightness profiles with power-law slopes that are similar to those measured from the surface density profiles of the surrounding cluster galaxies.

We must be cautious with the analysis of the surface brightness of the cD galaxies as a constant power law will rise above an $R^{1/4}$ law at large radii, a cD envelope may be erroneously detected as separate component, even though a single power law could describe the BCG completely.

In Figure 8.10, we have plotted the $r^{1/4}$ profiles versus the surface brightness in order to determine if the BCGs galaxies are also cD galaxies. At the view of that profiles, we can assign a cD halo to A1952 from the NOT sample, as we see can distinguish the characteristic 'break' from the de Vaucouleurs profile. In the ACS, we find the break in A2218 and MS1358. The rest of the galaxies does not seem to have a different profile from a De Vacouleurs law, in some cases, steeper than them.

8.3.3 Surface Brightness

Following several works in literature, (Schombert, 1986; Jordán et a., 2004; Liu & Mohr, 2004; Seigar, Graham & Jerjen, 2007), we have examined the surface brightness of the BCGs. We have fitted different profiles and examined its parameters. In Figures 8.3.3 and 8.3.3, we have plotted different fits to the surface brightness of the BCGs for the NOT and ACS sample respectively. The left upper panel shows the de Vaucouleurs fit, the right upper refers to the Sersic profile, the bottom left shows a Sersic plus Exponential profile and finally the bottom right plot shows a fit with two Sersic's profiles. All of them have been fitted using the same analysis that we have used in this thesis, GASP-2D, explained in Chapter 5 and also with GALFIT for comparison. The results are collected in Tables 8.5, 8.6 8.7 and 8.8, respectively.

The use of de Vaucouleurs $R^{1/4}$ law, de Vaucouleurs (1948), to describe BCG surface brightness profiles was proved by Schombert (1986) to offer a poor match, only achieving a good fit over a restricted range of surface brightness.

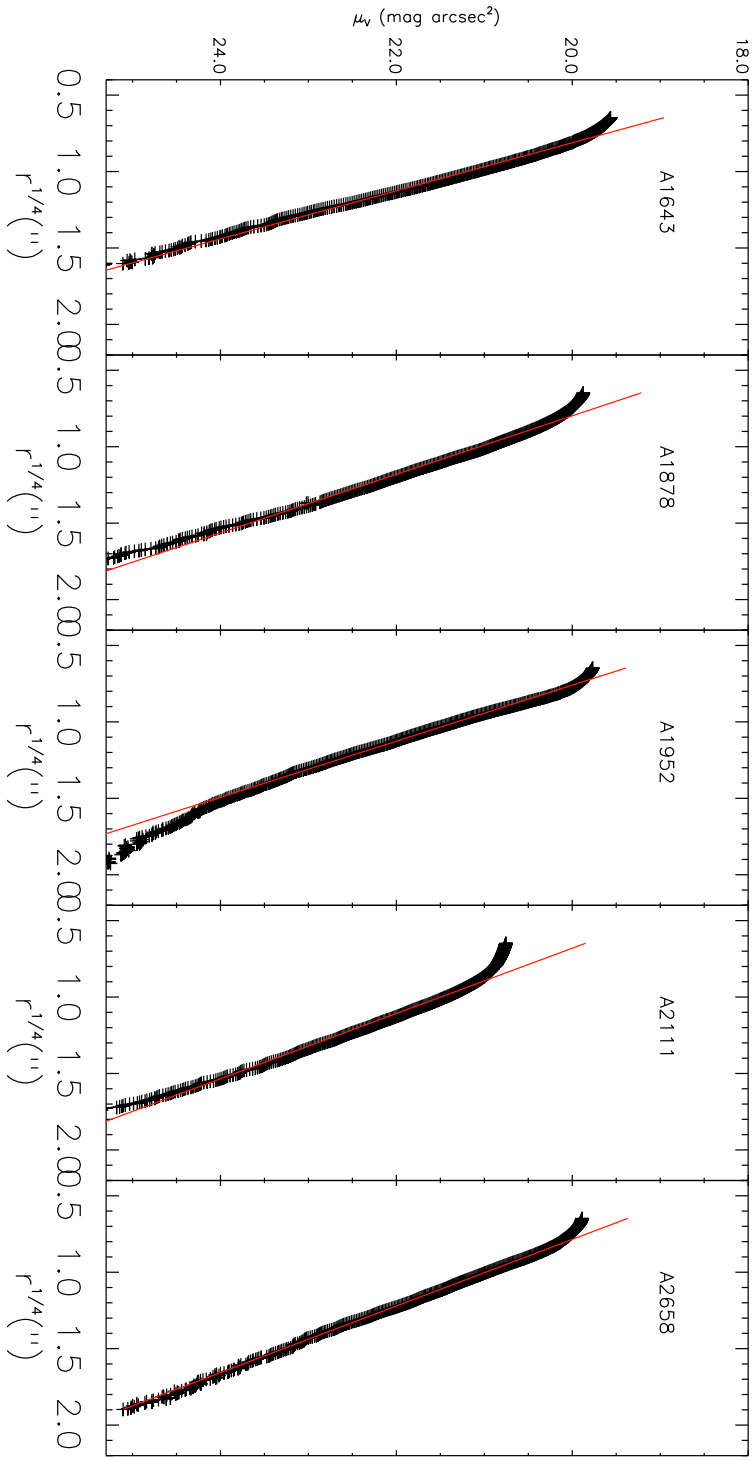

Figure 8.10: Deviation of the surface brightness profiles from the De Vaucouleurs profile for the NOT BCGs. Red line: De Vaucouleus fit. Black line: BCG profile.

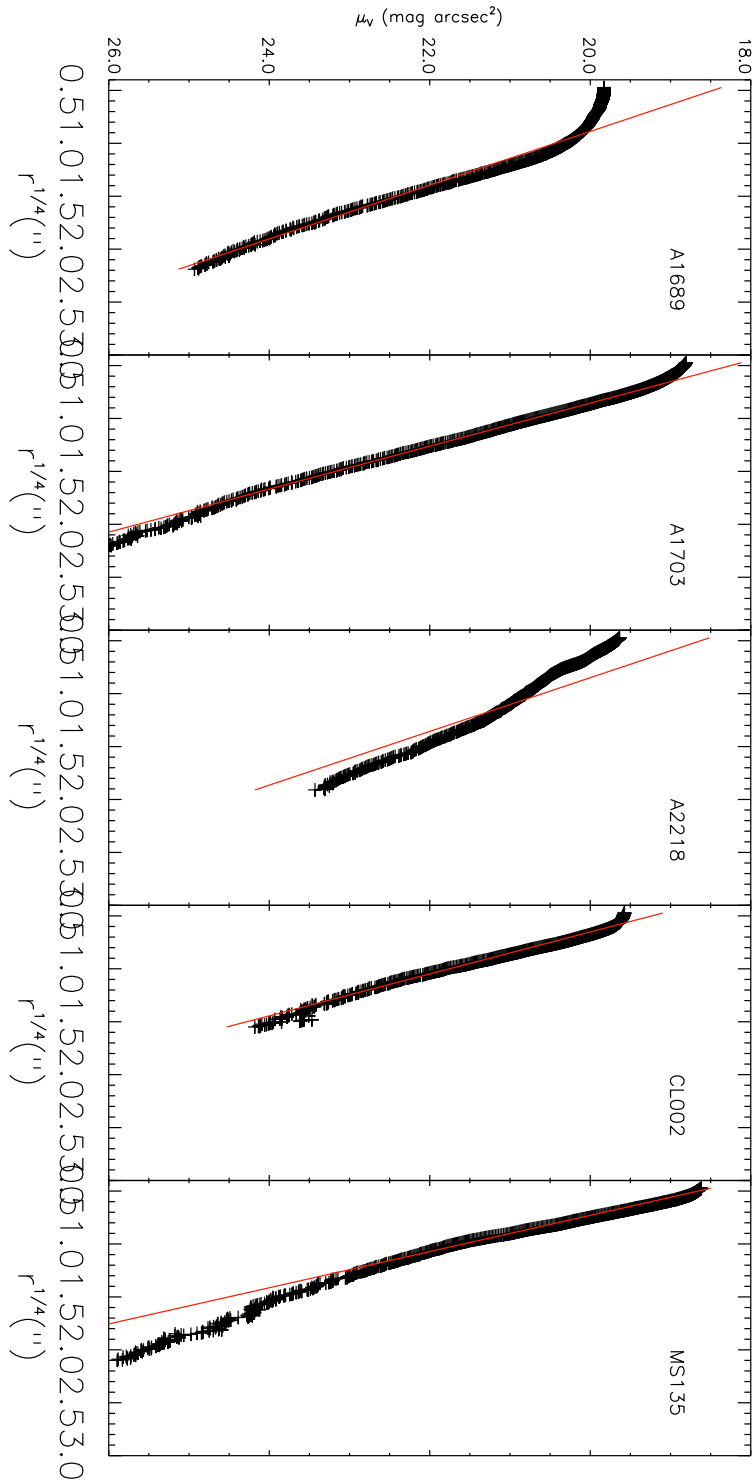

Figure 8.11: Deviation of the surface brightness profiles from the De Vaucouleurs profile for the ACS BCGs. Red line: De Vaucouleus fit. Black line: BCG profile.

Table 8.5: BCGs de Vaucouleurs fit

	Gasp − 2D			Galfit		
Name	$R_e('')$	ε	PA	$R_e('')$	ε	PA
A 1643	2.94	0.70	0.28	3.08	0.72	−1.25
A 1878	6.48	0.86	54.01	4.95	0.83	63.72
A 1952	5.45	0.90	134.11	24.39	0.74	−57.43
A 2111	10.02	0.74	177.60	6.83	0.61	−0.16
A 2658	10.85	0.84	43.82	15.56	0.65	26.80
A 1689	20.03	0.86	38.37	33.68	0.78	20.68
A 1703	8.20	0.86	7.90	12.03	0.77	2.08
A 2218	20.02	0.84	45.75	47.49	0.48	49.69
CL0024	7.43	0.82	5.72	6.83	0.74	−42.48
MS1358	4.11	0.94	8.24	15.56	0.49	−31.67

In fact, in the profiles presented in his work many of the BCGs profiles appear to be better fitted by power laws rather than de Vaucouleurs law. In addition, if the BCG is a cD galaxy, a constant power law will rise above an $R^{1/4}$ law at large radii and the fit will be erroneous.

The use of a single Sersic law, Sersic (1968), has been used in Graham et al. (1996) achieving very good results due to the flexibility of the n shape parameter, achieving, most of the BCGs larger values of n than 4. Also, many works have applied the use of two Sersics laws to measure the surface brightness of very deep exposures of cD galaxies, (Seigar, Graham & Jerjen, 2007).

Table 8.6: BCGs Sersic fit

	Gasp − 2D				Galfit			
Name	$R_e('')$	n	ε	PA	$R_e('')$	n	ε	PA
A 1643	2.22	3.16	0.70	0.32	2.07	2.14	0.75	0.41
A 1878	3.47	2,48	0.86	54.10	3.39	1.92	0.82	58.03
A 1952	15.17	6.57	0.90	132.75	60.61	6.92	0.76	−57.86
A 2111	3.62	1.86	0.75	176.85	4.02	1.59	0.67	−3.68
A 2658	10.94	4.02	0.84	43.61	13.20	3.41	0.66	26.37
A 1689	9.74	2.53	0.84	14.32	29.60	3.77	0.79	20.67
A 1703	6.16	3.31	0.84	171.26	15.33	4.74	0.76	2.41
A 2218	12.96	1.97	0.62	40.06	18.65	2.12	0.50	50.40
CL0024	10.00	4.43	0.83	174.14	38.53	5.56	0.74	−50.12
MS1358	8.24	5.44	0.91	152.31	168.70	9.14	0.54	−27.82

Table 8.7: BCGs Sersic plus Exponential fit

	Gasp − 2D								Galfit							
Name	$R_e('')$	n	ε_b	PA_b	$h('')$	ε_d	PA_d	B/T	$R_e('')$	n	ε_b	PA_b	$h('')$	ε_d	PA_d	B/T
A 1643	1.73	2.74	0.70	179.95	4.32	0.85	47.63	0.87	0.78	0.99	0.78	−2.11	2.09	0.73	2.73	
A 1878	2.48	2, 37	0.89	45.68	2.91	0.73	66.58	0.67	1.52	1.30	0.81	45.85	3.06	0.80	63.18	
A 1952	20.77	8.00	0.89	145.86	15.19	0.25	101.75	0.66	118.33	9.42	0.93	18.22	10.18	0.34	−59.27	
A 2111	1.11	1.07	0.90	15.37	2.74	0.66	173.95	0.16	1.42	1.04	0.95	22.86	3.36	0.59	−6.56	
A 2658	3.39	2.77	0.84	56.07	6.24	0.71	19.11	0.45	10.65	3.42	0.69	36.52	3.66	0.49	43.50	
A 1689	2.77	1.04	0.83	44.46	10.50	0.84	25.72	0.26	3.44	1.31	0.90	31.12	23.74	0.54	17.91	
A 1703	3.42	2.52	0.87	14.38	17.23	0.44	171.26	0.36	3.59	2.49	0.86	1.78	28.65	0.40	3.60	
A 2218	14.97	2.77	0.73	60.55	5.51	0.47	37.18	0.54	29.93	2.90	0.53	36.70	10.01	0.22	65.32	
CL0024	0.61	1.33	0.78	133.05	2.59	0.87	163.35	0.15	29.36	5.33	0.84	−52.58	247.81	0.01	−42.01	
MS1358	0.84	2.37	0.91	72.43	4.99	0.44	151.01	0.12	159.76	9.04	0.54	−26.56	124.33	0.01	−67.60	

Table 8.8: BCGs Sersic plus Sersic fit

Name	$R_e('')$	n_b	ε_b	PA_b	Galfit $R_e('')$	n_d	ε_d	PA_d	B/T
A 1643	1.04	1.22	0.77	−1.28	4.56	0.52	0.72	4.66	
A 1878	2.22	1.50	0.82	50.22	7.01	0.56	0.79	69.19	
A 1952	22.93	1.82	0.89	−58.56	1.47	1.75	0.95	−37.71	
A 2111	1.87	1.11	0.83	−1.20	6.85	0.68	0.59	−6.49	
A 2658	3.29	2.23	0.98	−21.98	21.59	1.11	0.42	27.42	
A 1689	4.50	1.54	0.84	23.76	28.19	0.43	0.56	16.22	
A 1703	4.29	2.66	0.82	0.61	83.87	0.38	0.16	5.90	
A 2218	19.65	2.25	0.51	49.68	0.00005	20.00	0.21	66.31	
CL0024	14.41	4.61	0.84	5.29	17.99	0.30	0.38	−56.18	
MS1358	3.07	3.45	0.87	−34.86	219.16	0.67	0.07	−20.81	

At analyzing the profiles we can say that in nearly all the cases, the de Vaucoleurs fit does not fit accurately the whole profile, as the BCGs profiles are steeper than them. On the contrary, a single Sersic law seems to be a good approximations for the profiles in a number of cases, A1878, A2658 or CL0024, achieving in all cases n values larger than 4.

If we apply two component profiles, we obtain that two Sersics law are describing quite accurately nearly all clusters, with the exceptions of MS1358, A1703 or A2218. However, let's note the low values of shape parameters in most of the cases.

However, MS1358 and A1703 are well described by a Sersic and Exponential law. Particularly remarkable is the profile of A2218, which its extense envelope is not very well fitted by none of this profiles. One possible explanation can be that this cluster seems to be a merger of two cluster, as many authors have suggested, (Kneib et al., 1995; Markevitch, 1997; Neumann & Böhringer, 1999; Machacek et al., 2002), and therefore its profile can be disturbed by the environmental influence of the merging cluster.

8.3.4 Hubble Diagram

The BCGs have been shown to vary little in luminosity within a fixed metric aperture (Sandage, 1972a,c; Postman et al., 2005) and in the past decade, the near-infrared K-band Hubble diagram has been studied in depth by numerous authors (Aragón-Salamanca, Baugh & Kauffmann, 1998; Brough et al., 2002) up to redshift $z \sim 1$. That band has turned out to be extremely suitable for the study of the BCG evolution because the k-correction remains unchanged by the star formation history of the galaxy, and the extinction is appreciably

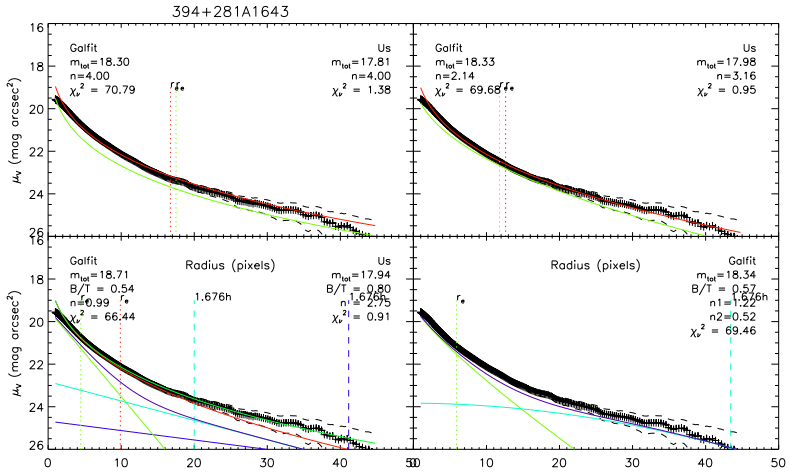
394+281A1643
Galfit
m_tot=18.30
n=4.00
χ_ν² = 70.79
Us
m_tot=17.81
n=4.00
χ_ν² = 1.38
Galfit
m_tot=18.33
n=2.14
χ_ν² = 69.68
Us
m_tot=17.98
n=3.16
χ_ν² = 0.95
Galfit
m_tot=18.71
B/T = 0.54
n=0.99
χ_ν² = 66.44
Radius (pixels)
1.676h
Us
m_tot=17.94
B/T = 0.80
n = 2.75
χ_ν² = 0.91
Radius (pixels)
Galfit
m_tot=18.34
B/T = 0.57
n1=1.22
n2=0.52
χ_ν² = 69.46
μ_V (mag arcsec²)

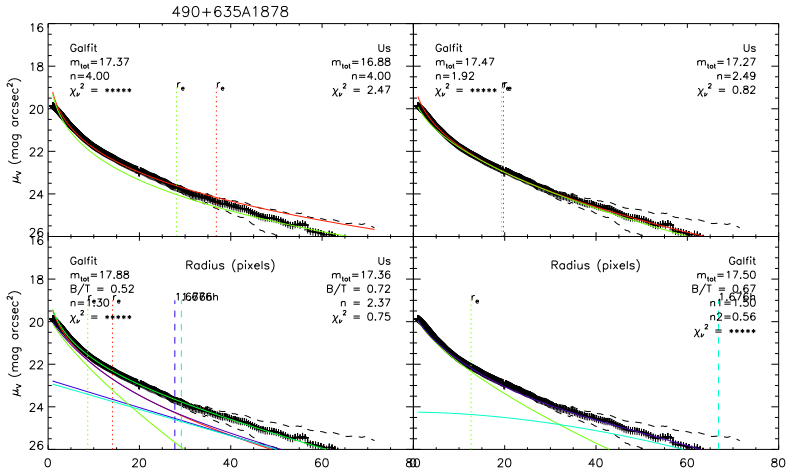
490+635A1878
Galfit
m_tot=17.37
n=4.00
χ_ν² = *****
Us
m_tot=16.88
n=4.00
χ_ν² = 2.47
Galfit
m_tot=17.47
n=1.92
χ_ν² = *****
Us
m_tot=17.27
n=2.49
χ_ν² = 0.82
Galfit
m_tot=17.88
B/T = 0.52
n=1.30
χ_ν² = *****
Radius (pixels)
Us
m_tot=17.36
B/T = 0.72
n = 2.37
χ_ν² = 0.75
Radius (pixels)
Galfit
m_tot=17.50
B/T = 0.67
n1=1.50
n2=0.56
χ_ν² = *****
μ_V (mag arcsec²)

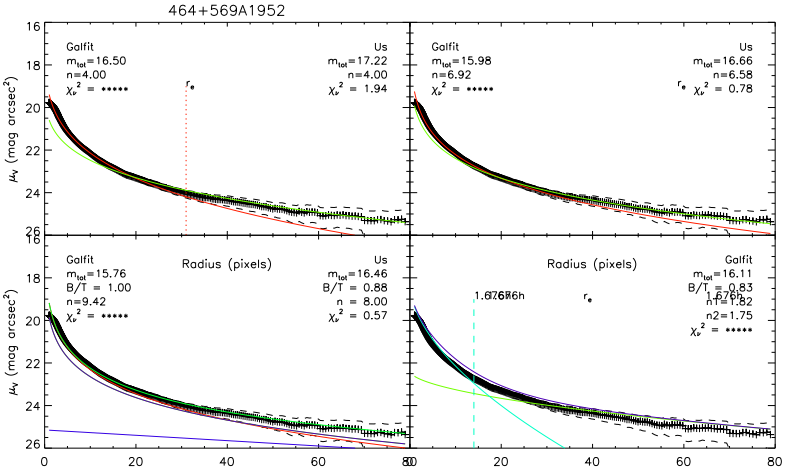
464+569A1952
Galfit
m_tot=16.50
n=4.00
χ_ν² = *****
Us
m_tot=17.22
n=4.00
χ_ν² = 1.94
Galfit
m_tot=15.98
n=6.92
χ_ν² = *****
Us
m_tot=16.66
n=6.58
χ_ν² = 0.78
Galfit
m_tot=15.76
B/T = 1.00
n=9.42
χ_ν² = *****
Radius (pixels)
Us
m_tot=16.46
B/T = 0.88
n = 8.00
χ_ν² = 0.57
Radius (pixels)
Galfit
m_tot=16.11
B/T = 0.83
n1=1.82
n2=1.75
χ_ν² = *****
μ_V (mag arcsec²)

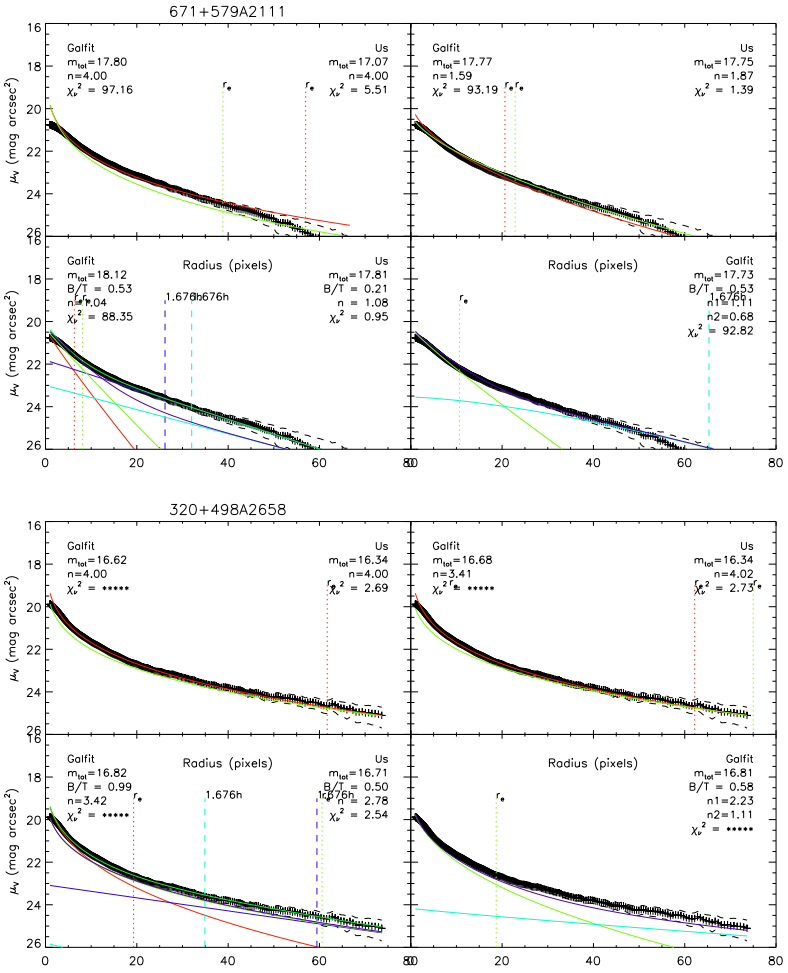

Figure 8.12: Surface brightness profiles for the NOT BCGs. Upper left: De Vaucouleurs fit (Red line, GASP-2D fit, Green Line, GALFIT fit). Upper right: Sersic fit (Red line, GASP-2D fit, Green Line, GALFIT fit). Bottom left: Sersic+Exponential fit, (Red line, GASP-2D Sersic fit, Green Line, GASP-2D Exponential fit, Blue line GASP-2D total fit; Green line, first Sersic fit, light blue, Exponential fit, violet line, total GASP-2D fit). Bottom right: Sersic+ Sersic fit, (Green line, first Sersic fit, light blue, second Sersic fit, violet, whole GASP-2D fit)

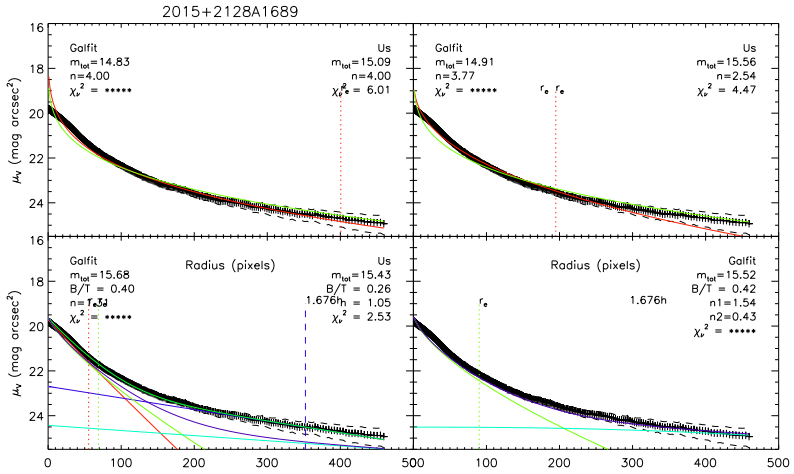
2015+2128A1689
Galfit
m_tot=14.83
n=4.00
χ_ν² = *****
Us
m_tot=15.09
n=4.00
χ_ν² = 6.01
Galfit
m_tot=14.91
n=3.77
χ_ν² = *****
Us
m_tot=15.56
n=2.54
χ_ν² = 4.47
Galfit
m_tot=15.68
B/T = 0.40
n=1.53
χ_ν² = *****
Radius (pixels)
Us
m_tot=15.43
B/T = 0.26
1.676h n = 1.05
χ_ν² = 2.53
Radius (pixels)
Galfit
m_tot=15.52
B/T = 0.42
n1=1.54
n2=0.43
χ_ν² = *****
μ_v (mag arcsec²)

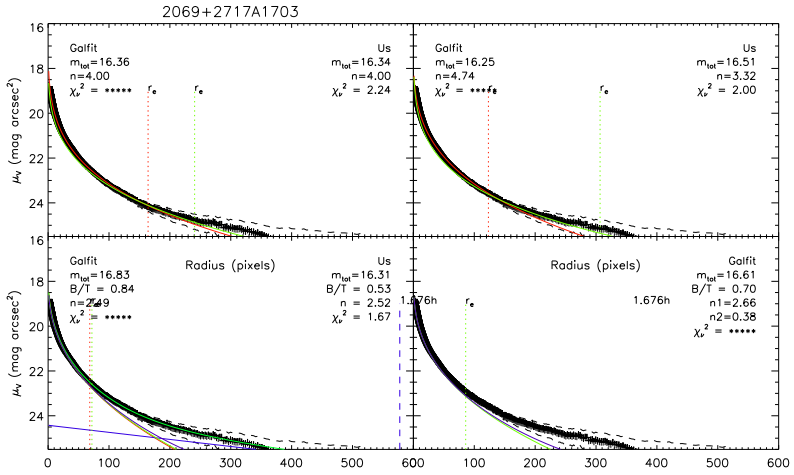
2069+2717A1703
Galfit
m_tot=16.36
n=4.00
χ_ν² = *****
Us
m_tot=16.34
n=4.00
χ_ν² = 2.24
Galfit
m_tot=16.25
n=4.74
χ_ν² = *****
Us
m_tot=16.51
n=3.32
χ_ν² = 2.00
Galfit
m_tot=16.83
B/T = 0.84
n=2.49
χ_ν² = *****
Radius (pixels)
Us
m_tot=16.31
B/T = 0.53
n = 2.52
χ_ν² = 1.67
Radius (pixels)
Galfit
m_tot=16.61
B/T = 0.70
n1=2.66
n2=0.38
χ_ν² = *****
μ_v (mag arcsec²)

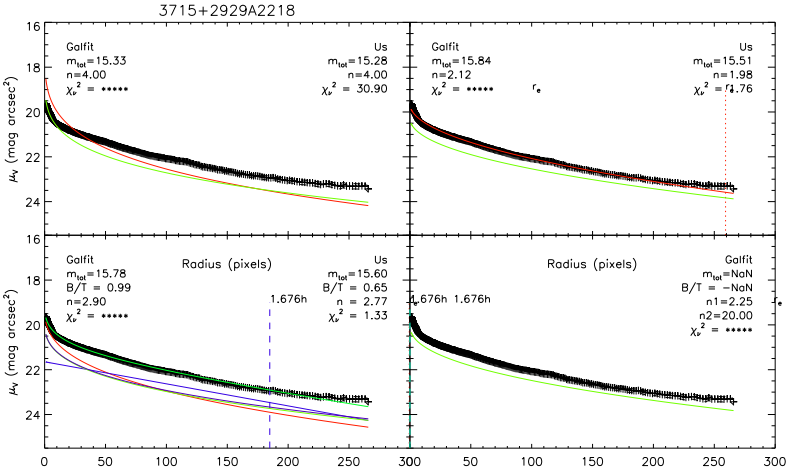
3715+2929A2218
Galfit
m_tot=15.33
n=4.00
χ_ν² = *****
Us
m_tot=15.28
n=4.00
χ_ν² = 30.90
Galfit
m_tot=15.84
n=2.12
χ_ν² = *****
Us
m_tot=15.51
n=1.98
χ_ν² = 1.76
Galfit
m_tot=15.78
B/T = 0.99
n=2.90
χ_ν² = *****
Radius (pixels)
Us
m_tot=15.60
B/T = 0.65
n = 2.77
χ_ν² = 1.33
Radius (pixels)
Galfit
m_tot=NaN
B/T = -NaN
n1=2.25
n2=20.00
χ_ν² = *****
μ_v (mag arcsec²)

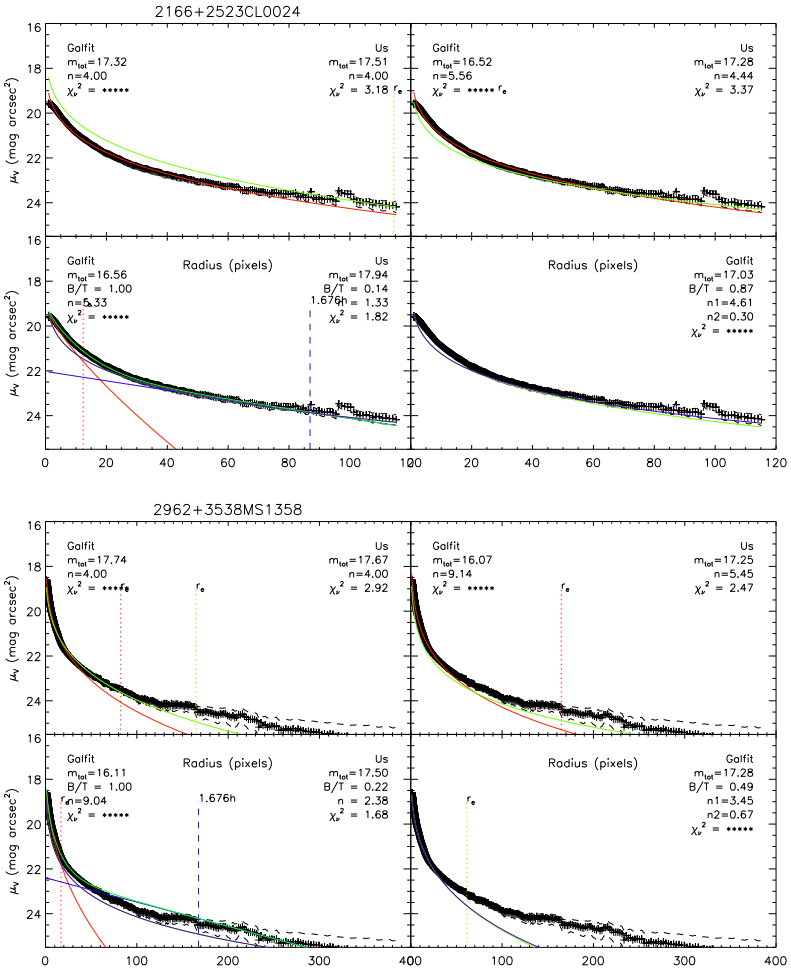

Figure 8.13: Surface brightness profiles for the ACS BCGs. Upper left: De Vaucouleurs fit (Red line, GASP-2D fit, Green Line, GALFIT fit). Upper right: Sersic fit (Red line, GASP-2D fit, Green Line, GALFIT fit). Bottom left: Sersic+Exponential fit, (Red line, GASP-2D Sersic fit, Green Line, GASP-2D Exponential fit, Blue line GASP-2D total fit; Green line, first Sersic fit, light blue, Exponential fit, violet line, total GASP-2D fit). Bottom right: Sersic+ Sersic fit, (Green line, first Sersic fit, light blue, second Sersic fit, violet, whole GASP-2D fit)

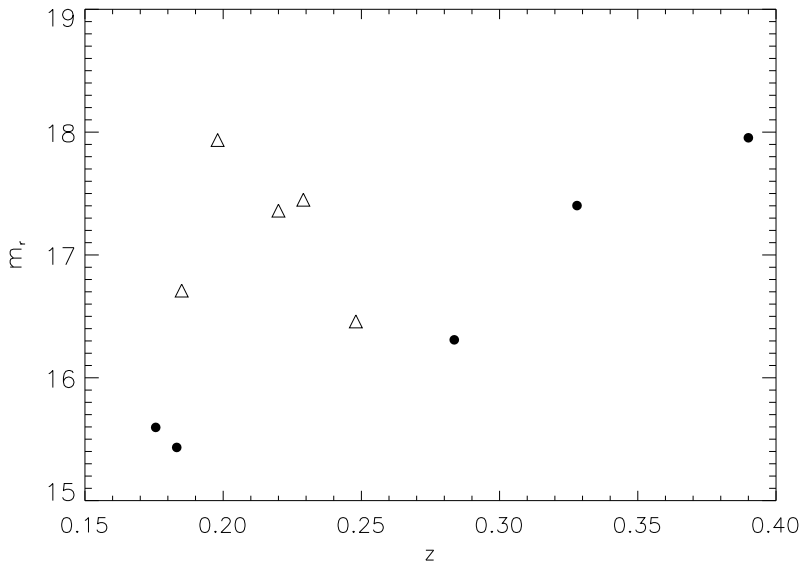

Figure 8.14: Hubble Diagram for the BCGs in NOT (Triangles) and ACS sample (Black Points).

smaller than at other wavelengths, (Charlot, Worthey & Bressan, 1996; Madau, Pozzetti & Dickinson, 1998).

In that section, we have study the Hubble diagram in the r-band for our clusters sample. Even though that band is more sensible to the star formation on the galaxies than the K band, has smaller dispersion than blue bands.

In Figure 8.14, we have plotted the Hubble Diagram for our sample, we observe that the data in the ACS sample, which are clusters that emit in X-ray describe a very well defined Hubble sequence as it is shown in the fit. For the rest of the clusters, the NOT sample, we do not find a trend in the Hubble Diagram.

As many authors have noted, (Aragón-Salamanca, Baugh & Kauffmann, 1998; Collins & Mann, 1998; Burke, Collins & Mann, 2000; Brough et al., 2005), the K-band Hubble diagram for BCGs is very well defined up to redshift 1, with small dispersion (within 0.3 mag). With the purpose of looking into the place of our BCGs sample in the K-band Hubble diagram and as we do not have K magnitudes, we have used a color transformation of R-K=2.6, Lauer & Postman (1994), following for example, Aragón-Salamanca, Baugh & Kauffmann (1998); Burke, Collins & Mann (2000).

Then, in Figure 8.15, we have set our BCGs sample (with red points and blue triangles for the ACS and NOT sample, respectively), together with the 45 BCGs in EMSS (Einstein Medium Sensitivity Survey), X-ray-selected clusters sample, Gioia & Luppino (1994) in K-band, extracted from Collins & Mann

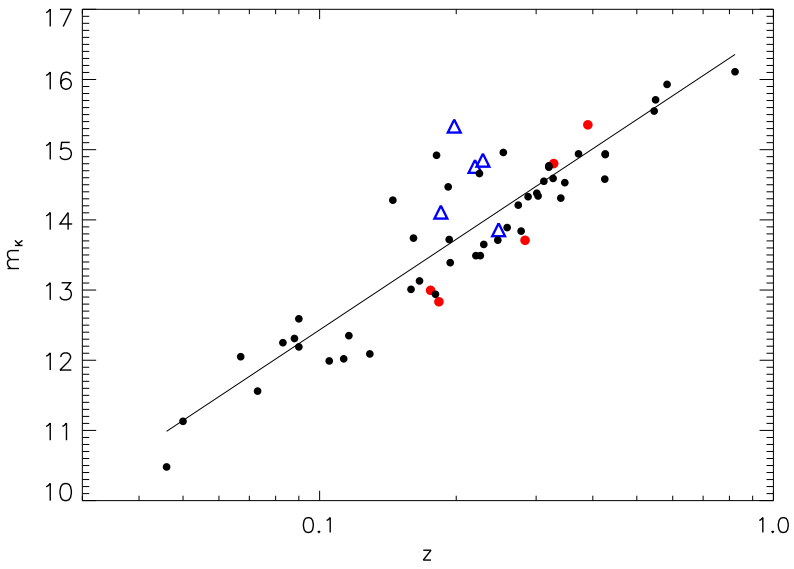

Figure 8.15: K-band Hubble Diagram for the BCGs in NOT (Blue Triangles) and ACS sample (Red Points). The black points are the BCGs in a X-ray selected sample given by Collins & Mann (1998). The line is the whole sample linear fit.

(1998), (black points, in the Figure 8.15)

As we see, our points are placed within the dispersion found in the Hubble Diagram. We see as the ACS sample BCGs, found in more massive and luminous X-ray clusters, seem to be found in the lower part of the relation, while the BCGs in NOT sample, belonging to less massive and rich clusters are placed in the upper part of the relation. Indeed, this is the z-range where the dispersion is large of the sample. Anyway, we have fitted the whole sample and we have found a dispersion of 0.268, however the dispersion for ACS sample together with Collins & Mann (1998) sample is 0.235, while the NOT sample with Collins & Mann (1998) achieves to 0.273. All of the are compatible with the errors found by Collins & Mann (1998), etc, however, the ACS sample are X-ray clusters selected in the same way then them. However, more data at low redshift needs to be available for filling the whole Hubble Diagram.

8.4 Are they Standard Candles?

Since the first identification of photometric homogeneity of BCGs, (Humason, Mayall & Sandage, 1956; Sandage, 1972a,b), the BCGs have been explored in detail in order to demonstrate that they could be treated as 'Standard Candles'

for performing cosmological probes.

The main piece of evidence in that sense, was the evidence of the spectacular small dispersion of 0.25 mag of the luminosities of the BCGs, with an adequate selection of the data in luminosity and cluster morphology.

Lauer & Postman (1994); Postman & Lauer (1995), performed the first studies in large samples of BCGs. They selected 119 BCGs up to redshift ≤ 0.05 from a sample of 153 clusters in the ACO catalogue, (Abell, Corwin & Olowin, 1989), basing their exclusions on the redshift, lack of significant overdensity or non-elliptical BCG morphology. They investigated into the relationship between L_m, the metric luminosity within the central 10 h^{-1} kpc of the BCGs and logarithmic slope of the surface brightness profiles α, finding a reduction of the cosmic scatter in L_m and an independence of the color, cluster richness and BCG location within the host cluster, concluding with the following sentence: *BCGs are a highly homogeneous population, making them suitable for statistical studies of galaxy peculiar velocities on large scales.*

In the following years, a large number of works, (Collins & Mann, 1998; Brough et al., 2002), etc, have been devoted to the corroborate the homogeneity of the BCGs. Some of them have established that the dispersion of BCGs in clusters with an X-ray luminosity $L_x \geq 2.3 \times 10^{44} ergs^{-1}$ in the passband $0.3 - 3.5keV$ is about half as large (0.24) as those in less luminous clusters, and their mean absolute magnitude in the raw K-band is 0.5 mag brighter. However, there are still few BCGs with redshift below 0.3 in these analyses so the evolutionary nature of this effect remains unclear.

We have found that our X-ray BCGs sample, achieves a small dispersion (of 0.23) in the Hubble Diagram. However, if we consider the rest of the sample that does not emit in X-ray, the dispersion, even if within the results previously found, amounts to 0.28. It seems like the homogeneity of the BCGs is patent. However, the use of 'Standard Candles' could be done only for clusters selected with a variety of properties, such as X-ray emitters or any other requirements like the ones specified in Postman & Lauer (1995).

At present, a cluster detection algorithm based on the optical properties of the BCGs, MaxBCG, Koester et al. (2007), have been developed. On one hand, this algorithm takes advantage of the colors of the brightest members and their spatially 'clustering' falling off as $\sim 1/r$ in two dimensions. On the other hand, they combine these information with the existence of the BCG residing at brightest end of the CMR sequence and its placement at the halo center. As a consequence, they have been able to recover 90% pure of the clusters at 0.1 <z<0.3 with 10 or more red galaxies through large, realistic, mock galaxy catalogues.

Part IV

Results and Conclusions

Chapter 9

Conclusions and Future Prospects

When I heard the learn'd astronomer;
When the proofs, the figures, were ranged in columns before me;
When I was shown the charts and the diagrams,
to add, divide, and measure them;
When I, sitting, heard the astronomer, where he lectured
with much applause in the lecture-room,
How soon, unaccountable, I became tired and sick,
Till rising and gliding out, I wander'd off by myself,
In the mystical moist night-air, and from time to time,
Look'd up in perfect silence at the stars.

Walt Whitman, 'Leaves of grass'

We have analyzed a sample of ten clusters of galaxies at medium redshift ($0.15 \leq z \leq 0.4$), covering a wide range of properties in luminosity, X-ray properties, richness, dynamical states... These sample is mainly subdivided in two subsamples: the NOT sample (five clusters observed from the ground, less massive and rich, with few literature available and with an area coverage slightly larger) and ACS sample (five more clusters observed from the space with plenty of literature available, rich, massive, X-ray emitters and with a smaller area coverage). A cluster in NOT sample, A2111 is also a X-ray emitter, so sometimes, it will be analyzed together with the ACS sample in order to compare its X-ray properties.

We have been able to study therefore the degree of cosmic variance from lower and higher redshift samples, as well as standing out the main properties of some individual objects. In that chapter, we summarize the major conclusions that has been derived from the results of the analysis of this sample.

9.1 Conclusions

9.1.1 Bright Galaxy Population

- We have examined the possible interlopers in our medium redshift clusters finding that the foreground contamination may be negligible in agreement with the results already found by Fasano et al. (2000). The background contamination has been corrected by excluding galaxies redder than the CMR due to the cosmological k-effect, and using the redshift information if any. We have checked that that subtraction, especially in the bright population, agrees with the extraction provided by field counts, finding an excellent agreement up to the completeness limit with the subtraction fields provided by McLeod et al. (1995).

- We have fitted the individual Color-Magnitude Relation (CMR) for our sample up to the completeness limit for the sample ($M_r = -19.5$ for the NOT sample and $M_r = -17.8$ for the ACS sample). The results of the fit for the ten clusters have a very small dispersion (0.013) and the results are in good agreement with the reported in the literature.

- The Color-Morphology relation has been examined finding that six clusters out of ten have a spiral-type galaxy population dominating over the early type population, while the four different clusters have the opposite behavior. The bright galaxy population is mostly early-type, defining the red sequence. The BCGs are elliptical galaxies in all cases but in the case of A1643, which the BCG is a lenticular fainter galaxy.

- We have compared the results found for the CMR for the whole sample with a low redshift sample of López-Cruz et al. (2004) finding an excellent agreement with them. We obtain a mean value for the slopes of our sample of -0.050 ± 0.014, which is the same as our sample together with the López-Cruz et al. (2004),-0.05 ± 0.008. In addition, those values are very similar to the slope value recovered by Mei et al. (2006) for two clusters at $z \approx 1.26$. That fact supports the no variation of the CMR up to redshift ≈ 0.3 at least and more probably at larger redshift. In other words, the stellar population for the bright early type galaxies was arranged just after the galaxy formation.

- We have looked into the possible Butcher-Oemler effect, by studying the blue galaxy fraction f_b of the bright galaxy population, $M_r \leq -20$, for the cluster sample in two apertures for the NOT sample, 420 kpc and 735 kpc and a 475 kpc aperture for the ACS sample. Those apertures have been considered as a replacement of the Butcher & Oemler (1984) canonical value of R_{30}. Those values are consistent with the values found in the literature.

- We have found an excellent agreement with the blue fraction values by De Propris et al. (2004); Aguerri et al. (2007) for a low redshift sample

even if we find outstanding cases such as A1878, which are also reflected in low redshift samples, De Propris et al. (2004); Varela (2004); Aguerri et al. (2007). Therefore, diversity seems to be the most remarkable trend up to this range of redshift, $z \sim 0.3$.

- We have performed a visual classification of the morphological visual types into Ellipticals, Lenticular, Spiral and Irregular galaxies. In order to check the consistency of the classification, we have compared them with the different visual classifications performed in the literature for the galactic population in the clusters in common. We have found that the NOT sample achieves an agreement of 70% with the classification given by Fasano et al. (2000), A1689, CL0024 and MS1358 obtain a 75%, 76.74% and 66.6% of identical morphological types respectively, for their comparison with the samples of Teague, Carter & Gray (1990); Duc et al. (2002) (for A1689), Treu et al. (2003) (for CL0024) and Fabricant, Franx & van Dokkum (2000) (for MS1358). The sample with the largest number of galaxies in common (CL0024 with 80 galaxies in common), is the one with better concordance.

- We have also computed the concentration parameters for our clusters sample, except for A2658, the cluster with the smallest area coverage. We have compared those values with the concentration values given by Butcher & Oemler (1978), at low redshift and Dressler et al. (1997) at higher redshift. We find that our concentration values span the full range of the values measured for both samples, even if we find that three clusters are placed in the low part of the concentration values in agreement with the tendencies noted by Butcher & Oemler (1978); Dressler et al. (1997) that the more irregular, less concentrated clusters could be populated by late type galaxies.

- The rate of interacting systems in our sample has also taking into consideration. We have computed the perturbation f-parameter, introduced by Varela et al. (2004) in order to account for the tidal forces for every galaxy. We find a median values of -1.85 and -1.76 for the NOT and ACS sample, respectively, while the median value found for Coma Cluster, Varela et al. (2004), is -2.7. In fact, we find that a 63.97% of the NOT clusters galaxies and a 60.05% from the ACS clusters galaxies have a perturbation parameter higher than -2, which is the value chosen by Varela et al. (2004) to select interacting systems. Therefore, those results suggest the presence of a higher degree of interaction in our clusters samples, with respect to Coma.

- We have faced the analysis of the Surface Brightness for the galactic population in NOT sample. We have examined the surface brightness by using the GASP-2D routine, Méndez-Abreu et al. (2008). We have previously performed five thousand simulations fitting one Sersic component and two Sersic + Disc components to mock galaxies in order to check the reliability

of the results. From the simulations, we have obtained that the minimum area for the galaxies in one and two components to obtain results that are not affected by the image conditions are 550 and 800 pixels respectively. This area is broadly correlated with the magnitude, obtaining a minimum magnitude of -19.5 pixels for the minimum area of 550 pixels. We have also seen that galaxies with $m_r > 20$, bulge surface brightness $\mu_{0,B} > 25.3$, disc surface brightness, $\mu_{0,D} > 25.3$ and $B/T > 0.7$ does not provide a good fit in two components and therefore it will be fitted in one component.

- We have elaborated an algorithm to decide whether or not a galaxy should be fitted into one or two components by ensuring that the final fits give real two component (bulge+disc) galaxies fitted by two components. This algorithm is based on a similar approach as Allen et al. (2006) for the MGC. The final classification gives us a 47% of the galaxies with areas higher than 800 pixels are better fitted by a Sersic-one component profile, while the 52% are better fitted by a two components (Sersic+Disc profiles).

- We have assigned a quantitative morphology classification basing on the results of the surface brightness profiles. We have considered three mainly types: Early-types (E/S0), Early-Spirals (Spe) and Late-Spirals (Spl) basing on the colors and number of components. We find that a 85.7% and about a 90% of the galaxies classified in one component give a good agreement with the classification. However, only a 41.16% and a 22% of the galaxies in two components agree in the morphological type.

- We have also compared the morphological visual classification for A2218, with the quantitatively classification method based on Sersic parameters given by Sánchez et al. (2007) with an agreement of 47.05%. These comparisons are in concordance with the studies previously performed. As it has been widely explored, we support the fact that the quantitative methods of classification are not reproducing the visual morphological trends of the galactic population.

- The structural parameters extracted from the surface brightness analysis have also been analyzed. We have fitted the Kormendy relation, Kormendy (1977) for the bulges of the early-type galaxies considered.

- We have found a dichotomy for the red and blue bulges of the galaxies in one component in the plane $n - r_e$ allowing to distinguish very clearly the early and late types. We have also found differences in the plane $r_e - color$ for the bulges of the galaxies.

- A comparison between our bulge structural parameters with the galaxies in Coma Cluster provided by Aguerri et al. (2004) has been performed. We obtain the same range of values for the effective radius, r_e and shape parameter, n for our samples and Coma, indicating that the bulge of the

galaxies in our medium redshift NOT clusters were set at redshift larger than 0.25 at least.

- Regarding to the structural disc parameters, we have compared the scales of the discs in NOT sample with the low-redshift field galaxies found by Graham (2001) on one hand and on the other, with the disc scales extracted from Coma galaxy sample by Aguerri et al. (2004). Interestingly, we have found that our disc scales are as large as those of field galaxies, while those discs in Coma represent only a small percentage. Indeed, a factor of two of difference between the mean values of Coma and our sample is patent. What is more, we have performed a Kolmogorov-Smirnov test between those populations finding that only the Coma cluster discs are significantly different from NOT discs and Graham (2001) field discs. These results are in agreement with an evolution hypothesis in the disc scales from lower redshift samples in clusters.

- The analysis of the spatial distribution has been performed by studying the galaxy local density in the whole sample of clusters. We have found that four clusters from the ACS sample are much denser than the NOT sample, in correlation with their richness.

- The Morphology-Density relation has been investigated. The results show, in agreement with previous findings at lower redshift, (Dressler, 1980; Dressler et al., 1997), that the elliptical galaxies are usually placed in denser regions of the core of the clusters while the late type galaxies are found in less denser regions. However, if we look at each cluster individually, we find that five clusters are dominated by late type galaxies in denser regions (A1643, A1878, A1689, A1703 and A2218), showing also a diversity in the Morphology-Density relation.

- Similar results have been found at analyzing the radius-morphology relation. In addition, we have found different rates of decrement for the morphological types.

- We have detected also seven clusters out of ten that are dominated by an early-type population, two more clusters with the late-type population dominating the core and one cluster with a very similar population. In addition, two clusters out of ten shows significantly different populations, indicating a morphological segregation, which is not evident at low redshift, (Adami, Biviano & Mazure, 1998).

- We have widely explored the Luminosity Function of the sample and its more adequate fit. We have concluded after examining a number of methods that for our clusters samples, especially the NOT sample, which is less deep than the ACS sample, the more adequate fit is provided by the Composite Luminosity Function which provides the following values $\alpha = -1.15$ and $M^* = -21.38$ for the NOT sample and $\alpha = -1.11$ and

$M^* = -21.64$ for the ACS sample, which is consistent with the values found in the literature.

- For the ACS sample, we observe an increase at the faint end, at about magnitudes $M_r = -17.5$, which are fainter that our completeness limit, in concordance with results by Biviano et al. (1995); Parolin, Molinari & Chincarini (2003); Boué et al. (2008), that show the need of different function for describing the faint end of the LF.

- The Luminosity Function has been analyzed for different morphological types. We have not been able to fit properly their Composite Luminosity Function. We have found a slopes of $\alpha = -0.5$ for early and late types, which is in the extreme of the boundaries for the fit, showing the no-convergence of the fit. That fact can be due to large errors in the binning, or additionally, the need of a different function for the fit than the Schechter Function.

- The LF for different colors, however, shows different behaviors for the red and blue population in the sample. We find flat slopes ($\alpha \approx$ -0.8) and $M^* \approx -21.1$ for the red population, while the blue population looks much steeper than the red ones, (around $\alpha \approx -1.3$) with much fainter M^* values (around ≈ -22.50). Those results agree with the conclusions given by Barkhouse, Yee & López-Cruz (2007) and goes in the sense, as some authors have concluded, (Binggeli, Sandage & Tammann, 1988; Barkhouse, Yee & López-Cruz, 2007), of the morphological Universality of the LF.

9.1.2 Brightest Cluster Galaxies

- In the Final Part of this thesis, we have faced the study of the Brightest Cluster Galaxies (BCGs) in the clusters. We have developed an algorithm for the extraction of the BCG from the cluster potential without changing its properties and the properties of the galaxies around. The results give a good quality extraction.

- We have also studied the Degree of Dominance of the BCGs in the cluster, showing a decreasing degree of dominance for fainter X-ray BCGs. However, the BCGs extracted from non X-ray clusters does not show any significant tendency with the magnitude of the BCG.

- Three BCGs out of ten, experiment a factor of two of difference between the Degree of Dominance and the difference in magnitude with the second brightest members. That fact can be explained as two from these three BCGs are set in clusters that have been shown to be mergers of two clusters.

- On the other hand, we have also seen as three BCGs have nearly the same values for the Degree of Dominance and the difference in magnitude

with the second brightest member. Two out of these three BCGs have the Degree of Dominance higher than 0.65, the value selected by Kim et al. (2002) to call a dominant BCG.

- We have not found any clear relation of the degree of dominance with redshift, with the exception of the non-significant case of BCG of CL0024, the most distant cluster from the sample, that has the smallest degree of dominance.

- Regarding to the relation of the cluster richness class with the degree of dominance, we have not found evident tendencies. However, the BCGs placed in the richest clusters spread all the ranges of degrees of dominance, while the dispersion seems to be less in the more poorer clusters.

- We have tested the nature of cD galaxies from our BCGs sample, ensuring that three out of ten BCGs, (in the clusters A1952, A2218 and MS1358) are cD galaxies.

- The analysis of the surface brightness of the BCGs has been performed. We have found that in any case, de Vaucouleurs law fit well the BCGs in our sample, contrary the fit of elliptical normal galaxies. We find, that the Sersic fit gives good results for seven out of ten BCGs, giving large values of the shape parameters in most of the cases.

- Two more BCGs, the ones placed in the clusters MS1358 and A1703 are well described by a Sersic+ Exponential law. However, the profile of A2218 can not be well described by none of these profiles. One possible explanation might be that the nature of merging of this cluster, (Kneib et al., 1995; Machacek et al., 2002), could have disturb the environmental influence of the merging clusters.

- We have inspected the Hubble Diagram in the K-band, that has been shown to be extremely suitable for the study of the BCG evolution, (Aragón-Salamanca, Baugh & Kauffmann, 1998; Brough et al., 2002; Collins & Mann, 1998). Our BCGs fit the Hubble Diagram finding a global dispersion of 0.268, while if we consider only the BCGs placed in ACS sample (X-ray emitters and richer), we find a dispersion of 0.235.

9.2 Future Prospects

As we have previously seen throughout this thesis, there is a lack of cluster data at medium redshift due to the need of achieving very good conditions of seeing to obtain quality data or, if we are lucky, observations from the Space.

Surprisingly, we saw in the last part of the thesis that most of the observation in K-band that have been performed in large sample of BCGs have been at medium-large redshift. Therefore, wide analysis of BCGs are needed at low-medium redshift to determine their 'Standard Candles' status.

Therefore, we would like to finish to taking benefit from these clusters sample by focusing on the following points:

- The study of the detailed surface brightness from the ACS sample in all the multi-wavelenght range, taking advantage of the already available multi-color observations to study color radial profiles.
- The extension, correction and automatization to all multi-bands the algorithm extraction of the BCGs.
- The extraction of photometric redshifts, (Benítez, 2000; Coe et al., 2006) using narrow-band filters (see, for example, ALHAMBRA survey, (Moles et al., 2004), to be able to extend to fainter magnitudes the analysis of the galactic population, in particular subjects such as, the luminosity function at the faint end, for example.
- If possible, it will be useful to take multi-bands observation from the NOT sample in order to extract also photometric redshifts (in narrow bands) and extent its magnitude limitation and, of course, the extension of the sample with more clusters, would be extremely worth for quantifying the degree of cosmic variance
- Finally, the analysis of large samples of BCGs at low and medium redshift would be very powerful to determine the real nature of BCGs as standard candles.

9.3 Conclusiones

Hemos analizado una muestra de diez cúmulos de galaxias a *redshift* medio ($0.15 \leq z \leq 0.4$), cubriendo un amplio rango de propiedades en luminosidades, propiedades en rayos-X, riqueza, estados dinámicos... Esta muestra esta principalmente subdividida en dos submuestras: NOT (cinco cumulos observados desde tierra, menos masivos y ricos, con poca literatura disponible y con una cobertura en área ligerament mayor) y ACS (cinco cúmulos observados desde el espacio con gran cantidad de literatura disponible, ricos, masivos, emisores en rayos-X y con una cobertura en área menor). Uno de los cúmulos en la muestra del NOT, A2111, emite también en rayos-X, con lo que, en algunos casos, será analizado junto con la muestra del ACS para comparación de sus propiedades-X.

Ha sido posible estudiar, por lo tanto, el grado de varianza cósmica en comparación con muestras a bajo y alto *redshift*, así como el destacamiento de las principales propiedades de algunos objetos individuales. En este capítulo, resumimos las principales conclusiones que se han derivado de los resultados del análisis de esta muestra.

9.3.1 Población Galáctica Brillante

- Hemos examinado los posible 'intrusos' en nuestros cúmulos a medio *redshift*, encontrando que la contaminación de galaxias delante del cúmulo es negligible, de acuerdo con los resultados encontrados por Fasano et al. (2000). La contaminación de fondo ha sido corregida, excluyendo las galaxias más rojas que la CMR debido al effecto-k cosmológico, y usando la información de *redshift*, si la hay. Hemos comprobado que la sustracción, especialmente en la población brillante, está de acuerdo con la extracción que provee las cuentas de campo, encontrando un excelente acuerdo hasta el limite de completitud con los campos de sustracción proporcionados por McLeod et al. (1995).

- Hemos ajustado la relación Color-Magnitud (CMR) para nuestra muestra hasta el correspondiente límite de completitud ($M_r = -19.5$ para NOT y $M_r = -17.8$ para ACS). Los resultados del ajuste para los diez cúmulos tienen una dispersión muy pequeña (0.013) y los resultados estan en concordancia con los encontrados en la literatura.

- La Relación Color-Magnitud ha sido examinada, encontrando que seis cúmulo de 10 tienen una población de galaxias espirales dominante sobre la población de galaxias tempranas, mientras que cuatro cúmulos tienen el comportamiento contrario. La población brillante de galaxias is casi toda temprana, definiendo la secuancia roja. Las BCGs son galaxias elípticas en todos los casos, excepto en el caso de A1643, cuya BCG es una galaxia lenticular algo más débil.

- Hemos comparado los resultados encontrados para la CMR de la muestra con una muestra a bajo *redshift*, López-Cruz et al. (2004), encontrando un acuerdo excelente con ellos. Obtenemos un valor medio para las pendientes de nuestra muestra de -0.050 ± 0.014, que es el mismo valor que nuestra muestra, junto con la de López-Cruz et al. (2004),-0.05 ± 0.008. Además, esos valores son muy similares a la pendiente extraida por Mei et al. (2006) para dos cúmulos a $z \approx 1.26$. Este hecho apoya la no-variación de la CMR hasta *redshift* ≈ 0.3 como mínimo y muy probablemente a mayor *redshift*. En otras palabras, la población estelar para las galaxias tempranas brillantes se formó justo después de la formación de la galaxia.

- Hemos investigado sobre el posible efecto Butcher-Oemler, estudiando la fracción de galaxias azules, f_b the la población galáctica brillante, $M_r \leq -20$, para la muestra de cúmulos en dos aperturas para la muestra NOT, 420 kpc y 735 kpc y una apertura de 475 kpc para la muestra ACS. Esas aperturas han sido consideradas como sustituto de valor canónico de Butcher & Oemler (1984) de R_{30}. Esos valores son consistentes con los valores encontrados en la literatura.

- Hemos encontrado un buena concordancia para las fracciones de azules de De Propris et al. (2004); Aguerri et al. (2007), incluso a pesar de casos destacables como A1878, que también esta reflejada en muestras a bajo *redshift*, (De Propris et al., 2004; Varela, 2004; Aguerri et al., 2007). Por lo tanto, la diversidad parece ser la tendencia más remarcable hasta este rango de redshift, $z \sim 0.3$.

- Hemos realizado una clasificación visual de los tipos morfológicos en galaxias Elípticas, Lenticulares, Espirales e Irregulares. Para probar la consistencia de la clasificación, la hemos comparado con diferentes clasificaciones visuales realizadas en la literatura para la población galáctica de los cúmulos en común. Hemos encontrado que la muestra NOT alcanza un acuerdo del 70% con la clasificación dada por Fasano et al. (2000). A1689, CL0024 y MS1358 obtienen un 75%, 76.74% y 66.6% de tipos morfológicos idénticos, respectivamente, de su comparación con las muestras de Teague, Carter & Gray (1990); Duc et al. (2002) (para A1689), Treu et al. (2003) (para CL0024) y Fabricant, Franx & van Dokkum (2000) (para MS1358). La muestra con el mayor número de galaxias en común (CL0024, con 80 galaxias) es la que, también tiene mayor concordancia.

- Hemos calculado también el parámetro de concentración de nuestra muestra, excepto para el caso de A2658, el cúmulo con menor área cubierta. Hemos comparado esos valores con dados por Butcher & Oemler (1978), a bajo *redshift* y Dressler et al. (1997) a *redshift* mayor. Encontramos que nuestros valores de concentración barren todo el rango de valores medidos para ambas muestras. Además tres cúmulos se encuentra en la parte baja de los valores de concentración, de acuerdo con las tendencias remarcadas por Butcher & Oemler (1978); Dressler et al. (1997) que los cúmulos más

irregulares, menos concentrados podrían estar poblados por galaxias de tipo tardío.

- La tasa de sistemas en interacción en nuestra muestra también se ha tenido en consideración. Hemos calculado el parametro de perturbación, f, introducido por Varela et al. (2004) para tener en cuenta las fuerzas de marea de cada galaxia. Encontramos valores de mediana de -1.85 y -1.76 para la muestra NOT y ACS respectivamente, mientras que el valor mediano encontrado en el Cúmulo de Coma, Varela et al. (2004), es -2.7. De hecho, encontramos que un 63.97% de las galaxias del NOT y un 60.05% de los cúmulos de la ACS, tienen parametros de perturbación mayores que -2, que es el valor escogido por Varela et al. (2004) para seleccionar sistemas en interacción. Por lo tanto, esos resultados sugieren la presencia de una mayor interacción en nuestros cúmulos, con respecto a Coma.

- Hemos afrontado el análisis del brillo superficial para la población galáctica de la muestra NOT. Hemos examinado el brillo superficial utilizando la rutina GASP-2D, Méndez-Abreu et al. (2008). Previamente, hemos realizado cinco mil simulaciones ajustando una componente de Sersic y dos componentes, Sersic+ Disco a galaxias simuladas con el fin de comprobar la fiabilidad de los resultados. A partir de las simulaciones, hemos obtenido que la superficie mínima para obtener resultados que no se vean afectados por las condiciones de la imagen, para las galaxias en una y dos componentes, son 550 y 800 píxeles respectivamente. Este area se corresponde con la magnitud, obteniendo una magnitud mínima de -19.5 pixeles para el área minima de 550 píxeles. También hemos visto que las galaxias con $m_r > 20$, brillo superficial del bulbo, $\mu_{0,B} > 25.3$, brillo superficial del disco, $\mu_{0,D} > 25.3$ y $B/T > 0.7$, no proporciona un buen ajuste en dos componentes y, por tanto, se ajustará en una componente.

- Hemos elaborado un algoritmo para decidir si una galaxia determinada debería ser ajustada en una o dos componentes, asegurando que el ajuste final en dos componentes consiste en galaxias reales en dos componentes (bulbo+disco). Este algoritmo está basado en un enfoque similar al de Allen et al. (2006) para el MGC. La clasificación final nos da un 47% de galaxias con áreas mayores que 800 píxeles que se ajustan mejor por un pérfil de una componente-Sersic, mientras que el 52% se ajusta mejor por dos componentes (perfiles Sersic+Disco).

- Hemos asignado una clasificación morfológica quantitativa basándonos en los resultados de los perfiles de brillo superficial. Hemos considerado tres tipos principales: Tempranas (E/S0), Espirales tempranas (Spe) y Espirales Tardías (Spl), basándonos en los colores y número de componentes. Encontramos que un 85.7% y sobre un 90% de las galaxias clasificadas en una componente dan un buen acuerdo con la clasificación. Sin embargo, solo un 41.16% y 22% de las galaxias en dos componentes concuerdan en el tipo morfológico.

- También se ha comparado la clasificación morfológica visual para A2218, con el método de clasificación quantitativa basada en los parámetros de Sersic obtenidos por Sánchez et al. (2007) con un acuerdo del 47.05%. Estas comparaciones estan en concordancia con los estudios realizados previamente. Como se ha explorado ampliamente, estos resultados apoyan el hecho de que los métodos quantitativos de clasificación no reproducen las tendencias morfológicas visuales de la población galáctica.

- Asímismo, los parámetros estructurales extraídos del análisis del brillo superficial han sido analizados. Hemos ajustado la relación de Kormendy para los bulbos de las galaxias tempranas.

- Hemos encontrado una dicotomía para los bulbos de las galaxias rojas y azules en una componente en el plano $n - r_e$, permitiéndonos distinguir muy claramente entre tipos tempranos y tardíos. Hemos encontrado diferencias en el plano $r_e - color$ para los bulbos de las galaxias.

- Se ha realizado una comparación entre los parametros estructurales del bulbo con las galaxias en el Cúmulo de Coma, obtenidas de Aguerri et al. (2004). Obtenemos el mismo rango de valores para el radio efectivo, r_e y el parámetro de forma, n para nuestra muestra y Coma, indicando que los bulbos de las galaxias en la muestra NOT se formaron a *redshift* mayores que 0.25 como mínimo.

- En cuanto a los parámetros estructurales del disco, hemos comparado las escalas de los discos en la muestra NOT con las galaxias a bajo *redshift* dadas por Graham (2001) por un lado y por otro, con las escalas de los discos extraidos de la muestra de galaxias del cúmulo de Coma de Aguerri et al. (2004). Interesantemente, hemos encontrado que las escalas de nuestros discos son tan grandes como las de las galaxias de campo, mientras que esos discos en Coma representan solo un pequeño porcentaje. De hecho, está patente un factor dos de diferencia entre los valores medios de Coma y los de nuestra muestra. Además, hemos realizado un test Kolmogov-Smirnov entre esas poblaciones, encontrando que los los discos en Coma son significantemente diferentes de los discos del NOT y los discos de campo de Graham (2001). Estos resultados estan de acuerdo con una hipótesis de evolución en las escalas de los discos comparados con cúmulos a bajo *redshift*.

- El análisis de la distribución espacial se ha realizado estudiando la densidad local de galaxias en la muestra completa de cúmulos. Hemos encontrado que cuatro cúmulo de la muestra de la ACS son mucho más densos que la muestra del NOT, en correlación con su riqueza.

- Se ha investigado la relación Morfología-Densidad. Los resultados muestran, de acuerdo con resultados anteriores a *redshift* más bajos, (Dressler, 1980; Dressler et al., 1997), que las galaxias elípticas están localizadas en regiones más densas de los cúmulos, mientras que las galaxias tardías se

encuentran en regiones menos densas. Sin embargo, si analizamos cada cúmulo individualmente, encontramos que cinco cúmulos están dominados por galaxias tardías en regiones densas (A1643, A1878, A1689, A1703 y A2218), mostrando una diversidad en la relación Morfología-Densidad.

- Resultados similares se han encontrado al analizar la relación morfología-radio. Además, hemos encontrado diferentes tasas de decrecimiento para tipos morfológicos distintos.

- Hemos detectado también siete cúmulos de diez dominados por una población temprana, dos cúmulos más con población tardía dominando el núcleo y un cúmulo con una población muy similar. Además, dos cúmulos de diez, muestran poblaciones significantemente diferentes, indicando una segregación morfológica, que no es evidente a bajo *redshift*, (Adami, Biviano & Mazure, 1998).

- Hemos explorado ampliamente la Función de Luminosidad de la muestra y su ajuste más adecuado. Hemos concluido, después de analizar numerosos métodos, que para nuestra muestra de cúmulos, especialmente la del NOT, que es menos profunda que la muestra del ACS, el ajuste más adecuado viene dado por la Función de Luminosidad Compuesta, con los siguientes valores $\alpha = -1.15$ y $M^* = -21.38$ para la muestra NOT y $\alpha = -1.11$ y $M^* = -21.64$ para la muestra ACS, consistente con los valores encontrados en la literatura.

- Para la muestra ACS, hemos observado un incremento en la parte débil, en magnitudes en torno a $M_r = -17.5$, que son más débiles que nuestro limite de completitud, en concordancia con resultados de Biviano et al. (1995); Parolin, Molinari & Chincarini (2003); Boué et al. (2008), que muestran la necesidad de establecer diferentes funciones para describir el final débil de la función de Luminosidad.

- Se ha analizado la función de luminosidad para diferentes tipos morfológicos. No se ha podido ajustar adecuadamente su Función de Luminosidad Compuesta. Hemos encontrado valores de $\alpha = -0.5$ para tipos tempranos y tardíos, que están en los extremos de los límites del ajuste, indicando la no convergencia. Este hecho se puede deber a las grandes barras de error en el espaciado en magnitud, o adicionalmente, la necesidad de funciones de luminosidad diferente de la de Schechter para el ajuste.

- La Función de Luminosidad para diferentes colores de galaxias, sin embargo, muestra diferentes tendencias para la población roja y azul de la muestra. Encontramos pendiente planas, ($\alpha \approx$ -0.8) y $M^* \approx -21.1$ para la población roja, mientras que la población azul tiene una pendiente mucho más pronunciada que las rojas, (sobre $\alpha \approx -1.3$) con valores mucho más débiles de M^* (sobre ≈ -22.50). Estos resultados están de acuerdo con las conclusiones dadas por Barkhouse, Yee & López-Cruz (2007) y van en

el sentido, como algunos autores han sugerido, (Binggeli, Sandage & Tammann, 1988; Barkhouse, Yee & López-Cruz, 2007), de la Universalidad de la Función de Luminosidad.

9.3.2 Galaxia Más Brillante del Cúmulo

- La parte final de la tesis, ha sido dedicada al estudio de las Galaxias Más Brillantes del Cúmulo (BCGs, en inglés). Hemos desarrollado un algorimo para la extracción de la BCG del potencial del cúmulo sin cambiar sus propiedades y las propiedades de las demás galaxias. Los resultados muestran un extracción de calidad.

- Hemos estudiado el grado de dominancia de las BCGs en el cúmulo, mostrando un decrecimiento del grado de dominancia para las BCGs en rayos-X más débiles. Sin embargo, las BCGs extraidas de los cúmulos no emisores de rayos-X no muestran ninguna tendencia significativa con la magnitud de la BCG.

- Tres BCGs de diez, experimentan un factor dos de diferencia entre el grado de dominancia y la diferencia en magnitud con el segundo miembro más brillante. Este hecho se puede explicar debido al hecho de que dos de estas tres BCGs se encuentran en cúmulos que han mostrado indicios de ser fusiones de dos cúmulos.

- Por otra parte, hemos visto que tres BCGs tienen casi el mismo valor de Grado de Dominancia que la diferencia en magnitud con el segundo miembro más brillante. Dos de estas tres BCGs, tienen un grado de dominancia mayor que 0.65, el valor seleccionado por Kim et al. (2002) para considerar dominante a una BCG.

- No hemos encontrado una relación clara entre el grado de dominacia y el *redshift*, con la excepción del caso no significativo de CL0024, el cúmulo mas distante de la muestra, que tiene el menor grado de dominancia.

- En cuanto a la relación de la clase de riqueza del cúmulo con el grado de dominancia, no hemos encontrado tendencias evidentes. Sin embargo, las BCGs situadas en los cúmulos mas ricos se extienden en todos los rangos de grados de dominancia, mientras que la dispersión parece ser menor en cúmulos más pobres.

- Hemos analizado la naturaleza de galaxias cD de nuestra muestra de BCGs, asegurando que tres de 10 BCGs al menos, (en los cúmulos A1952, A2218 y MS1358) son galaxias cD.

- Se ha realizado el análisis del brillo superficial de las BCGs. Hemos encontrado que en ningún caso, el ajuste de ley de de Vaucouleurs ajusta bien para las BCGs de nuestra muestra, al contrario que las galaxias elipticas normales. Encontramos, que el ajuste de Sersic da buenos resultados para

siete de diez BCGs, dando valores altos del parámetro en la mayoría de los casos.

- Dos BCGs más, las situadas en los cúmulos MS1358 y A1703 estan bien descritas por una ley de Sersic y un disco exponencial. Sin embargo, el perfil de A2218 no se puede describir bien por ninguno de estos perfiles. Una posible explicación podría ser que la naturaleza de *merging* de este cúmulo, (Kneib et al., 1995; Machacek et al., 2002), pudiera haber distorsionado la influencia ambiental del cúmulo.

- Hemos incluido el Diagrama de Hubble en la banda-K, que se ha demostrado que es muy adecuado para estudiar la evolución de la BCG, (Aragón-Salamanca, Baugh & Kauffmann, 1998; Brough et al., 2002; Collins & Mann, 1998). Nuestras BCGs se situan el Diagrama de Hubble encontrando una dispersión global de 0.268, mientras que si consideramos solo las BCGs situadas en la muestra de la ACS (cúmulos en rayos-X y más ricos), encontramos una dispersión de 0.235.

Bibliography

Abell G.O., 1958, ApJS, 3, 211

Abell G.O., 1962, *in IAU Symp. 15, Problems of Extra-Galactic Research, ed. G. C. McVittie (New York: Macmillan), 213*

Abell G.O., 1964, ApJ, 140,1624

Abell G.O., 1965, ARA&A, 3,1

Abell G.O., 1972, *In External Galaxies and Quasi-Stellar Objects, IAU Symp No 44, ed. D. S. Evans*, p. 341

Abell G.O., Corwin H.C. & Olowin R.P., 1989, AJSS, 70,1

Acton F.S, 1970, *Numerical Methods That Work*, 1990, corrected edition, (Washington: Mathematical Association of America), 464

Adami C., Biviano A., & Mazure, A., 1998, A&A, 331, 439

Aguerri, J.A.L., Balcells, M., & Peletier, R.F., 2001, A&A, 367, 428

Aguerri, J.A.L., Iglesias-Páramo, J., Vílchez J.M., & Muñoz-Tuñón, C., 2004, ApJ, 127, 1344

Aguerri, J.A.L. et al., 2005, AJ, 130, 475

Aguerri, J.A.L., Sánchez-Janssen R., & Muñoz-Tuñón, C., 2007, A&A, 471, 17

Alexov A. & Silva D.R., 2003, AJ, 126, 2644

Allen S.W. et al., 1992, MNRAS, 259, 67

Allen P. D., Driver S. P., Graham A. W., Cameron E., Liske J., & De Propris R., 2006, MNRAS, 371, 2

Amorin R. O. et al., 2007, A&A, 467, 541

Andersson K.E. & Madejski G.M., AJ, 607, 190

Andredakis Y.C., Peletier R.F. & Balcells M., 1995, MNRAS, 275, 874

Andreon S., Davoust E. & Heim T., 1997, A&A, 323, 337

Andreon S., 2004, ARA&A, 416, 865

Andreon S., Quintana H., Tajer M., Galaz G. & Surdej J., 2006, MNRAS, 365, 915

Andreon S., Punzi G. & Grado A., 2005, MNRAS, 360, 727

Aragón-Salamanca A., Ellis R.S., Couch W.J. & Carter D., 1993, MNRAS, 262, 764

Aragón-Salamanca A., Baugh C.M. & Kauffmann G., 1998, MNRAS, 297, 427

Arimoto N. & Yoshii Y., 1987, A&A, 173, 23

Armstrong R.D. & Kung M.T., 1978, Appl Stat, 27, 363

Ascasibar Y., Sevilla R., Yepes G., Müller V. & Gottlöber S., 2006, MNRAS, 371, 193

Ascaso, B., & González-Casado G., 2003, *Estudio comparativo de modelos de distribución de materia en cúmulos de galaxias*, UPC, 1400503621 PT Asc

Ascaso, B., & Moles M., 2007 ApJ, 660L, 89

Ascaso, B., Moles M., Aguerri J.A.L., Sánchez-Janssen R. & Varela J., 2008, A&A, (submitted)

Ascaso, B., Aguerri J.A.L., Moles M. & Sánchez-Janssen R., 2008 (to be submitted)

Ascaso, B., Benitez N., Ford H. & Postman M. , 2008 in preparation

Barkhouse W.A., Yee H.K.C. & López-Cruz O., 2007, AJ, 671, 1417

Baum, W.A., 1959, PASP, 71, 106

Barway S., Kembhavi A., Wadedakar Y., Ravikumar C.D. & Mayya Y.D., 2007, ApJ, 661, 37

Babu G.J. & Singh K., 1983, *Ann. Stat.*, 11, 999

Bautz L.P. & Morgan W.W., 1970, ApJ, 162, 149

Beijersbergen M., Hoekstra H., van Dokkum P. G. & van der Hulst T., 2002, MNRAS, 329, 385

Bekki K., Couch W.J. & Shioya Y., 2002, ApJ, 577, 651

Bender R., Saglia R. P., Ziegler B., Belloni P., Greggio L. & Hopp U., 1998, ApJ, 493, 529

Benítez N., 2000, ApJ, 536, 571

Bernardi M. et al., 2003, AJ, 125, 1882

Bernardi M., Hyde J. B., Sheth R. K., Miller C. J. & Nichol R. C., 2007, AJ, 133, 1741

Berta S. et al., 2006, A&A, 451, 881

Bertin E., & Arnouts S., 1996, A&AS, 117, 393

Binggeli B., Sandage A. & Tarenghi M., 1984, AJ, 89, 64

Binggeli B., Tammann G.A. & Sandage A., 1987, AJ, 94, 251

Binggeli B., Sandage A. & Tammann G.A., 1988, ARA&A, 26, 509

Binggeli B. & Jerjen H., 1998, A&A, 333, 17

Bird C.M., 1994, AJ, 107, 1637

Biviano A. et al. 1995, ARA&A, 297, 610

Blakeslee, J. P., Anderson, K. R., Meurer, G. R., Benítez, N., & Magee, D., 2003, in ASP Conf. Ser. 295, Astronomical Data Analysis Software and Systems XII, ed. H. E. Payne, R. I. Jedrzejewski, & R. N. Hook (San Francisco: ASP), 12, 257

Böhringer H. et al., 2000, AJSS, 129, 435

Böhringer H., Soucail G., Mellier Y, Ikebe Y. & Schuecker P., 2000, ARA&A, 353, 124

Bonamente M. et al. 2006, AJ, 647, 25

Bonnarel F. et al. 2000, A&AS, 143, 33

Boué G., Adami C., Durret F., Mamon G.A. & Cayatte V., 2008, ARA&A, 479, 335

Bower R., Lucey J.R. & Ellis R. S. 1992a, MNRAS, 254, 589

Bower R., Lucey J.R. & Ellis R. S. 1992b, MNRAS, 254, 601

Bower R. G., Kodama T. & Terlevich A., 1998, MNRAS, 299, 1193

Broadhurst T., Huang X., Frye B. & Ellis R., 2000, ApJ, 534, 15

Broadhurst T. et al., 2005, ApJ, 621, 53

Broadhurst T. et al., 2005, AJ, 619, 43

Brodie J.P. & Huchra J.P., 1991, ApJ, 379, 157

Brough S., Collins C. A., Burke D. J., Mann R. G. & Lynam P. D., 2002, MNRAS, 329, L53

Brough S., Collins C. A., Burke D. J., Lynam P. D. & Mann R. G., 2005, MNRAS, 364, 1354

Buote D.A., 2002, *X-Ray Observations of Cluster Mergers: Cluster Morphologies and Their Implications*, 79, 272

Burke D.J., Collins C.A. & Mann R.G., 2000, ApJ, 532, 105

Butcher H., & Oemler A., 1978, ApJ, 226, 559

Butcher H., & Oemler A., 1984, ApJ, 285, 426

Byun Y.I. & Freeman K.C., 1995, ApJ, 448, 563

Cannon D.B., Ponman T.J. & Hobbs I.S., 1999, MNRAS, 302, 9

Caon, N., Capaccioli, M., & D'Onofrio, M., 1993, MNRAS, 265, 1013

Caon, N. et al., 2005, ApJS, 157, 218

Coe D., Benítez N., Sánchez S. F., Jee M., Bouwens R. & Ford H., 2006, AJ, 132, 926

Charlot S., Worthey G. & Bressan A., 1996, ApJ, 457, 625

Colless M.M., 1989, MNRAS, 237, 799

Colley W.N., Tyson J.A. & Turner E.L., 1996, ApJ, 461, 83

Collins C.A. & Mann R.G., 1998, MNRAS, 297, 128

Consolice C.J, Gallagher J.S. & Wyse R.F.G., 2001, ApJ, 559, 791

Crawford C.S., Allen S.W., Ebeling H., Edge A.C. & Fabian A.C, 1999, MNRAS, 306, 857

Crawford K., 2005, S&T, 110, 123

Curtis H.D., 1918, *Pub.Lick Obs.*, 13, 55

Czoske O. et al., 2001, ARA&A, 372, 391

de Jong R.S., 1996, A&A, 313, 45

De Jong R. S., 1996, A&AS, 118, 557

De Lucia G. et al., 2004, ApJ, 610, 77

De Lucia G. et al., 2007, MNRAS, 374, 809

De Lucia G. & Blaizot J., 2007, MNRAS, 375, 2

De Propris R. et al., 2003, MNRAS, 342, 725

De Propris R., Stanford S.A., Eisenhardt P.R. & Dickinson M., 2003b, AJ, 598, 20

De Propris R. et al., 2004, MNRAS, 351, 125

De Propris R. et al., 2007, ApJ, 666, 212

de Souza R.E., Gadotti D. & dos Anjos S., 2004, ApJS, 153, 411

de Vaucouleurs G., 1948, *Ann d'Astrophys.*, 11, 247

de Vaucouleurs G., 1959, *Handbuch der Physik*, 53, 275

de Vaucouleurs G., 1963, ApJS, 8, 31

Demarco R., Magnard F., Durret F. & Márquez I., ARA&A, 407, 437

Diego J.M., Sandvik H.B., Protopapas P., Tegmark M., Benítez N. & Broadhurst T., 2005, MNRAS, 362, 1247

Djorgovski S. & Davis M., 1987, ApJ, 313, 59

Dressler A., 1978, ApJ, 223, 765

Dressler A., 1980, ApJ, 236, 351

Dressler A., 1984, ARA&A, 22, 185

Dressler A., Lynden-Bell D., Burstein D., Davies R.L., Faber S.M., Terlevich, R & Wegner G., 1987, ApJ, 313, 42

Dressler A. & Gunn J.E., 1992, ApJS, 78, 1

Dressler A. et al., 1997, ApJ, 490, 577

Driver S.P, Phillipps S., Davies J.I., Morgan I. & Disney M.J., 1994, MNRAS, 268, 393

Driver S.P et al., 2006, MNRAS, 368, 414

Dubinski J., 1998, ApJ, 502, 141

Duc P.A. et al., 2002, ARA&A, 382, 60

Edge A. C., 1991 MNRAS, 250, 103

Efron B. & Tibshirani R., 1986, *Stat. Sci.*, 1, 54

Efstathiou G., Ellis R.S. & Peterson B.A., 1988, MNRAS, 232, 431

Eliche-Moral M.C., Balcells M., Aguerri J.A.L. & González-García A.C., 2006, A&A, 457, 91

Ellingson E., Lin H., Yee H.K.C. & Carlberg R.G., 2001, ApJ, 547, 609

Ellis R.S., et al., 1997, ApJ, 483, 582

Estrada J. et al., 2007, ApJ, 660, 1176

Faber S.M. & Gallagher J.S., 1976, ApJ, 204, 365

Fabian A.C., Nulsen P.E.J. & Canizares C.R., 1982, MNRAS, 201, 303

Fabricant D., McClintock J.E. & Bautz M.W., 1991, AJ, 381, 33

Fabricant D., Franx M. & van Dokkum P., 2000, AJ, 539, 577

Fasano, G., Poggianti B., Couch W.J., Bettoni D., Kjaergaard P. & Moles M., 2000, A&A, 542, 673

Fasano, G., Bettoni D., D'Onofrio M., Kjaergaard P. & Moles M., 2002, A&A, 387, 26

Fasano, G. et al., 2006, ARA&A, 445, 805

Fetisova T.S., 1982, *Soviet Astron.*, 25, 647

Ferrarese L. et al., 2006, AJSS, 164, 334

Fisher D., Illingworth G. & Franx M., 1995, ApJ, 438, 539

Fisher D., Fabricant D., Franx M. & van Dokkum P., 1998, AJ, 498, 195

Fitchett M., 1988, MNRAS, 230, 161

Fletchter R., 1970, *Comput Journal*, 13, 317

Franceschini et al., 1998, AJ, 506, 600

Freeman, K.C., 1970, ApJ, 160, 811

Frei Z. & Gunn J.E., 1994, AJ, 108, 1476

Gaidos E.J., 1997, AJ, 113, 117

Gal R.R. et al., 2003, AJ, 125, 2064

Garilli B., Maccagni D., Carrasco L. & Recillas E., 1995, in ASP Conf. Ser. 86, Fresh Views of Elliptical Galaxies (San Francisco:ASP), 297

Garilli B., Bottini D., Maccagni D., Carrasco L. & Recillas E., 1996, ApJS, 105, 191

Gerhard O.E. & Fall S.M., 1983, MNRAS, 203, 1253

Gioia I.M. & Luppino G.A., 1994, ApJS, 94, 583

Godwin J. G & Peach J. V.,1977, MNRAS, 181, 323

González R.E., Lares M., Lambas D.G. & Valotto C., 2006, ARA&A, 445, 51

Goto T. et al., 2003, PASJ, 55, 739

Goto T., 2005, ApJ, 621, 188

Graham A., Lauer T. R., Colless M., & Postman M., 1996, ApJ, 465, 534

Graham A.W., 2001, AJ, 121, 820

Graham A.W. & de Blok W.J.G., 2001, ApJ, 556, 177

Graham A.W. & Guzman, 2003, AJ, 125, 2936

Graham A.W., 2003, AJ, 125, 3398

Griersmith D., 1980, AJ, 85, 1295

Gunn J.E. & Gott J.R., 1972, ApJ, 176, 1

Gunn J.E. & Oke J.B., 1975, ApJ, 195, 255

Hack W.J., 1999, CALACS Operation and Implementation, ISR ACS-99-03

Halkola A., Seitz S. & Pannella M., 2006, MNRAS, 372, 1425

Halkola A., Seitz S. & Pannella M., 2007, AJ, 656, 739

Hansen S.M. et al., 2005, ApJ, 633, 122

Hashimoto Y., Böhringer H., Henry J.P., Hasinger G. & Szokoly G., 2007, ARA&A, 467, 485

Hauser et al., 1995, COBE Diffuse Infrared Background Experiment (DIRBE) Explanatory Supplement. ed. M. G. (Greenbelt, MD: NASA/GSFC)

Henriksen M., Wang Q.D. & Ulmer M., 1999, MNRAS, 307, 67

Hilker M., Mieske S. & Infante L., 2003, ARA&A, 397, 9

Hoekstra H., Marijn F. & Kuijken K., 1998, AJ, 504, 636

Hoessel J.G. & Schneider D.P., 1985, AJ, 90, 1648

Hubble E.P., 1926, ApJ, 64, 321

Hubble E.P., 1936, ApJ, 84, 158

Humason M.L., Mayall, N.U. & Sandage A.R. 1956, AJ, 61, 79

Hubble E. P. & Humason M.L., 1931, ApJ, 74, 43

James F. & Roos M., 1975, *Minuit: A system for Function Minimizations and Analysis of Parameter Errors and Correlations*, Computer Physics Communications, 10, 343

Jarrett T.H., Chester T., Huchra J. & Schneider S., 1998, AAS, 192, 5515

Jones C. & Forman W., 1984, ApJ, 276, 38

Jørgensen, I., Franx M. & Kjaergaard P., 1992, A&AS, 95, 489

Jørgensen, I., 1994, PASP, 106, 967

Jørgensen, I., Franx M. & Kjaergaard P., 1996, MNRAS, 280, 167

Jørgensen, I., Franx M., Hjorth J. & van Dokkum P.G., 1999, MNRAS, 308, 833

Jordán A., Coté P., West M.J., Marzke R.O., Minniti D., & Rejkuba M., 2004, AJ, 127, 24

Kassiola A. & Kovner I., 1993, AJ, 417, 474

Kauffmann G., Guiderdoni B. & White S.D.M., 1994, MNRAS, 267, 981

Kauffmann G., 1996, MNRAS, 281, 487

Kelson D. D., van Dokkum P. G., Franx M., Illingworth G. D., & Fabricant D., 1997, ApJ, 478, L13

Kelson D. D., Illingworth G.D., van Dokkum P. G. & Franx M., 2000, AJ, 531, 159

Kim RS.J., Annis J., Strauss M.A. & Lupton R.H., 2002, ASPC, 268, 395

Kneib J.P. et al., 1995, ARA&A, 303, 27

Kneib J.P., Ellis R.S., Smail I., Couch W.J. & Sharples R.M., 1996, AJ, 471, 643

Kneib J.P., et al., 2003, AJ, 598, 804

Kneib J.P., Ellis R.S., Santos M.R. & Richard J., 2004, AJ, 607, 703

Kodama T., 1999, ASPC, 163, 250

Kodama T., Balogh M.L, Smail I., Bower R.G. & Nakata F., 2004, MNRAS, 354, 1103

Koester B.P. et al., 2007, AJ, 660, 221

Koo D.C., 1985, AJ, 90, 418

Koo D.C., Guzmán R., Gallego J. & Wirth G.D., 1997, AJ, 478, 49

Kormendy J., 1977, ApJ, 217, 406

Kormendy J. & Djorgovski S., 1989, ARA&A, 27, 235

Kotov O., Vikhlinin A., 2005, AJ, 633, 781

Kristian J., Sandage A. & Westphal J.A., 1978, ApJ, 221, 383

Lacey C. & Silk J., 1991, ApJ, 381, 14

Landolt, A. U. 1992, AJ, 104, 340

Lanzetta K.M., Yahil A. & Fernández-Soto A., 1996, *Nature*, 381, 759

LaRoque S.J. et al., 2006, AJ, 652, 917

Lavery R.J. & Henry J.P., 1986, AJ, 304, 5

Lauer T. R. & Postman M., 1994, ApJ, 425, 418

Lauer T. R. et al., 2007, ApJ, 662, 808

Le Borgne J.F., Pelló R. & Sanahuja B., 1992, A&AS, 95, 87

Lieu R., Mittaz J.P.D. & Zhang S., 2006, AJ, 648, 176

Liu Y.T. & Mohr J.J., 2004, AJ, 617, 879

Limousin M. et al., 2008, arXiv:0802.4292v1

Liske J., Lemon D.J. Driver S.P., Cross N.J.G. & Couch W.J., 2003, MNRAS, 344, 307

Loh Y.S. & Strauss M.A. 2006, MNRAS, 366, 373

Łokas E.L., Prada F., Wojtak R., Moles M. & Göttlober S., MNRAS, 366, 26

López-Cruz O., Yee H.K.C., Brown J.P., Jones C. & Forman W., 1997, ApJ, 475, 97

López-Cruz O., Barkhouse W.A., & Yee H.K.C., 2004, ApJ, 614, 679L

Lugger P.M., 1986, ApJ, 303, 535

Lumsden S.L., Collins C.A., Nichol R.C., Eke V.R. & Guzzo L., 1997, MNRAS, 290, 119

Luppino G.A., Cooke B.A., McHardy I.M. & Ricker G.R., 1991, AJ, 102, 1

Madau P., Pozzetti L. & Dickinson M., 1998, ApJ, 498, 106

Machacek M.E., Bautz M.W., Canizares C. & Garmire G.P., 2002, ApJ, 567, 188

MacArthur L.A., Courteau S. & Holtzman, J.A., 2003, ApJ, 582, 689

Malamuth E.M. & Richstone D.O., 1984, ApJ, 276, 413

Margoniner V.E. & De Carvalho R.R., 2000, AJ, 119, 1562

Margoniner V.E., De Carvalho R.R., Gal R.R. & Djorgovski S.G., 2001, ApJ, 548, 143

Markevitch M., 1997, ApJ, 483, 109

Matthews T.A., Morgan W.W. & Schmidt M., 1964, ApJ, 140, 135

Melnick J. & Sargen W.L.W., 1977, ApJ, 215, 401

Merritt D., 1985, ApJ, 289, 18

Metcalfe N., Shanks T., Campos A., McCracken H.J. & Fong R., MNRAS, 323, 795

Miller N. A., Oegerle W. R. & Hill J. M., 2006, ApJ, 131, 2426

Miralda-Escudé J. & Babul A., 1995, ApJ, 449, 18

McGlynn T.A. & Ostriker J.P., 1980, ApJ, 241, 915

McHardy I. M., Stewart G. C., Edge A. C., Cooke B.,Yamashita K. & Hatsukade I., 1990, MNRAS, 242, 215

McLeod B.A., Bernstein G.M., Rieke M.J., Tollestrup E.V & Fazio G.G, 1995, ApJS, 96, 117

Méndez-Abreu J., Aguerri J.A.L, Corsini E. M. & Simonneau E., 2008, A&A, 478, 353

Mei S. et al., 2006, ApJ, 664, 759

Merritt D., 1984, ApJ, 276, 26

Merritt D., 1985, ApJ, 289, 18

Metevier A.J., Koo D.C., Simard L. & Phillips A.C., 2006, AJ, 643, 764

Miller N. A., Oegerle W. R. & Hill J. M., 2006, ApJ, 131, 2426

Mobasher B., Ellis R.S. & Sharples R.M, 1986 , MNRAS, 223, 11

Moles, M., Garcia-Pelayo, J., Masegosa, J., Aparicio, A., & Quintana, J., 1985, A&A, 152, 271

Moles, M., Campos A., Kjaegaard P., Fasano G. & Bettoni D., 1998, ApJ, 495, 31

Moles M. et al., 2004, *The ALHAMBRA SURVEY for a systematic study of cosmic evolution*, Proceedings JENAM

Molinari E., Buzzoni A. & Chincarini G., 1996, A&AS, 119, 391

Möllenhoff, C. 2004, A&A, 415, 63

Montogomery, K. A., Marschall, L.A., & Janes, K. A. 1993, AJ, 106, 181

Morandi A., Ettori S. & Moscardini L., 2007, MNRAS, 379, 518

Morgan W. W., 1958, PASP, 70, 364

Morgan W. W., 1962, ApJ, 135, 1

Moore B., et al. 1996, Nature, 379, 613

Navarro J.F., Frenk C.S. & White S.D.M., 1995, MNRAS, 275, 720

Nelder J.A. & Mead R. 1965, *Computer Journal*, 7, 308

Neumann D.M. & Böhringer H., 1999, AJ, 512, 630

Nelson A.E., González A.H., Zaritsky D. & Dalcanton J.J., 2002, ApJ, 566, 103

Oemler A.Jr., 1973, ApJ, 180, 11

Oemler A.Jr., 1974, ApJ, 194, 1

Oemler A.Jr., 1976, ApJ, 209, 693

Oke J.B. & Sandage A., 1968, ApJ, 154, 21

Ostriker J.P. & Tremaine S.D., 1975, ApJ, 440, 28

Parolin I., Molinari E. & Chincarini G., 2003, ARA&A, 407, 823

Patel P., Maddox S., Pearce F. R., Aragón-Salamanca A. & Conway E., 2006, MNRAS, 370, 851

Patton D.R. et al., 2000, ApJ, 536, 153

Pence W., 1976, ApJ, 203, 39

Peng C.Y., Ho L.C., Impey C.D. & Rix H., 2002, AJ, 124, 266

Pignatelli E., Fasano G. & Cassata P., 2006, ARA&A, 446, 373

Pinkney J., Roettiger K., Burns J.O. & Bird C.M., 1996, AJSS, 104, 1

Piranomonte S. et al., 2001, *in ASP Conf. Ser. 225, Virtual Observatories of the Future, ed. R. J. Brunner, S. G. Djorgovski, & A. S. Szalay (San Francisco: ASP), 73*

Poggianti B.M., 1997, A&AS, 122, 399

Popesso P., Böhringer H., Brinkmann J., Voges W.& York D.G, 2004, ARA&A, 423, 449

Popesso P., Böhringer H., Romaniello M. & Voges W., 2005, ARA&A, 433, 415

Popesso P., Biviano A., Böhringer H. & Romaniello M., 2006, ARA&A, 445, 19

Porter A.C., Schneider D.P. & Hoessel J.G., 1991, AJ, 101, 1561

Postman M. & Lauer T.R., 1995, ApJ, 440, 28

Postman M. et al., 2005, ApJ, 623, 721

Pracy M.B., Driver S.P., De Propris R., Couch W.J & Nulsen P.E.J., 2005, MNRAS, 364, 1147

Pratt G.W., Böhringer H. & Finoguenov A., 2005, ARA&A, 433, 777

Press W.H. & Schechter P., 1974, ApJ, 187, 425

Press W. H. et al., 1992, Numerical recipes in FORTRAN: The art of Scientic Computing (Cambridge: Cambridge Univ. Press)

Prieto M. et al., 2001, A&A, 367, 405

Quilis, V., Moore, B. & Bower, R., 2000, Science, 288,1617

Quintana H., Infante L., Fouque P., Carrasco E.R., Cuevas H., Hertling G. & Nuñez I., AJSS, 126,1

Rakos K.D. & Schombert J.M., 1995, ApJ, 439, 47

Rakos K.D., Dominis D. & Steindling S., 2001, ARA&A, 369, 750

Rakos K.D. & Schombert J.M., 2005, AJ, 130, 1002

Ramella M. et al. 2007, A&A, 470, 39

Reynolds J. H. 1913, MNRAS, 74, 132

Rhee G.F.R.N & Latour H.J., 1991, A&A, 243, 38

Romer A.K. et al., 1994, *Nature*, 372, 75

Rögnvaldsson Ö.E. et al., 2001, MNRAS, 332, 131

Rood H.J., 1969, ApJ, 158, 657

Rood H.J. & Sastry G.N., 1971, PASP, 83, 313

Sánchez-Janssen R., Iglesias-Páramo J., Muñoz-Tuñón C., Aguerri J. A. L. & Vílchez J. M., 2004, *Outskirts of Galaxy Clusters: Intense Life in the Suburbs. Edited by Antonaldo Diaferio, IAU Colloquium*, 195,438

Sánchez S.F., Cardiel N., Verheijen M.A.W., Pedraz S. & Covone G., 2007, MNRAS, 376, 125

Sandage A., 1961, *The Hubble Atlas of Galaxies*, Carnegie Inst. of Wash. Publ. No 618, Washington, D.C.

Sandage A., 1972a, ApJ, 173, 485

Sandage A., 1972c, ApJ, 176, 21

Sandage A., 1972b, ApJ, 178, 1

Sandage A. & Hardy E., 1973, ApJ, 183, 743

Sandage A., 1976, ApJ, 205, 6

Sandage A., Kristian J. & Westphal J.A., 1976, AJ, 205, 688

Sandage A. & Visvanathan N., 1978, ApJ, 223, 707

Sandage A., Tammann G.A. & Yahil A., 1979, ApJ, 232, 352

Sanromà M. & Salvador-Solé E., 1990, ApJ, 360, 16

Sarazin C. L., 1980, AJ, 236, 75

Sarazin C. L., Rood H. J. & Struble M. F., 1982, A&A, 108, 7

Schechter P., 1976, ApJ, 203, 297

Schechter P. & Press W.H., 1976, ApJ, 203, 557

Schlegel D.J., Finkbeiner D.P. & Davis M., 1998, ApJ, 500, 525

Schombert J. M., 1986, ApJS, 60, 603

Schombert J. M., 1987, ApJS, 64, 643

Schombert J. M., 1988, ApJ, 328, 475

Secker J., Harris W.E. & Plummer J.D., 1997, PASP, 109, 1377

Seigar M.S., Graham A.W. & Jerjen H., 2007, MNRAS, 378, 1575

Sersic J.L., 1968, Atlas de Galaxias Australes (Córdoba: Obs. Astron. Univ. Nac)

Shapley H., 1933, *Proc. Nat. Acad. Sci*, 19, 591

Smail I., 1997, ApJ, 479, 70

Smith R.J. et al., 2004, AJ, 128, 1558

Smith G. P., Kneib J.P., Smail I., Mazzotta P., Ebeling H., Czoske O., 2005, MNRAS, 359, 417

Simard L., 1998, *in Astronomical Data Analysis Software Systems VII, ed. R. Albrecht, R. N.Hook & H.A. Bushouse (San Francisco: ASP)*, ASP Conf. Ser., 145, 108

Simard L. et al., 1999, ApJ, 519, 563

Soucail G., Ota N., Böhringer H., Czoske O., Hattori M. & Mellier Y., 2000, A&A, 355, 433

Soucail G., Kneib J.P. & Golse G., 2004, A&A, 417, 33

Stanford S. A., Eisenhardt, P.R. & Dickinson M., 1998, ApJ, 492, 461

Stocke J.T. et al., 1991, AJSS, 76, 813

Stott J.P., Edge A.C., Smith G.P., Swinbank A.M. & Ebeling H., 2008, MNRAS, 384, 1502

Sunyaev R.A. & Zel'dovich Y., 1970, *Comments Astrophys. Space Phys.*, 2, 66

Sunyaev R.A. & Zel'dovich Y., 1972, *Comments Astrophys. Space Phys.*, 4, 173

Struble M.F. & Rood H.R., 1991, ApJS, 77, 363

Taylor A.N., Dye S., Broadhurst T.J., Benítez N. & van Kampen E., 1998, AJ, 501, 539

Teague P.F., Carter D. & Gray P.M., AJSS, 72, 715

Terlevich R., Davies R.L., Faber S.M. & Burstein D., 1981, MNRAS, 196, 381

Thompson L.A. & Gregory S.A., 1993, AJ, 106, 2197

Tonry J.L., 1987, in IAU Symp., 127, *Structure and Dynamics of Elliptcial Galaxies, ed. P.T. de Zeeuw (Dordrecht: Reidel)*, 89

Tremaine S.D. & Richstone D.O., 1977, ApJ, 212, 311

Trentham N., Tully R.B. & Verheijen M.A.W., 2001, MNRAS, 325, 385

Treu T. et al., 2003, AJ, 591, 53

Trevese D et al., 1992, A&AS, 94, 327

Trujillo, I., Aguerri, J.A.L., Cepa J. & Gutiérrez C.M., 2001a, MNRAS, 321, 269

Trujillo, I., Aguerri, J.A.L., Cepa J. & Gutiérrez C.M., 2001b, MNRAS, 328, 977

Trujillo, I., Aguerri, J.A.L., Gutiérrez, C.M., & Cepa, J., 2001, AJ, 122, 38

Trujillo, I. & Aguerri, J.A.L., 2004, MNRAS, 355, 82

Tsuboi M., Miyazaki A., Kasuga T., Matsuo H. & Kuno N., 1998, PASJ, 50, 169

Tully R.B. & Fisher J.R., 1977, ARA&A, 54, 661

Tully R.B., Mould J.R. & Aaronson M., 1982, ApJ, 257, 527

Tyson J.A. & Fischer P., 1995, AJ, 446, 55

Tyson J.A., Kochanski G.P. & Dell'Antonio I.P., 1998, AJ, 498, 107

Uyaniker B., Reich W., Sclickeiser & Wielebinski R., 1997, A&A, 325, 516

van den Bergh S., 1960, *Publications of the David Dunlap Observatory*, 2, 159

van den Bergh S., 1997, AJ, 113, 2054

van Dokkum P. G., & Franx, M. 1996, MNRAS, 281, 985

van Dokkum P.G. et al., 1998, ApJ, 500, 714

van Haarlem M.P., Frenk C.S. & White S.D.M., 1997, MNRAS, 287, 817

Varela J., 2004, Ph.D. Thesis, Universidad Complutense de Madrid

Varela J. et al., 2004, A&A, 420, 873

Visvanathan N., & Griersmith D., 1977, A&A, 59, 317

Visvanathan N., & Sandage A., 1977, ApJ, 216, 214

Visvanathan N., 1981, ARA&A, 100, 20

Wang Q.D., Ulmer M. & Lavery R.J., 1997, MNRAS, 288, 702

Wang Y., Bahcall N. & Turner E.L, 1998, AJ, 116, 2081

Wang, Q.D, Owen, F. & Ledlow, M., 2004, ApJ, 611, 821

Wegner G. et al., 1999, MNRAS, 305, 259

Wheelock, S. L., et al. 1994, IRAS Sky Survey Atlas: Explanatory Supplement (Pasadena: JPL 94-11)

White S.D.M. & Frenk C.S., 1991, ApJ, 379, 52

Whitmore B.C. & Gilmore D.M., 1991, ApJ, 367, 94

Whitmore B.C., Gilmore D.M. & Jones C., 1993, ApJ, 407, 489

Xue S. & Wu X., AJ, 576, 152

Yagi M. et al., 2002, AJ, 123, 87

Yasuda et al., 2001, AJ, 122, 1104

Yee H.K.C., Ellingson E., Morris S.L., Abraham R.G. & Carlberg R.G., 1998, AJSS, 166, 211

Yee H.K.C., Gladders M.D. & López-Cruz O., 1999, ASPC, 199, 166

York D. G., et al. 2000, AJ, 120, 1579

Zemcov M., Borys C., Halpern M., Mauskopf P. & Scott D., 2007, MNRAS, 376, 1073

Zekser K.C. et al., AJ, 640, 639

Zhang Y.Y., Böhringer H., Mellier Y., Soucail G. & Forman W., 2005, ARA&A, 429, 85

Zibetti S., White S. D. M., Schneider D. P., Brinkmann J., 2005, MNRAS, 358, 949

Zwicky F., 1952, PASP, 63, 61

Zwicky F., 1953, *Helvet. phys. acta*, 26, 241

Zwicky F., 1956, *Pro. Third Berkeley Symposium on Mathematical Statistics and Probability*, 3, 113

Zwicky F., Herzog E., Wild P., Karpowick, & Kowal C., 1961-1968, *Catalogue of Galaxies and of Clusters of Galaxies*, Vols 1-6 Pasadena: Calif. Inst. Technol.

Part V

Appendix

Appendix A

Catalogue of galaxies belonging to the NOT sample

Imposible fotografiar el bostezo indolente del Universo

Arturo Pérez-Reverte, 'El pintor de batallas.'

Name	α (J2000)			δ (J2000)			z	M_r	M_B	Morph
A 1643	12:	55:	52.30	44:	05:	47.30		-19.88	-20.46	S
A 1643	12:	55:	52.44	44:	05:	52.70		-19.52	-20.82	
A 1643	12:	55:	54.14	44:	05:	52.70		-19.79	-18.64	
A 1643	12:	55:	59.31	44:	05:	53.20		-19.36	-17.98	
A 1643	12:	55:	53.80	44:	03:	15.20		-19.79	-18.61	S
A 1643	12:	55:	55.18	44:	03:	47.50		-20.67	-19.46	S0
A 1643	12:	55:	49.83	44:	04:	08.80		-19.82	-19.24	
A 1643	12:	55:	49.75	44:	04:	05.50		-20.61	-19.63	S
A 1643	12:	55:	47.93	44:	04:	01.20		-20.36	-19.10	E
A 1643	12:	55:	48.06	44:	04:	06.70		-18.24	-17.09	
A 1643	12:	55:	51.98	44:	04:	05.90		-18.93	-19.06	
A 1643	12:	55:	59.67	44:	04:	05.20		-19.64	-18.62	S
A 1643	12:	55:	53.06	44:	04:	06.60		-18.89	-17.82	
A 1643	12:	55:	55.75	44:	04:	07.30		-19.39	-18.88	
A 1643	12:	56:	01.43	44:	04:	07.90		-19.71	-19.19	
A 1643	12:	55:	53.64	44:	04:	13.70		-20.09	-19.36	S
A 1643	12:	55:	50.96	44:	04:	31.00		-21.15	-20.05	E
A 1643	12:	55:	59.04	44:	04:	26.90		-19.00	-17.81	
A 1643	12:	55:	55.35	44:	04:	34.40		-20.69	-20.35	E
A 1643	12:	55:	54.88	44:	04:	33.90		-20.14	-19.56	S
A 1643	12:	55:	56.61	44:	04:	38.20		-18.70	-20.14	
A 1643	12:	55:	52.33	44:	04:	46.80		-18.42	-19.14	

A 1643	12:	55:	52.97	44:	04:	50.00		-19.82	-19.09	
A 1643	12:	55:	52.96	44:	04:	39.20	0.1978	-19.73	-19.60	S
A 1643	12:	55:	52.70	44:	04:	44.50		-20.42	-19.74	S0
A 1643	12:	55:	54.94	44:	04:	45.60		-19.29	-19.15	
A 1643	12:	55:	48.16	44:	04:	49.50		-19.49	-18.74	
A 1643	12:	55:	47.94	44:	04:	51.60		-19.59	-18.95	
A 1643	12:	55:	51.98	44:	04:	53.10		-19.57	-19.08	
A 1643	12:	55:	55.21	44:	04:	53.10		-18.00	-17.50	
A 1643	12:	55:	54.40	44:	04:	53.70		-18.26	-17.50	
A 1643	12:	55:	59.29	44:	04:	57.10		-20.02	-18.94	S
A 1643	12:	55:	56.07	44:	04:	58.00		-18.49	-17.59	
A 1643	12:	55:	54.00	44:	05:	12.40		-21.61	-20.35	S0
A 1643	12:	56:	01.63	44:	05:	09.10		-19.45	-18.11	
A 1643	12:	55:	49.61	44:	05:	09.50		-18.25	-17.15	
A 1643	12:	55:	47.67	44:	05:	15.70		-18.15	-17.15	
A 1643	12:	55:	54.61	44:	05:	21.40		-19.23	-17.99	
A 1643	12:	55:	53.05	44:	05:	23.40		-20.19	-18.97	S0
A 1643	12:	56:	00.41	44:	05:	29.90		-19.20	-18.91	
A 1643	12:	55:	48.02	44:	05:	35.90		-19.73	-18.91	
A 1643	12:	55:	52.36	44:	05:	38.40		-19.16	-19.35	
A 1643	12:	55:	52.76	44:	05:	37.90		-19.88	-19.97	S
A 1643	12:	55:	54.21	44:	05:	44.70		-19.41	-18.29	
A 1643	12:	56:	01.53	44:	03:	29.90		-18.65	-20.27	
A 1643	12:	55:	50.27	44:	03:	30.50		-19.27	-18.68	
A 1643	12:	55:	53.07	44:	05:	47.80		-18.67	-17.64	
A 1643	12:	55:	48.08	44:	05:	51.70		-18.23	-17.80	
A 1643	12:	55:	34.43	44:	08:	50.30		-19.53	-18.37	
A 1643	12:	55:	44.49	44:	08:	53.60		-19.09	-18.13	
A 1643	12:	55:	45.49	44:	06:	39.60		-18.15	-19.35	
A 1643	12:	55:	44.70	44:	06:	35.60		-19.65	-18.94	
A 1643	12:	55:	38.43	44:	06:	29.90		-18.50	-17.72	
A 1643	12:	55:	38.94	44:	06:	35.20		-18.31	-17.92	
A 1643	12:	55:	45.18	44:	06:	46.30		-19.68	-18.40	E
A 1643	12:	55:	32.98	44:	06:	50.40		-19.92	-19.46	S
A 1643	12:	55:	33.62	44:	06:	30.00		-18.06	-17.72	
A 1643	12:	55:	37.87	44:	06:	57.10		-18.59	-17.40	
A 1643	12:	55:	46.43	44:	06:	58.80		-18.14	-17.06	
A 1643	12:	55:	33.82	44:	07:	12.50		-20.93	-19.67	E
A 1643	12:	55:	36.30	44:	07:	15.70		-18.80	-18.47	
A 1643	12:	55:	41.25	44:	07:	15.00		-18.32	-17.59	
A 1643	12:	55:	39.33	44:	07:	21.30		-19.72	-18.39	S
A 1643	12:	55:	37.74	44:	07:	23.30		-18.00	-17.63	
A 1643	12:	55:	38.60	44:	07:	29.10		-18.09	-16.93	
A 1643	12:	55:	46.75	44:	07:	35.40		-18.99	-17.90	
A 1643	12:	55:	42.78	44:	07:	48.60		-18.24	-16.93	
A 1643	12:	55:	36.40	44:	07:	53.40		-20.71	-20.57	I

A 1643	12:	55:	36.55	44:	07:	54.10		-20.34	-20.10	
A 1643	12:	55:	36.63	44:	08:	20.30		-20.17	-20.49	I
A 1643	12:	55:	36.38	44:	08:	24.40		-19.77	-19.13	S0
A 1643	12:	55:	36.57	44:	08:	30.40		-20.27	-19.84	E
A 1643	12:	55:	43.31	44:	08:	28.90		-18.20	-18.04	
A 1643	12:	55:	38.31	44:	08:	38.70		-18.02	-17.76	
A 1643	12:	55:	37.59	44:	06:	21.10		-19.42	-18.66	S
A 1878	14:	12:	54.12	29:	16:	16.60		-18.74	-17.61	
A 1878	14:	12:	49.83	29:	13:	40.60		-18.90	-18.43	
A 1878	14:	12:	47.43	29:	13:	55.50		-18.53	-20.39	
A 1878	14:	12:	47.82	29:	13:	53.40		-21.69	-20.68	S
A 1878	14:	12:	53.32	29:	13:	47.00		-18.37	-18.29	
A 1878	14:	12:	54.23	29:	13:	57.60		-20.23	-20.50	S
A 1878	14:	12:	50.11	29:	13:	59.90		-18.63	-19.32	
A 1878	14:	12:	49.97	29:	14:	02.60		-20.45	-19.30	S
A 1878	14:	12:	56.80	29:	14:	03.60		-20.38	-20.06	I
A 1878	14:	12:	54.78	29:	14:	03.90		-18.55	-17.39	
A 1878	14:	12:	47.17	29:	14:	05.80		-20.04	-19.70	I
A 1878	14:	12:	49.47	29:	14:	09.90		-21.57	-20.53	S
A 1878	14:	12:	49.03	29:	14:	07.80		-18.94	-21.00	
A 1878	14:	12:	52.50	29:	14:	11.40		-20.94	-20.28	S
A 1878	14:	12:	54.85	29:	14:	17.30		-19.91	-19.67	S
A 1878	14:	12:	54.65	29:	14:	23.80		-19.23	-19.19	
A 1878	14:	12:	47.85	29:	14:	17.10		-19.70	-18.95	
A 1878	14:	12:	54.15	29:	14:	19.30		-20.80	-19.49	E
A 1878	14:	12:	52.75	29:	14:	20.20		-18.72	-20.18	
A 1878	14:	12:	52.18	29:	14:	28.40	0.2220	-22.36	-21.69	E
A 1878	14:	12:	46.85	29:	14:	26.40		-21.02	-20.50	I
A 1878	14:	12:	54.72	29:	14:	31.90		-21.42	-20.23	E
A 1878	14:	12:	56.29	29:	14:	31.40		-20.24	-19.80	I
A 1878	14:	12:	51.24	29:	14:	48.20		-20.10	-20.01	S
A 1878	14:	12:	51.04	29:	14:	39.30		-19.72	-20.22	
A 1878	14:	12:	50.98	29:	14:	42.30		-20.84	-21.55	I
A 1878	14:	12:	46.74	29:	14:	40.00		-18.44	-18.10	
A 1878	14:	12:	53.29	29:	14:	41.40		-20.30	-20.22	
A 1878	14:	12:	53.32	29:	14:	44.60		-19.55	-21.50	
A 1878	14:	12:	49.12	29:	14:	42.50		-21.38	-20.33	S
A 1878	14:	12:	50.12	29:	14:	47.30		-20.40	-19.13	S0
A 1878	14:	12:	52.25	29:	14:	53.70		-20.41	-20.57	S
A 1878	14:	12:	51.99	29:	14:	57.10		-19.53	-19.92	
A 1878	14:	12:	50.96	29:	14:	56.60		-21.29	-20.33	S
A 1878	14:	12:	46.14	29:	14:	55.60		-19.94	-19.35	S0
A 1878	14:	12:	46.58	29:	14:	59.10		-20.94	-19.69	S0
A 1878	14:	12:	53.29	29:	14:	56.90		-18.53	-17.55	
A 1878	14:	12:	48.23	29:	15:	01.10		-19.28	-18.27	
A 1878	14:	12:	50.01	29:	15:	05.00		-18.23	-17.10	

A 1878	14:	12:	56.61	29:	15:	05.30	-19.18	-19.30	
A 1878	14:	12:	49.37	29:	15:	12.10	-18.79	-17.72	
A 1878	14:	12:	50.60	29:	15:	13.20	-18.64	-18.42	
A 1878	14:	12:	49.68	29:	15:	14.20	-19.56	-19.22	
A 1878	14:	12:	55.12	29:	15:	14.70	-18.85	-17.83	
A 1878	14:	12:	51.24	29:	15:	22.10	-19.89	-19.95	S
A 1878	14:	12:	53.39	29:	15:	22.30	-19.01	-18.65	
A 1878	14:	12:	51.04	29:	15:	28.90	-19.51	-21.46	
A 1878	14:	12:	53.49	29:	15:	27.70	-18.76	-18.14	
A 1878	14:	12:	52.60	29:	15:	41.10	-18.61	-18.01	
A 1878	14:	12:	52.43	29:	15:	48.70	-21.00	-19.79	S0
A 1878	14:	12:	55.73	29:	15:	56.70	-18.18	-17.32	
A 1878	14:	12:	53.61	29:	16:	00.80	-19.77	-18.60	
A 1878	14:	12:	53.04	29:	16:	07.40	-18.86	-21.15	
A 1878	14:	12:	47.96	29:	16:	09.50	-19.69	-19.16	
A 1878	14:	13:	00.54	29:	13:	56.90	-21.15	-20.41	S0
A 1878	14:	12:	56.76	29:	14:	03.60	-20.00	-20.14	I
A 1878	14:	12:	56.78	29:	12:	00.30	-19.87	-18.86	S0
A 1878	14:	12:	57.80	29:	12:	01.60	-20.47	-19.97	S0
A 1878	14:	12:	59.05	29:	12:	14.40	-20.60	-20.01	E
A 1878	14:	12:	59.84	29:	12:	19.50	-20.45	-21.96	S
A 1878	14:	13:	00.58	29:	12:	22.90	-20.30	-19.90	S
A 1878	14:	13:	01.89	29:	12:	17.50	-19.55	-18.93	S
A 1878	14:	13:	05.79	29:	12:	20.80	-18.24	-18.48	
A 1878	14:	12:	58.97	29:	12:	33.00	-18.13	-17.07	
A 1878	14:	13:	01.29	29:	12:	36.90	-20.97	-20.65	S0
A 1878	14:	13:	05.52	29:	12:	36.60	-18.59	-18.07	
A 1878	14:	13:	02.23	29:	12:	40.50	-18.23	-18.12	
A 1878	14:	13:	05.38	29:	12:	42.80	-18.24	-17.75	
A 1878	14:	12:	58.42	29:	12:	53.60	-18.05	-19.13	
A 1878	14:	12:	58.26	29:	12:	54.90	-19.49	-20.04	
A 1878	14:	13:	05.59	29:	12:	54.20	-20.53	-19.81	E
A 1878	14:	13:	04.82	29:	12:	55.40	-19.03	-18.41	
A 1878	14:	13:	02.81	29:	12:	55.70	-19.44	-18.73	S
A 1878	14:	12:	58.70	29:	12:	56.60	-18.92	-18.15	
A 1878	14:	13:	04.41	29:	13:	00.70	-20.06	-19.78	S
A 1878	14:	12:	55.45	29:	13:	04.30	-19.48	-19.63	I
A 1878	14:	12:	55.11	29:	13:	09.90	-19.13	-19.64	
A 1878	14:	12:	57.07	29:	13:	19.80	-18.08	-18.08	
A 1878	14:	12:	57.65	29:	13:	22.20	-18.09	-17.93	
A 1878	14:	13:	00.40	29:	13:	37.50	-19.13	-18.71	
A 1878	14:	12:	57.01	29:	13:	43.90	-19.27	-18.62	
A 1878	14:	12:	57.70	29:	13:	48.90	-19.78	-19.18	S0
A 1878	14:	13:	03.99	29:	13:	53.50	-19.36	-19.74	
A 1878	14:	13:	02.65	29:	14:	01.20	-18.08	-18.25	
A 1952	14:	41:	07.84	28:	38:	29.40	-22.05	-21.10	E

A	1952	14:	40:	59.08	28:	38:	35.40	-20.11	-19.24	S
A	1952	14:	41:	01.82	28:	35:	57.10	-20.13	-19.75	S
A	1952	14:	40:	59.60	28:	36:	07.40	-19.18	-18.44	
A	1952	14:	41:	02.64	28:	36:	14.50	-18.79	-18.40	
A	1952	14:	41:	01.57	28:	36:	31.50	-18.30	-18.20	
A	1952	14:	40:	59.42	28:	36:	42.00	-19.05	-18.36	
A	1952	14:	41:	04.07	28:	36:	47.50	-19.94	-19.04	E
A	1952	14:	41:	04.47	28:	36:	49.70	-18.71	-20.59	
A	1952	14:	41:	01.82	28:	37:	09.60	-18.17	-20.22	
A	1952	14:	41:	01.92	28:	37:	14.50	-20.76	-20.80	E
A	1952	14:	41:	02.66	28:	37:	10.00	-22.11	-21.94	S0
A	1952	14:	41:	03.13	28:	37:	10.10	-21.41	-20.84	E
A	1952	14:	41:	02.67	28:	37:	02.40	-20.63	-19.99	
A	1952	14:	40:	58.41	28:	36:	52.50	-19.89	-19.03	S0
A	1952	14:	41:	01.19	28:	37:	00.50	-21.20	-20.33	E
A	1952	14:	40:	59.94	28:	37:	22.10	-18.59	-17.95	
A	1952	14:	40:	59.55	28:	37:	34.20	-18.29	-17.81	
A	1952	14:	41:	01.81	28:	37:	34.70	-19.48	-18.91	
A	1952	14:	41:	01.58	28:	37:	48.30	-18.21	-20.37	
A	1952	14:	41:	01.32	28:	37:	43.20	-21.57	-21.82	E
A	1952	14:	41:	01.53	28:	37:	44.30	-19.21	-18.96	
A	1952	14:	40:	59.15	28:	37:	47.80	-18.93	-20.67	
A	1952	14:	40:	59.50	28:	37:	48.80	-19.90	-19.01	
A	1952	14:	40:	58.98	28:	37:	51.40	-18.41	-18.51	
A	1952	14:	41:	03.17	28:	37:	52.50	-18.10	-17.71	
A	1952	14:	40:	59.94	28:	38:	00.10	-20.38	-19.53	E
A	1952	14:	41:	08.82	28:	37:	59.00	-19.72	-19.04	E
A	1952	14:	41:	05.82	28:	38:	02.20	-18.68	-17.82	
A	1952	14:	41:	00.90	28:	38:	04.70	-19.54	-18.59	
A	1952	14:	41:	04.06	28:	38:	08.40	-19.13	-19.23	
A	1952	14:	41:	07.98	28:	38:	09.40	-19.08	-18.20	
A	1952	14:	41:	03.17	28:	38:	21.10	-18.04	-18.15	
A	1952	14:	41:	05.43	28:	38:	21.80	-19.11	-18.99	
A	1952	14:	41:	02.63	28:	35:	50.80	-18.52	-18.54	
A	1952	14:	40:	59.43	28:	38:	27.20	-19.17	-19.37	
A	1952	14:	41:	01.91	28:	35:	54.80	-19.06	-20.83	
A	1952	14:	40:	59.20	28:	38:	24.20	-19.32	-18.60	
A	1952	14:	41:	13.59	28:	37:	29.60	-22.13	-21.43	S0
A	1952	14:	41:	05.84	28:	37:	41.60	-20.22	-19.27	
A	1952	14:	41:	14.94	28:	37:	42.60	-21.80	-20.98	S0
A	1952	14:	41:	05.68	28:	37:	46.70	-18.22	-18.33	
A	1952	14:	41:	08.53	28:	37:	49.00	-19.26	-19.18	
A	1952	14:	41:	03.16	28:	37:	52.20	-18.08	-17.86	
A	1952	14:	41:	15.18	28:	35:	29.10	-18.16	-20.08	
A	1952	14:	41:	15.04	28:	35:	21.20	-19.32	-21.52	
A	1952	14:	41:	15.18	28:	35:	24.30	-19.61	-21.59	

A 1952	14:	41:	03.94	28:	35:	21.30	-20.35	-19.38	E
A 1952	14:	41:	13.55	28:	35:	21.80	-19.77	-19.72	
A 1952	14:	41:	05.92	28:	35:	29.90	-20.77	-19.82	S0
A 1952	14:	41:	08.36	28:	35:	28.50	-18.46	-18.64	
A 1952	14:	41:	08.59	28:	35:	30.80	-19.01	-19.42	
A 1952	14:	41:	08.51	28:	35:	32.50	-20.41	-20.52	S
A 1952	14:	41:	04.76	28:	35:	32.40	-19.40	-19.16	
A 1952	14:	41:	07.83	28:	35:	32.30	-18.39	-20.48	
A 1952	14:	41:	07.59	28:	35:	35.00	-21.58	-21.23	S
A 1952	14:	41:	11.01	28:	35:	33.00	-19.87	-18.93	
A 1952	14:	41:	10.10	28:	35:	33.70	-19.03	-18.15	
A 1952	14:	41:	05.91	28:	35:	38.50	-19.36	-18.50	
A 1952	14:	41:	08.19	28:	35:	44.50	-21.61	-20.93	S0
A 1952	14:	41:	03.56	28:	35:	44.20	-19.69	-19.45	
A 1952	14:	41:	13.72	28:	35:	54.10	-18.37	-18.45	
A 1952	14:	41:	13.55	28:	35:	52.00	-18.78	-21.38	
A 1952	14:	41:	03.27	28:	35:	56.30	-19.34	-18.51	
A 1952	14:	41:	08.00	28:	36:	03.20	-18.96	-18.97	
A 1952	14:	41:	09.73	28:	36:	02.80	-18.20	-17.44	
A 1952	14:	41:	05.67	28:	36:	05.30	-18.64	-17.72	
A 1952	14:	41:	12.15	28:	36:	07.00	-19.45	-18.73	
A 1952	14:	41:	10.72	28:	36:	07.50	-18.10	-18.28	
A 1952	14:	41:	14.47	28:	36:	26.20	-19.86	-19.18	
A 1952	14:	41:	05.45	28:	36:	26.40	-18.40	-17.58	
A 1952	14:	41:	04.06	28:	36:	26.50	-18.06	-20.09	
A 1952	14:	41:	04.22	28:	36:	27.80	-18.35	-19.37	
A 1952	14:	41:	12.94	28:	36:	27.30	-19.29	-18.61	
A 1952	14:	41:	06.81	28:	36:	31.50	-20.01	-21.90	E
A 1952	14:	41:	07.10	28:	36:	37.30	-20.67	-20.27	E
A 1952	14:	41:	07.03	28:	36:	39.20	-22.10	-22.55	S0
A 1952	14:	41:	03.36	28:	36:	37.10	-20.43	-19.40	E
A 1952	14:	41:	14.04	28:	36:	40.80	-18.80	-18.92	
A 1952	14:	41:	03.11	28:	36:	46.60	-20.74	-19.93	S0
A 1952	14:	41:	04.07	28:	36:	52.70	-19.32	-20.90	
A 1952	14:	41:	03.57	28:	37:	00.30	-22.61	-24.23	E
A 1952	14:	41:	03.14	28:	36:	57.00	-19.55	-21.16	
A 1952	14:	41:	10.75	28:	36:	47.30	-19.16	-21.67	
A 1952	14:	41:	06.34	28:	37:	01.30	-18.75	-18.04	
A 1952	14:	41:	06.48	28:	37:	06.90	-20.14	-19.23	
A 1952	14:	41:	08.25	28:	37:	13.80	-21.85	-21.21	S
A 1952	14:	41:	12.33	28:	37:	11.00	-19.03	-19.11	
A 1952	14:	41:	06.26	28:	37:	12.20	-18.15	-17.28	
A 1952	14:	41:	09.40	28:	37:	13.00	-18.55	-18.59	
A 1952	14:	41:	09.72	28:	37:	17.80	-19.85	-20.07	S
A 1952	14:	41:	05.02	28:	37:	34.90	-18.05	-20.08	
A 1952	14:	41:	06.27	28:	37:	27.50	-20.01	-20.84	S0

A	1952	14:	41:	05.49	28:	37:	33.90		-19.02	-21.47	
A	1952	14:	41:	05.32	28:	37:	35.90		-19.18	-20.34	
A	1952	14:	41:	04.78	28:	37:	31.60		-19.79	-21.64	
A	1952	14:	41:	04.76	28:	37:	35.50		-19.83	-19.94	
A	1952	14:	41:	04.77	28:	35:	05.50		-18.30	-18.55	
A	1952	14:	41:	06.32	28:	37:	18.30		-18.30	-17.78	
A	1952	14:	41:	14.57	28:	37:	18.70		-19.65	-19.37	
A	1952	14:	41:	11.82	28:	37:	19.30		-18.39	-18.59	
A	1952	14:	41:	07.53	28:	37:	23.60		-19.14	-18.20	
A	1952	14:	41:	04.29	28:	37:	23.00		-18.54	-18.27	
A	1952	14:	41:	05.23	28:	35:	06.80		-19.10	-18.75	
A	1952	14:	41:	03.35	28:	37:	29.50		-20.17	-19.26	
A	1952	14:	41:	06.39	28:	37:	33.60		-18.12	-17.60	
A	1952	14:	41:	12.23	28:	35:	06.70		-19.05	-18.27	
A	1952	14:	41:	08.44	28:	35:	09.00		-18.39	-17.78	
A	1952	14:	41:	05.36	28:	37:	40.50		-18.42	-17.71	
A	1952	14:	41:	10.78	28:	35:	12.30		-18.24	-18.05	
A	1952	14:	41:	13.01	28:	35:	15.30		-19.08	-19.23	
A	1952	14:	41:	10.45	28:	35:	16.60		-19.36	-19.26	
A	1952	14:	41:	14.88	28:	35:	29.70		-18.45	-19.98	
A	2111	15:	39:	35.52	34:	26:	56.20		-20.46	-19.56	S
A	2111	15:	39:	37.64	34:	27:	03.80	0.2295	-21.26	-20.22	S0
A	2111	15:	39:	31.84	34:	27:	05.10		-19.01	-18.09	
A	2111	15:	39:	38.48	34:	24:	32.40		-19.37	-18.96	
A	2111	15:	39:	40.16	34:	24:	18.10		-19.38	-18.33	
A	2111	15:	39:	39.34	34:	24:	44.50		-20.26	-19.31	E
A	2111	15:	39:	38.45	34:	24:	51.40		-20.02	-19.08	
A	2111	15:	39:	40.16	34:	24:	55.70		-20.49	-19.27	S0
A	2111	15:	39:	42.76	34:	24:	56.60		-18.32	-17.38	
A	2111	15:	39:	37.84	34:	24:	57.00		-18.55	-17.54	
A	2111	15:	39:	39.81	34:	25:	00.50		-18.06	-17.79	
A	2111	15:	39:	37.21	34:	25:	08.50		-19.67	-18.70	S
A	2111	15:	39:	40.49	34:	25:	27.30	0.2282	-22.67	-21.51	E
A	2111	15:	39:	39.75	34:	25:	23.10		-19.57	-18.85	
A	2111	15:	39:	39.20	34:	25:	11.50		-21.13	-20.38	E
A	2111	15:	39:	39.39	34:	25:	13.40	0.2211	-21.34	-20.61	E
A	2111	15:	39:	36.23	34:	25:	12.10		-20.34	-19.21	S0
A	2111	15:	39:	34.90	34:	25:	14.50		-18.97	-18.02	
A	2111	15:	39:	40.27	34:	25:	34.80		-20.07	-21.06	
A	2111	15:	39:	38.15	34:	25:	18.10		-20.21	-19.01	S0
A	2111	15:	39:	37.53	34:	25:	18.70		-19.62	-18.72	S
A	2111	15:	39:	36.64	34:	25:	29.00		-18.96	-18.34	
A	2111	15:	39:	33.61	34:	25:	34.00		-18.48	-17.78	
A	2111	15:	39:	36.79	34:	25:	39.10	0.2312	-20.90	-19.65	S0
A	2111	15:	39:	39.69	34:	25:	21.20		-20.40	-19.70	
A	2111	15:	39:	31.27	34:	25:	40.00		-20.24	-19.65	

A 2111	15:	39:	38.68	34:	25:	38.90		-18.16	-17.04	
A 2111	15:	39:	37.29	34:	25:	45.90		-18.49	-17.33	
A 2111	15:	39:	36.42	34:	25:	50.10		-20.46	-19.50	E
A 2111	15:	39:	41.20	34:	25:	50.90		-20.53	-19.36	S0
A 2111	15:	39:	40.18	34:	25:	50.80		-18.60	-17.90	
A 2111	15:	39:	33.99	34:	25:	51.30		-19.30	-18.23	
A 2111	15:	39:	37.44	34:	25:	54.80		-20.12	-18.98	E
A 2111	15:	39:	39.52	34:	25:	56.90		-19.23	-18.23	
A 2111	15:	39:	39.91	34:	25:	57.20		-18.53	-17.69	
A 2111	15:	39:	41.69	34:	26:	01.70		-18.03	-16.89	
A 2111	15:	39:	31.72	34:	26:	07.20		-20.49	-19.37	S0
A 2111	15:	39:	36.84	34:	26:	07.20		-20.44	-19.68	I
A 2111	15:	39:	38.07	34:	26:	09.50		-18.64	-19.00	
A 2111	15:	39:	34.11	34:	26:	19.20		-20.80	-20.58	S
A 2111	15:	39:	34.26	34:	26:	12.50	0.2289	-21.97	-21.11	S0
A 2111	15:	39:	38.18	34:	26:	06.90		-19.72	-19.53	
A 2111	15:	39:	32.26	34:	26:	12.80		-19.25	-18.22	
A 2111	15:	39:	38.58	34:	26:	28.20		-20.23	-19.24	S
A 2111	15:	39:	39.03	34:	26:	38.10		-19.29	-19.48	
A 2111	15:	39:	38.70	34:	26:	38.80	0.2246	-20.85	-20.29	S
A 2111	15:	39:	37.81	34:	26:	35.90		-18.12	-17.73	
A 2111	15:	39:	31.99	34:	26:	36.10		-18.39	-18.00	
A 2111	15:	39:	35.47	34:	26:	43.70		-20.70	-19.87	S0
A 2111	15:	39:	41.19	34:	26:	41.30		-20.27	-20.24	I
A 2111	15:	39:	40.90	34:	26:	45.40		-19.28	-19.45	
A 2111	15:	39:	37.59	34:	26:	44.20		-18.92	-18.91	
A 2111	15:	39:	33.13	34:	26:	45.60		-19.25	-18.91	
A 2111	15:	39:	37.16	34:	26:	45.70		-18.26	-17.93	
A 2111	15:	39:	38.38	34:	26:	50.50		-18.01	-17.13	
A 2111	15:	39:	32.78	34:	24:	22.40		-19.21	-18.31	
A 2111	15:	39:	41.34	34:	24:	34.30	0.2294	-20.97	-20.81	S
A 2111	15:	39:	41.81	34:	24:	42.70	0.2292	-22.61	-22.18	E
A 2111	15:	39:	42.27	34:	24:	40.40		-19.08	-20.81	
A 2111	15:	39:	41.26	34:	24:	43.60		-20.43	-22.04	S
A 2111	15:	39:	47.09	34:	27:	37.90	0.2368	-21.25	-20.57	S0
A 2111	15:	39:	42.81	34:	27:	44.60		-19.68	-19.55	I
A 2111	15:	39:	52.99	34:	27:	48.60	0.2297	-20.98	-19.94	S0
A 2111	15:	39:	54.29	34:	25:	06.60		-18.05	-17.24	
A 2111	15:	39:	51.92	34:	25:	18.80		-18.85	-18.83	
A 2111	15:	39:	44.40	34:	25:	22.70		-19.46	-19.41	
A 2111	15:	39:	44.15	34:	25:	21.30		-18.78	-20.66	
A 2111	15:	39:	54.03	34:	25:	24.60		-18.87	-18.31	
A 2111	15:	39:	53.10	34:	25:	26.50		-18.75	-17.73	
A 2111	15:	39:	47.96	34:	25:	32.10		-20.49	-19.52	E
A 2111	15:	39:	52.98	34:	25:	41.10		-19.31	-18.24	
A 2111	15:	39:	43.94	34:	25:	46.70		-19.45	-19.01	

A 2111	15:	39:	42.69	34:	25:	52.10		-18.13	-16.99	
A 2111	15:	39:	42.04	34:	26:	04.00		-19.44	-18.39	
A 2111	15:	39:	42.02	34:	25:	59.60		-18.96	-20.78	
A 2111	15:	39:	44.85	34:	25:	58.50		-19.19	-19.08	
A 2111	15:	39:	47.82	34:	26:	00.00		-19.08	-18.05	
A 2111	15:	39:	53.40	34:	25:	59.60		-18.94	-18.56	
A 2111	15:	39:	52.50	34:	26:	02.20		-20.40	-19.62	S
A 2111	15:	39:	47.49	34:	26:	11.10		-18.84	-18.00	
A 2111	15:	39:	42.59	34:	26:	14.00		-19.82	-18.96	
A 2111	15:	39:	43.06	34:	26:	23.00		-18.42	-17.36	
A 2111	15:	39:	42.02	34:	26:	30.30	0.2258	-22.09	-20.96	E
A 2111	15:	39:	43.25	34:	26:	32.90		-19.02	-18.04	
A 2111	15:	39:	48.31	34:	26:	36.70		-18.79	-18.43	
A 2111	15:	39:	49.35	34:	26:	41.50	0.2299	-21.54	-21.03	S
A 2111	15:	39:	50.11	34:	26:	44.40		-19.48	-19.02	
A 2111	15:	39:	52.85	34:	26:	46.80		-20.45	-19.95	E
A 2111	15:	39:	42.09	34:	26:	49.20		-19.55	-18.52	
A 2111	15:	39:	45.75	34:	26:	57.40	0.2292	-21.07	-20.05	E
A 2111	15:	39:	42.98	34:	27:	00.30		-18.40	-18.28	
A 2111	15:	39:	42.30	34:	27:	02.60		-18.20	-17.92	
A 2111	15:	39:	52.55	34:	27:	07.50		-19.06	-20.58	
A 2111	15:	39:	52.04	34:	27:	07.60		-19.01	-21.29	
A 2111	15:	39:	52.15	34:	27:	12.20		-21.13	-21.23	S
A 2111	15:	39:	42.28	34:	27:	17.10		-20.12	-19.17	
A 2111	15:	39:	51.51	34:	27:	31.30		-19.54	-18.61	
A 2111	15:	39:	48.27	34:	27:	34.80		-18.70	-18.45	
A 2111	15:	39:	47.70	34:	25:	16.40		-19.85	-18.96	
A 2111	15:	39:	47.89	34:	27:	39.90		-20.28	-19.32	E
A 2111	15:	39:	47.34	34:	25:	10.20	0.2309	-21.07	-20.81	E
A 2111	15:	39:	47.26	34:	25:	15.90		-20.43	-20.38	S
A 2658	23:	44:	47.99	-12:	18:	46.20		-19.12	-18.24	
A 2658	23:	44:	55.21	-12:	18:	37.00		-18.98	-18.20	
A 2658	23:	44:	49.55	-12:	18:	34.40		-19.65	-18.99	
A 2658	23:	44:	49.62	-12:	18:	31.90		-18.68	-18.01	
A 2658	23:	44:	50.35	-12:	18:	25.50		-21.89	-21.06	S
A 2658	23:	44:	49.13	-12:	18:	19.80		-19.29	-18.34	
A 2658	23:	44:	47.27	-12:	18:	13.40		-19.24	-19.14	
A 2658	23:	44:	46.97	-12:	18:	10.40		-20.94	-20.12	S0
A 2658	23:	44:	49.36	-12:	18:	07.90		-18.44	-17.53	
A 2658	23:	44:	52.22	-12:	18:	04.60		-19.99	-18.90	E
A 2658	23:	44:	54.99	-12:	18:	05.60		-18.08	-17.23	
A 2658	23:	44:	54.27	-12:	17:	59.30		-21.42	-20.39	E
A 2658	23:	44:	50.42	-12:	17:	56.40		-19.39	-18.41	
A 2658	23:	44:	51.64	-12:	17:	53.30		-18.71	-18.11	
A 2658	23:	44:	47.44	-12:	17:	47.40		-20.92	-19.87	E
A 2658	23:	44:	50.34	-12:	17:	32.70		-18.84	-20.30	

A 2658	23:	44:	49.28	-12:	17:	38.20	-18.19	-19.65	
A 2658	23:	44:	50.26	-12:	17:	20.90	-21.07	-20.35	S0
A 2658	23:	44:	49.84	-12:	17:	26.70	-21.32	-20.95	E
A 2658	23:	44:	49.80	-12:	17:	39.50	-22.39	-22.02	E
A 2658	23:	44:	54.96	-12:	17:	38.80	-18.80	-18.35	
A 2658	23:	44:	55.87	-12:	17:	37.60	-18.22	-17.40	
A 2658	23:	44:	51.86	-12:	17:	35.30	-19.57	-18.55	
A 2658	23:	44:	47.85	-12:	17:	31.10	-18.14	-17.23	
A 2658	23:	44:	50.96	-12:	17:	19.10	-20.24	-19.17	E
A 2658	23:	44:	55.84	-12:	17:	17.60	-20.18	-19.15	S0
A 2658	23:	44:	51.40	-12:	17:	11.00	-18.35	-18.28	
A 2658	23:	44:	56.18	-12:	17:	07.50	-21.14	-20.31	S
A 2658	23:	44:	51.13	-12:	16:	48.00	-20.61	-19.49	E
A 2658	23:	44:	46.13	-12:	16:	49.10	-18.82	-18.35	
A 2658	23:	44:	49.65	-12:	16:	35.80	-20.56	-19.43	S0
A 2658	23:	44:	47.99	-12:	16:	36.20	-18.29	-17.66	
A 2658	23:	44:	51.63	-12:	16:	28.80	-18.70	-17.79	
A 2658	23:	44:	53.27	-12:	16:	23.60	-18.27	-17.77	

Appendix B

Surface Brightness Fit of the NOT clusters galaxies

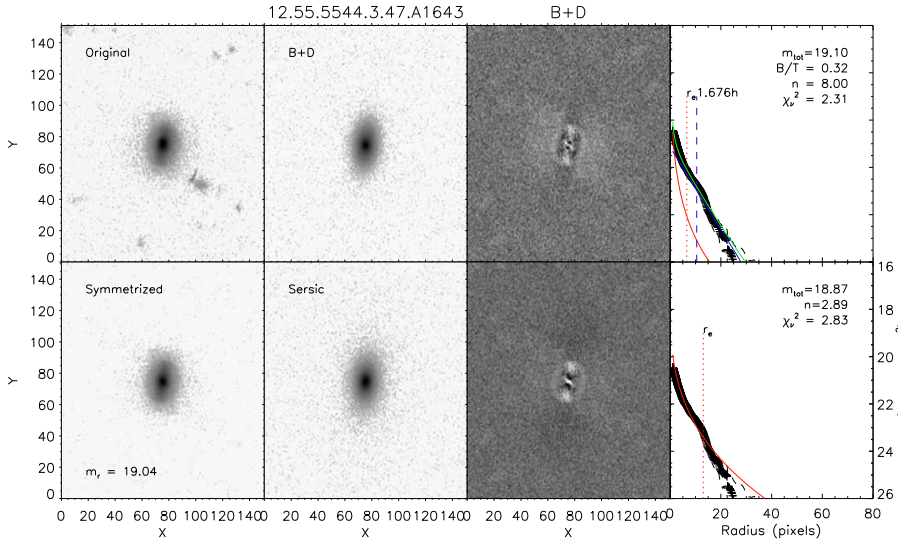

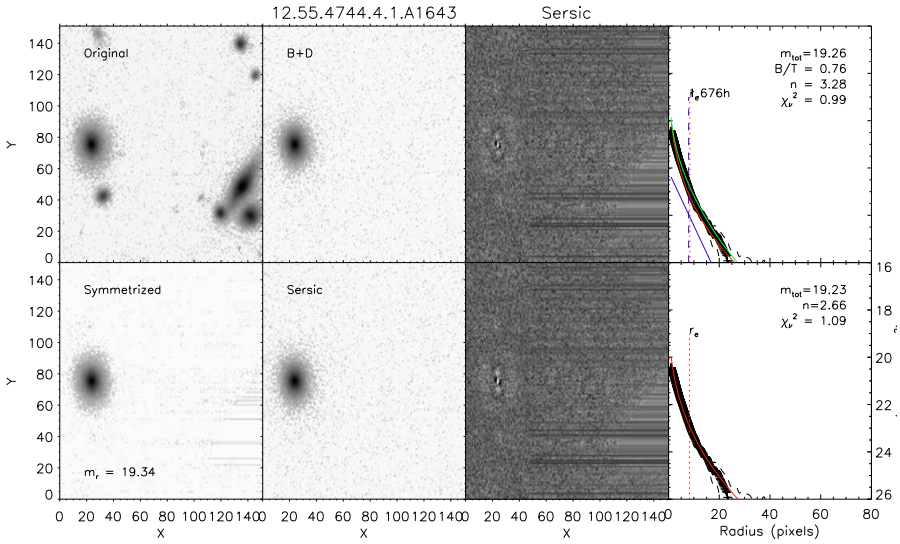
12.55.4744.4.1.A1643
Sersic
Original
B+D
Symmetrized
Sersic
m_r = 19.34
m_tot=19.26
B/T = 0.76
n = 3.28
χ_ν² = 0.99
r_e
1.676h
m_tot=19.23
n=2.66
χ_ν² = 1.09
X
Y
Radius (pixels)

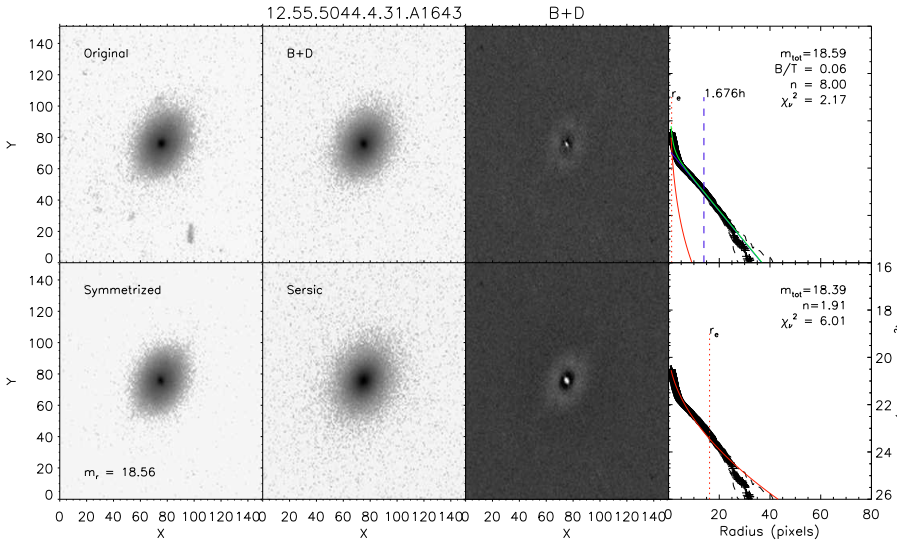
12.55.5044.4.31.A1643
B+D
Original
B+D
Symmetrized
Sersic
m_r = 18.56
m_tot=18.59
B/T = 0.06
n = 8.00
χ_ν² = 2.17
r_e
1.676h
m_tot=18.39
n=1.91
χ_ν² = 6.01
X
Y
Radius (pixels)

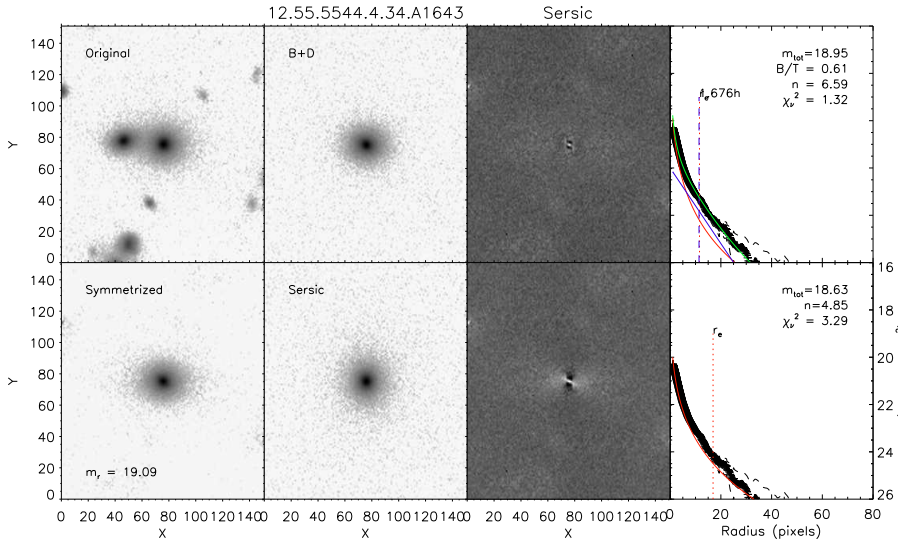
12.55.5544.4.34.A1643
Sersic
Original
B+D
Symmetrized
Sersic
m_r = 19.09
m_tot=18.95
B/T = 0.61
n = 6.59
χ_ν² = 1.32
r_e.676h
m_tot=18.63
n=4.85
χ_ν² = 3.29
r_e
X
Y
Radius (pixels)

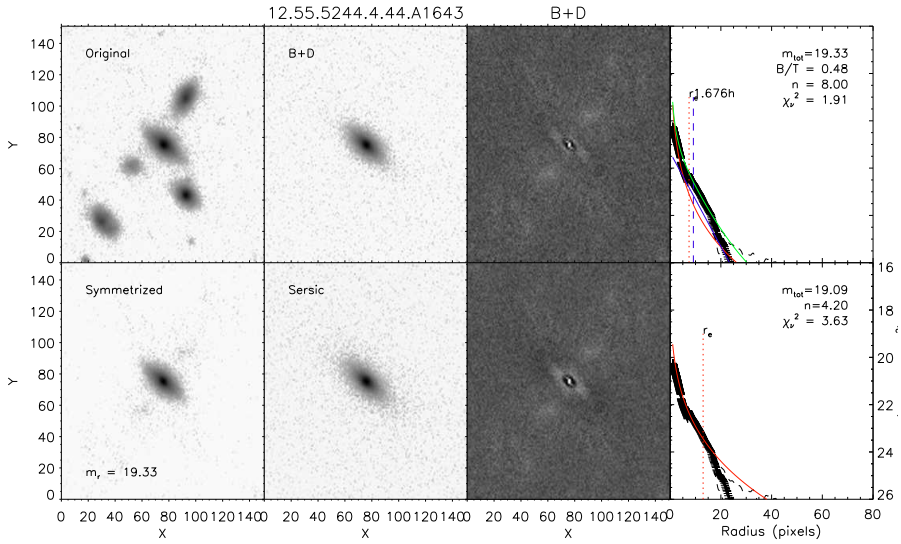
12.55.5244.4.44.A1643
B+D
Original
B+D
Symmetrized
Sersic
m_r = 19.33
m_tot=19.33
B/T = 0.48
n = 8.00
χ_ν² = 1.91
r_e.676h
m_tot=19.09
n=4.20
χ_ν² = 3.63
r_e
X
Y
Radius (pixels)

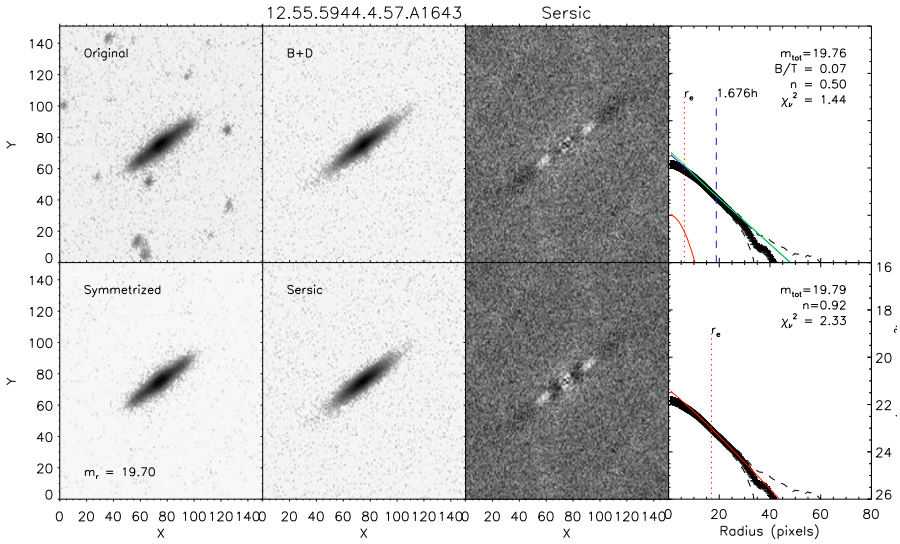
12.55.5944.4.57.A1643
Sersic
Original
B+D
Symmetrized
Sersic
m_tot=19.76
B/T = 0.07
n = 0.50
χ_ν² = 1.44
1.676h
m_tot=19.79
n=0.92
χ_ν² = 2.33
m_r = 19.70
X
Y
Radius (pixels)

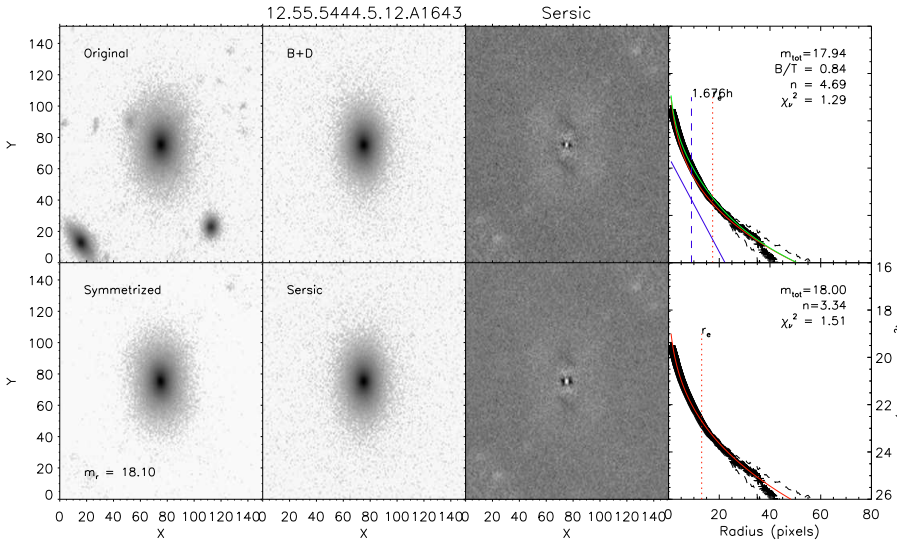
12.55.5444.5.12.A1643
Sersic
Original
B+D
Symmetrized
Sersic
m_tot=17.94
B/T = 0.84
n = 4.69
χ_ν² = 1.29
1.676h
m_tot=18.00
n=3.34
χ_ν² = 1.51
m_r = 18.10
X
Y
Radius (pixels)

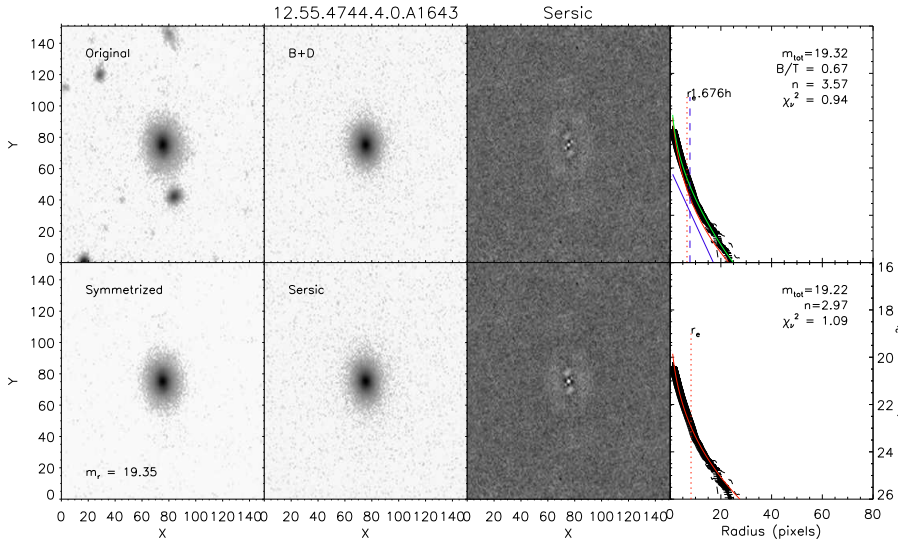
12.55.4744.4.0.A1643
Sersic
Original
B+D
Symmetrized
Sersic
m_r = 19.35
m_tot=19.32
B/T = 0.67
n = 3.57
χ_ν² = 0.94
r_e
1.676h
m_tot=19.22
n=2.97
χ_ν² = 1.09
X
Y
Radius (pixels)

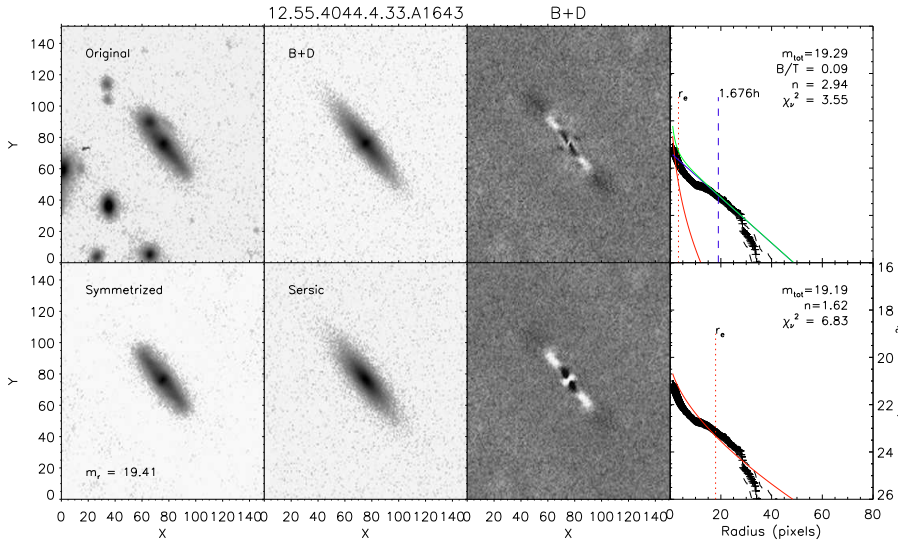
12.55.4044.4.33.A1643
B+D
Original
B+D
Symmetrized
Sersic
m_r = 19.41
m_tot=19.29
B/T = 0.09
n = 2.94
χ_ν² = 3.55
r_e
1.676h
m_tot=19.19
n=1.62
χ_ν² = 6.83
X
Y
Radius (pixels)

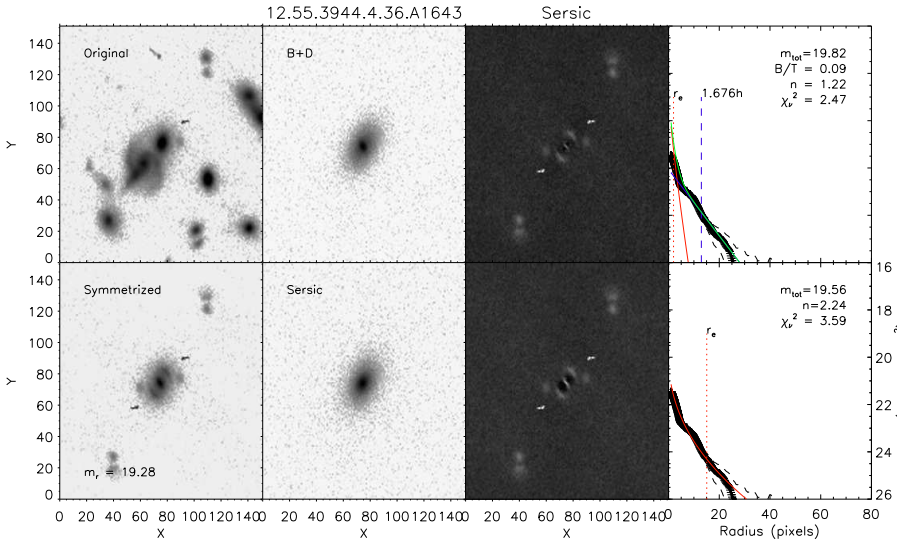
12.55.3944.4.36.A1643
Sersic
Original
B+D
Symmetrized
Sersic
m_tot=19.82
B/T = 0.09
n = 1.22
χ_ν² = 2.47
1.676h
m_tot=19.56
n=2.24
χ_ν² = 3.59
m_r = 19.28
X
Y
Radius (pixels)

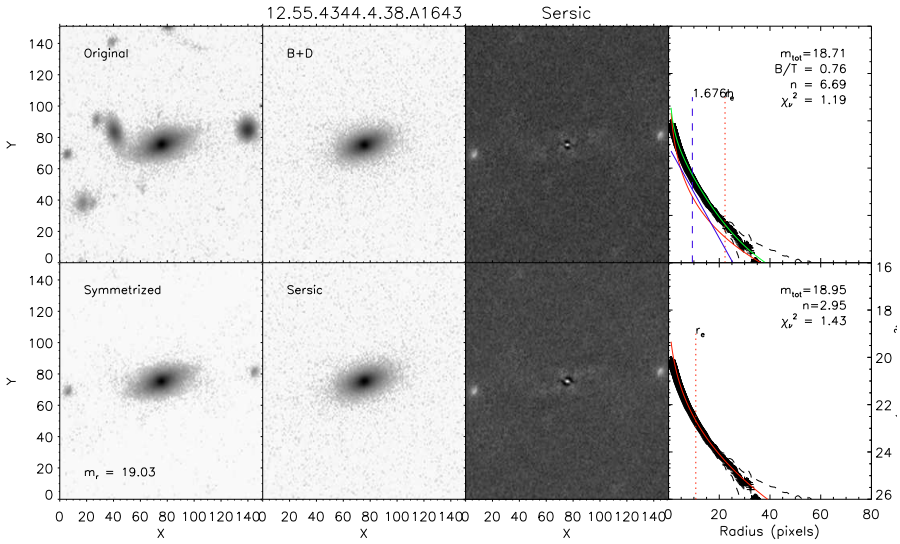
12.55.4344.4.38.A1643
Sersic
Original
B+D
Symmetrized
Sersic
m_tot=18.71
B/T = 0.76
n = 6.69
χ_ν² = 1.19
1.676h
m_tot=18.95
n=2.95
χ_ν² = 1.43
m_r = 19.03
X
Y
Radius (pixels)

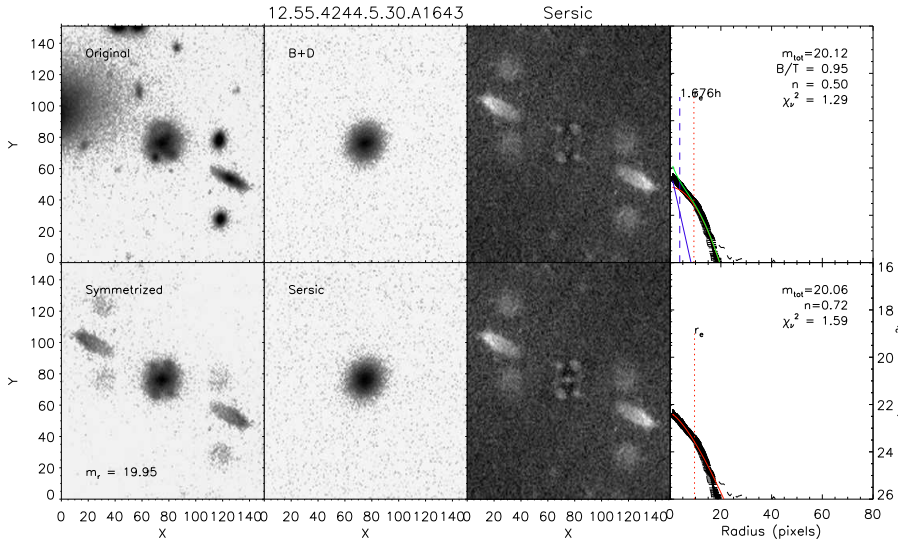
12.55.4244.5.30.A1643
Sersic
Original
B+D
Symmetrized
Sersic
m_r = 19.95
m_tot=20.12
B/T = 0.95
n = 0.50
χ_ν² = 1.29
1.676h
m_tot=20.06
n=0.72
χ_ν² = 1.59
r_e
X
Y
Radius (pixels)

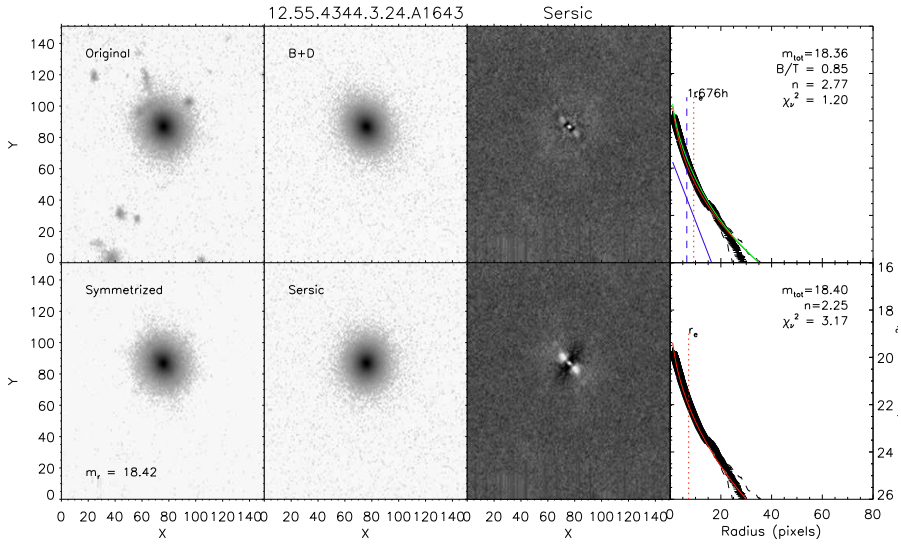
12.55.4344.3.24.A1643
Sersic
Original
B+D
Symmetrized
Sersic
m_r = 18.42
m_tot=18.36
B/T = 0.85
n = 2.77
χ_ν² = 1.20
1.676h
m_tot=18.40
n=2.25
χ_ν² = 3.17
r_e
X
Y
Radius (pixels)

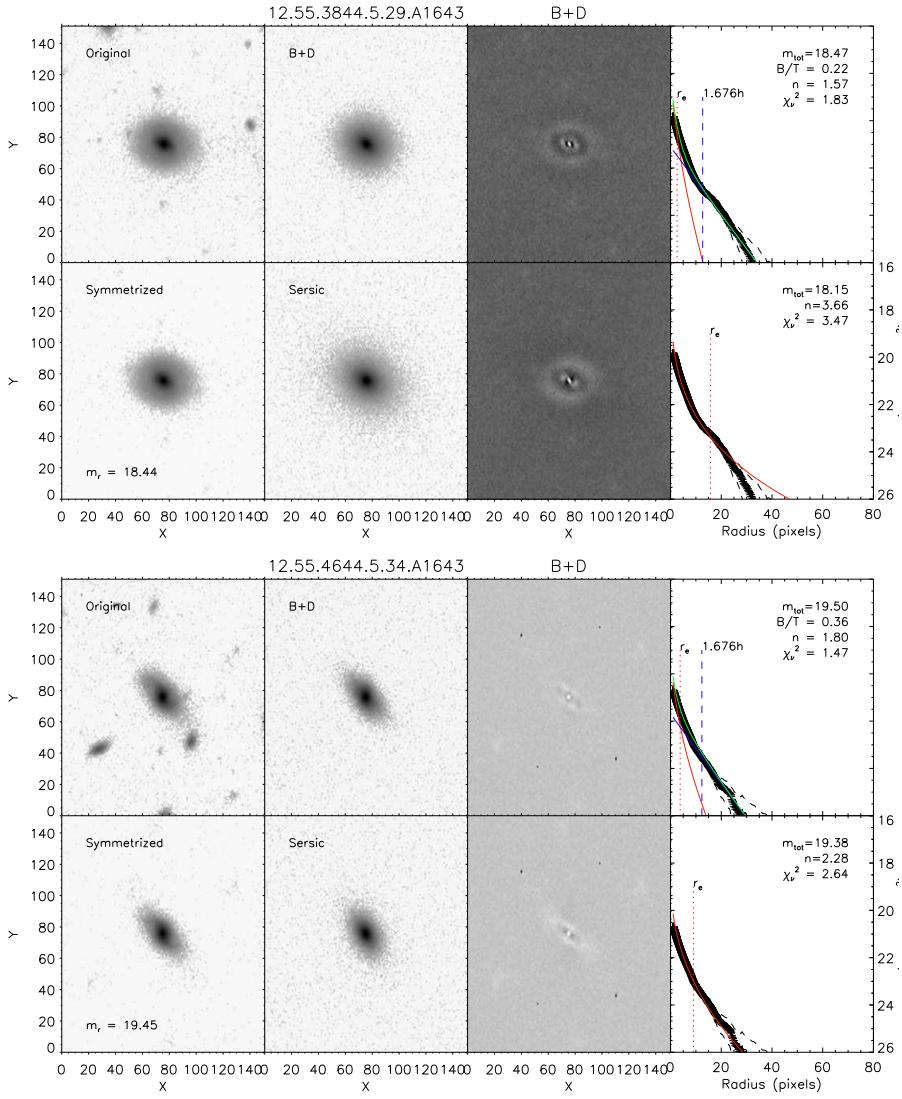
12.55.3844.5.29.A1643
B+D
Original
B+D
Symmetrized
Sersic
m_r = 18.44
m_tot=18.47
B/T = 0.22
n = 1.57
χ_ν² = 1.83
r_e
1.676h
m_tot=18.15
n=3.66
χ_ν² = 3.47
X
Y
Radius (pixels)
12.55.4644.5.34.A1643
B+D
Original
B+D
Symmetrized
Sersic
m_r = 19.45
m_tot=19.50
B/T = 0.36
n = 1.80
χ_ν² = 1.47
r_e
1.676h
m_tot=19.38
n=2.28
χ_ν² = 2.64
X
Y
Radius (pixels)

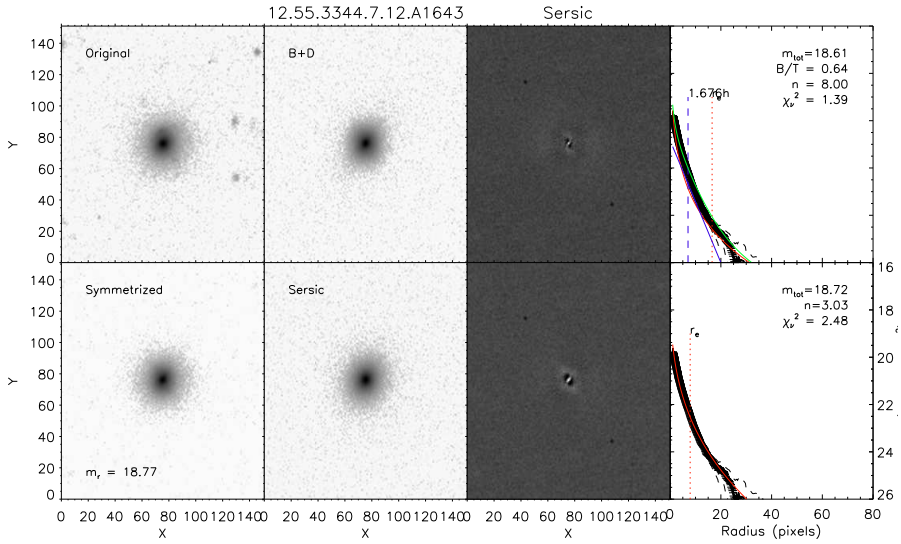
12.55.3344.7.12.A1643
Sersic
Original
B+D
Symmetrized
Sersic
m_r = 18.77
m_tot=18.61
B/T = 0.64
n = 8.00
χ_ν² = 1.39
1.676h
r_e
m_tot=18.72
n=3.03
χ_ν² = 2.48
X
Y
Radius (pixels)

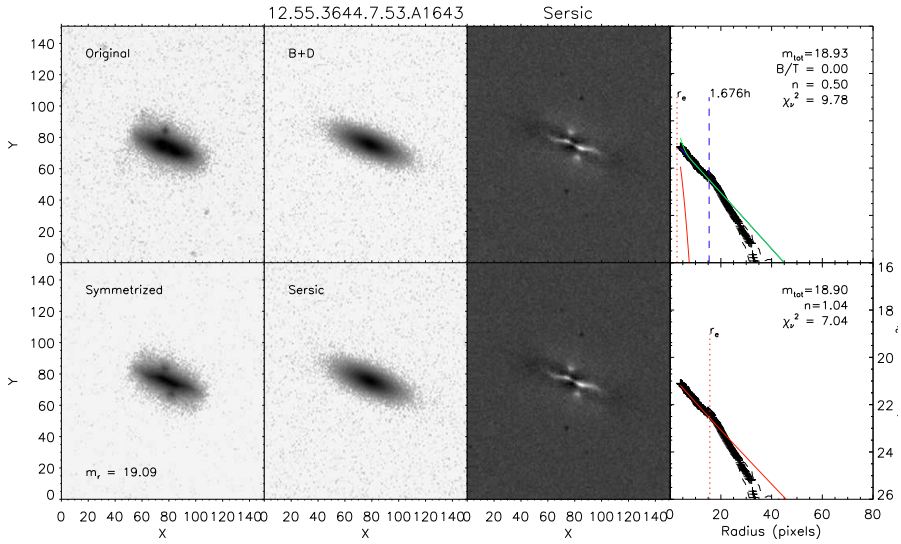
12.55.3644.7.53.A1643
Sersic
Original
B+D
Symmetrized
Sersic
m_r = 19.09
m_tot=18.93
B/T = 0.00
n = 0.50
χ_ν² = 9.78
r_e
1.676h
m_tot=18.90
n=1.04
χ_ν² = 7.04
X
Y
Radius (pixels)

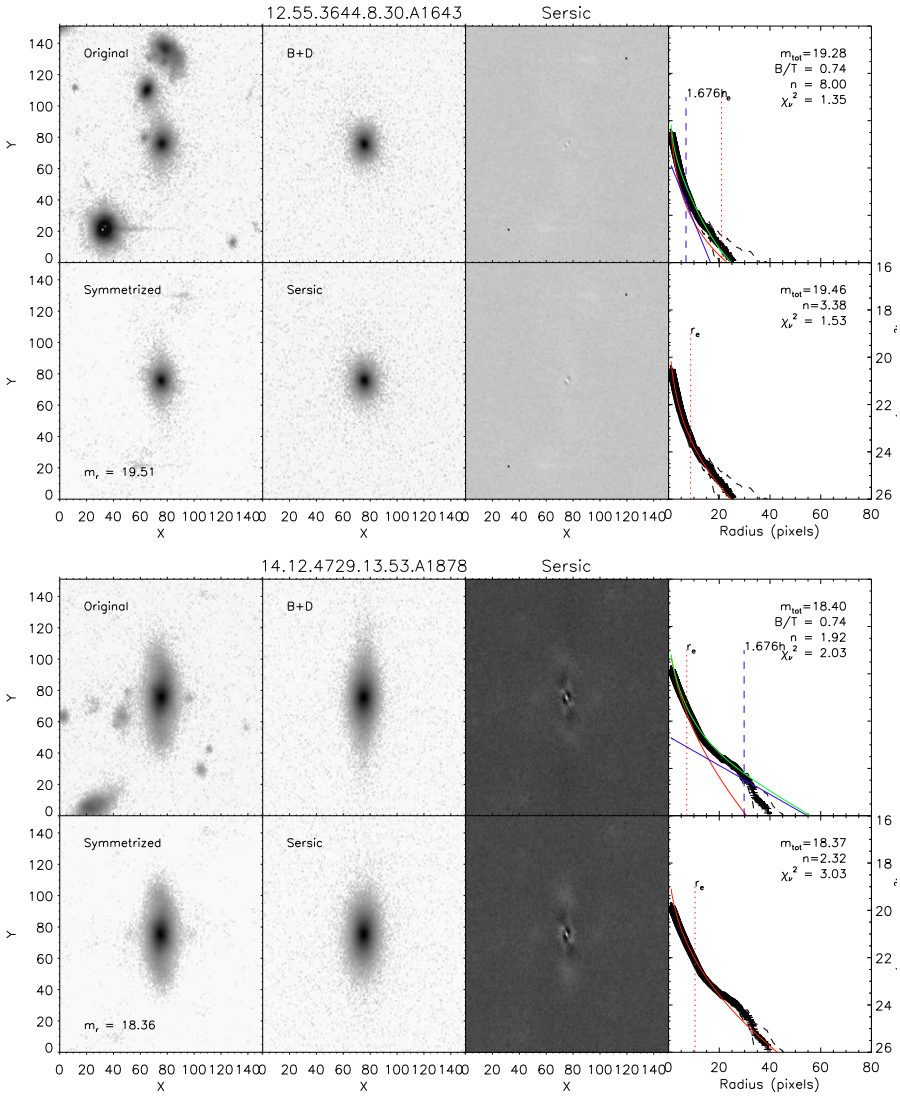
12.55.3644.8.30.A1643
Sersic
Original
B+D
Symmetrized
Sersic
m_r = 19.51
m_tot=19.28
B/T = 0.74
n = 8.00
χ_ν² = 1.35
1.676h_e
m_tot=19.46
n=3.38
χ_ν² = 1.53
r_e
Radius (pixels)
14.12.4729.13.53.A1878
Sersic
Original
B+D
Symmetrized
Sersic
m_r = 18.36
m_tot=18.40
B/T = 0.74
n = 1.92
χ_ν² = 2.03
1.676h_e
r_e
m_tot=18.37
n=2.32
χ_ν² = 3.03
r_e
Radius (pixels)
X
Y

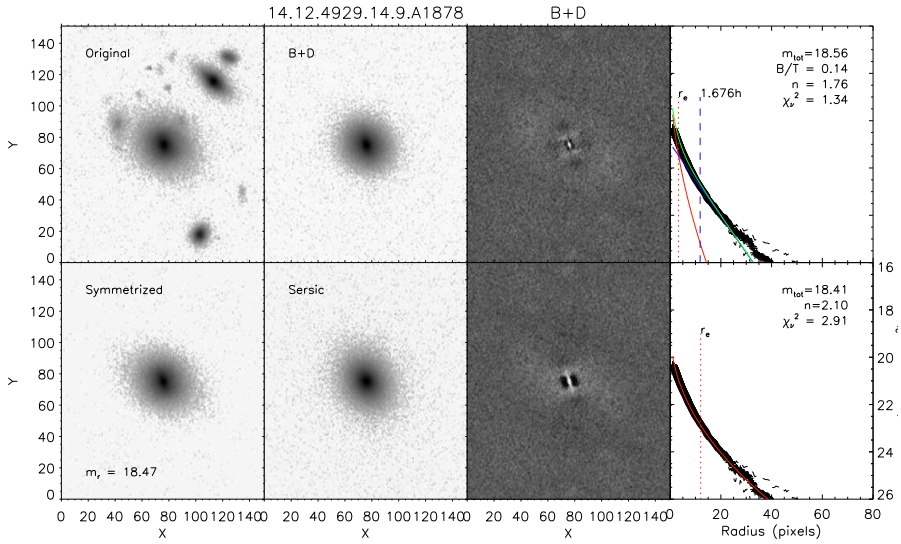
14.12.4929.14.9.A1878
B+D
Original
B+D
Symmetrized
Sersic
m_r = 18.47
m_tot=18.56
B/T = 0.14
n = 1.76
χ_ν² = 1.34
r_e
1.676h
m_tot=18.41
n=2.10
χ_ν² = 2.91
X
Y
Radius (pixels)

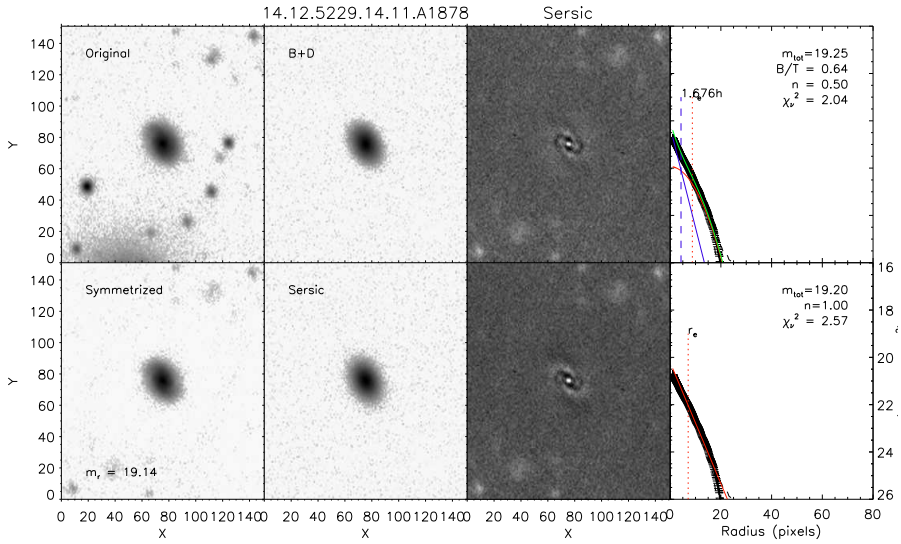
14.12.5229.14.11.A1878
Sersic
Original
B+D
Symmetrized
Sersic
m_r = 19.14
m_tot=19.25
B/T = 0.64
n = 0.50
χ_ν² = 2.04
1.676h
m_tot=19.20
n=1.00
χ_ν² = 2.57
r_e
X
Y
Radius (pixels)

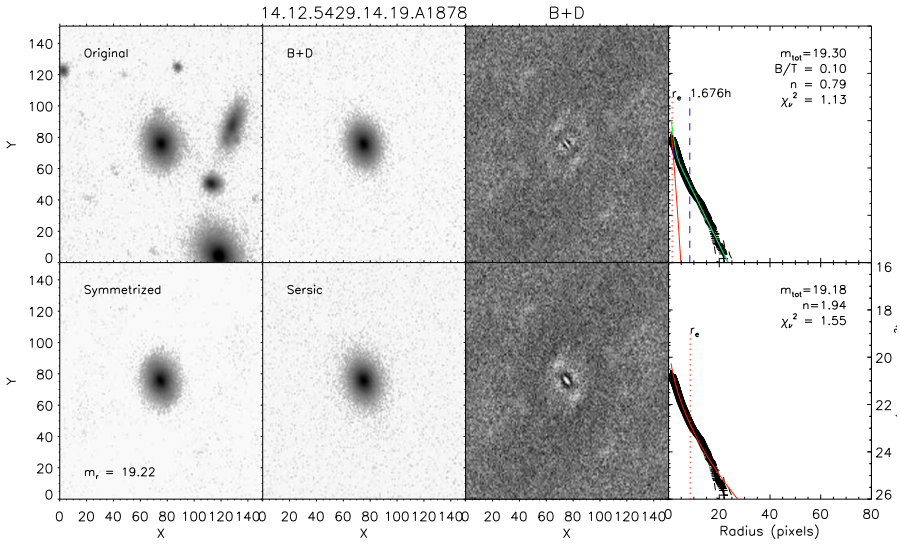
14.12.5429.14.19.A1878
B+D
Original
B+D
Symmetrized
Sersic
m_r = 19.22
m_tot=19.30
B/T = 0.10
n = 0.79
χ_ν² = 1.13
r_e
1.676h
m_tot=19.18
n=1.94
χ_ν² = 1.55
X
Y
Radius (pixels)

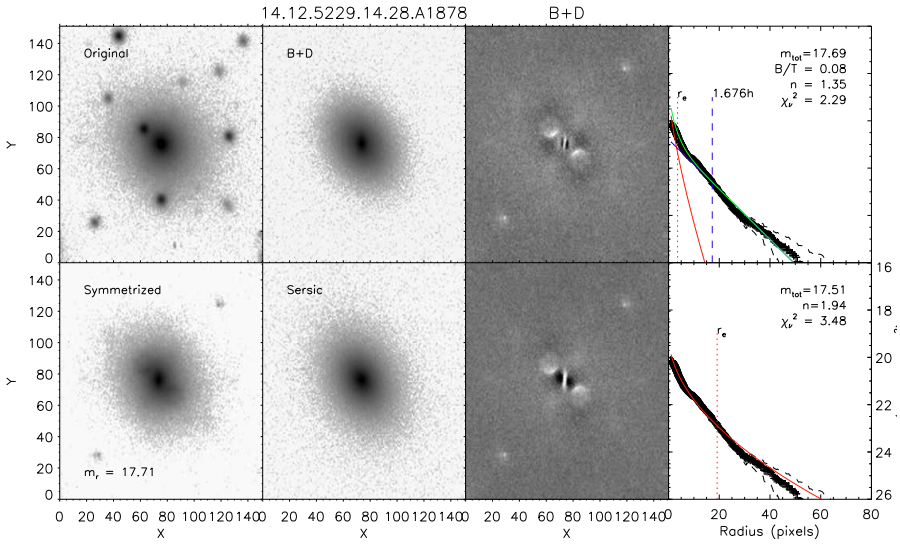
14.12.5229.14.28.A1878
B+D
Original
B+D
Symmetrized
Sersic
m_r = 17.71
m_tot=17.69
B/T = 0.08
n = 1.35
χ_ν² = 2.29
r_e
1.676h
m_tot=17.51
n=1.94
χ_ν² = 3.48
X
Y
Radius (pixels)

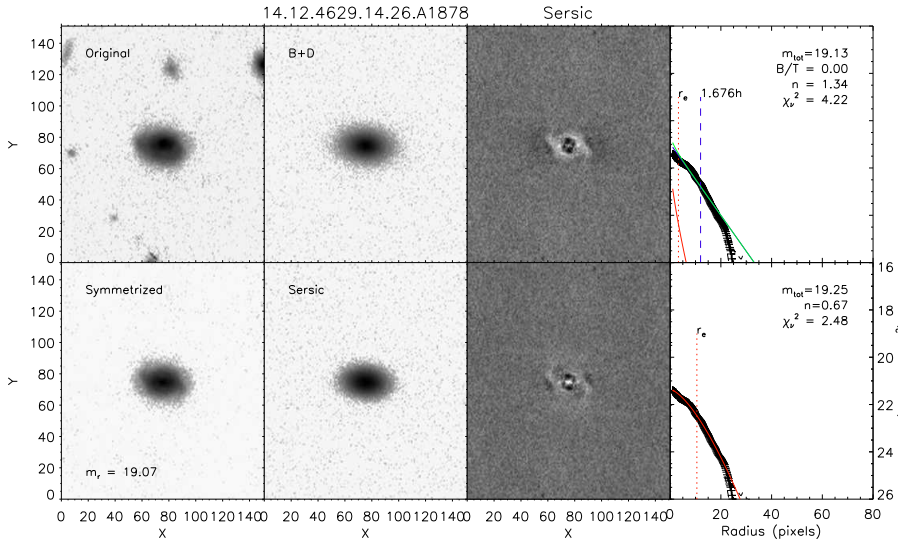
14.12.4629.14.26.A1878
Sersic
Original
B+D
Symmetrized
Sersic
m_r = 19.07
m_tot=19.13
B/T = 0.00
n = 1.34
χ_ν² = 4.22
r_e
1.676h
m_tot=19.25
n=0.67
χ_ν² = 2.48
X
Y
Radius (pixels)

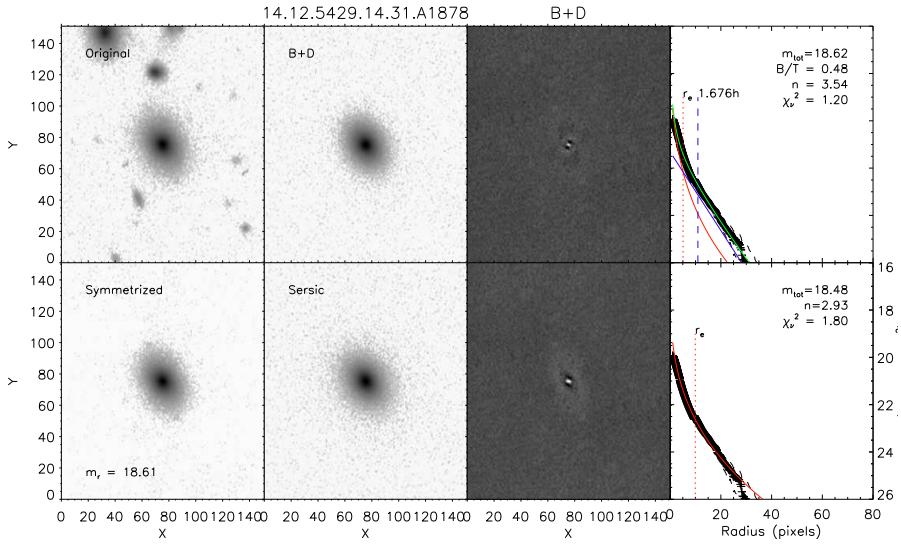
14.12.5429.14.31.A1878
B+D
Original
B+D
Symmetrized
Sersic
m_r = 18.61
m_tot=18.62
B/T = 0.48
n = 3.54
χ_ν² = 1.20
r_e
1.676h
m_tot=18.48
n=2.93
χ_ν² = 1.80
X
Y
Radius (pixels)

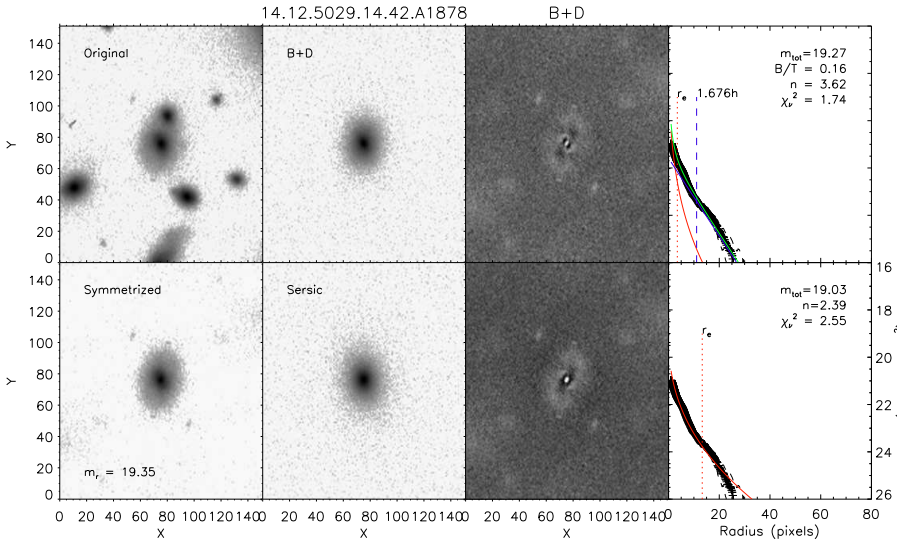
14.12.5029.14.42.A1878
B+D
Original
B+D
Symmetrized
Sersic
m_r = 19.35
m_tot=19.27
B/T = 0.16
n = 3.62
χ_ν² = 1.74
r_e
1.676h
m_tot=19.03
n=2.39
χ_ν² = 2.55
X
Y
Radius (pixels)

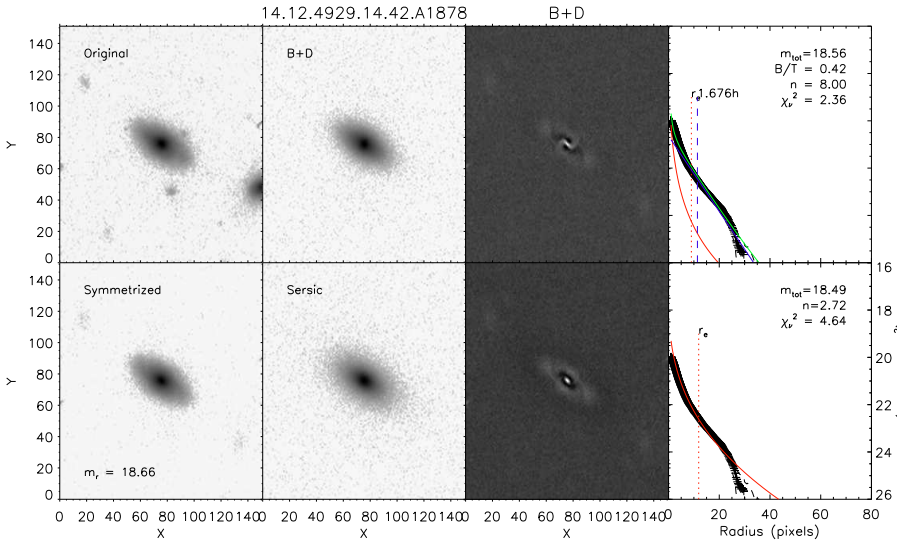
14.12.4929.14.42.A1878
B+D
Original
B+D
Symmetrized
Sersic
m_r = 18.66
m_tot=18.56
B/T = 0.42
n = 8.00
χ_ν² = 2.36
r_e
1.676h
m_tot=18.49
n=2.72
χ_ν² = 4.64
X
Y
Radius (pixels)

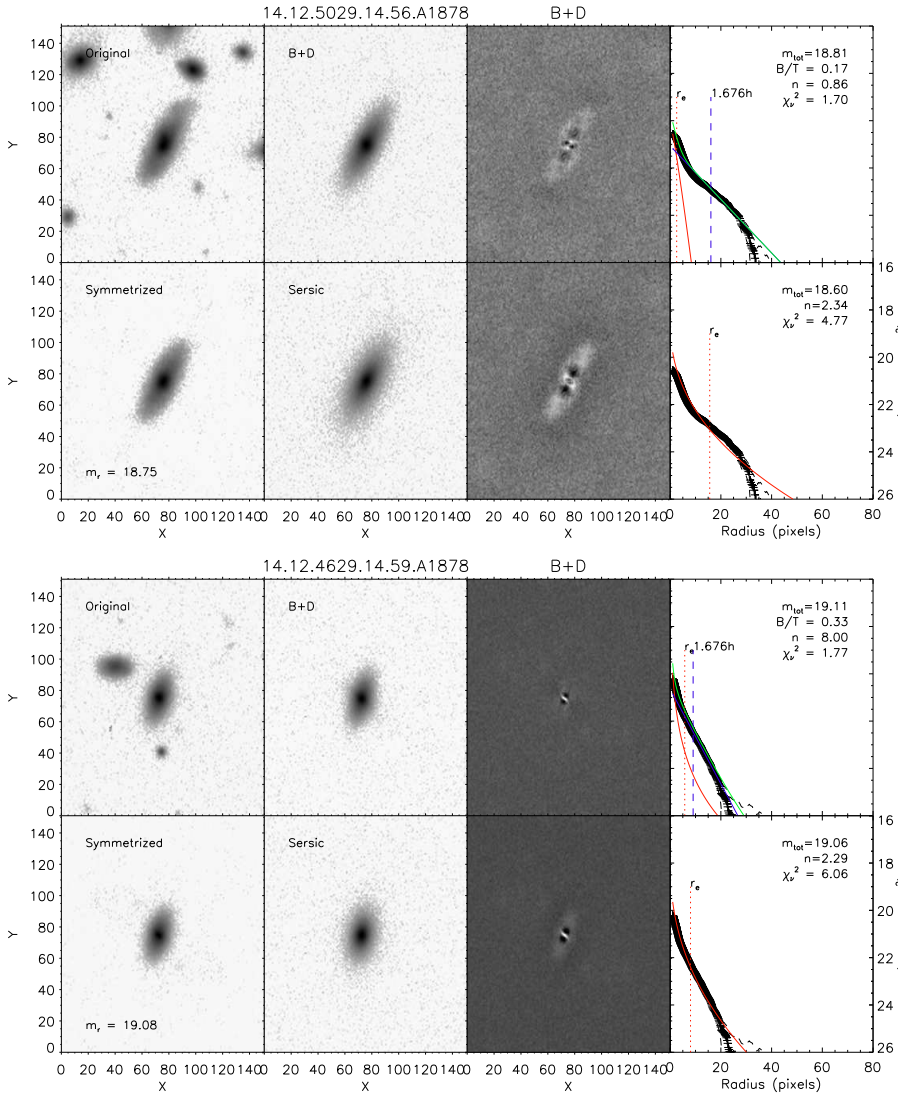
14.12.5029.14.56.A1878
B+D
Original
B+D
Symmetrized
Sersic
m_r = 18.75
m_tot=18.81
B/T = 0.17
n = 0.86
χ_ν² = 1.70
r_e
1.676h
m_tot=18.60
n=2.34
χ_ν² = 4.77
X
Y
Radius (pixels)
14.12.4629.14.59.A1878
B+D
Original
B+D
Symmetrized
Sersic
m_r = 19.08
m_tot=19.11
B/T = 0.33
n = 8.00
χ_ν² = 1.77
r_e
1.676h
m_tot=19.06
n=2.29
χ_ν² = 6.06
X
Y
Radius (pixels)

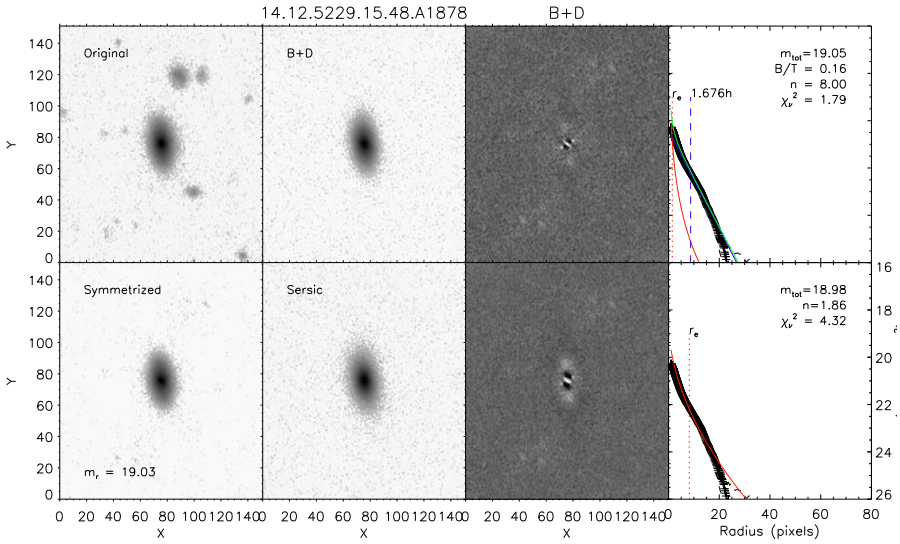
14.12.5229.15.48.A1878
B+D
Original
B+D
Symmetrized
Sersic
m_r = 19.03
m_tot=19.05
B/T = 0.16
n = 8.00
χ_ν² = 1.79
r_e 1.676h
m_tot=18.98
n=1.86
χ_ν² = 4.32
r_e
X
Y
Radius (pixels)

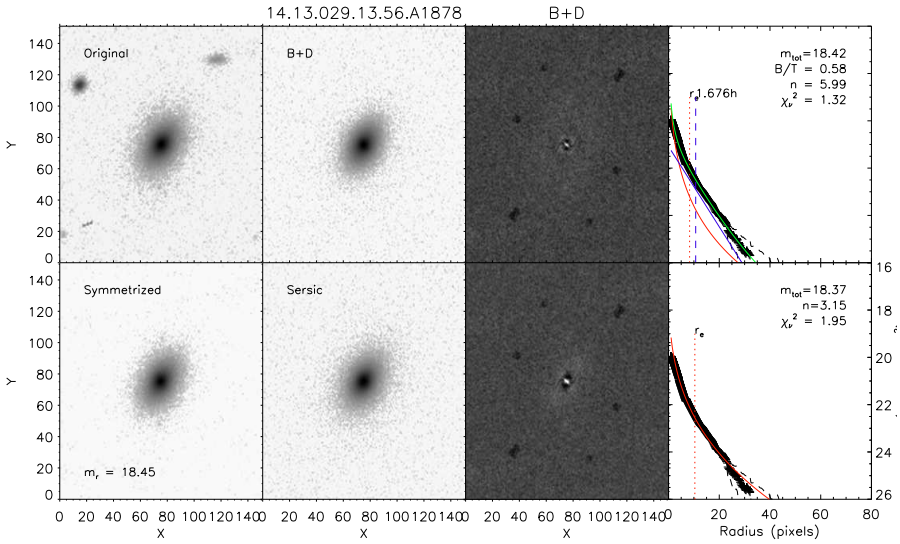
14.13.029.13.56.A1878
B+D
Original
B+D
Symmetrized
Sersic
m_r = 18.45
m_tot=18.42
B/T = 0.58
n = 5.99
χ_ν² = 1.32
r_e 1.676h
m_tot=18.37
n=3.15
χ_ν² = 1.95
r_e
X
Y
Radius (pixels)

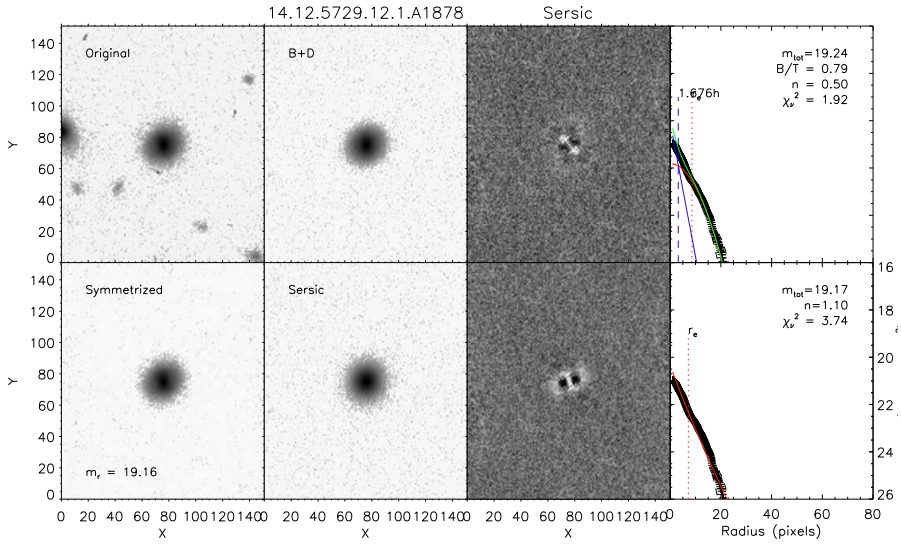
14.12.5729.12.1.A1878
Sersic
Original
B+D
Symmetrized
Sersic
m_r = 19.16
m_tot=19.24
B/T = 0.79
n = 0.50
χ_ν² = 1.92
1.676h
r_e
m_tot=19.17
n=1.10
χ_ν² = 3.74
X
Y
Radius (pixels)

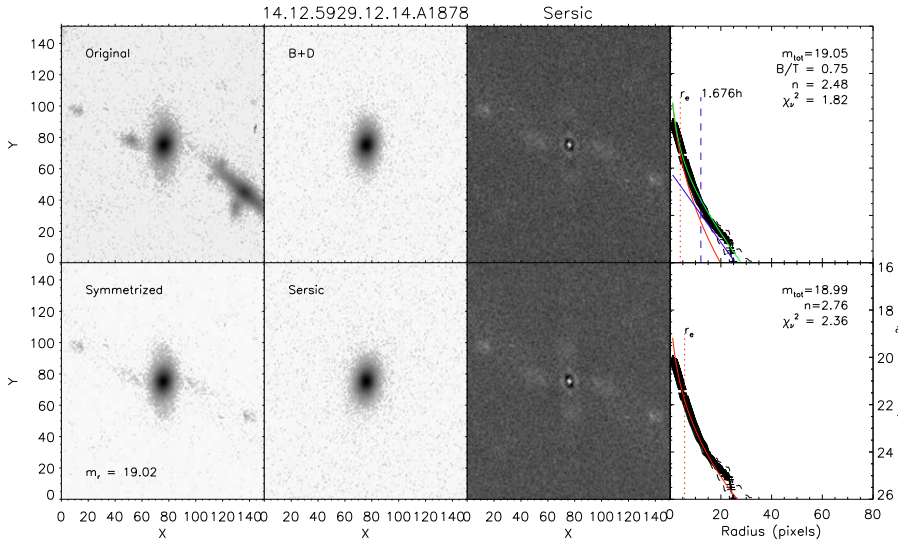
14.12.5929.12.14.A1878
Sersic
Original
B+D
Symmetrized
Sersic
m_r = 19.02
m_tot=19.05
B/T = 0.75
n = 2.48
χ_ν² = 1.82
r_e
1.676h
m_tot=18.99
n=2.76
χ_ν² = 2.36
X
Y
Radius (pixels)

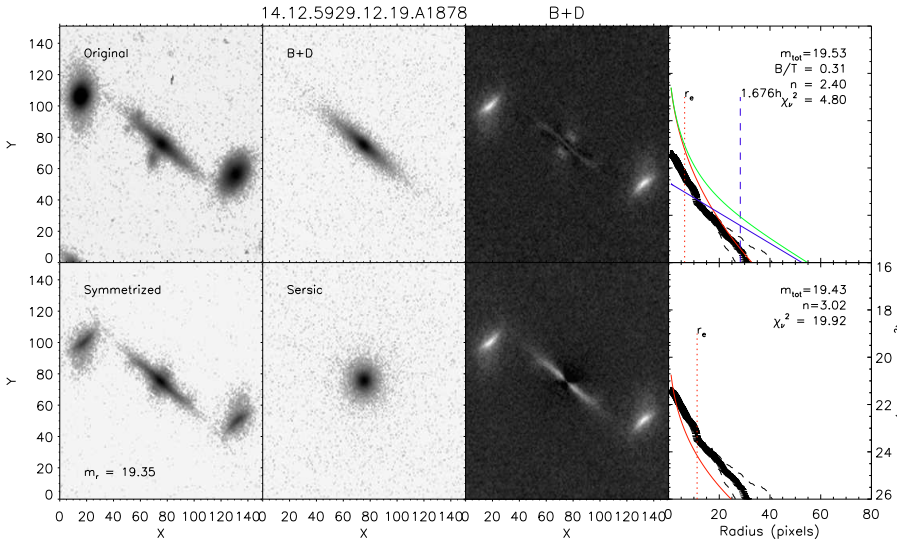
14.12.5929.12.19.A1878
B+D
Original
B+D
Symmetrized
Sersic
m_r = 19.35
m_tot=19.53
B/T = 0.31
n = 2.40
χ_ν² = 4.80
1.676h
r_e
m_tot=19.43
n=3.02
χ_ν² = 19.92
X
Y
Radius (pixels)

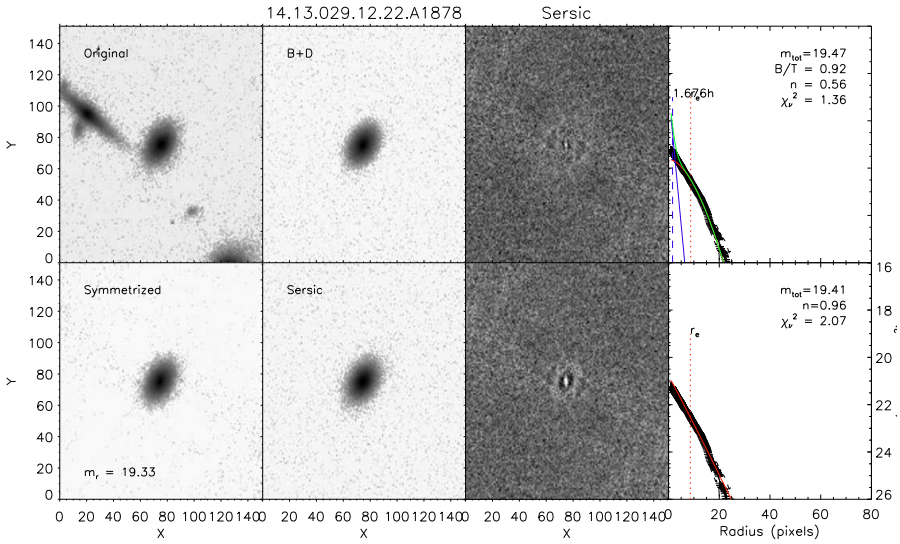
14.13.029.12.22.A1878
Sersic
Original
B+D
Symmetrized
Sersic
m_r = 19.33
m_tot=19.47
B/T = 0.92
n = 0.56
χ_ν² = 1.36
1.676h
r_e
m_tot=19.41
n=0.96
χ_ν² = 2.07
X
Y
Radius (pixels)

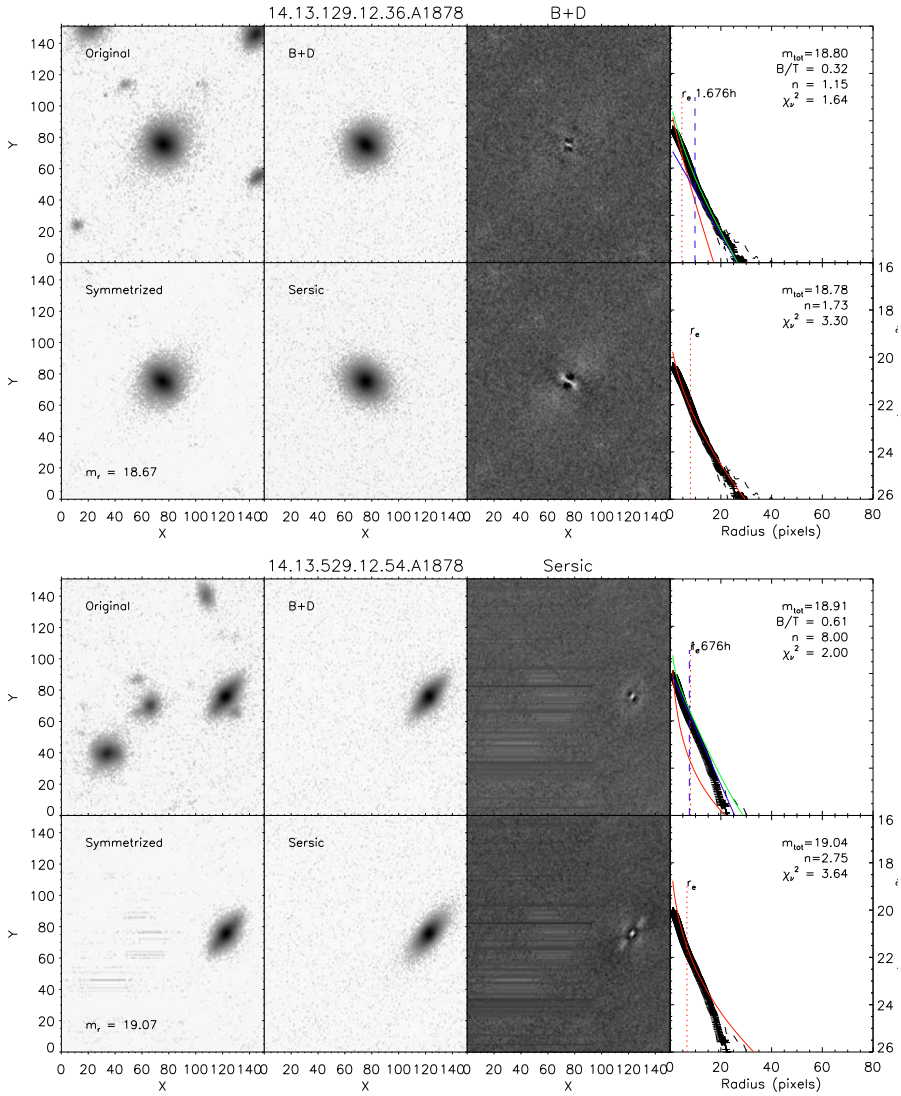
14.13.129.12.36.A1878
B+D
Original
B+D
Symmetrized
Sersic
m_r = 18.67
m_tot=18.80
B/T = 0.32
n = 1.15
χ_ν² = 1.64
r_e 1.676h
m_tot=18.78
n=1.73
χ_ν² = 3.30
r_e
X
Y
Radius (pixels)
14.13.529.12.54.A1878
Sersic
Original
B+D
Symmetrized
Sersic
m_r = 19.07
m_tot=18.91
B/T = 0.61
n = 8.00
χ_ν² = 2.00
r_e 676h
m_tot=19.04
n=2.75
χ_ν² = 3.64
r_e
X
Y
Radius (pixels)

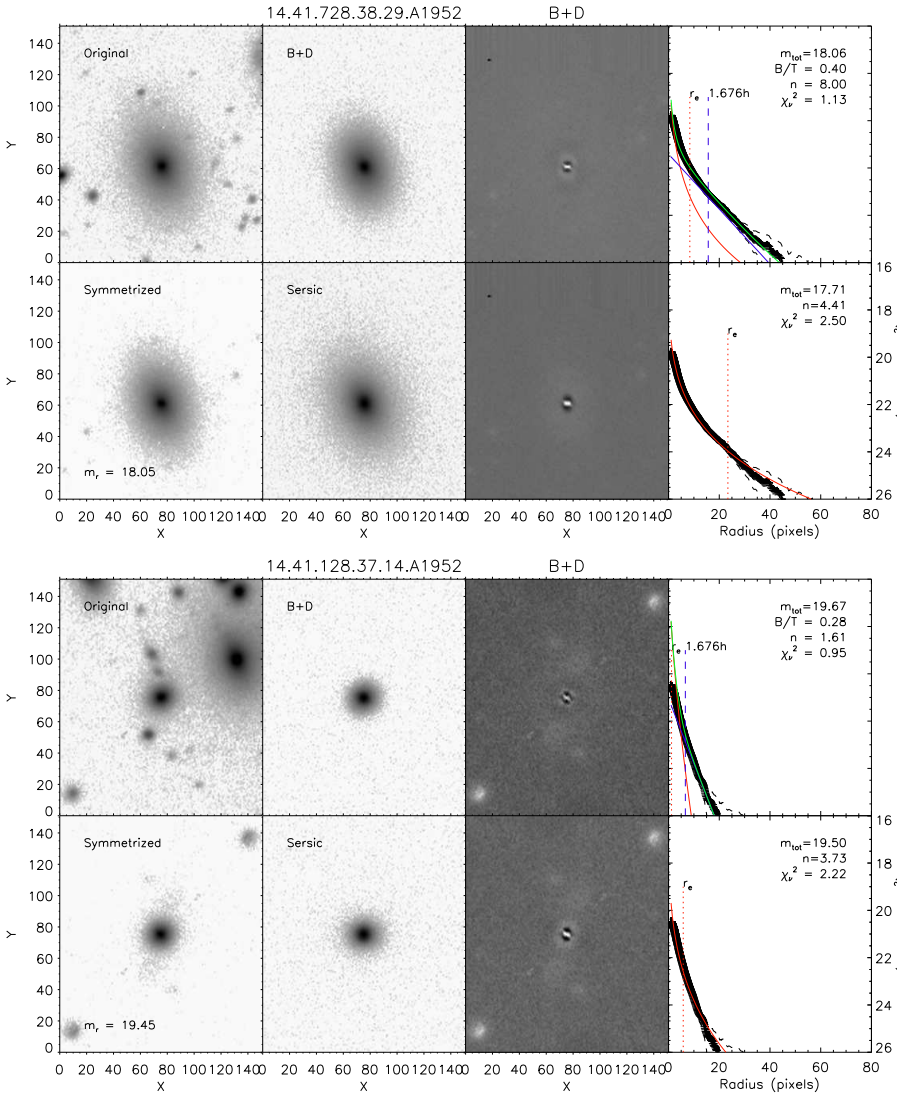
14.41.728.38.29.A1952
B+D
Original
B+D
Symmetrized
Sersic
m_r = 18.05
m_tot=18.06
B/T = 0.40
n = 8.00
χ_ν² = 1.13
r_e 1.676h
m_tot=17.71
n=4.41
χ_ν² = 2.50
r_e
X
Y
Radius (pixels)
14.41.128.37.14.A1952
B+D
Original
B+D
Symmetrized
Sersic
m_r = 19.45
m_tot=19.67
B/T = 0.28
n = 1.61
χ_ν² = 0.95
r_e 1.676h
m_tot=19.50
n=3.73
χ_ν² = 2.22
r_e
X
Y
Radius (pixels)

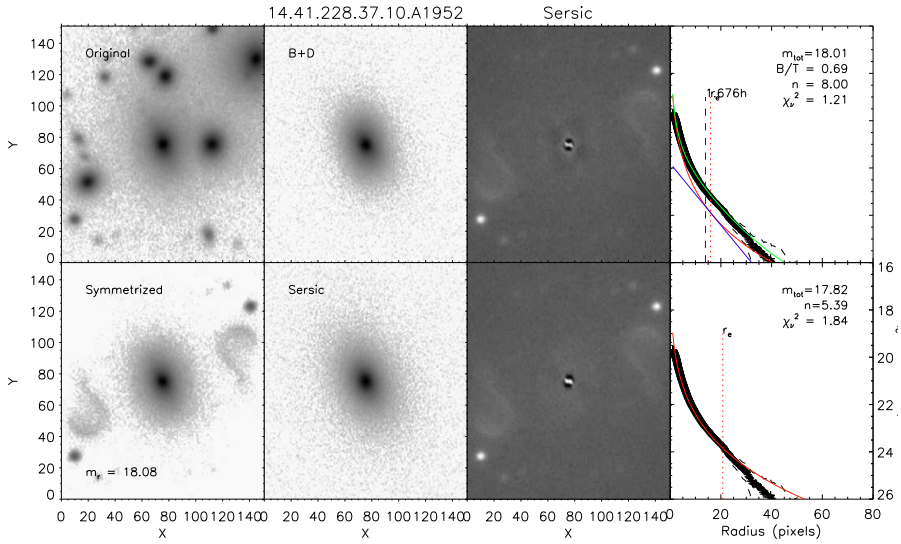
14.41.228.37.10.A1952
Sersic
Original
B+D
Symmetrized
Sersic
m_r = 18.08
m_tot=18.01
B/T = 0.69
n = 8.00
χ_ν² = 1.21
1.676h
m_tot=17.82
n=5.39
χ_ν² = 1.84
r_e
X
Y
Radius (pixels)

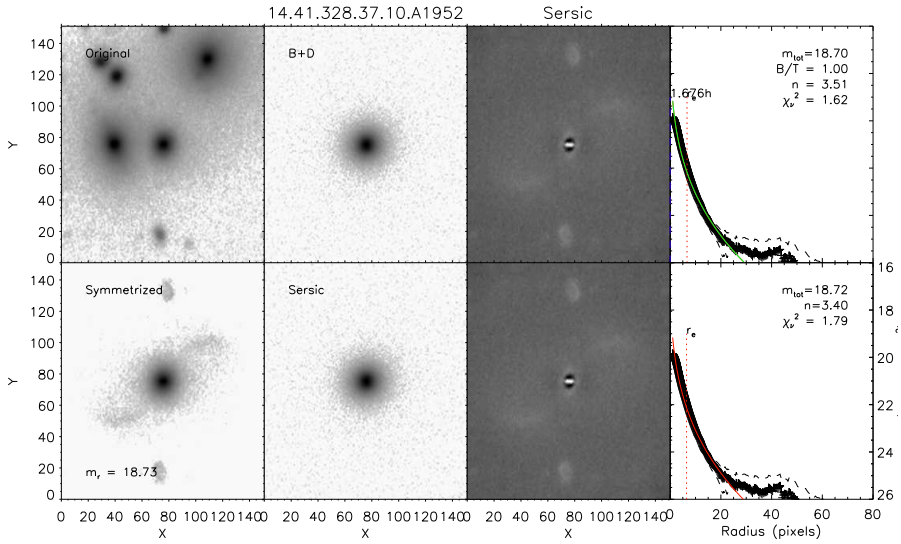
14.41.328.37.10.A1952
Sersic
Original
B+D
Symmetrized
Sersic
m_r = 18.73
m_tot=18.70
B/T = 1.00
n = 3.51
χ_ν² = 1.62
1.676h
m_tot=18.72
n=3.40
χ_ν² = 1.79
r_e
X
Y
Radius (pixels)

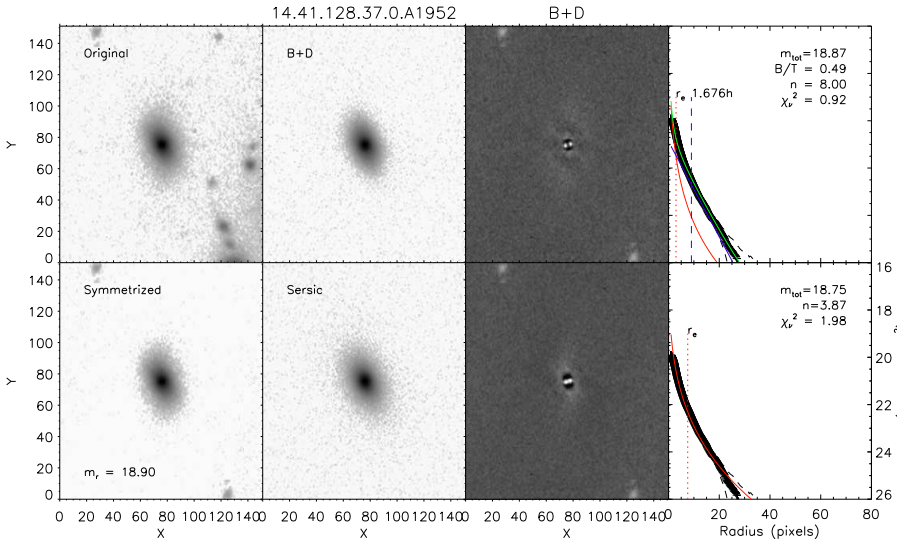
14.41.128.37.0.A1952
B+D
Original
B+D
Symmetrized
Sersic
m_r = 18.90
m_tot=18.87
B/T = 0.49
n = 8.00
χ_ν² = 0.92
r_e 1.676h
m_tot=18.75
n=3.87
χ_ν² = 1.98
r_e
X
Y
Radius (pixels)

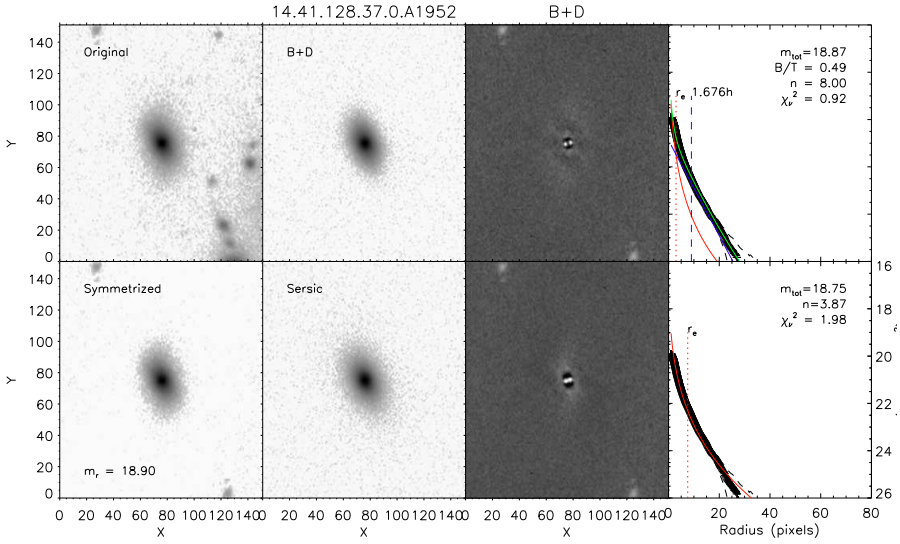
14.41.128.37.0.A1952
B+D
Original
B+D
Symmetrized
Sersic
m_r = 18.90
m_tot=18.87
B/T = 0.49
n = 8.00
χ_ν² = 0.92
r_e 1.676h
m_tot=18.75
n=3.87
χ_ν² = 1.98
r_e
X
Y
Radius (pixels)

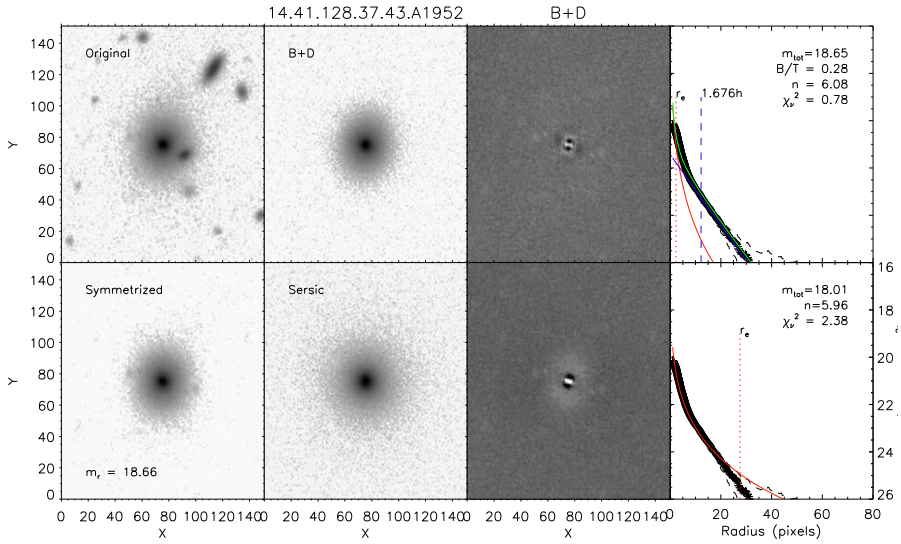
14.41.128.37.43.A1952
B+D
Original
B+D
Symmetrized
Sersic
m_r = 18.66
m_tot=18.65
B/T = 0.28
n = 6.08
χ_ν² = 0.78
r_e
1.676h
m_tot=18.01
n=5.96
χ_ν² = 2.38
X
Y
Radius (pixels)

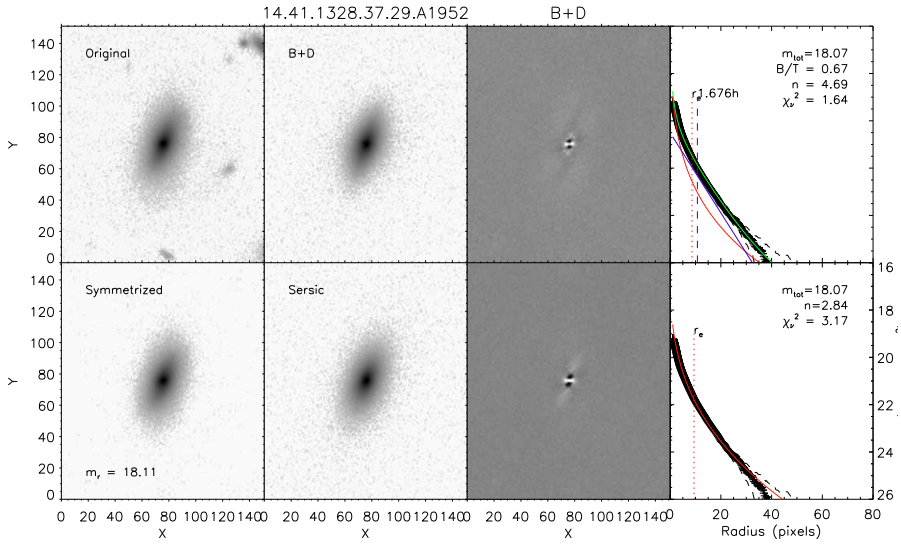
14.41.1328.37.29.A1952
B+D
Original
B+D
Symmetrized
Sersic
m_r = 18.11
m_tot=18.07
B/T = 0.67
n = 4.69
χ_ν² = 1.64
r_e
1.676h
m_tot=18.07
n=2.84
χ_ν² = 3.17
X
Y
Radius (pixels)

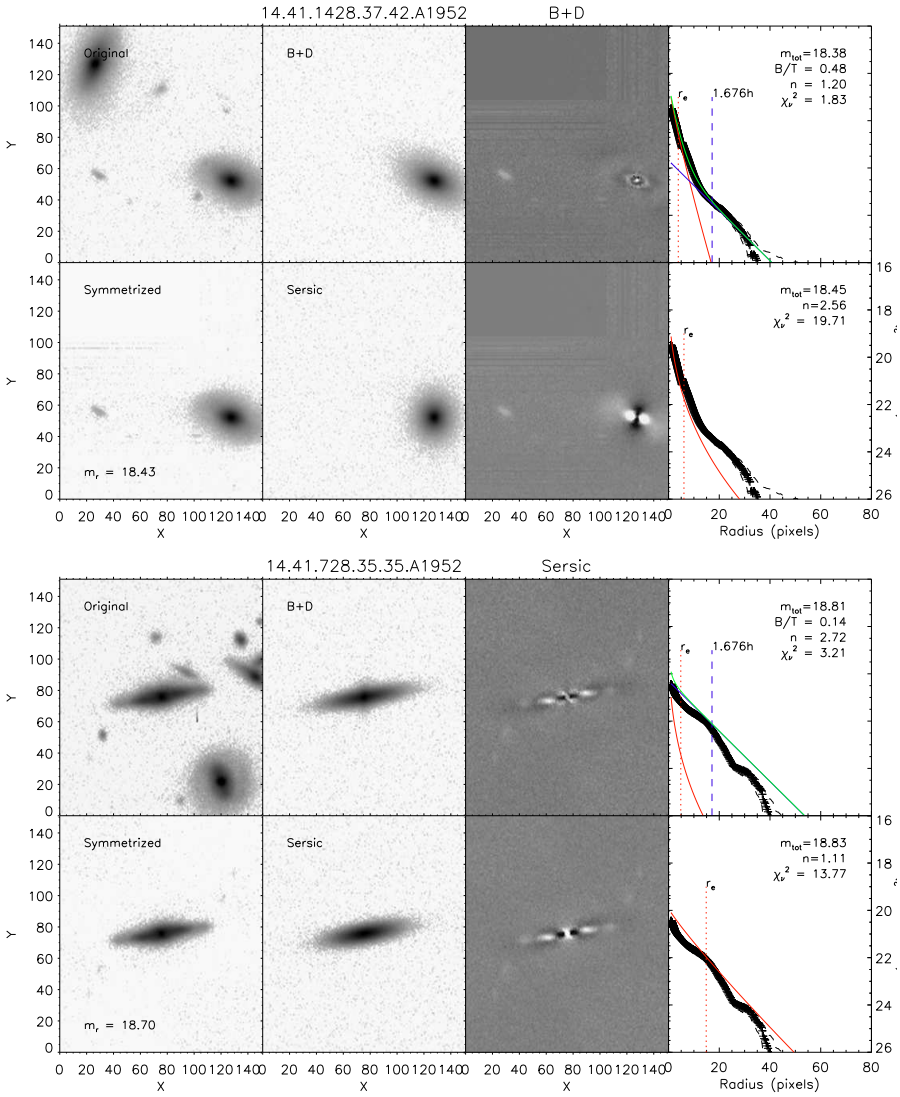
14.41.1428.37.42.A1952
B+D
Original
B+D
Symmetrized
Sersic
m_r = 18.43
m_tot=18.38
B/T = 0.48
n = 1.20
χ_ν² = 1.83
1.676h
r_e
m_tot=18.45
n=2.56
χ_ν² = 19.71
X
Y
Radius (pixels)
14.41.728.35.35.A1952
Sersic
Original
B+D
Symmetrized
Sersic
m_r = 18.70
m_tot=18.81
B/T = 0.14
n = 2.72
χ_ν² = 3.21
1.676h
r_e
m_tot=18.83
n=1.11
χ_ν² = 13.77
X
Y
Radius (pixels)

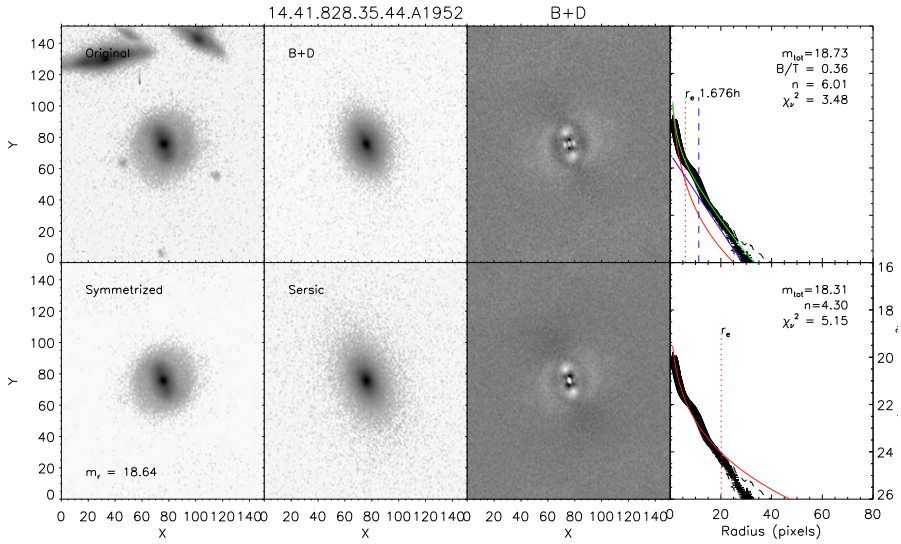
14.41.828.35.44.A1952
B+D
Original
B+D
Symmetrized
Sersic
m_r = 18.64
m_tot=18.73
B/T = 0.36
n = 6.01
χ_ν² = 3.48
r_e 1.676h
m_tot=18.31
n=4.30
χ_ν² = 5.15
r_e
X
Y
Radius (pixels)

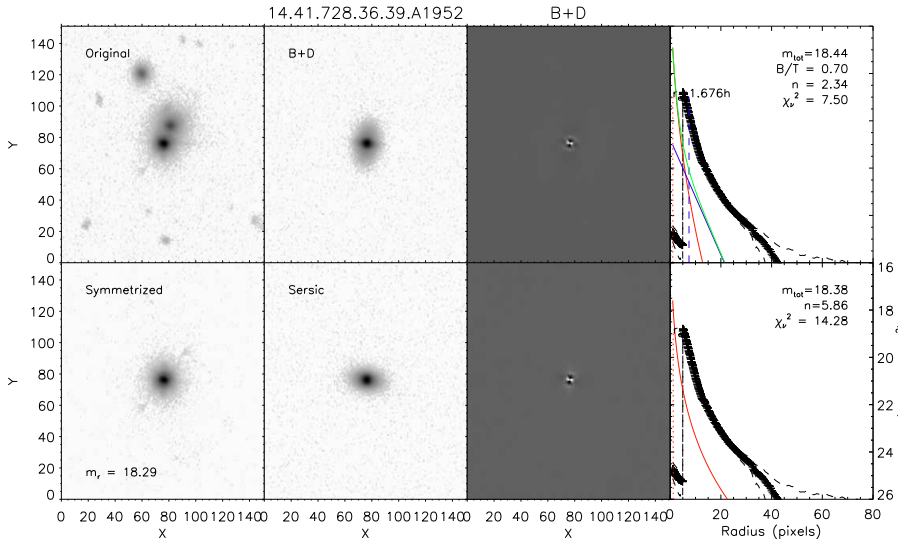
14.41.728.36.39.A1952
B+D
Original
B+D
Symmetrized
Sersic
m_r = 18.29
m_tot=18.44
B/T = 0.70
n = 2.34
χ_ν² = 7.50
1.676h
m_tot=18.38
n=5.86
χ_ν² = 14.28
X
Y
Radius (pixels)

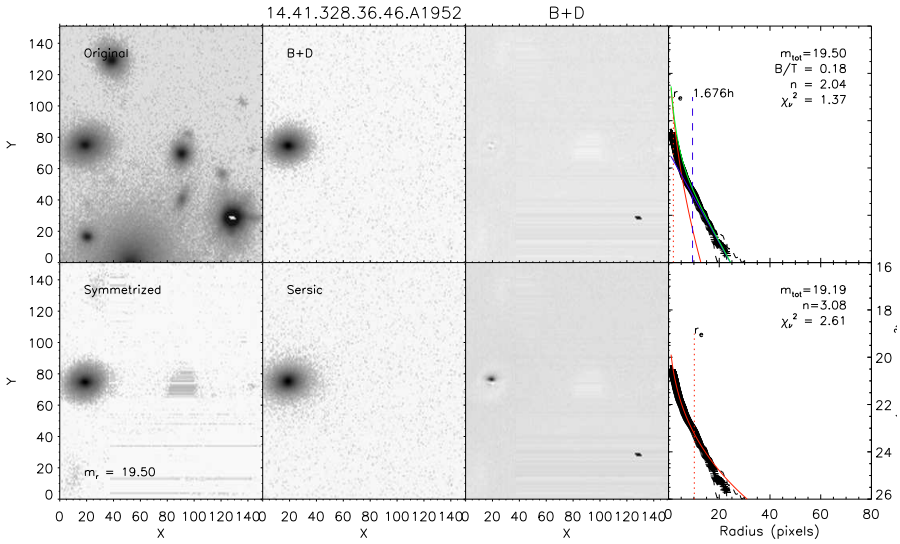
14.41.328.36.46.A1952
B+D
Original
B+D
Symmetrized
Sersic
m_r = 19.50
m_tot=19.50
B/T = 0.18
n = 2.04
χ_ν² = 1.37
r_e
1.676h
m_tot=19.19
n=3.08
χ_ν² = 2.61
X
Y
Radius (pixels)

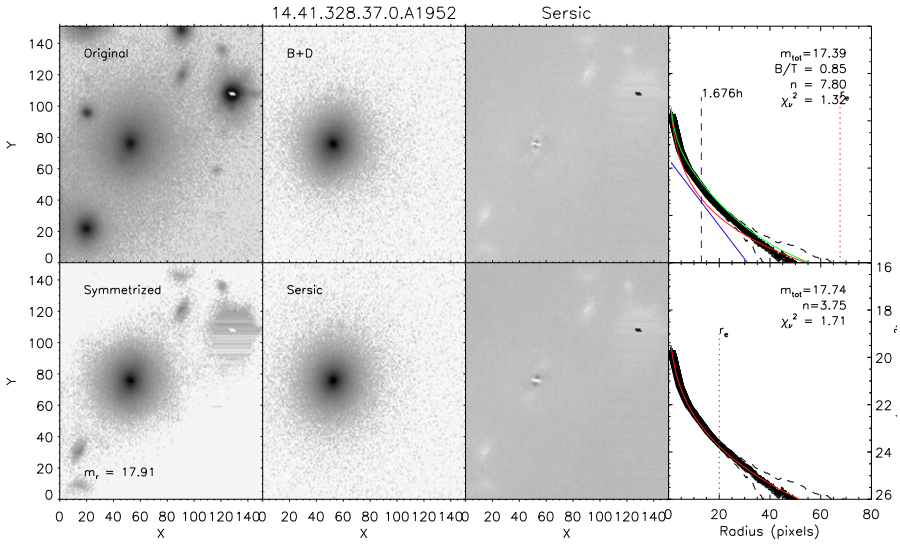
14.41.328.37.0.A1952
Sersic
Original
B+D
Symmetrized
Sersic
m_r = 17.91
m_tot=17.39
B/T = 0.85
n = 7.80
χ_ν² = 1.32
1.676h
r_e
m_tot=17.74
n=3.75
χ_ν² = 1.71
X
Y
Radius (pixels)

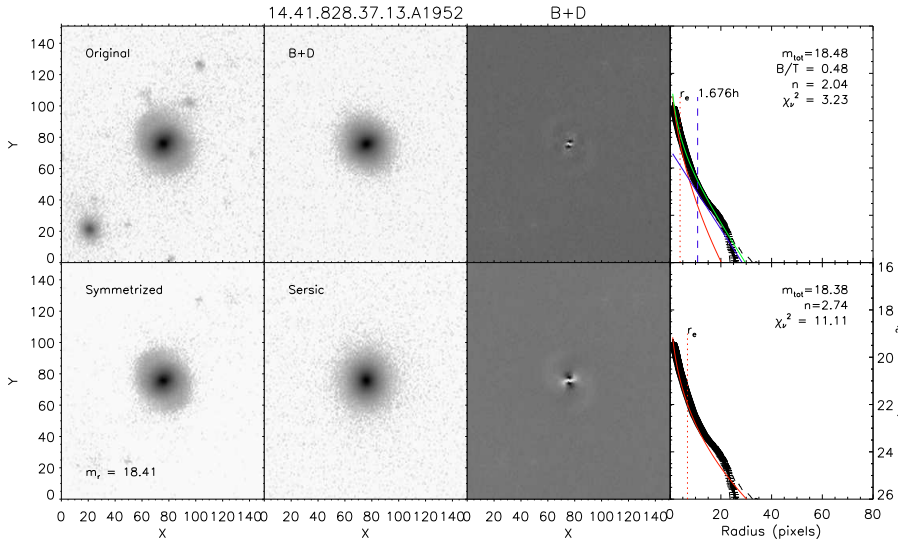
14.41.828.37.13.A1952
B+D
Original
B+D
Symmetrized
Sersic
m_r = 18.41
m_tot=18.48
B/T = 0.48
n = 2.04
χ_ν² = 3.23
r_e 1.676h
m_tot=18.38
n=2.74
χ_ν² = 11.11
r_e
X
Y
Radius (pixels)

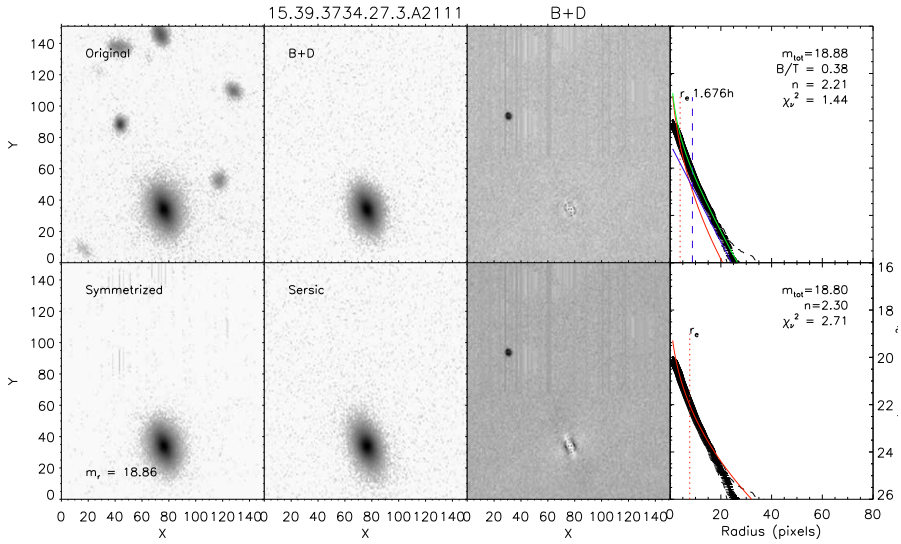
15.39.3734.27.3.A2111
B+D
Original
B+D
Symmetrized
Sersic
m_r = 18.86
m_tot=18.88
B/T = 0.38
n = 2.21
χ_ν² = 1.44
r_e 1.676h
m_tot=18.80
n=2.30
χ_ν² = 2.71
r_e
X
Y
Radius (pixels)

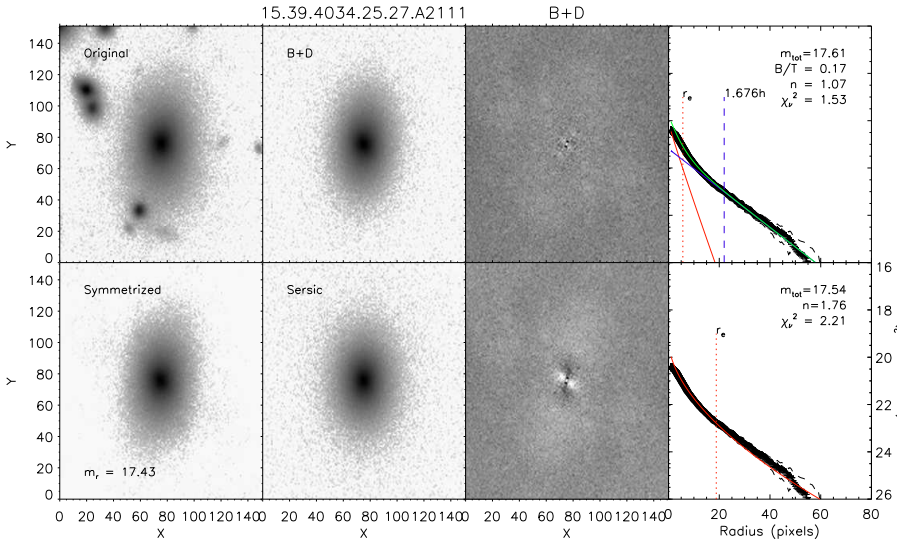
15.39.4034.25.27.A2111
B+D
Original
B+D
Symmetrized
Sersic
m_r = 17.43
m_tot=17.61
B/T = 0.17
n = 1.07
χ_ν² = 1.53
1.676h
r_e
m_tot=17.54
n=1.76
χ_ν² = 2.21
X
Y
Radius (pixels)

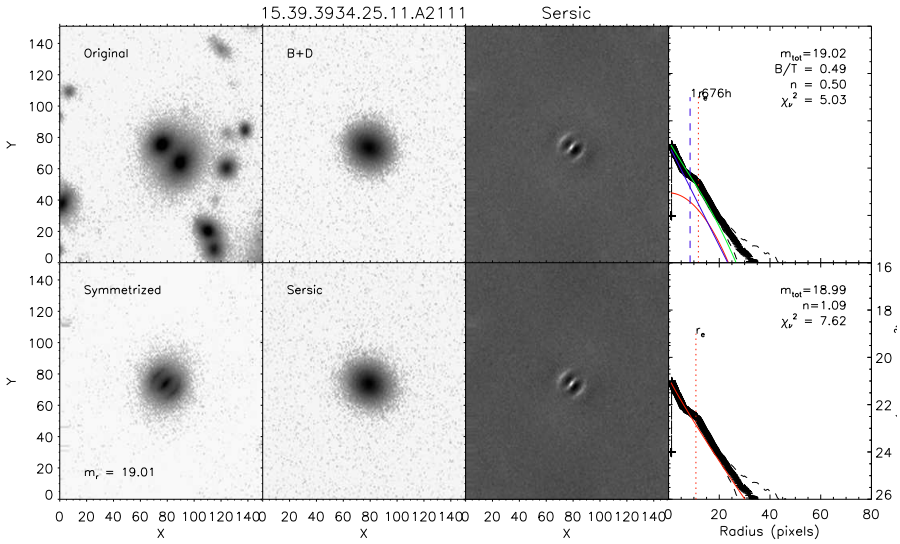
15.39.3934.25.11.A2111
Sersic
Original
B+D
Symmetrized
Sersic
m_r = 19.01
m_tot=19.02
B/T = 0.49
n = 0.50
χ_ν² = 5.03
1.676h
r_e
m_tot=18.99
n=1.09
χ_ν² = 7.62
X
Y
Radius (pixels)

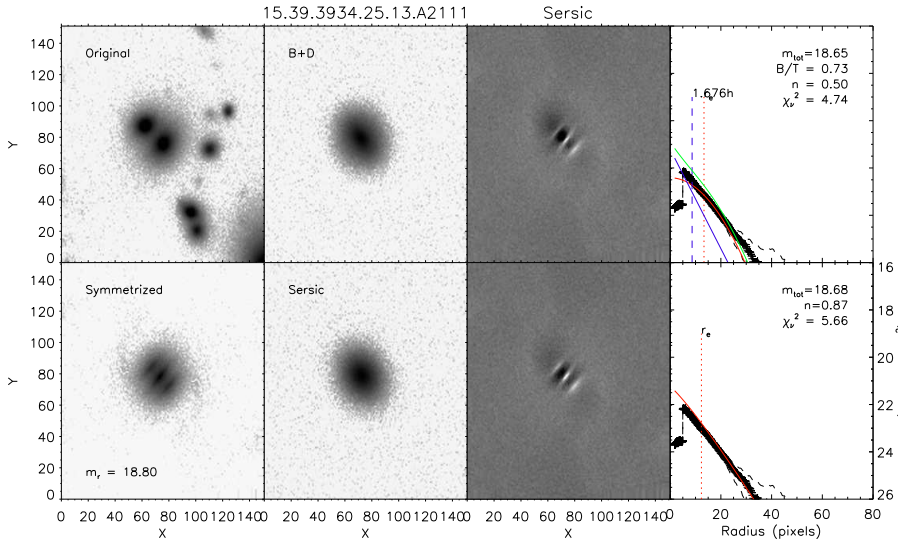
15.39.3934.25.13.A2111
Sersic
Original
B+D
Symmetrized
Sersic
m_r = 18.80
m_tot=18.65
B/T = 0.73
n = 0.50
χ_ν² = 4.74
1.676h
m_tot=18.68
n=0.87
χ_ν² = 5.66
r_e
X
Y
Radius (pixels)

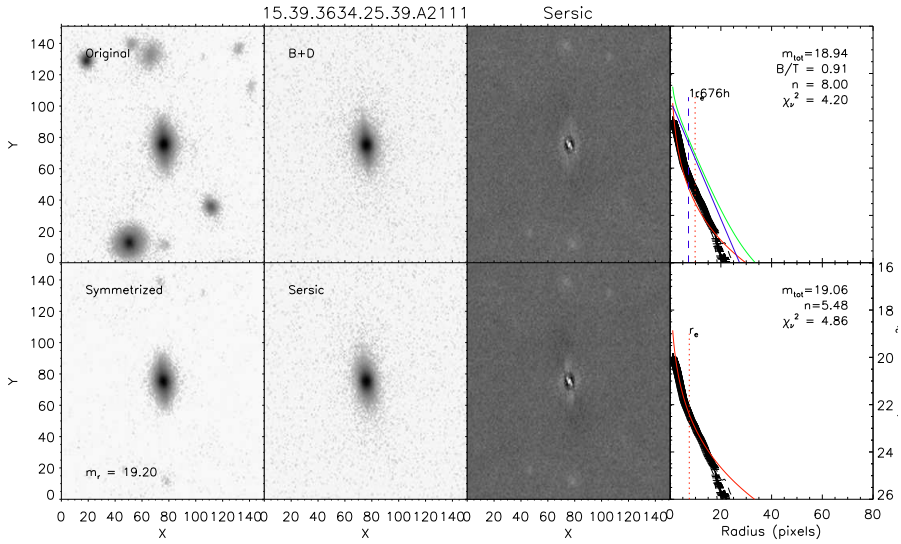
15.39.3634.25.39.A2111
Sersic
Original
B+D
Symmetrized
Sersic
m_r = 19.20
m_tot=18.94
B/T = 0.91
n = 8.00
χ_ν² = 4.20
1.676h
m_tot=19.06
n=5.48
χ_ν² = 4.86
r_e
X
Y
Radius (pixels)

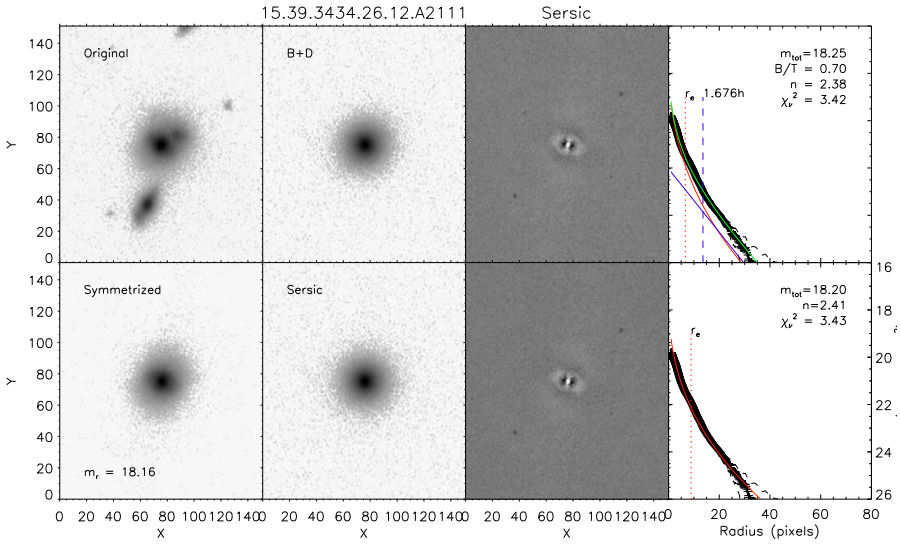
15.39.3434.26.12.A2111
Sersic
Original
B+D
Symmetrized
Sersic
m_r = 18.16
m_tot=18.25
B/T = 0.70
n = 2.38
χ_ν² = 3.42
r_e 1.676h
m_tot=18.20
n=2.41
χ_ν² = 3.43
r_e
X
Y
Radius (pixels)

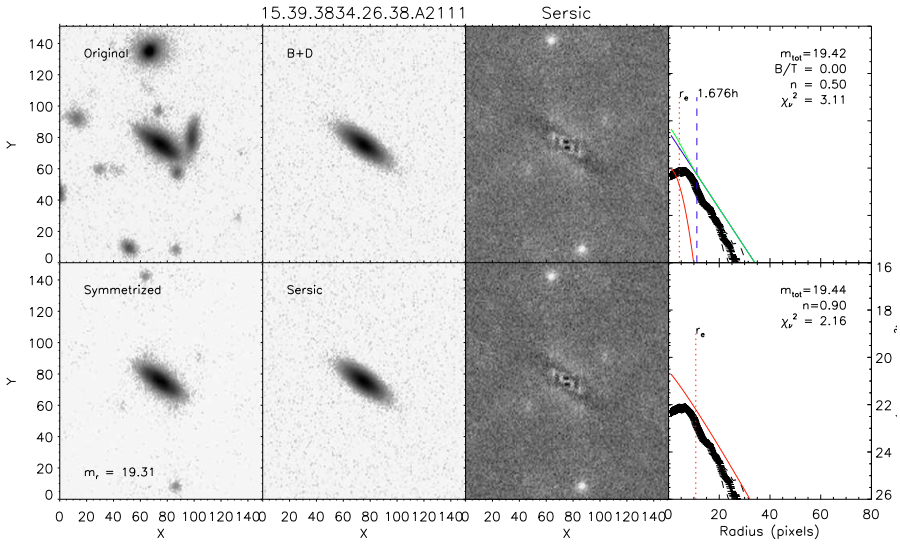
15.39.3834.26.38.A2111
Sersic
Original
B+D
Symmetrized
Sersic
m_r = 19.31
m_tot=19.42
B/T = 0.00
n = 0.50
χ_ν² = 3.11
r_e 1.676h
m_tot=19.44
n=0.90
χ_ν² = 2.16
r_e
X
Y
Radius (pixels)

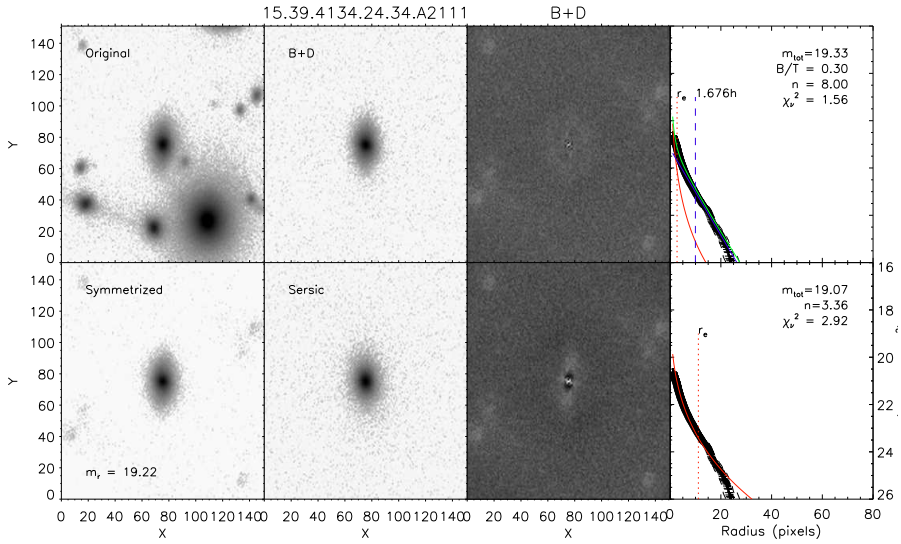
15.39.4134.24.34.A2111
B+D
Original
B+D
Symmetrized
Sersic
m_r = 19.22
m_tot=19.33
B/T = 0.30
n = 8.00
χ_ν² = 1.56
r_e
1.676h
m_tot=19.07
n=3.36
χ_ν² = 2.92
X
Y
Radius (pixels)

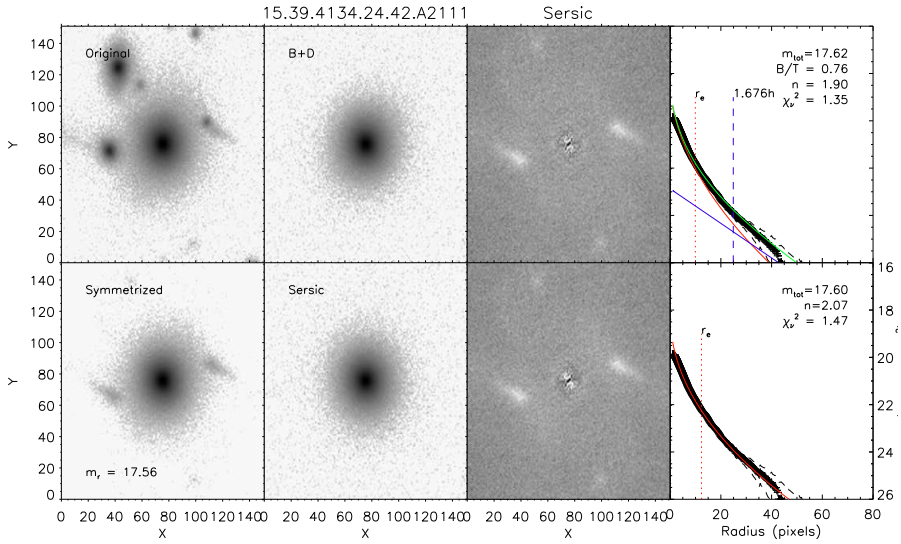
15.39.4134.24.42.A2111
Sersic
Original
B+D
Symmetrized
Sersic
m_r = 17.56
m_tot=17.62
B/T = 0.76
n = 1.90
χ_ν² = 1.35
r_e
1.676h
m_tot=17.60
n=2.07
χ_ν² = 1.47
X
Y
Radius (pixels)

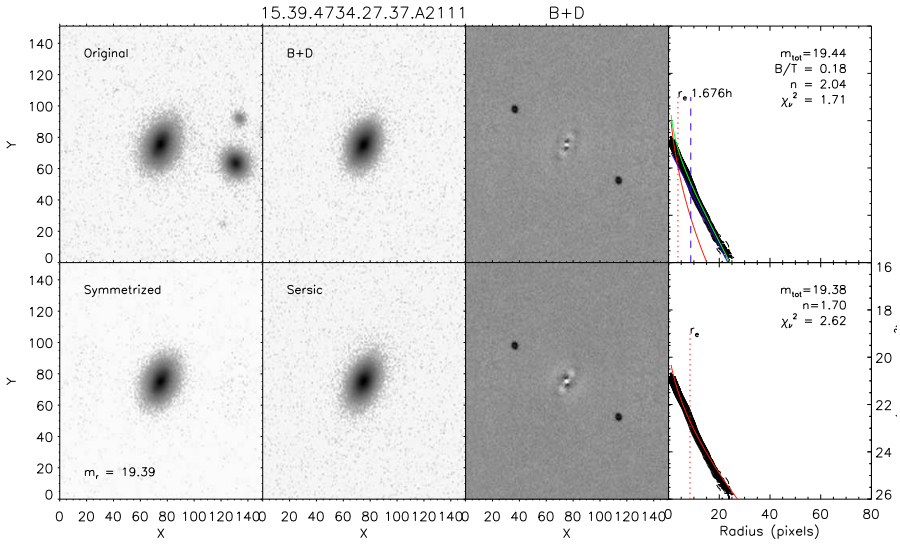
15.39.4734.27.37.A2111
B+D
Original
B+D
Symmetrized
Sersic
m_r = 19.39
m_tot=19.44
B/T = 0.18
n = 2.04
χ_ν² = 1.71
r_e 1.676h
m_tot=19.38
n=1.70
χ_ν² = 2.62
r_e
X
Y
Radius (pixels)

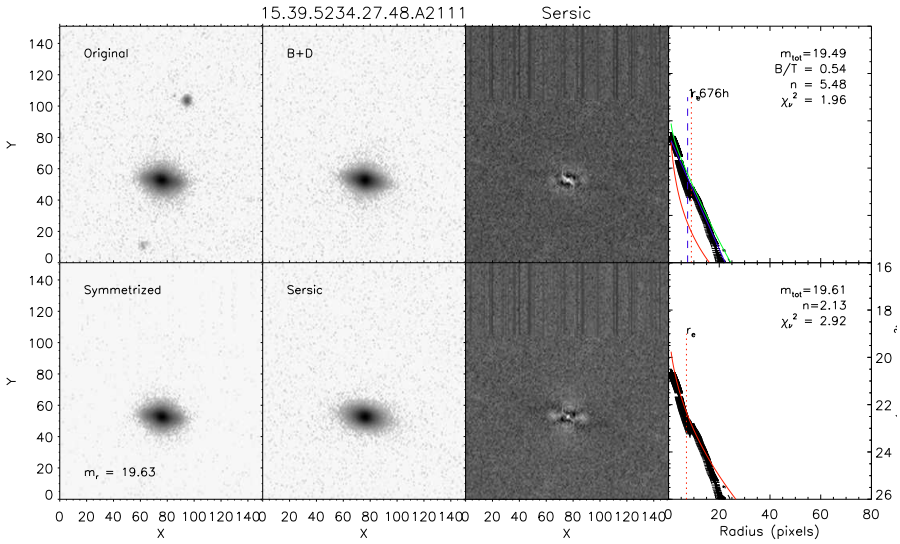
15.39.5234.27.48.A2111
Sersic
Original
B+D
Symmetrized
Sersic
m_r = 19.63
m_tot=19.49
B/T = 0.54
n = 5.48
χ_ν² = 1.96
r_e 1.676h
m_tot=19.61
n=2.13
χ_ν² = 2.92
r_e
X
Y
Radius (pixels)

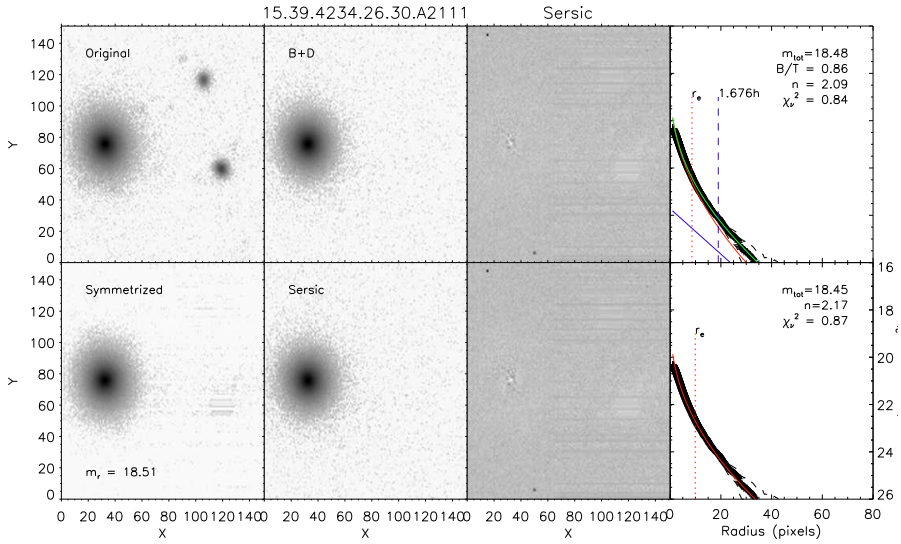
15.39.4234.26.30.A2111
Sersic
Original
B+D
Symmetrized
Sersic
m_r = 18.51
m_tot=18.48
B/T = 0.86
n = 2.09
χ_ν² = 0.84
1.676h
r_e
m_tot=18.45
n=2.17
χ_ν² = 0.87
X
Y
Radius (pixels)

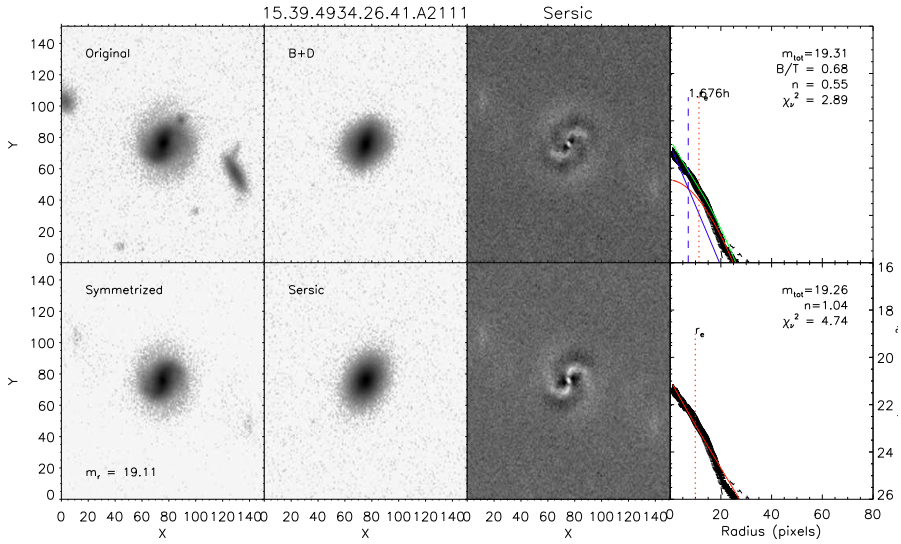
15.39.4934.26.41.A2111
Sersic
Original
B+D
Symmetrized
Sersic
m_r = 19.11
m_tot=19.31
B/T = 0.68
n = 0.55
χ_ν² = 2.89
1.676h
r_e
m_tot=19.26
n=1.04
χ_ν² = 4.74
X
Y
Radius (pixels)

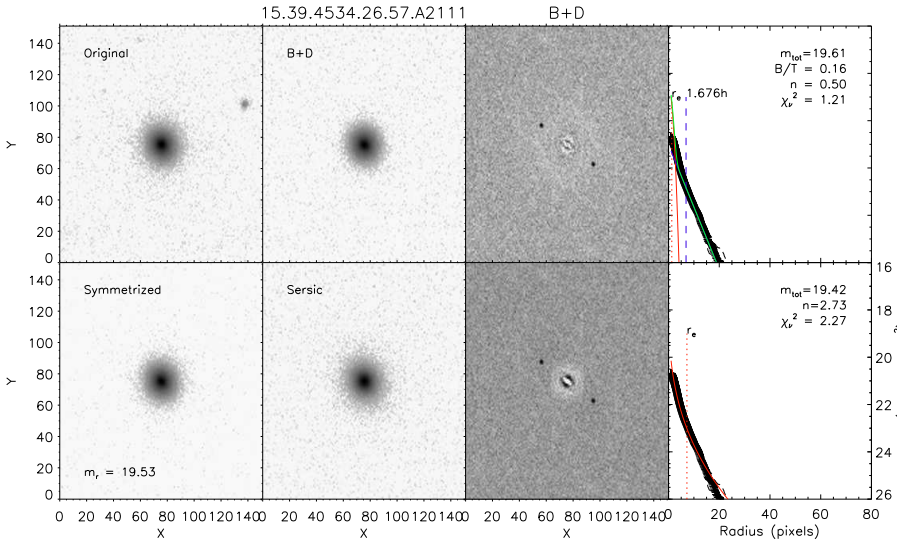
15.39.4534.26.57.A2111
B+D
Original
B+D
Symmetrized
Sersic
m_r = 19.53
m_tot=19.61
B/T = 0.16
n = 0.50
χ_ν² = 1.21
r_e 1.676h
m_tot=19.42
n=2.73
χ_ν² = 2.27
r_e
X
Y
Radius (pixels)

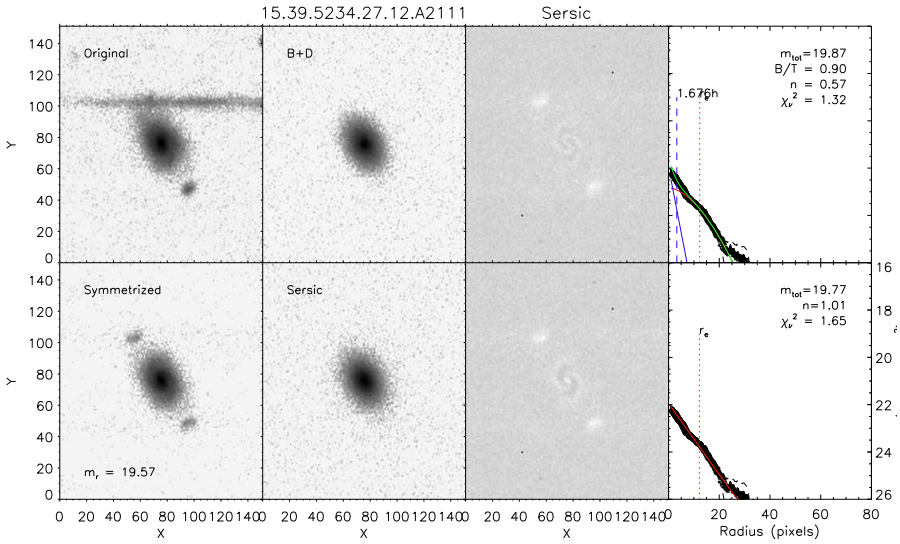
15.39.5234.27.12.A2111
Sersic
Original
B+D
Symmetrized
Sersic
m_r = 19.57
m_tot=19.87
B/T = 0.90
n = 0.57
χ_ν² = 1.32
1.676h
r_e
m_tot=19.77
n=1.01
χ_ν² = 1.65
r_e
X
Y
Radius (pixels)

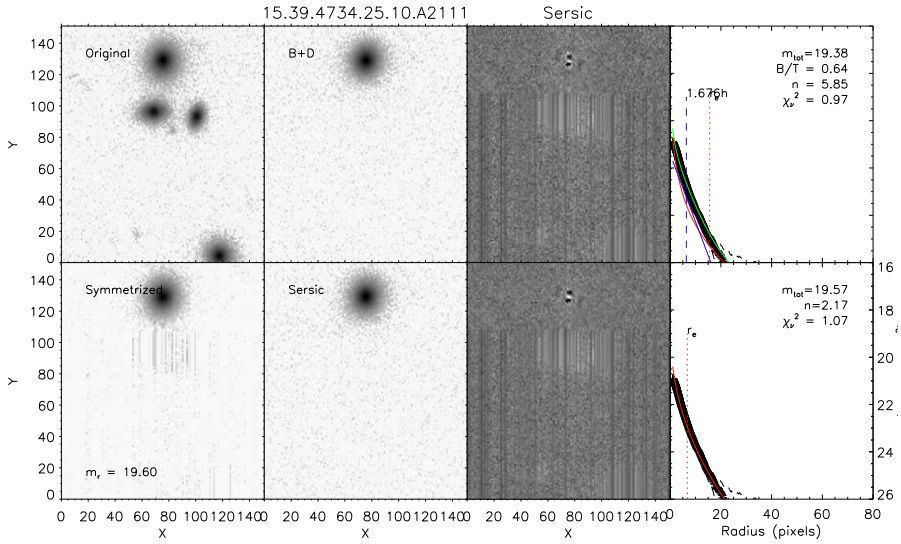
15.39.4734.25.10.A2111
Sersic
Original
B+D
Symmetrized
Sersic
m_r = 19.60
m_tot=19.38
B/T = 0.64
n = 5.85
χ_ν² = 0.97
1.676h
r_e
m_tot=19.57
n=2.17
χ_ν² = 1.07
X
Y
Radius (pixels)

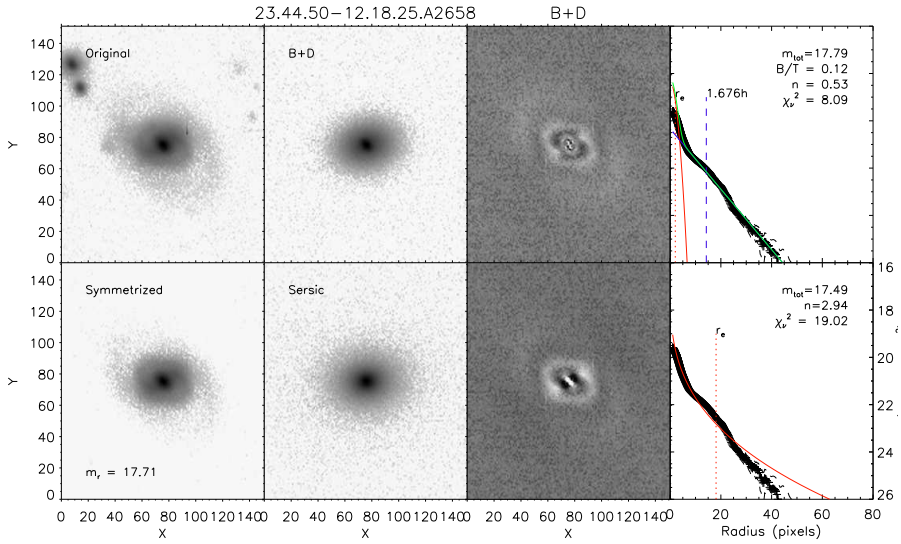
23.44.50−12.18.25.A2658
B+D
Original
B+D
Symmetrized
Sersic
m_r = 17.71
m_tot=17.79
B/T = 0.12
n = 0.53
χ_ν² = 8.09
1.676h
r_e
m_tot=17.49
n=2.94
χ_ν² = 19.02
X
Y
Radius (pixels)

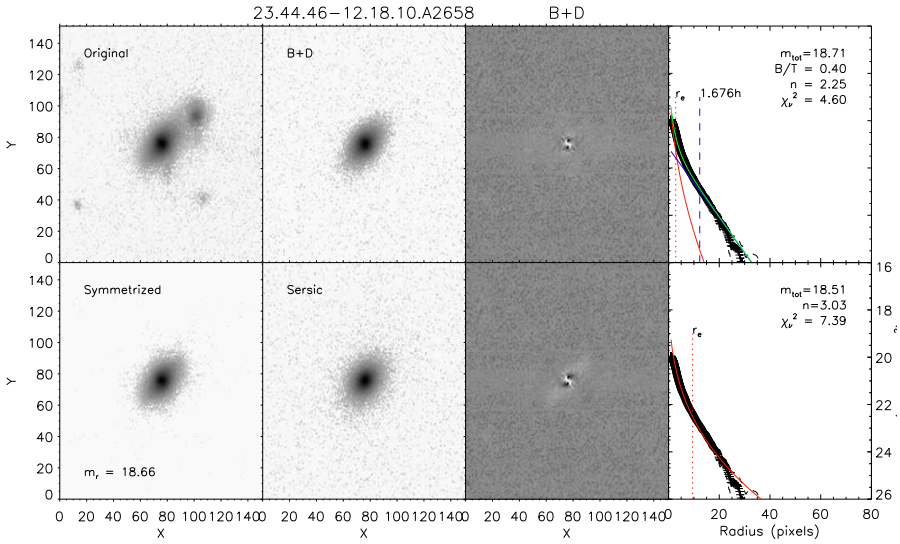
23.44.46−12.18.10.A2658
B+D
Original
B+D
Symmetrized
Sersic
m_r = 18.66
m_tot=18.71
B/T = 0.40
n = 2.25
χ_ν² = 4.60
r_e
1.676h
m_tot=18.51
n=3.03
χ_ν² = 7.39
X
Y
Radius (pixels)

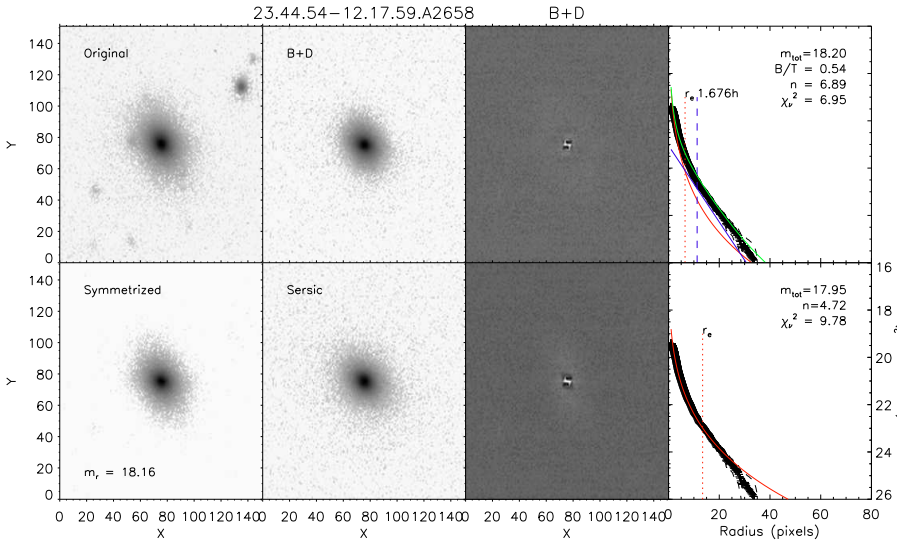
23.44.54−12.17.59.A2658
B+D
Original
B+D
Symmetrized
Sersic
m_r = 18.16
m_tot=18.20
B/T = 0.54
n = 6.89
χ_ν² = 6.95
r_e
1.676h
m_tot=17.95
n=4.72
χ_ν² = 9.78
X
Y
Radius (pixels)

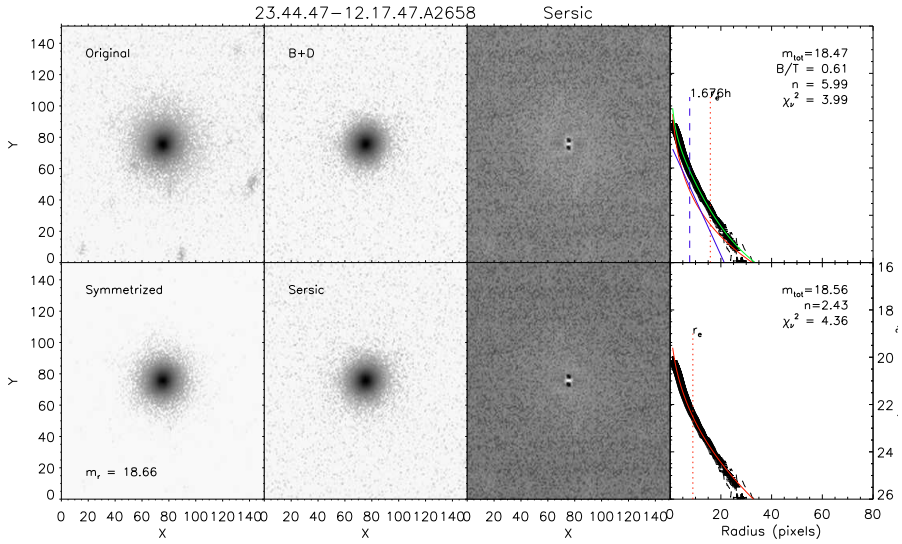
23.44.47−12.17.47.A2658
Sersic
Original
B+D
Symmetrized
Sersic
m_r = 18.66
m_tot=18.47
B/T = 0.61
n = 5.99
χ_ν² = 3.99
1.676h
m_tot=18.56
n=2.43
χ_ν² = 4.36
r_e
X
Y
Radius (pixels)

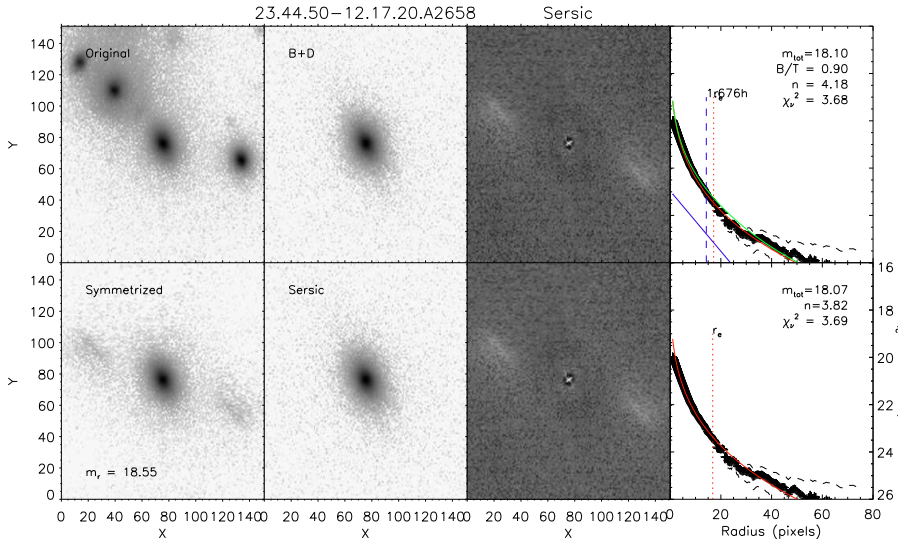
23.44.50−12.17.20.A2658
Sersic
Original
B+D
Symmetrized
Sersic
m_r = 18.55
m_tot=18.10
B/T = 0.90
n = 4.18
χ_ν² = 3.68
1.676h
m_tot=18.07
n=3.82
χ_ν² = 3.69
r_e
X
Y
Radius (pixels)

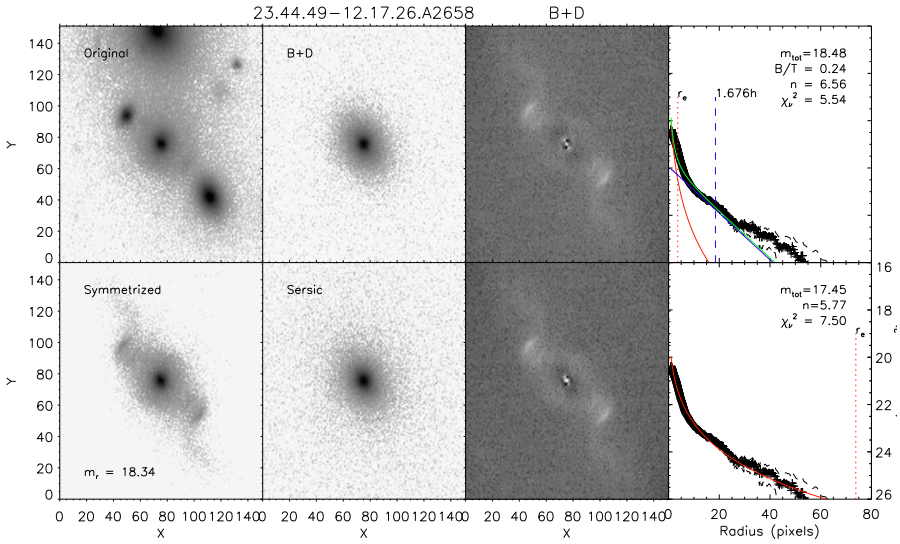
23.44.49−12.17.26.A2658
B+D
Original
B+D
Symmetrized
Sersic
m_r = 18.34
m_tot=18.48
B/T = 0.24
n = 6.56
χ_ν² = 5.54
1.676h
m_tot=17.45
n=5.77
χ_ν² = 7.50
X
Y
Radius (pixels)

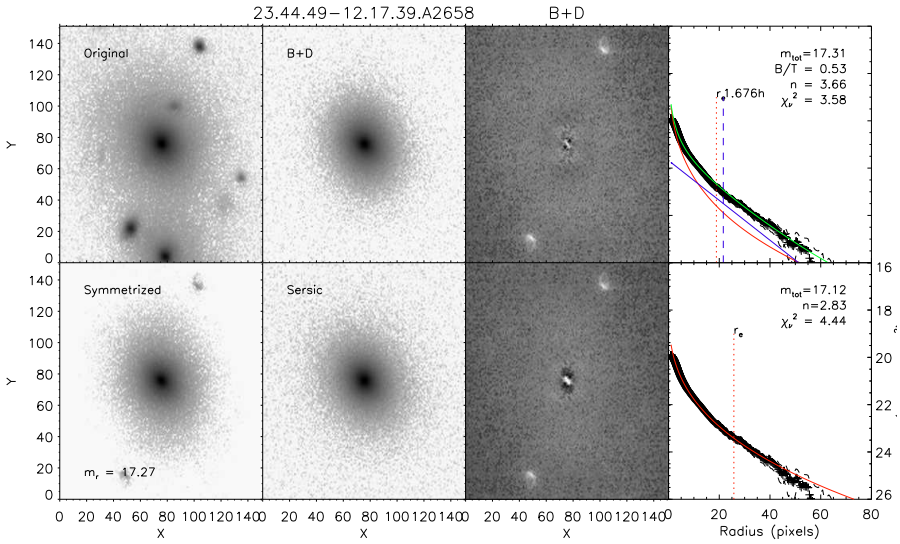
23.44.49−12.17.39.A2658
B+D
Original
B+D
Symmetrized
Sersic
m_r = 17.27
m_tot=17.31
B/T = 0.53
n = 3.66
χ_ν² = 3.58
1.676h
m_tot=17.12
n=2.83
χ_ν² = 4.44
X
Y
Radius (pixels)

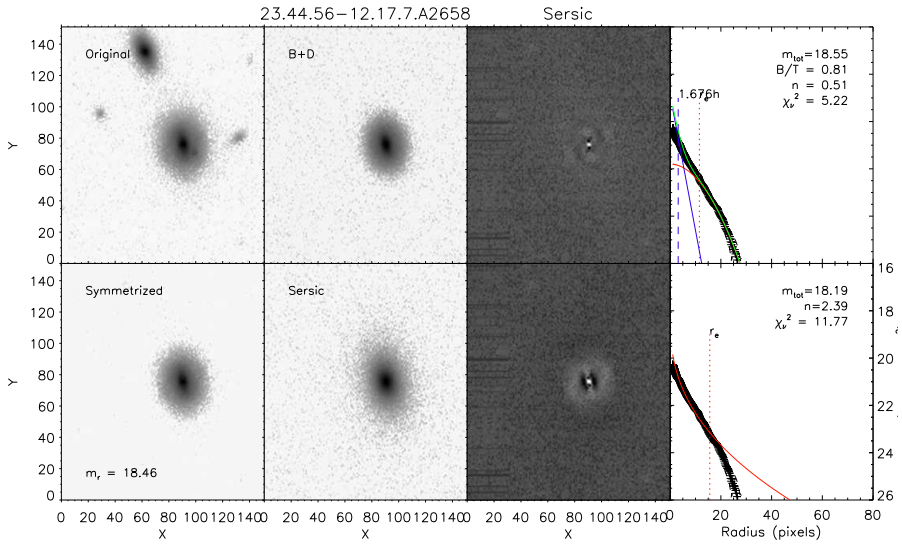

Figure B.1: Upper row: Original Galaxy, Sersic+Disc model, Sersic+Disc Residual and 1-Dimensional Profile with the Sersic+Disc model profile. Bottom row: Original Galaxy, Sersic model, Sersic Residual and 1-Dimensional Profile with the Sersic model profile.

Appendix C

NOT BCGs sustraction

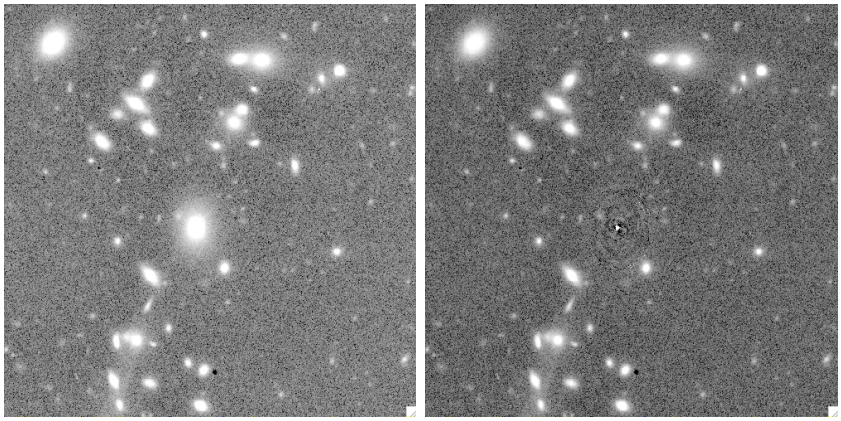

Figure C.1: A1643 BCGs subtraction in Gunn-r filter. More details in the text.

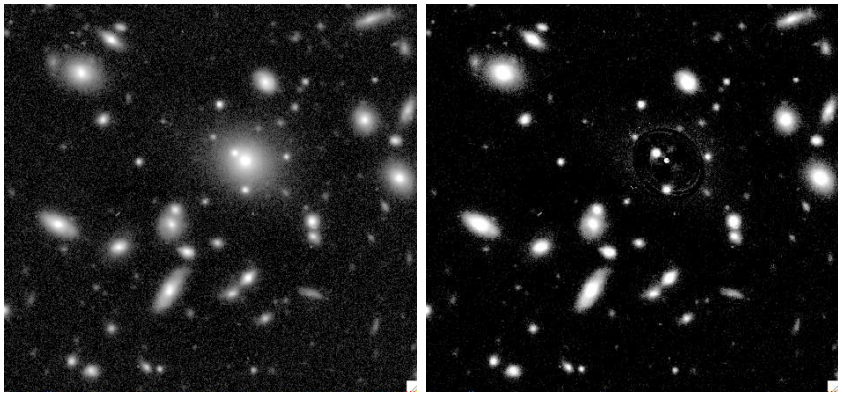

Figure C.2: A1878 BCGs subtraction in Gunn-r filter. More details in the text.

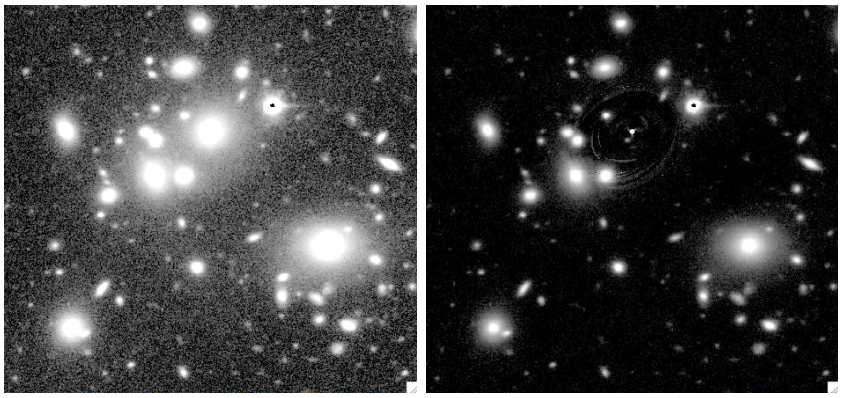

Figure C.3: A1952 BCGs subtraction in Gunn-r filter. More details in the text.

Figure C.4: A2111 BCGs subtraction in Gunn-r filter. More details in the text.

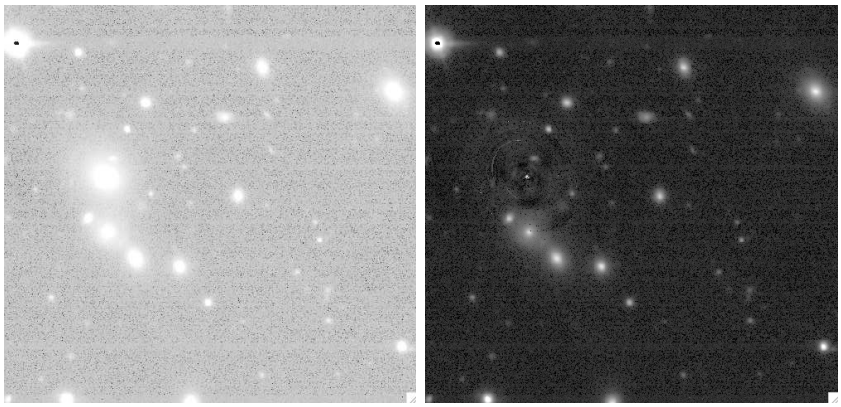

Figure C.5: A2658 BCGs subtraction in Gunn-r filter. More details in the text.

Appendix D

ACS BCGs sustraction

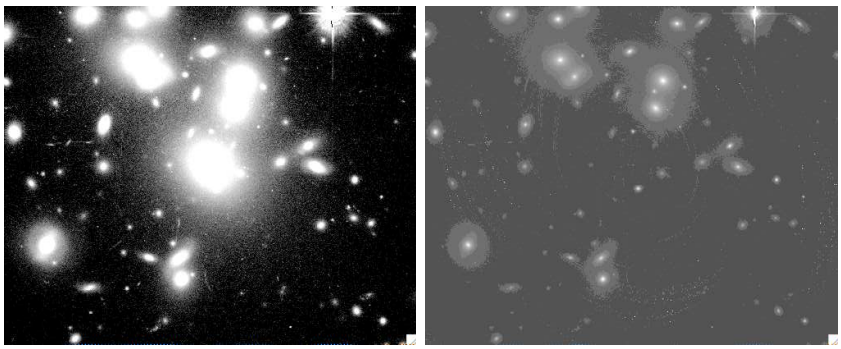

Figure D.1: A1689 BCGs subtraction in Gunn-r filter. More details in the text.

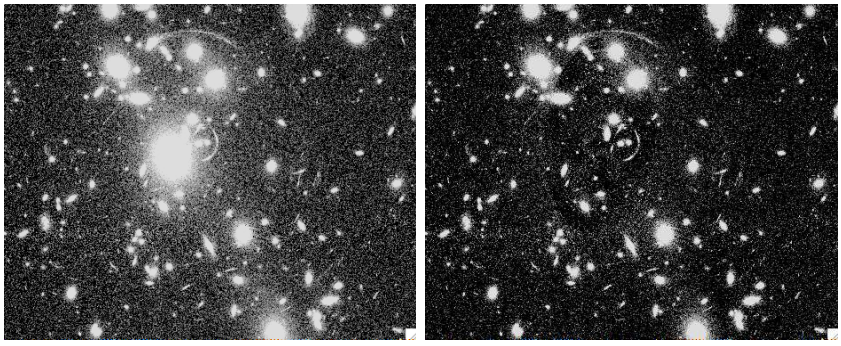

Figure D.2: A1703 BCGs subtraction in Gunn-r filter. More details in the text.

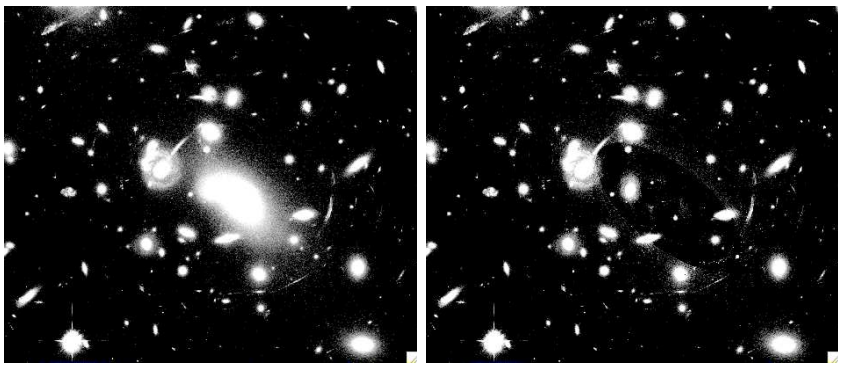

Figure D.3: A2218 BCGs subtraction in Gunn-r filter. More details in the text.

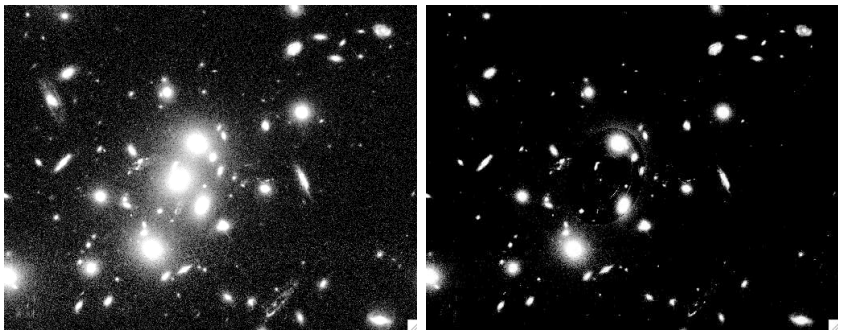

Figure D.4: CL0024 BCGs subtraction in Gunn-r filter. More details in the text.

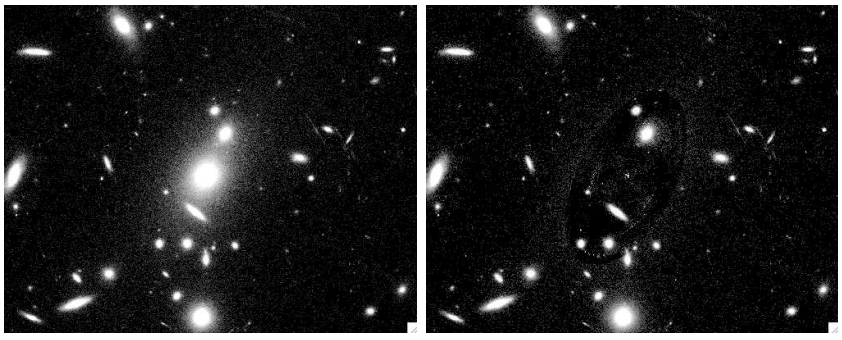

Figure D.5: MS1358 BCGs subtraction in Gunn-r filter. More details in the text.